UC 403
LBL-28958

Lawrence Berkeley Laboratory
UNIVERSITY OF CALIFORNIA

EARTH SCIENCES DIVISION

Acoustic and Elastic Diffraction Tomography and Its Application to Fracture Detection

M. A. C. Tura
(Ph.D. Thesis)

April 1990

For Reference

Not to be taken from this room

Prepared for the U.S. Department of Energy under Contract Number DE-AC03-76SF00098.

LBL-28958
Copy 1
Bldg. 50 Library.

DISCLAIMER

This document was prepared as an account of work sponsored by the United States Government. While this document is believed to contain correct information, neither the United States Government nor any agency thereof, nor the Regents of the University of California, nor any of their employees, makes any warranty, express or implied, or assumes any legal responsibility for the accuracy, completeness, or usefulness of any information, apparatus, product, or process disclosed, or represents that its use would not infringe privately owned rights. Reference herein to any specific commercial product, process, or service by its trade name, trademark, manufacturer, or otherwise, does not necessarily constitute or imply its endorsement, recommendation, or favoring by the United States Government or any agency thereof, or the Regents of the University of California. The views and opinions of authors expressed herein do not necessarily state or reflect those of the United States Government or any agency thereof or the Regents of the University of California.

LBL-28958

Acoustic and Elastic Diffraction Tomography and Its Application to Fracture Detection

M. A. C. Tura

Ph.D. Thesis

Department of Materials Science and Mineral Engineering
University of California

and

Earth Sciences Division
Lawrence Berkeley Laboratory
University of California
Berkeley, CA 94720

April 1990

This work was supported by the U.S. Department of Energy under
Contract No. DE-AC03-76SF00098.

Acoustic and Elastic Diffraction Tomography and Its Application to Fracture Detection

By

Mehmet Ali Can Tura

B.Eng. (University of Istanbul) 1983
M.S. (University of California) 1986

DISSERTATION

Submitted in partial satisfaction of the requirements for the degree of

DOCTOR OF PHILOSOPHY

in

ENGINEERING
MATERIALS SCIENCE AND MINERAL ENGINEERING

in the

GRADUATE DIVISION

of the

UNIVERSITY OF CALIFORNIA at BERKELEY

Approved:

Chair	Lane Johnson	25 April 90
Co-Chair	Alex Becker	26 April 90
	Thomas V. McEvily	13 APRIL 90
	T. F. Morrison	19 April '90

****

Acoustic and Elastic Diffraction Tomography and Its Application to Fracture Detection

Mehmet Ali Can Tura

Abstract

The inverse problem of fracture detection is approached using a waveform imaging method. The Born approximation is utilized for the linearization of the nonlinear inverse scattering problem. This method is preferable over existing linearized methods because it can account for the diffractions in the medium. The inversion is performed using two separate methods, the conventional backpropagation method and a quadratic programming method with constraints. Initially, the two-dimensional acoustic problem is discussed and the following developments are treated: estimation of a background velocity to be used in the inversion, sensitivity of the inversion algorithm to velocity and how this can be utilized to reduce unwanted wave modes, effect of the total field on the inversion, incorporation of free-surfaces, inversion with slanted boreholes, and two-and-a-half-dimensional corrections.

The inversion methods are applied to field data collected from a 10.0 by 21.5 m rectangular region where fractures were known to exist. This region was chosen from the Grimsel test site facility in Switzerland. A complete coverage of the rectangular area with 0.5 m spacing of three-component receivers and a piezoelectric source was carried out. A data processing scheme, necessary to bring the field data into a form that can be used in the inversion algorithms, is developed and applied to the crosshole field data. Results of backpropagation, quadratic programming and ray tomography crosshole

inversions agree well and show possible fracture zones which are confirmed by core samples.

The theory for the elastic case is developed next. The operators acting on the elastic parameters are discussed and their properties used for the inversion of individual elastic parameters. This inverse problem is in general ill-conditioned. A method that stabilizes the inverse problem using multi-frequencies and constrained angles is introduced and tested on synthetic data.

A fractured medium will in general be transversely isotropic. Therefore, the theory is extended to the transverse isotropy case for SH-waves and elliptical anisotropy for quasi-P waves. Reconstruction of multi-parameters in a transversely isotropic medium is also discussed. Incorporation of elliptical anisotropy is seen to improve the isotropic inversion results of the field data previously obtained.

Lane Johnson

Lane R. Johnson

Committee chairman

Dedication

This thesis is dedicated to my mother, Dr. Sabahat Sansa, for her love and courage

Acknowledgments

I would like to thank Dr. Lane Johnson for being an excellent advisor and my committee members for their support and constructive criticism throughout my graduate studies at Berkeley. Many useful discussions with my former advisor, Dr. Shimon Coen, have helped considerably in shaping this research. I am grateful to Dr. Ernest Major for providing the field data and resources of the Computational Center for Seismology at the Earth Science Division of the Lawrence Berkeley Laboratory. Many thanks to Fred Eastwood, Dr. Qiang Zhou, Dr. John Peterson, Jr., and Carlos Torres-Verdin who have contributed to the realization of this thesis. It has been a great experience to have had such exceptional fellow graduate students both at the Engineering Geosciences Department and the Geology and Geophysics Department.

I am fortunate to have such a great family whom have made it all possible. Last, but certainly not the least, I would like to thank Michéle Diana Marquet for her love and support, and Chris and Karen Marquet together with Carlos Torres-Verdin and Ekrem Yener for being such great friends.

This research was supported by the U.S. Department of Energy under contract No. DE-AC03-76SF00098.

Table of Contents

Chapter 1 Introduction 1

Chapter 2 Acoustic Inversion 8

2.1 Theory 8

2.1.1 Forward problem 8

2.1.2 Inversion by backpropagation 11

2.1.3 Inversion by quadratic programming 12

2.2 Wavenumber domain coverage 14

2.2.1 Single frequency 14

2.2.2 Multi-frequency 19

2.3 Synthetic point diffractor examples 20

2.4 Effects of velocity and frequency variation 23

2.5 Synthetic fracture examples 25

2.6 Inversion with the total field 30

2.7 Inversion with free-surfaces 32

2.8 Inversion with slanted boreholes 35

2.9 Inversion with point sources (2.5-D corrections) 38

Chapter 3 Application to Field Data 78

3.1 Geology of the FRI test site 78

3.2 Data gathering and analysis 79

3.3 Data processing 80

3.4 Inversion of the field data 83

3.4.1 S-wave and tube-wave reduction 84

3.4.2 Diffraction tomography inversion results 86

3.4.3 Comparison with transmission ray tomography 87

Chapter 4 Elastic Inversion 101

4.1 Forward problem 101

4.2 Inversion of SH-waves 104

4.3 Inversion of P-SV waves 109

4.3.1 P-to-P scattering inversion 113

4.3.2 Inversion of other modes 115

4.4 Parameter operators and synthetic examples 116

4.5 A stable inversion method 120

Chapter 5 Inversion in a Transversely Isotropic Medium 132

5.1 SH-wave forward problem 132

5.2 SH-wave inverse problem 135

5.2.1 Single parameter inversion 136

5.2.2 Multi-parameter inversion 137

5.3 Quasi-P wave inverse problem 139

5.3.1 Wavenumber domain coverage 140

5.4 Application to field data 142

Chapter 6 Discussion and Conclusions 155

Appendix A Acoustic Green's Function 160

Appendix B I. Decomposition of the Green's Function 162

Appendix B II. Derivatives of the Green's Function 164

Appendix C SH-wave Green's Function 166

Appendix D P-SV wave Green's Function 168

Appendix E SH-waves in a Transversely Isotropic Medium 172

Appendix F SH-wave Green's Function for Transverse Isotropy 175

References 177

Chapter 1

Introduction

In recent years, detection of fractures has become an important topic in geophysics. Enhanced oil recovery, storage of nuclear and toxic waste, hydrological and geothermal applications all rely on the accurate detection and characterization of fractures. Fracture detection with well logs has been routinely conducted and well-developed techniques for this purpose exist (for a review, see Crary et al., 1987; Suau and Gartner, 1980). Recently, imaging techniques similar to migration were introduced into well logging (Hornby, 1989). Currently, the constraint of well logging applications is that it can only give information about the fractures in a limited region surrounding the borehole and with a limited view. More recently, vertical seismic profiling (VSP) and crosshole measurements have been used for fracture detection and characterization. These approaches in general use measurements of P-waves, S-waves, and tube-waves and calculate velocity, shear-wave anisotropy and attenuation properties of the medium to determine bulk properties of the fractured rock mass (Stewart et al., 1981; Green and Mair, 1983; Fehler and Pearson, 1984; Carswell and Moon, 1984; Ollson et al., 1984; Beydoun et al., 1985; Hardin and Cheng, 1987; Majer et al., 1988).

In order to determine the detailed structure of fracturing, a ray equation or wave equation based inversion method can be used. A comparison of these two different inversion methods is given by Lo et al. (1987) and will also be discussed here. An example of the ray method applied to field data from granitic rock, similar to the field case investigated here, can be found in Wong et al. (1984). In fracture detection applications, because the fractured rock volume will be small compared to the background rock volume, although in some cases the variation in parameters being

inverted for can be large, weak scattering can in general be assumed. In addition, in most applications the background rock will be homogeneous, allowing the free-space Green's function to be used in the formulation of the inverse problem. As a result, diffraction tomography, a wave equation approach which assumes a homogeneous background medium and uses the Born or Rytov approximation to linearize the inverse scattering problem, is well suited for studying fractures.

Other linearized inversion methods besides diffraction tomography exist but in general have not been formulated for cases other than surface profiling (Lines, 1988). One of these methods uses the Kirchoff approximation to linearize the inverse problem. This method is particularly useful for imaging of sharp contrasts (Geoltrain and Cohen, 1989; Beylkin and Burridge, 1990). Other methods use the Born approximation with exact Green's function for a homogeneous background medium (Cohen and Bleistein, 1979) or WKBJ approximated Green's function in order to account for a variable background medium (Clayton and Stolt, 1981). The method of Cohen and Bleistein (1979) is quite similar to diffraction tomography except that they solve the inverse problem in the time-space domain for surface data whereas here it is solved in the frequency-wavenumber domain for any geometry of sources and receivers as long as they are along a line. Also, as is demonstrated in section 2.2, the diffraction tomography approach gives more physical insight into the inverse problem considered with its wavenumber domain coverage diagrams.

In cases where a homogeneous background approximation cannot be made, a ray tomography inversion, to obtain the slowly varying part of the background velocity (as well as source and receiver locations if there is any ambiguity), followed by a variable background high-resolution wave tomography inversion (using the ray theory inversion as a background model) can be expected to give good results (e.g. Pratt and

Goultry, 1989). In such a scheme incorporating a variable background, the Born approximation is still used and the Green's function has to be approximated as well.

In addition to the above mentioned methods, there is a whole group of imaging techniques developed by geophysicists under the name of migration (Gardner, 1985). The main difference between migration and linearized inversion is that inversion is expected to recover the physical properties of the scatterer as well as its shape whereas in migration only the shape is required. It is important to note that in practice the actual amplitude recovery of the scatterer in the linearized inversion approach is a difficult task and will be discussed in the field data applications of the methods.

Besides the linearized approach, there are also well-developed nonlinear approaches to the solution of the inverse problem. One of these is an iterative diffraction tomography method which calculates the higher order terms in the Born series (Lesselier and Vuillet-Laurent, 1985; Duchêne et al., 1985, 1987, 1988). Another approach uses a sinc-basis function to solve the nonlinear problem (Johnson and Tracy, 1983; Tracy and Johnson, 1983; Johnson et al., 1983; Berggren et al., 1986). Although both of these approaches have not entered geophysical applications in a wide sense, a generalized least-squares method is gaining popularity for surface seismic data (Tarantola, 1984; Mora, 1987; Beydoun and Mendes, 1989) and borehole data (Pratt and Goultry, 1989). These nonlinear approaches are computer intensive and may not be necessary. For example, in the fracture application considered here, linearization of the inverse problem via the Born approximation is expected to give good results and iterations should not be required.

The theory of diffraction tomography is discussed in section 2.1. The principles of the method were laid out by Wolf (1969). After being used in medical imaging (for a review, see Kak and Slaney, 1987) it was introduced into geophysical applications by Devaney (1984) for plane-wave sources. The method was formulated for line sources

and receivers by Wu and Toksöz (1987). In the diffraction tomography approach, the inversion is usually performed using either the backpropagation method or the interpolated inverse Fourier transform method (for a comparison, see Kak and Slaney, 1987). Here, the backpropagation method together with a new quadratic programming method is used. The advantage of the quadratic programming method is that constraints on the inversion velocities can be introduced. This method was recently applied to diffusion tomography by Zhou (1989), because a more stable inversion method was necessary to accommodate the dispersive nature of the electromagnetic fields (for a comparison, see Tura and Zhou, 1989). In fracture detection, this method is especially useful because the fracture velocity will in general be lower than the background velocity and this property can be used as a constraint in the inversion.

In this study, the Born approximation rather than the Rytov approximation is used to linearize the inverse problem because it is expected to give better results in the fracture case, since fractures are thin structures and form a sharp velocity contrast (see Kak and Slaney, 1987; Pratt and Worthington, 1988; Lo et al., 1988).

In section 2.4, the sensitivity of the inversion method to velocity and frequency is analyzed. In general, inversion with a lower velocity than the background velocity results in an under focusing whereas using a higher velocity results in an over focusing effect and both cases degrade the image quality. In both cases, due to the incorrect phase used in the backpropagation operators, energy leaks from the real part to the imaginary part of the image. The importance of this section is for two reasons. The first is to show the need to obtain an accurate background velocity for the inversion and the second is to show how the inversion algorithm will implicitly filter out modes of wave propagation with different velocities than the inversion velocity. This second point is discussed in section 3.4.1 and an example of the implicit filtering of fracture-generated tube-waves and S-waves in a P-wave inversion is given.

Section 2.6 discusses inversion with the total field rather than the scattered field. Although the approach of leaving the incident field in the inversion is expected to produce incorrect results in migration (Chang and McMechan, 1986), this is not observed in the diffraction tomography inversion results considered here.

In sections 2.7 and 2.8, extension of the theory to free-surfaces and slanted boreholes is formulated and applied to synthetic data. The free-surfaces are accounted for by constructing image sources and receivers, in which case the waves reflecting from the free-surface and interacting with the medium are turned from noise into valuable information. The result is a considerable improvement in the reconstruction of the physical parameters.

Slanted boreholes can be handled by introducing sine and cosine functions into the formulation of the problem. This case is especially useful for deep drilling applications where the boreholes can be bent. The problem is formulated for arbitrary angles of source and receiver boreholes and an application to synthetic data together with the wavenumber domain coverage diagrams is given.

The theory discussed in section 2.1 applies to line sources in a two-dimensional (2-D) medium, but in practice we have point sources and receivers. Therefore, the approach by Esmersoy (1986) is used in section 2.9 to generate an approximate filter that transforms a two-and-a-half-dimensional (2.5-D) medium (point sources and receivers in a 2-D medium) to a 2-D one. The 2.5-D corrections are also tested on synthetic data, before being applied to the field data, and give good results.

In chapter 3, the theory is applied to field data with the objective of detecting fractures. Although the basic theory of diffraction tomography has been available for some time, the method has not been applied to field data up to now. This is not only because of the difficulties associated with the data acquisition, but also because a new

data processing scheme (compared to conventional surface seismic data processing) is necessary to bring the data into a form to which the inversion methods can be applied.

The methods are applied to field data recorded in the FRI zone of the Grimsel test site facility in Switzerland. This zone was specifically chosen because of the fractures it contains. The geology of the region is discussed in section 3.1. Although the region was believed to consist of simple fracturing in a homogeneous granite, the medium was found to be more complex and anisotropic. Data gathering and field procedures are discussed in section 3.2.

The data processing scheme is introduced in section 3.3. This scheme initially estimates a background attenuation value and then, using the optimized first arrival times, finds a common source gather, common receiver gather and an average wavelet. The average wavelet is used to remove the incident field. The deconvolution is performed in the frequency domain for each of the three different wavelet types. The deconvolved data are muted at the beginning and windowed at the end of the traces in order to reduce random noise and unwanted wavetypes. The last step before inversion is the application of the 2.5-D corrections to the data set.

In section 3.4, inversion of the processed data is discussed. A method to estimate the background velocity to be used in the inversion is introduced and applied to the data. Finally, the data are inverted and the results are compared with the geology and the ray tomography inversions. It is seen that major fracture zones can be identified.

The elastic case is considered in chapter 4. Initially, multi-parameter inversion in the backpropagation and quadratic programming framework is investigated. In this approach, the parameters can be reconstructed by performing inversions for the same number of frequencies as the unknowns and solving the resulting matrix (Devaney, 1985). In general, this matrix will be ill-conditioned (Beylkin and Burridge, 1990) and the results can be improved by using a large number of frequencies. This approach will

improve the stability but will reduce resolution in turn. This or any alternate approach to solving the multi-parameter inverse problem will make use of the characteristics of the operators acting on the individual parameters. In section 4.4, these operators are displayed and analyzed. As a result, a method developed for acoustic medical imaging by Norton (1983) that utilizes the properties of each operator in an optimal fashion is extended to the elastic case and applied to the more difficult problem of seismic imaging. In this approach the most unstable parameters can be obtained in a stable fashion by use of the physical nature of the problem considered.

As will be discussed in chapter 3, a 7-8% transverse isotropy with the symmetry axis normal to the plane of fracturing is observed by displaying the first arrival time data as a function of ray angle. Therefore, in chapter 5, the theory is extended to account for transverse isotropy for SH-waves and elliptical anisotropy for quasi-P waves. The theory is developed for anisotropic velocity perturbations in an anisotropic background, but in the application of the methods to field data only the background is considered to be anisotropic. Multi-parameter inversion is also discussed in this chapter and the differences brought to the isotropic wavenumber domain coverage diagrams are shown. From the application of this theory to field data, it is seen that the anisotropy is not as strong as the predicted 7-8%. One reason for this can be given by noting that the anisotropy indicated by the travel time variations is not on a microscopic scale and can also be interpreted as being due to inhomogeneities associated with fracturing. It is also possible that diffraction tomography, a wave equation based inversion scheme, is not affected by anisotropy as strongly as transmission ray tomography.

Chapter 2

Acoustic Inversion

In this chapter, the inverse scattering problem of a 2-D acoustic medium with perturbations in parameters from a homogeneous background is considered. This problem is a linearized form of the general inverse scattering problem. The linearization is carried out by expressing the general nonlinear inverse problem in terms of a Born series and keeping the first (or linear) term. This approximation will hold if the changes in the parameters are small compared to the background. As a result, the method discussed in this thesis will apply only to a subset of the general class of inverse problems. The advantage of the method is that no approximations other than the Born approximation is necessary to solve the problem. Also, due to the analytical formulation, the inversion is fast compared to other methods.

The method described here can be applied to any scale of problems ranging from nondestructive testing of materials (small-scale or high-frequency) to large-scale geophysical problems. In the formulation of the problem, the sources and receivers are required to be on a line but the general problem can also be solved without this requirement.

2.1 Theory

2.1.1 Forward problem

The formulation of the forward problem has been treated extensively by various authors. Here, the recent formulation of Wu and Toksöz (1987) is followed.

The acoustic wave equation for a 2-D medium can be given as

$$\nabla^2 U(\vec{r}) + \frac{\omega^2}{c^2(\vec{r})} U(\vec{r}) = 0 \,, \tag{2.1}$$

in the source-free region. Here, $U(\vec{r})$ is the total pressure field at $\vec{r}$, where $\vec{r}$ is the distance from the origin of the coordinate system to the considered point in the 2-D medium, ω is the angular frequency, $c(\vec{r})$ is the velocity at $\vec{r}$, and ∇^2 is the Laplacian operator.

Defining the object function as

$$O(\vec{r}) = 1 - (c_0^2 / c^2(\vec{r})) \,, \tag{2.2}$$

where c_0 is the background velocity, equation 2.1 can be written as

$$\nabla^2 U(\vec{r}) + k^2 U(\vec{r}) = k^2 O(\vec{r}) U(\vec{r}) \,, \tag{2.3}$$

where $k = \omega/c_0$ is the wavenumber of the field in the background medium. Representing the total field as a superposition of the incident field and scattered field or $U(\vec{r}) = U_0(\vec{r}) + U_s(\vec{r})$, and using equation 2.1, equation 2.3 becomes

$$\nabla^2 U_s(\vec{r}) + k^2 U_s(\vec{r}) = k^2 O(\vec{r}) U(\vec{r}) \,. \tag{2.4}$$

The right-hand side of equation 2.4 can be treated as an equivalent source, therefore using the free-space Green's function the scattered field can be given as

$$U_s(\vec{r}) = - k^2 \int_v O(\vec{r}') U(\vec{r}') G(|\vec{r} - \vec{r}'|) \, d\vec{r}' \,. \tag{2.5}$$

Here, $G(|\vec{r} - \vec{r}'|) = \frac{i}{4} H_0^{(1)}(k|\vec{r} - \vec{r}'|)$ is the free-space Green's function in 2-D (see Appendix A), with $H_0^{(1)}$ being the zero order Hankel function of the first-kind and the integration is over the object volume. Using the Born approximation, $U \approx U_0 = G$, we have

$$U_s(\vec{r}_s, \vec{r}_g) = - k^2 \int_v O(\vec{r}) G(\vec{r}, \vec{r}_s) G(\vec{r}_g, \vec{r}) \, d\vec{r} \,. \tag{2.6}$$

Here, $\vec{r}_s$ and $\vec{r}_g$ are respectively the distances from the origin to the considered source and receiver. Taking the Fourier transform of the scattered field (see Appendix A for Fourier transform conventions) over the source and receiver lines (with the assumption that the sources and receivers lie along lines) and substituting the value of the 2-D Green's function in the transform domain (see section I of Appendix B), we have

$$\tilde{U}_s(k_s,k_g) = \frac{k^2}{4\gamma_s\gamma_g} \exp(i\gamma_s d_s + i\gamma_g d_g) \int_V O(\vec{r}) \exp[- ik(\hat{g} - \hat{i})\cdot\vec{r}] \, d\vec{r} \, . \tag{2.7}$$

Here, k_s and k_g are the wavenumbers over source and receiver lines, γ_s and γ_g are the perpendicular wavenumbers, $-\hat{i} = \hat{s}$ and $\hat{g}$ are the unit vectors in the direction of propagation of plane-waves from the source line to the receiver line, and d_s and d_g are the perpendicular distances from the source and receiver lines to the origin of the coordinate system (see d_s in Figure 2.1.1a). The integration in equation 2.7 is in the form of a Fourier transform, therefore we can write

$$\tilde{O}(\vec{K}) = \frac{4\gamma_s\gamma_g}{k^2} \tilde{U}_s(k_s,k_g) \exp[- i(\gamma_s d_s + \gamma_g d_g)] \, , \tag{2.8}$$

where $\vec{K} = k(\hat{g} - \hat{i}) = \hat{x}K_x + \hat{z}K_z$, with $\hat{x}$ and $\hat{z}$ being the unit vectors in the horizontal and vertical directions, and K_x and K_z being the horizontal and vertical wavenumbers.

Equation 2.8 yields a linear relationship between the object function and the Fourier transform of the scattered field.

Given the scattered field, the object function can be reconstructed by various methods. The two main methods used to accomplish this task are the backpropagation method and the interpolated inverse Fourier transform method (for a comparison, see Kak and Slaney, 1987). In the next section we review the backpropagation method and discuss a quadratic programming method to carry out the inversion.

2.1.2 Inversion by backpropagation

Taking the inverse Fourier transform of equation 2.8 and changing the variables of integration from K_x, K_z to k_s, k_g we have

$$O(\vec{r}) = \frac{1}{(2\pi)^2} \iint dk_s\, dk_g\, J(K_x,K_z|k_s,k_g) \frac{4\gamma_s\gamma_g}{k^2} \tilde{U}(k_s,k_g) \exp[-i(\gamma_s d_s + \gamma_g d_g)]$$

$$\times \exp[i(K_x x + K_z z)] , \qquad (2.9)$$

where $J(K_x,K_z|k_s,k_g)$ is the Jacobian of the transformation from K_x, K_z to k_s, k_g.

For different geometries of sources and receivers the mapping of k_s, k_g to K_x, K_z will be different. This mapping is discussed in sections 2.2 and 2.8. For various commonly used data gathering geometries this relationship can be given as follows: For the crosshole case of Figure 2.1.1a

$$K_x = \gamma_s - \gamma_g , \; K_z = k_s + k_g , \text{ therefore, } J(K_x,K_z|k_s,k_g) = \frac{|k_s\gamma_g + k_g\gamma_s|}{\gamma_s\gamma_g} . \qquad (2.10)$$

For the vertical seismic profiling with receivers in the borehole to the right of the medium or VSPR case of Figure 2.1.1b

$$K_x = k_s + \gamma_g , \; K_z = k_g - \gamma_s , \text{ therefore, } J(K_x,K_z|k_s,k_g) = \frac{|k_s k_g + \gamma_g\gamma_s|}{\gamma_s\gamma_g} . \qquad (2.11)$$

For the vertical seismic profiling with receivers in the borehole to the left of the medium or VSPL case of Figure 2.1.1c

$$K_x = k_s - \gamma_g , \; K_z = k_g - \gamma_s , \text{ therefore, } J(K_x,K_z|k_s,k_g) = \frac{|k_s k_g - \gamma_g\gamma_s|}{\gamma_s\gamma_g} . \qquad (2.12)$$

For the surface reflection profiling where sources and receivers are on the surface or SRP case of Figure 2.1.1d

$$K_x = k_g + k_s , \; K_z = -\gamma_s - \gamma_g , \text{ therefore, } J(K_x,K_z|k_s,k_g) = \frac{|k_s\gamma_g - k_g\gamma_s|}{\gamma_s\gamma_g} . \qquad (2.13)$$

Equation 2.9 can be discretized and solved using the Fourier transform of the observed scattered field and equations 2.10-2.13, depending on the data gathering geometry considered, to obtain a band-limited version of the object function. These finer points of the inversion are discussed in detail in the following sections.

2.1.3 Inversion by quadratic programming

The quadratic programming method can be applied to the considered problem by writing equation 2.7 as

$$p_i = \sum_{j=1}^{N} s_{ij} o_j \ , \tag{2.14}$$

where

$$p_i = \widetilde{U}_s(k_s,k_g) \frac{4\gamma_s\gamma_g}{k^2} \exp[- i(\gamma_s d_s + \gamma_g d_g)] \ , \tag{2.15}$$

and

$$s_{ij} = \exp[- i(K_x x + K_z z)] \ , \tag{2.16}$$

for the i *th* combination of (k_s,k_g) and the j *th* pixel, with $j = 1,.....,N = LK$, and o_j being the object function at the j *th* pixel (see Figure 2.1.1a). The mapping of k_s, k_g to K_x, K_z is as given in equations 2.10-2.13.

For M wavenumber combinations and N pixels, we can write

$$\mathbf{SO} = \mathbf{P} \ , \tag{2.17}$$

with $\mathbf{P} = [\ p_1, p_2,....., p_M]^T$, $\mathbf{O} = [o_1, o_2,....., o_N]^T$ and $\mathbf{S} = [s_{ij}]_{NxM}$. Minimizing the L_2 norm of the misfit of the solution $\mathbf{O}'$ or

$$\Omega(\mathbf{O}') = \|\mathbf{SO}' - \mathbf{P}\|^2 = \mathbf{O}'^T\mathbf{S}^T\mathbf{SO}' - 2\mathbf{P}^T\mathbf{S}^T\mathbf{O}' + \mathbf{P}^T\mathbf{P} \ , \tag{2.18}$$

subject to constraints

$$L_i \le O'_i \le U_i \; ; \; i = 1,.....,N \; , \tag{2.19}$$

where L_i and U_i are the lower and upper bounds on the object function, constitutes a quadratic programming problem with constraints.

Smoothing can be incorporated into the minimization problem (Peterson, 1986; Constable et al., 1987; Zhou, 1989) and will also cause stability. For this purpose, R_1 and R_2 are defined respectively to be the summations of the squared differences of the object function between adjacent pixels in the horizontal and vertical directions or

$$R_1 = \sum_{l=1}^{L} \sum_{k=2}^{K} (O_{(l-1)K+k} - O_{(l-1)K+k-1})^2 = \|\mathbf{D_1 O}\|^2 \, , \tag{2.20}$$

$$R_2 = \sum_{k=1}^{K} \sum_{l=1}^{L-1} (O_{lK+k} - O_{(l-1)K+k})^2 = \|\mathbf{D_2 O}\|^2 \, , \tag{2.21}$$

where K and L are the number of pixels in the horizontal and vertical directions (Figure 2.1.1a), and $\mathbf{D_1}$ and $\mathbf{D_2}$ are two N by N matrices. The problem in equation 2.18 can be reposed to minimize R_1 and R_2 together with the misfit or to minimize

$$\Omega(\mathbf{O'}) = \|\mathbf{SO'} - \mathbf{P}\|^2 + \lambda_1 \|\mathbf{D_1 O'}\|^2 + \lambda_2 \|\mathbf{D_2 O'}\|^2 \, , \tag{2.22}$$

where λ_1 and λ_2 are the damping parameters which control the smoothness in the horizontal and vertical directions. Equation 2.22 can be rewritten as

$$\Omega(\mathbf{O'}) = \mathbf{O'}^{\mathbf{T}}(\mathbf{S}^{\mathbf{T}}\mathbf{S} + \lambda_1 \mathbf{D}_1^{\mathbf{T}}\mathbf{D}_1 + \lambda_2 \mathbf{D}_2^{\mathbf{T}}\mathbf{D}_2)\mathbf{O'} - 2\mathbf{P}^{\mathbf{T}}\mathbf{S}^{\mathbf{T}}\mathbf{O'} + \mathbf{P}^{\mathbf{T}}\mathbf{P} \, . \tag{2.23}$$

The matrix $\mathbf{D}_1^{\mathbf{T}}\mathbf{D}_1$ can be given as

$$\mathbf{D}_1^{\mathbf{T}}\mathbf{D}_1 = \begin{bmatrix} \mathbf{H} & 0 & 0 & ..... & 0 \\ 0 & \mathbf{H} & 0 & ..... & 0 \\ 0 & 0 & \mathbf{H} & ..... & 0 \\ 0 & 0 & 0 & ..... & 0 \\ 0 & 0 & 0 & ..... & \mathbf{H} \end{bmatrix}_{L \times L} \, , \tag{2.24}$$

with

$$\mathbf{H} = \begin{bmatrix} 1 & -1 & 0 & \cdots\cdots & 0 \\ -1 & 2 & -1 & \cdots\cdots & 0 \\ 0 & -1 & 2 & \cdots\cdots & 0 \\ 0 & 0 & -1 & \cdots\cdots & -1 \\ 0 & 0 & 0 & \cdots\cdots & 1 \end{bmatrix}_{K\times K}, \tag{2.25}$$

and the matrix $\mathbf{D}_2^T\mathbf{D}_2$ can be given as

$$\mathbf{D}_2^T\mathbf{D}_2 = \begin{bmatrix} \mathbf{I} & -\mathbf{I} & 0 & \cdots\cdots & 0 \\ -\mathbf{I} & 2\mathbf{I} & -\mathbf{I} & \cdots\cdots & 0 \\ 0 & -\mathbf{I} & 2\mathbf{I} & \cdots\cdots & 0 \\ 0 & 0 & -\mathbf{I} & \cdots\cdots & -\mathbf{I} \\ 0 & 0 & 0 & \cdots\cdots & \mathbf{I} \end{bmatrix}_{L\times L}, \tag{2.26}$$

with

$$\mathbf{I} = \begin{bmatrix} 1 & 0 & 0 & \cdots\cdots & 0 \\ 0 & 1 & 0 & \cdots\cdots & 0 \\ 0 & 0 & 1 & \cdots\cdots & 0 \\ 0 & 0 & 0 & \cdots\cdots & 0 \\ 0 & 0 & 0 & \cdots\cdots & 1 \end{bmatrix}_{K\times K}. \tag{2.27}$$

Therefore, the aim of the quadratic programming method is to minimize equation 2.23 subject to the constraints given in equation 2.19 in order to obtain a smoothed inversion. This minimization problem can also be formulated as a linear programming problem and different methods of smoothing can also be incorporated.

2.2 Wavenumber domain coverage

An advantage of the perturbation theory approach for solving the inverse problem is that physical insight into the nature of the problem can be gained from the analytical formulation possible. In this section we demonstrate this aspect of the method.

2.2.1 Single frequency

Equation 2.8 implies that each scattered plane-wave observed from a plane-wave source, or each $(\hat{\mathbf{s}},\hat{\mathbf{g}})$ pair, at a certain wavenumber k, will give a value of the object

function's transform $\tilde{O}(\vec{K})$ at $\vec{K} = \hat{x}K_x + \hat{z}K_z = k(\hat{g} - \hat{i})$, where $\hat{i} = -\hat{s}$. If we were to know $\tilde{O}(\vec{K})$ for every $\vec{K}$ in the (K_x,K_z) space, we could, in theory, reconstruct $O(\vec{r})$ uniquely (using inverse Fourier transforms), which would in turn yield the unknown velocity $c(\vec{r})$ uniquely.

In practice, there are several reasons that prevent us from obtaining a full coverage of $\tilde{O}(\vec{K})$ in the $\vec{K}$ space. The first one is that we are dealing with discretely spaced sources and receivers, therefore we will have a discrete coverage of $\tilde{O}(\vec{K})$. The second is that if we were able to generate and record plane-waves at every possible angle, the resulting coverage would be limited to a circle of radius $2k = 2\omega/c_0$. Due to the nature of the source function as well as temporal and spatial aliasing constraints the data will be band-limited, therefore k will be band-limited as well and large wavenumbers or sharp variations in the object function will not be recovered. The third reason is that in geophysical applications we are not able to generate and record plane-waves at every possible angle due to the discrete spacing and constrained geometry of the sources and receivers in the field. Usually, we are limited to the geometries shown in Figures 2.1.1 and here we discuss how these geometries further reduce the wavenumber domain coverage. In section 2.8 more general geometries are discussed and treated in a similar manner.

In order to understand the mapping between the transform of the observed scattered field and the object function's transform, we will start from a simple example. For a plane-wave source in the $\hat{s} = \hat{x}$ direction and scattered plane-waves measured from 90° to -90° from the $\hat{x}$-axis, the coverage of $\tilde{O}(\vec{K})$ will be as shown by the semi-circle on the right side of Figure 2.2.1. This figure is obtained by first drawing $k\hat{s}$ and then each $k\hat{g}$ (note that $|k\hat{s}| = |k\hat{g}| = k$, therefore the drawn vector lengths are equal). Extending this mapping procedure, if we were able to generate plane-waves from all angles and measure the scattered field at all angles as well we would have coverage in a

circle of radius 2k which is the maximum coverage possible. The plane-wave decomposition discussed in section I of Appendix B and utilized in section 2.1 enables us to follow this approach, but the angles that the plane-waves can be generated will be discrete and depend on the specific geometry of the experiment considered.

Using equations 2.10-2.13 we plot the coverage of the object function in the wavenumber domain for the geometries of Figures 2.1.1 in Figures 2.2.2. Since the object function $O(\vec{\mathbf{r}})$ is real, or the medium is assumed to be non-attenuative, $\tilde{O}(\vec{\mathbf{K}})$ is complex conjugate symmetric, or $\tilde{O}^*(\vec{\mathbf{K}}) = \tilde{O}(-\vec{\mathbf{K}})$, therefore knowing $\tilde{O}(\vec{\mathbf{K}})$ we can obtain $\tilde{O}$ at $-\vec{\mathbf{K}}$ by taking its complex conjugate. These additional wavenumbers are included in all wavenumber domain plots throughout this thesis, unless stated otherwise.

The wavenumber domain plots are normalized so that the Nyquist wavenumber over the source and receiver lines is unitary or $\Delta x = \Delta s = \Delta g = \pi$, since $k_s^N = k_g^N = (2\pi)/(2\Delta x)$. Also, c_0 is set to 2π since then k will be equal to the frequency used in the inversion.

In Figures 2.2.2, the inversion frequency is 1 Hz and 40 sources and receivers are used for each geometry considered. Each point in this figure represents a single plane-wave pair from the source line to the receiver line. Increasing the number of sources and receivers (or equivalently, extending the length of the borehole) would result in a plot with denser points, which would especially help increase the coverage in the less dense sections near the boundaries of the plotted coverage, but the actual boundaries of these regions would not change. In other words, the boundaries of the plotted regions are fixed by the choice of the experiment geometry or by the source and receiver positioning which can only generate plane-waves in a certain range. For example, a sample in one of the two inner circles of Figure 2.2.d cannot be obtained with the SRP geometry.

In the crosshole case, Figure 2.2.2a, the coverage in the horizontal direction is sparse or the image will not be resolved well in the vertical direction. In addition, the sampling of the object function's transform is dense at low-wavenumbers and becomes sparse as the wavenumbers increase.

In the VSPR case, Figure 2.2.2b, the coverage of the object function's transform is quite well other than the region where the horizontal wavenumbers equal the vertical wavenumbers.

In the VSPL case, Figure 2.2.2c, the coverage of the object function's transform is again quite well other than the region where the horizontal wavenumbers equal the vertical wavenumbers with opposite sign.

In the SRP case, Figure 2.2.2d, the coverage in the horizontal direction has two large holes, therefore the image will not be resolved well in the vertical direction similar to the crosshole case. In addition, the sampling of the object function is quite dense in the high-wavenumber sections contrary to the crosshole case.

Considering the coverage of the crosshole case and the SRP case two conclusions can be drawn: i) If the SRP or backscattering experiment were to be done inside boreholes vertical to the surface rather than on the surface, the combination of this experiment with the crosshole experiment would give a coverage in a circle of radius 2k, i.e., the maximum coverage possible (rotate Figure 2.2.2d by 90° and add to Figure 2.2.2a), ii) The SRP or backscattering experiment recovers high-wavenumber components of the object function or sharp changes in the object whereas the crosshole or forward scattering experiment recovers low-wavenumber components of the object function or smooth changes in the object. Therefore, in a single frequency inversion algorithm these two geometries are complementary and both should be carried out to obtain a good image.

In Figures 2.2.2, the inversion frequency was conveniently chosen to give an inversion wavenumber k which had the same value as the Nyquist wavenumber of the source and receiver lines, k_s^N and k_g^N, yielding maximum coverage. If the inversion frequency is chosen to have a lower value, the coverage will shrink, preserving its shape, into a circle of radius 2k, with the new k value. Therefore, unsampled regions, especially near the boundaries, can be obtained by performing inversions for a range of frequencies. By averaging these inversions the general results can be improved. This will be discussed later on in detail.

The frequency band width of the data is determined by the source spectrum and Nyquist criteria or sampling. As long as we are in the usable frequency range, the inversion frequency can be increased as well as decreased. Figures 2.2.3 show the wavenumber domain coverage for a frequency of 1.25 Hz and for 40 source and receiver pairs for each geometry. In this case, the coverage will grow to a circle of radius 2k or 2.5 m^{-1} as is reflected in the axis of these plots. We see that although higher wavenumbers can be obtained in the inversions, the range of plane-waves that can be generated is further reduced (compare Figures 2.2.2 and 2.2.3).

The analysis given in this section is helpful in designing an experiment and can be summarized as follows. Depending on the shape of the object being imaged, determine how to lay out sources and receivers to get the best coverage. Depending on the size and shape of the object being imaged, determine the largest wavenumber to be used in the inversion (for a discussion, see Aki and Richards, 1980, p.749). Using the largest wavenumber and the background velocity, determine the maximum frequency using $f_{max} = kc_0/(2\pi)$. Use a source that has a band width larger than the maximum frequency and sample in time accordingly. Determine the ideal source and receiver sampling using, $\Delta x = (2\pi)/(2k)$. Gather data with this sampling. After processing,

invert the data at various frequencies starting from f_{max} and decreasing to a frequency determined by experience, and average the resulting inversions.

2.2.2 Multi-frequency

In this section, we look at a property of the backscattering or SRP geometry. From Figure 2.2.2d it can be seen that if the scattered field is recorded only when $k\hat{\mathbf{s}} = -k\hat{\mathbf{g}}$ or only the plane-wave component of the scattered field in the opposite direction to the plane-wave from the source is recorded, for all possible angles of plane-waves that can be generated with this geometry, values of $\tilde{O}(\vec{\mathbf{K}})$ will be obtained on a circle of radius 2k, the outer rim of the coverage diagram of Figure 2.2.2d. By varying the frequency, which will in effect change the radius of this circle, and taking only the components of the scattered field discussed above, it can be seen that coverage in a circle of radius 2k, the maximum coverage possible can be approximately obtained. For 40 source and receiver pairs and for 20 frequencies from 0 to 1 Hz with 0.05 Hz steps, this mapping is shown in Figure 2.2.4a. Although most of the available data have not been used in this mapping the coverage is well distributed and close to the maximum coverage achievable. Some problems with the horizontal wavenumber directions, which are inherent to the SRP geometry, still remain. The coverage outlined here is actually the coverage of Born inversion in the time domain since now we are dealing with a multi-frequency experiment.

In field data, because of the source function, low-frequencies will not be obtainable, therefore in practice we will have the coverage shown in Figure 2.2.4b instead.

If the object being imaged is a point diffractor in the center of the medium then the amplitude of the object function in the wavenumber domain will be a constant. In such a case the amplitude in the radial direction of Figure 2.2.4b will give the source

function. The amplitude as a function of angle on a specific circle, or a specific frequency, will give the source radiation pattern at that frequency and for the considered angle, since the value observed at each angle will correspond to a plane-wave incident and recorded at that same angle.

Using this approach, the properties of the source used, i.e., source function and radiation pattern, could be obtained from a scale model backscattering experiment consisting of a point diffractor and the results used in field applications for deconvolution of the wavelet and radiation pattern corrections.

2.3 Synthetic point diffractor examples

In this section we apply the backpropagation algorithm, equation 2.9, in order to invert for a point diffractor. Here we only consider the geometries discussed in Figures 2.1.1. The importance of the point diffractor example is that the Born approximation in this case is exact (single scattering) and imaging a point diffractor will give us the impulse response of the geometry considered showing the resolving capabilities of the various data acquisition geometries.

The synthetic data are generated using the pseudo spectral finite difference (PSFD) method (Gazdag, 1981; Kosloff and Baysal, 1982; Eastwood, 1988), with absorbing boundary conditions, which will give the exact total field (including multiples). This method is used in the single scattering case as an initial test of the method before applying it to more complicated models. The source function used in the generation of the data is the derivative of a Gaussian pulse. The model considered is shown in Figure 2.3.1a. Here, 20 sources are placed on the left boundary with 0.5 m intervals. The receivers are placed with the same 0.5 m intervals so as to form the VSPR (20 receivers on the top boundary), crosshole (20 receivers on the right boundary), and backscattering (20 receivers on the left boundary) geometries. The background velocity

is 4800 m/s and the diffractor is located at the center of the medium with a velocity of 4500 m/s.

In the data processing, first the incident field is obtained by a run through the medium without the diffractors and then subtracted from the total field observed. This is followed by a wavelet deconvolution in the frequency domain using the inverse of the source function mentioned above.

The inversion wavelength is chosen to be at least 1 m or twice the source or receiver spacing, therefore, the maximum frequency used in the inversion is 4800 Hz.

Figure 2.3.1b is the result of the crosshole inversion at 4800 Hz. The sidelobes in the vertical direction can be clearly seen in the image, indicating low-resolution in this direction as discussed in the previous section. Figure 2.3.1c is the image obtained by averaging frequencies ranging from 3900 to 4800 Hz, with 122 Hz intervals. The ' > ' and ' < ' pattern occuring due to limited view at the diffractor location in Figure 2.3.1b is reduced in Figure 2.3.1c because of the improved coverage near the boundaries of Figure 2.2.2a.

Figure 2.3.1d is the inversion result for the VSPL geometry with the receiver borehole to the left of the image area (see Figure 2.1.1c). Here the diffractor is recovered quite well with some ambiguity in the horizontal, vertical and 45° from the horizontal toward the vertical directions. Figure 2.3.1e is the average of the images in the same frequency range as the previous example. The result of Figure 2.3.1e is only slightly better than Figure 2.3.1d due to the good single frequency coverage in the VSP geometries (see Figure 2.2.2c). In the VSPR case with the receiver borehole to the right of the image area, the same results can be expected with ambiguity in the opposite 45° direction.

Figures 2.3.1f and g are the single frequency and averaged inversion results of the backscattering experiment with sources and receivers on the left boundary of the

image area. As expected the resolution in the horizontal direction is not good (Figure 2.3.1f) and some improvements can be seen in the averaged result (Figure 2.3.1g).

These examples demonstrate what can be expected from each of the different geometries considered without the effects of the size and variations in amplitude of the object being imaged. As long as the assumption of linearity holds, imaging of more complicated structures can be analyzed by assuming a superposition of the point diffractor inversion results.

We next investigate how the inversion will be affected by the location of the diffractors and spatial sampling. Forward data can be generated conveniently using equation 2.6 with the 2-D Green's function. These data will only contain single scattering and will be used in cases where multiple scattering is not prominent. The data generated by this method will be used throughout this thesis and will be called Born forward data.

For the following examples, Born forward data are generated for a 10 m horizontal by 20 m vertical area with 40 sources and receivers separated by 0.5 m intervals and placed in a crosshole fashion (along the z direction in FIgures 2.3.2). The point diffractor has a 4500 m/s velocity and the background velocity is 5500 m/s. For these velocity values, the object function will have a value of - 0.5 at the diffractor location and 0.0 elsewhere.

In Figures 2.3.2a-d we display the absolute value of the inversion results with the imaginary part of the image plotted next to the real part, separated by 5 empty traces. The inversions are performed at a wavelength of 1 m, twice the source and receiver spacing, or at 5500 Hz which is the maximum frequency, f_{max}, for this example. The impulse at the origin or top-left corner is a reference value, in order to compare images, set to - 0.5 or the expected amplitude of the object function.

For Figures 2.3.2a-c the diffractor is located at 5.25 m horizontal and 10.25 m vertical. In Figure 2.3.2a the data are inverted with 0.5 m horizontal and vertical sampling, in Figure 2.3.2b with 0.25 m sampling and in Figure 2.3.2c with 0.125 m sampling. It is seen that when the diffractor is not located at the inversion grid points and if the inversion is performed at the maximum frequency, the spatial sampling must be at least half the source and receiver spacing. Denser spatial sampling beyond this value brings no apparent improvement to the images (Figure 2.3.2c). This is so because when the data are inverted at the maximum frequency of 5500 Hz, they do not contain such high-wavenumber components of the object function necessitating a denser spatial sampling than 0.25 m.

Figure 2.3.2d is the result of an inversion at 5500 Hz with 0.25 m spatial sampling when the diffractor is located at 10.25 m horizontal and 0.25 m vertical. Although the result in this figure is quite good it is not as good as the inversion obtained when the diffractor is located near the center of the model (Figure 2.3.2b). This is so because as the object moves away from the center of the medium the limited view problem becomes more severe. Therefore, structures near the boundaries of the inversion area will not be reconstructed as well as structures in the interior.

2.4 Effects of velocity and frequency variation

The background velocity used in the inversion and the frequency which the inversions are being performed at are two important variables that will be further investigated.

In the inversion of field data, the background velocity is unknown. Therefore, it is important to investigate its effect on the inversion by inverting synthetic data for a range of velocities around the correct background velocity. This experiment will lead us to the development of a method to estimate the background velocity.

For the velocity and frequency experiments the same model used in the last part of the previous section is considered. The only difference is that now the point diffractor is located at 5 m horizontal and 10 m. Figures 2.4.1a-e show respectively the inversion results for inversion velocities ranging from 5420 to 5580 m/s with 40 m/s intervals. Although the range of velocity variations is small compared to the background velocity, the effect on the inversion is drastic. The result in Figure 2.4.1c is the inversion with the correct background velocity of 5500 m/s. As the velocity varies, the backpropagation is done with an incorrect phase of propagation, therefore, the image becomes out of focus and the energy leaks from the real part to the imaginary part of the image.

Besides the conceptual understanding it brings, this example suggests a method to estimate an accurate inversion velocity for the field data cases. This follows from observing the ratio of the energy in the real part of the image to the imaginary part as a function of inversion velocity. In the case with the correct inversion velocity (Figure 2.4.1c) this ratio is high (in an ideal case of full coverage it would be infinity), otherwise it decreases depending on the accuracy of the inversion velocity being used. Figure 2.4.2 is a display of this function. This figure shows the ratio of the maximum of the absolute value of the real part to the maximum of the absolute value of the imaginary part of the inversions for intervals of 5 m/s. We see that this figure resembles a Gaussian function and peaks at the correct inversion velocity of 5500 m/s. In chapter 3, this test will be used on the field data and shown to be very effective not only in estimating an accurate inversion velocity but also in estimating other inversion parameters.

In the previous sections we took averages of the inversions at different frequencies without a detailed discussion. Here, we demonstrate that such an approach is plausible and can be used to improve image quality.

Using the same model as above, we generate Born forward data at various frequencies and invert the data at the corresponding frequencies. The inversion results are shown in Figures 2.4.3a-d for frequencies of 4028 Hz, 4517 Hz, 5005 Hz and 5493 Hz. In the low-frequency end or Figure 2.4.3a, the image is smoother and more spread out. As the frequency increases, the image becomes sharper and tighter as expected. Overall, the inversions in these figures give a good reconstruction for all the frequencies and therefore, averaging of images is encouraged and used in the applications considered here.

In field data applications where there is noise from various sources, such as random noise or from various other wave modes, averaging is especially useful since it will increase the signal-to-noise ratio in the inverted images.

2.5 Synthetic fracture examples

In this section the pseudo spectral finite difference (PSFD) method is used to generate forward data for a model representing the field case to which the methods are applied to in chapter 3. The model has a background velocity of 5500 m/s and a perturbation velocity of 4500 m/s along two lines representing two fracture zones (Figure 2.5.3). A 10 m horizontal by 20 m vertical area is considered with a sampling interval of 0.25 m in space and 0.008 ms in time. As mentioned in section 2.3, absorbing boundary conditions are implemented and the source function used is the derivative of a Gaussian pulse.

For a source located at S_1 (see Figure 2.5.1a) a snapshot of the wavefield as it is propagating in the medium is shown in Figure 2.5.1b. In this figure the outer circle represents the incident field and the inner semi-circle represents the scattered field. Due to the absorbing boundary conditions, as the wavefield approaches the boundary it is attenuated. Figure 2.5.1c is yet another snapshot of the wavefield where the source is

now located at S_2 in Figure 2.5.1a. Here we see several inner semi-circles. These additional semi-circles are due to the multiple scattering in the zone representing the fractures. This example demonstrates that the data generated by this method are exact in the sense that multiple scattering in the medium is contained in the data. Because the inversion is performed using the Born approximation, which only accounts for single scattering, the inversion results of this data set will indicate how well the Born approximation holds in the fracture case considered.

For the experiment considered (see Figure 2.5.2a), 40 sources are placed on the left boundary of the model and the receivers are located as follows: The first 20 receivers are located on the top boundary (indicated by an A) and form the VSPL geometry, the next 40 receivers are located on the right boundary (indicated by a B) and form the crosshole geometry and the remaining receivers are located on the left boundary (indicated by a C) and form the backscattering geometry. The sources and receivers are spaced with 0.5 m intervals. Figures 2.5.2b-d are respectively the seismograms for the source at the top-left corner, at center-left and at the bottom-left corner (indicated by S_1, S_2 and S_3 in Figure 2.5.2a) and all receivers along lines A, B and C. In general, the incident field is the strong first arriving wavefield in these figures and the scattered field is the secondary arrivals. Because the initial time steps are calculated analytically, when a source is located close to a receiver, the initial section of the considered trace will be truncated, as can be seen in the first trace of Figure 2.5.2b. These sections are later generated and added to the appropriate traces.

In the data processing, the incident field is obtained by a run through the medium without the diffractors and then subtracted from the total field observed, followed by a wavelet deconvolution in the frequency domain.

Due to aliasing considerations, discussed in sections 2.2.1 and 2.3, the inversions are done at a maximum frequency of 5500 Hz with sampling in the horizontal

and vertical directions of 0.5 m. For comparison reasons, the input model is shown once again in Figure 2.5.3. The backpropagation inversion result for the crosshole geometry at 5500 Hz is shown in Figure 2.5.4a. The quadratic programming inversion result for the same geometry at 5500 Hz with negativity constraints, which force the object function to have values less than zero (or the inversion velocities to be less than the background velocity), is shown in Figure 2.5.4b. In most applications concerning fractures negativity constraints can be used since the fracture velocity will in general be lower than the background velocity. It can be seen that the Born approximation is quite valid in the simulated fracture case and the inversions give good results.

In the crosshole geometry inversion with the backpropagation and the quadratic programming methods three distinct features can be seen. The first is the extension of the object (or simulated fractures) along the line of diffractors. This is due to the limited coverage in the wavenumber domain or limited view, arising from the source and receiver geometry in the crosshole configuration. The next is the sidelobes parallel to the diffractor line seen in Figure 2.5.4a. This is because the coverage of the object function in the wavenumber domain is discrete and limited to low-wavenumber components by the inversion being done at a specific finite frequency. It is not seen in the quadratic programming inversion of Figure 2.5.4b because of the information given to the inversion by the negativity constraints. The third effect is that the diffractor line is thick and the diffractors are not distinctly resolved as can be seen by a comparison with the input model (Figure 2.5.3). This is caused by the wavenumber domain coverage being constrained to low-wavenumbers (slow variations) in the crosshole case. This will also contribute to the stretching of the object along the line of diffractors.

Figure 2.5.4c is a cross-section of the images in Figures 2.5.3, 2.5.4a and b taken at a horizontal distance of 5 m in the vertical direction from 0 to 20 m. The sidelobes in the backpropagation inversion can be seen here clearly. In this figure, the

values of the backpropagation inversion for velocities greater than the background velocity of 5500 m/s are seen to be quite high. This is because although the inversion is a sinc-type function in the object function domain, the transformation from the object function domain to the velocity domain is nonlinear and will increase the artificial velocities higher than the background velocity. A normalized plot of this transformation is shown in Figure 2.5.4d and displays the large variation for positive values of the object function.

Contrary to the backpropagation method, the quadratic programming method does not have sidelobes. This is due to the additional information brought to the inversion by the negativity constraints which will not allow positive sidelobes to exist, resulting in a considerable improvement, although the limited view problem is inherent to the crosshole geometry and will still exist. In the backpropagation case, the sidelobes can be reduced by inverting the data at a range of frequencies and averaging the results, thereby increasing the coverage of the object function in the wavenumber domain.

For the crosshole geometry, the average of backpropagation inversions from 2440 to 5500 Hz with 122 Hz intervals is shown in Figure 2.5.4e. The inversion result suggests once again that in the backpropagation method averaging of images is useful and improves the image quality.

Computationally, the single frequency quadratic programming inversion is an order of magnitude slower than the multi-frequency backpropagation inversion. Due to this reason and also because negativity constraints can be applied to the field data case we consider here, we do not average quadratic programming inversion results throughout this thesis, although this can be done.

For the backscattering geometry with sources and receivers in the left borehole, the average of backpropagation inversions from 2440 to 5500 Hz with 122 Hz intervals is shown in Figure 2.5.4f. Although the image quality is not good and only the tip of the

diffractors close to the source-receiver locations are resolved, they are resolved distinctly or each diffractor is resolved. This is because the coverage of the backscattering experiment contains high-wavenumber components of the object function, contrary to the crosshole case (see section 2.2.1 for a discussion).

Figure 2.5.4g is the VSPL geometry inversion results averaged over the same range of frequencies as for the previous examples. Here we do not see the diffractors at all. This is because the Fourier transform of a line passing through the origin is a line in the transform domain in a direction perpendicular to the direction of the line transformed. Therefore, the diffractor line at - 45° from the horizontal lies at 45° from the horizontal in the wavenumber domain. Considering Figure 2.2.2c, we see that this is exactly the region where we do not have coverage of the object function in the VSPL geometry, therefore we will not be able to reconstruct such a model with this data gathering geometry.

To prove this point we generate Born forward data for the VSPR geometry with 0.25 m spacing of diffractors, as in the PSFD examples, using equation 2.6 with the 2-D Green's function. This data will only contain single scattering but this does not affect the argument being made here. Inversion of the data gives a good image, as shown in Figure 2.5.4h, and proves the point discussed above, since for the VSPR geometry we have a good coverage of the diffractor line in the wavenumber domain (see Figure 2.2.2b).

As a result, depending on the information available regarding the object to be imaged, a certain geometry can be designed and used in order to obtain the best coverage. For this case it is seen that the VSPR geometry is preferable over the VSPL geometry.

One important point before closing this section will be made on how diffractor separation will affect the inversion results. To discuss this point we generate Born

forward data for a 10 m horizontal by 20 m vertical area consisting of a cluster of diffractors along a line starting at 2.5 m horizontal and 5.0 m vertical and ending at 7.5 m horizontal and 15.0 m vertical with a 4500 m/s velocity. We will only consider the crosshole geometry with 0.5 m spacing of sources and receivers. The background velocity in these examples is 5500 m/s and the inversion frequency is 5500 Hz.

Figures 2.5.5a-d are respectively the inversions of the medium with 10, 20, 200 and 2000 diffractors on the specified line. The spatial sampling in the inversion is 0.25 m. For 10 diffractors, Figure 2.5.5a, the horizontal spacing of diffractor is 0.5 m and the vertical is 1.0 m, therefore the inversion results are quite good. For 20 diffractors, Figure 2.5.5b, the horizontal spacing of diffractors is 0.25 m and the vertical is 0.5 m and the reconstruction is not as good. This is because the diffractors are located at a separation where the discrete Fourier transform of the model cannot be sampled well with this data set. As the diffractor spacing approaches continuity, Figures 2.5.5c and d, the inversion results start improving, since, the Fourier transform of a continuous function is continuous as well. This example outlines the differences to be expected when going from a discrete case (synthetic examples) to a continuous case (field data).

2.6 Inversion with the total field

The wavefield that is measured in the field is the total field but in the inversion the scattered field is required, therefore, the scattered field must be extracted from the total field. This is an important step in the data processing. In synthetic examples this is accomplished by generating the incident field via a run through the medium without the diffractors. This is not possible in field applications.

There have been several approaches to solving this problem. A common one is to remove the incident field before the inversion, as is done here with the field data. Another less frequented approach is to deconvolve the incident field after the inversion

(Chang and McMechan, 1986). In this section we apply the inversion routine to the incident field and total field, in order to see their effects on the image, and from these results suggest another method for removing the incident field from the total field.

We use the PSFD data generated in the previous section for the inversions in this section. Application of the inversion algorithm to the incident field of the crosshole case (receivers on line B in Figure 2.5.2a), averaged from 2440 to 5500 Hz with 120 Hz steps, is given in Figure 2.6.1a. Here we see that most of the energy has been backpropagated to the boundaries of the inversion region and the interior contains only minor anomalies. As a result, we claim that in the specific field case we are considering the incident field does not cause any considerable damage to the inversions.

Figure 2.6.1b shows the averaged inversion of the total field with the 1 m region surrounding the boundaries set to the background velocity value. As can be seen, although the incident field is left in, the inversion is quite successful.

These two inversions suggest another method for removing the incident field effects. This method would involve a simple step of subtraction of the total field image from the incident field image. The resulting image from the application of this process is shown in Figure 2.6.1c and is almost identical to the image obtained by subtracting the incident field prior to inversion, Figure 2.5.4e. This follows from the linearity of the inversion process. For this method, it is again necessary to estimate the incident field in order to form the incident field inversion. The advantage of the method is that we can visually see the effect of the incident field on the inversion.

On field data, both methods; removal of the incident field before inversion and removal of the incident field after the total field inversion must be carried out in order to asses the effectiveness of either scheme.

For the other geometries, removal of the incident field is a routine procedure. In VSP type applications removal of the downgoing wavefield is actually the removal of

the incident field. In the SRP case, the incident field arrives at early times and is in general decoupled from the scattered wavefield. In exploration seismology an additional reduction of the incident wavefield, together with surface-waves, is obtained by using angle sensitive receiver arrays.

2.7 Inversion with free-surfaces

In most field applications the inversion area is bounded by free-surfaces. The inversion algorithm in its present state cannot account for the free-surfaces and all wavefields interacting with the free-surface will enter into the inversion as noise and disturb the resulting image.

The PSFD method is used to generate forward data for a medium bounded by free-surfaces from above and below or a double free-surface case. The model considered is shown in Figure 2.7.1a and other than the free-surfaces it is the same as the one used in section 2.5. As shown in Figure 2.7.1a, in this experiment 40 sources are placed on the right boundary and the receivers are located as follows: The first 20 receivers are located on the top boundary (indicated by an A), the next 40 receivers are located on the right boundary (indicated by a B) followed by 20 receivers on the bottom boundary (indicated by a C) and 40 receivers receivers on the left boundary (indicated by a D). Figure 2.7.1b shows a snapshot of the incident field in this medium when the source is located at S_1 in Figure 2.7.1a. The incident field reflected from the upper and lower boundaries can be identified clearly. The resulting seismograms from such a medium are quite complicated compared to the full-space seismograms, as can be seen in Figure 2.7.1c. In this Figure, the source is at the center of the right borehole (indicated by S_2 in Figure 2.7.1a) and all receivers along lines A, B, C and D are shown.

All images in this section are the result of averaging inversions from 2440 to 5500 Hz with 122 Hz intervals. The inversion result of the crosshole data containing the

scattered field is shown in Figure 2.7.2a. Here we see a sharp horizontal zone in the center of the image. In addition, the boundaries are disturbed as well but cannot be seen in this figure because in order to better resolve the interior of the image, a 1 m region from the boundaries to the interior of the image is set to the background value. Inversion of the crosshole data with the total field is shown in Figure 2.7.2b, where the full image in the object function space is shown in order to see the effects of the incident field at the boundaries. The positive zone in the center of the image in the scattered field case, Figure 2.7.2a, has become negative in this case showing that part of the reflected incident field from the free-surface is mapped here. Inverting only the incident field, Figure 2.7.2c, shows this point more clearly.

The VSPR inversion result of the scattered field with free-surfaces and sources in the right borehole, Figure 2.7.2d, shows the effects of the free-surfaces as positive images next to the actual negative images. In the VSP case, the images are not harmed by the free-surfaces as much as they are in the crosshole case. The VSP inversion with the total field is shown in Figure 2.7.2e and this result is again better than the crosshole inversion with the total field.

To improve the inversion results of the crosshole case, we will use image sources and receivers. This approach can be outlined by referring to Figures 2.7.3. The wavefields observed at the receiver from a medium with a single diffractor and a free-surface are as displayed in Figures 2.7.3a-c. Waves 1 and 2 are part of the incident field (see Figure 2.7.1b) whereas waves 3 to 6 are part of the scattered field. In the direct inversion discussed above waves 4 to 6 are multiply scattered fields that harm the inversion. By removing the free-surface, and constructing the image source and receiver, parts of the unwanted waves 4 to 6 become singly scattered waves and contribute to the inversion rather than harming it.

The construction of the image source and receiver for a single source-receiver pair is done by going to a 2 by 2 matrix from the 1 by 1 matrix as follows: The (S,G) pair data are assigned to the (S, image G) and (image S, G) pair with a negative sign and to the (image S, image G) pair with a positive sign, where the locations of S, G, image S and image G are as given in Figures 2.7.3d-f.

As a result of this mapping some of the multiply scattered fields are transformed into singly scattered fields. Figures 2.7.3b and e show how a wave interacting with the free-surface and the object is now only interacting with the object or how the double scattering has become single scattering and will now contribute to the inversion. Figures 2.7.3c and f shows how a third order scattering is transformed into a first order scattering, again contributing to the inversion. The outlined wave types in Figure 2.7.3e and f are the waves that are transformed into signal from noise. Although the dominant part of the wavefield is transformed successfully by this method, there will still be second and higher order scattering terms, caused by the interaction of the wavefield with the object and free-surfaces, that will harm the inversion. In the synthetic examples we will see that most of these unwanted wavefields will actually be mapped to the free-surface locations. The extension of this method to multisources and multireceivers or more free-surfaces is straightforward. An important result of this approach is that the limited view problem is considerably reduced because of being able to account for the steep-angled shown in Figures 2.7.3e and f.

The absolute value of the averaged crosshole geometry inversion result, with the application of the image method, is shown in Figure 2.7.4a. Here the vertical axis is 60 m long, rather than 20 m, due to the increase in the inversion area resulting from the application of the imaging method to two free-surfaces. In this image we see that some of the second or higher order scattered fields map to the free-surface locations as mentioned previously. Folding this image at the two free-surface locations and

averaging the resulting three images, we arrive at Figure 2.7.4b. In Figures 2.7.4b and c a 1 m region from the boundaries to the interior of the image is set to the background value in order to remove the free-surface effects from the boundaries of the images. The free-surface effects at the center of the image in Figure 2.7.2a do not exist in Figure 2.7.4b and the result is even better than the full-space inversion of Figure 2.5.4e, especially at the tip of the diffractors. This is due to the increase in the wavenumber domain coverage made possible by being able to account for plane-waves with steeper angles, generated by the wavetypes shown in Figures 2.7.3e and f. The total field inversion with the image principle is shown in Figure 2.7.4c. The inversion technique is quite successful even for the total field which includes the waves denoted by a 2 in Figure 2.7.3a.

2.8 Inversion with slanted boreholes

In some field applications, the geometry of the measurements may not be the conventional ones we have discussed. A common example is the geometry that can result from the diversion of a drill bit during drilling. In general, the diffraction tomography method can accommodate any layout of sources and receivers as long as they are on lines. This requirement is necessary due to the Fourier transforms taken over the source and receiver lines. In cases were the boreholes are highly curved, the problem must be reconsidered.

In this section, the diffraction tomography method is generalized to slanted boreholes. This generalization is accomplished by constructing the rotation operator that gives the mapping of (k_s,k_g) to (K_x,K_z) for the considered geometry. Here we give a general formula that can be applied to any configuration of slanted boreholes. Figure 2.8.1 shows the general layout that will be considered with the angles Φ and η being arbitrary in the 0° to 180° range. The experiment area is divided into three regions,

where each region requires a different formulation. For each region, the possible range of plane-waves that can be generated due to the geometry of the source and receiver lines is shown in Figure 2.8.1, with $\tilde{\mathbf{i}}$ and $\tilde{\mathbf{g}}$ being the unit vectors in the direction of propagation of plane-waves from the source line and to the receiver line.

From Figure 2.8.1 it can be seen that the rotation or mapping of (k_s,k_g) to (K_x,K_z) can be accomplished by a formulation incorporating angles. Noting that k_s is the wavenumber along the source line, k_g is the wavenumber along the geophone line and γ_s and γ_g are the perpendicular wavenumbers to k_s and k_g, we can write, for region I

$$K_x = k_s\,|\cos(\Phi)| - \gamma_s \sin(\Phi) + k_g\,|\cos(\eta)| + \gamma_g \sin(\eta)$$

$$K_z = k_s \sin(\Phi) - \gamma_s \cos(\Phi) + k_g \sin(\eta) - \gamma_g \cos(\eta)\,, \tag{2.28}$$

for region II

$$K_x = k_s\,|\cos(\Phi)| + \gamma_s \sin(\Phi) + k_g\,|\cos(\eta)| + \gamma_g \sin(\eta)$$

$$K_z = k_s \sin(\Phi) + \gamma_s \cos(\Phi) + k_g \sin(\eta) - \gamma_g \cos(\eta)\,, \tag{2.29}$$

and for region III

$$K_x = k_s\,|\cos(\Phi)| - \gamma_s \sin(\Phi) + k_g\,|\cos(\eta)| - \gamma_g \sin(\eta)$$

$$K_z = k_s \sin(\Phi) - \gamma_s \cos(\Phi) + k_g \sin(\eta) + \gamma_g \cos(\eta)\,. \tag{2.30}$$

The Jacobian of the transformation can be obtained by taking the derivatives of these equations with respect to (k_s,k_g) and is found to be, for region I

$$J(K_x,K_x|k_s,k_g) =$$

$$\Big|\, |\cos(\Phi)| \sin(\eta) + |\cos(\Phi)| \cos(\eta)\,\frac{k_g}{\gamma_g} + \sin(\eta)\sin(\Phi)\,\frac{k_s}{\gamma_s} + \sin(\Phi)\cos(\eta)\,\frac{k_s k_g}{\gamma_s \gamma_g}$$

$$- \sin(\Phi)\,|\cos(\eta)| - \cos(\Phi)\,|\cos(\eta)|\,\frac{k_s}{\gamma_s} + \sin(\eta)\sin(\Phi)\,\frac{k_g}{\gamma_g} + \cos(\Phi)\sin(\eta)\,\frac{k_s k_g}{\gamma_s \gamma_g}\,\Big|\,, \tag{2.31}$$

for region II

$$J(K_x,K_x|k_s,k_g) =$$

$$\Big| \, |\cos(\Phi)| \sin(\eta) + |\cos(\Phi)| \cos(\eta) \frac{k_g}{\gamma_g} - \sin(\eta) \sin(\Phi) \frac{k_s}{\gamma_s} - \sin(\Phi) \cos(\eta) \frac{k_s k_g}{\gamma_s \gamma_g}$$

$$- \sin(\Phi) \, |\cos(\eta)| + \cos(\Phi) \, |\cos(\eta)| \frac{k_s}{\gamma_s} + \sin(\eta) \sin(\Phi) \frac{k_g}{\gamma_g} - \cos(\Phi) \sin(\eta) \frac{k_s k_g}{\gamma_s \gamma_g} \Big| \, , \quad (2.32)$$

and for region III

$$J(K_x,K_x|k_s,k_g) =$$

$$\Big| \, |\cos(\Phi)| \sin(\eta) - |\cos(\Phi)| \cos(\eta) \frac{k_g}{\gamma_g} + \sin(\eta) \sin(\Phi) \frac{k_s}{\gamma_s} - \sin(\Phi) \cos(\eta) \frac{k_s k_g}{\gamma_s \gamma_g}$$

$$- \sin(\Phi) \, |\cos(\eta)| - \cos(\Phi) \, |\cos(\eta)| \frac{k_s}{\gamma_s} - \sin(\eta) \sin(\Phi) \frac{k_g}{\gamma_g} - \cos(\Phi) \sin(\eta) \frac{k_s k_g}{\gamma_s \gamma_g} \Big| \, . \quad (2.33)$$

Depending on the region being studied, substituting the above equations into equation 2.9 where appropriate, will give the inversion formula for the geometry considered.

The wavenumber domain coverage diagrams can be drawn using equations 2.28 to 2.30 for each region and for any angle of source and receiver boreholes in the indicated range.

In practice, there are some constraints on the use of regions II and III. The experiment being conducted must be in the form of a transmission experiment, which images the area in between the source and receiver boreholes (or region I), or backscattering experiment, which requires the sources and receivers to be in the same borehole, bringing a constraint to regions II and III. With this in mind, we see that the wavenumber domain coverage diagrams in the backscattering experiment will be the same for regions II and III.

The coverage of the object function in the wavenumber domain is shown for two cases with 32 source and receiver pairs. In the first case, the source borehole angle Φ is 135° and the receiver borehole angle η is 45°. This geometry forms a backscattering experiment. The coverage in region II is the same as the coverage in region III and is shown in Figure 2.8.2a. This coverage is the conventional backscattering coverage mentioned before (see Figure 2.2.2d) but now it is rotated 45° since the source and receiver borehole (or line) angle has changed by 45°. The second example is for a transmission experiment where Φ is 90° and η is 45°. The coverage in region I, Figure 2.8.2b, resembles the crosshole coverage (Figure 2.2.2a) with the main difference being that the coverage in Figure 2.8.2b is spread out to a wider area and therefore the inversion result for this case can be expected to be better.

The inversion algorithms are demonstrated on Born forward data, for the case where Φ is 90° and η is 45°. The model is a 32 m by 32 m area with 1 m intervals of sources and receivers. There are three diffractors, as can be seen in Figure 2.8.3a, with an object function value of 0.16 at the diffractor locations and 0.0 elsewhere. The single frequency inversion for region I is seen in Figure 2.8.3b and the reconstruction of the object function is quite good.

2.9 Inversion with point sources (2.5-D corrections)

The theory discussed in the previous sections was for line sources whereas in field applications data are gathered from point sources. If we assume the medium is 2-D and imaged by point sources, a correction to the data must be applied for the recorded wavefield to represent a line source wavefield.

To correct for the 2.5-D effects of the wavefield in the inversion we follow the approach by Esmersoy (1986). The Green's function for a point source in a 3-D medium can be given as $G(\vec{\mathbf{R}},\vec{\mathbf{r}}_s) = \exp[ik|\vec{\mathbf{R}} - \vec{\mathbf{r}}_s|]/\{4\pi|\vec{\mathbf{R}} - \vec{\mathbf{r}}_s|\}$ where,

$\vec{R} = \hat{x}x + \hat{y}y + \hat{z}z$. Substituting this point source Green's function into equation 2.6 and assuming a 2-D medium we have

$$U_s^{2.5\text{-}D}(\vec{r}_s,\vec{r}_g) = -\frac{k^2}{16\pi^2}\iint_{z\ x} O(\vec{r})\left[\int_y \frac{\exp[ik|\vec{R}-\vec{r}_s|]}{|\vec{R}-\vec{r}_s|}\frac{\exp[ik|\vec{r}_g-\vec{R}|]}{|\vec{r}_g-\vec{R}|}dy\right]dx\,dz\,. \quad (2.34)$$

The integral in brackets over y can be evaluated using the method of steepest descent (Brekovskikh, 1980) yielding

$$[\ldots] \cong \left(\frac{2\pi}{k}\right)^{1/2}\exp[\frac{i\pi}{4}]\frac{\exp[ik(|\vec{r}-\vec{r}_s|+|\vec{r}_g-\vec{r}|)]}{(|\vec{r}-\vec{r}_s|+|\vec{r}_g-\vec{r}|)^{1/2}\,|\vec{r}-\vec{r}_s|^{1/2}\,|\vec{r}_g-\vec{r}|^{1/2}}\,. \quad (2.35)$$

Substituting equation 2.35 into equation 2.34 we have

$$U_s^{2.5\text{-}D}(\vec{r}_s,\vec{r}_g) = -\left[\frac{k^3}{128\pi^3}\right]^{1/2}\iint_{z\ x} O(\vec{r})\frac{\exp\left[\frac{i\pi}{4}\right]\exp[ik(|\vec{r}-\vec{r}_s|+|\vec{r}_g-\vec{r}|)]}{(|\vec{r}-\vec{r}_s|+|\vec{r}_g-\vec{r}|)^{1/2}\,|\vec{r}-\vec{r}_s|^{1/2}\,|\vec{r}_g-\vec{r}|^{1/2}}$$

$$dx\,dz\,. \quad (2.36)$$

In the line source case, the asymptotic form of the 2-D Green's function can be given as

$$G(\vec{r},\vec{r}') \cong \frac{i}{4}\left(\frac{2}{\pi k|\vec{r}-\vec{r}'|}\right)^{1/2}\exp[-i\pi/4]\exp[ik|\vec{r}-\vec{r}'|]\,, \quad (2.37)$$

substituting in equation 2.6 we get

$$U_s(\vec{r}_s,\vec{r}_g) \cong -\frac{ik}{8\pi}\iint_{z\ x} O(\vec{r})\frac{\exp[ik(|\vec{r}-\vec{r}_s|+|\vec{r}_g-\vec{r}|)]}{|\vec{r}-\vec{r}_s|^{1/2}\,|\vec{r}_g-\vec{r}|^{1/2}}\,dx\,dz\,. \quad (2.38)$$

Equation 2.36 and 2.38 indicate that by knowing the scattered field from a 2.5-D medium, we can obtain the approximate field of an equivalent 2-D medium by the relation

$$U_s = -[ikc^3]\, w(\omega) * \left[\frac{\exp[i3\pi/4]}{|\omega|^{3/2}}\, U_s^{2.5\text{-}D}\right], \tag{2.39}$$

where $w(\omega) = i\,\mathrm{sgn}(\omega)/(2|\omega|^{3/2})$, and ' * ' denotes convolution. Therefore, for the 2.5-D corrections the wavelet deconvolved frequency domain scattered field data are first multiplied by the filter $\exp[i3\pi/4]/\omega^{3/2}$, then inverse Fourier transformed and multiplied by a second filter $\{t/(2\pi)\}^{1/2}$, which is the inverse Fourier transform of $w(\omega)$, and finally Fourier transformed again and multiplied by $[-ikc^3]$, to yield the approximate 2-D scattered field in the frequency domain. To form the relation in equation 2.39, $w(k) * \exp[ikd] = (2\pi)^{1/2}\, d^{1/2} \exp[ikd]$, is used where $k = \omega/c_0$ and $d = |\vec{r} - \vec{r}_s| + |\vec{r}_g - \vec{r}| > 0$.

2.5-D Born forward data can be generated using equation 2.6 with the 3-D Green's function. In section 2.5 it was demonstrated that multiple scattering effects were not prominent in the fracture case considered and Born data could be used for simulation. Born forward data are generated at various frequencies for the same model as the PSFD forward data model (Figure 2.5.3) except that spatial sampling is 0.5 m rather than 0.25 m, that is, there are half as many diffractors on the lines representing the fractures in the Born forward data case.

Figure 2.9.1a shows the inversion of the data without the 2.5-D corrections. The application of the 2.5-D processing discussed above to the Born forward data forms the corrected data. The result of inverting the corrected data with the backpropagation algorithm is shown in Figure 2.9.1b. In both applications, the images are averaged from 2760 to 5520 Hz with 120 Hz intervals and the absolute value of the real and imaginary parts of the object function are displayed. The value at the origin or upper-left corner is the reference or expected value of the inversion.

It is seen that inverting a point source data set with a line source inversion algorithm without corrections (Figure 2.9.1a) results in a reconstruction of diffractors

with wrong amplitudes. As can be seen from this figure, not only are the resultant values smaller than the reference or expected value but also, due to the phase-shift, the imaginary part of the image has nearly the same amplitude as the real part. These effects are removed in the resulting image of the corrected data (Figure 2.9.1b) and a good inversion is obtained. The resulting amplitudes are slightly lower than the expected amplitudes due to the smoothing brought by averaging of frequencies.

It is seen that the 2.5-D corrections are quite useful, especially when seeking the correct amplitudes in the inversion results. In addition, the real to imaginary ratio test, outlined in section 2.4, will perform well only if these corrections are applied to the data set, since then the phase-shift will be removed and the amplitude ratios preserved.

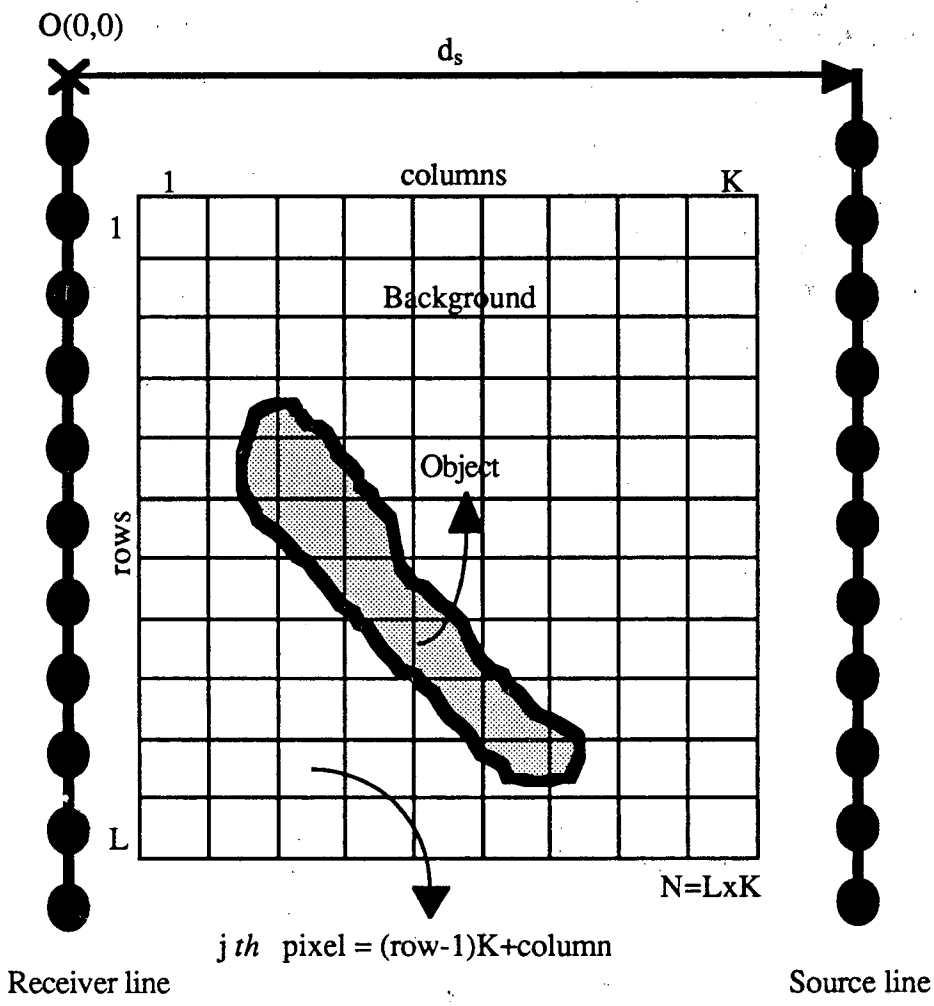

Figure 2.1.1a Crosshole data gathering geometry and gridding conventions.

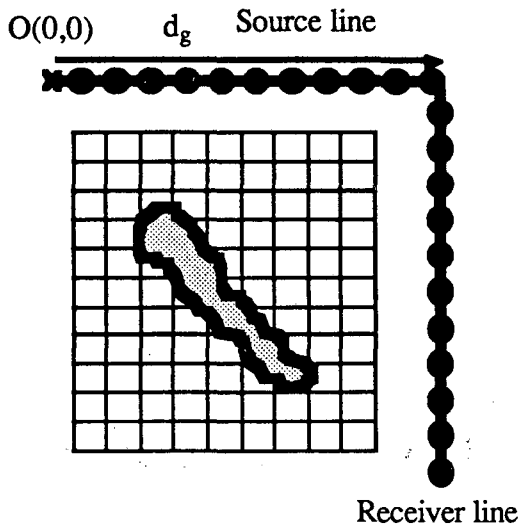

Figure 2.1.1b VSPR data gathering geometry.

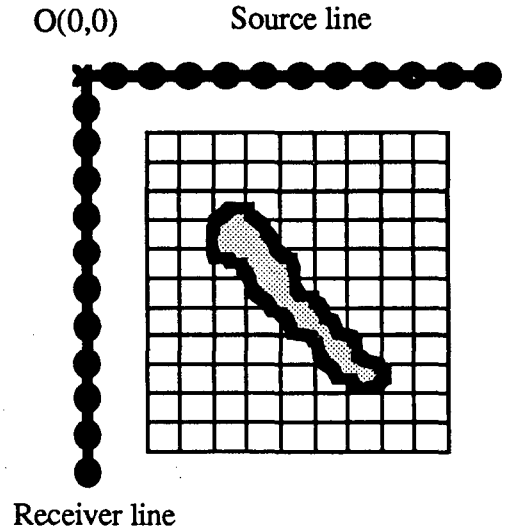

Figure 2.1.1c VSPL data gathering geometry.

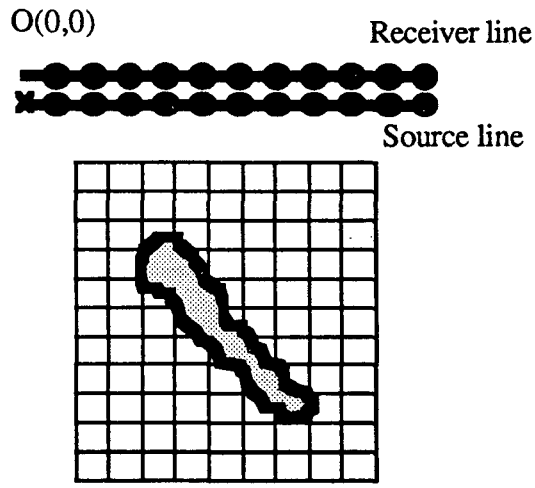

Figure 2.1.1d SRP data gathering geometry.

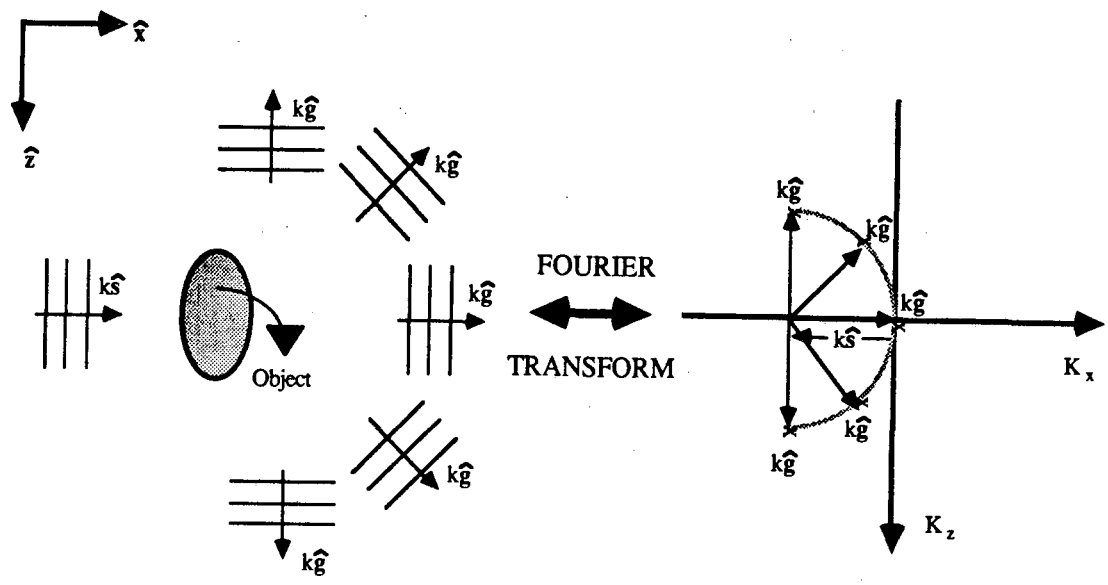

Figure 2.2.1 Plane-waves imaging the object (left side) and the information they carry on the object in the wavenumber domain (right side).

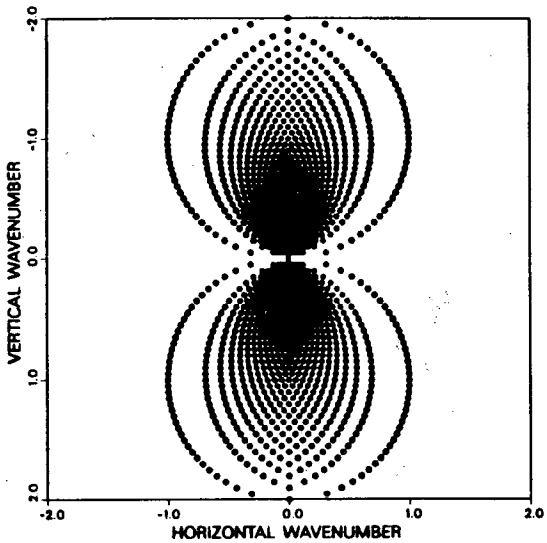

Figure 2.2.2a Crosshole geometry.

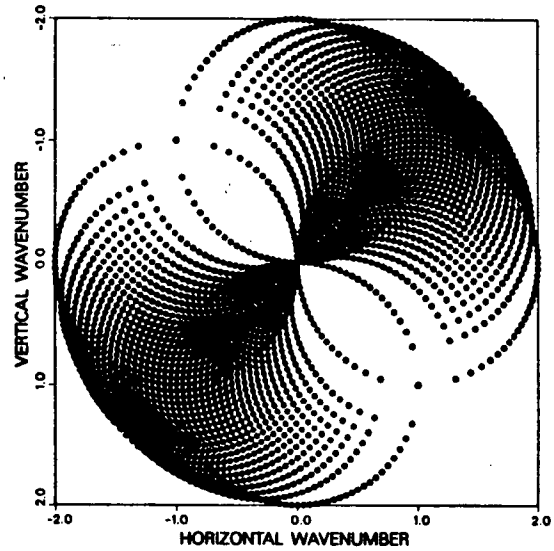

Figure 2.2.2b VSPR geometry.

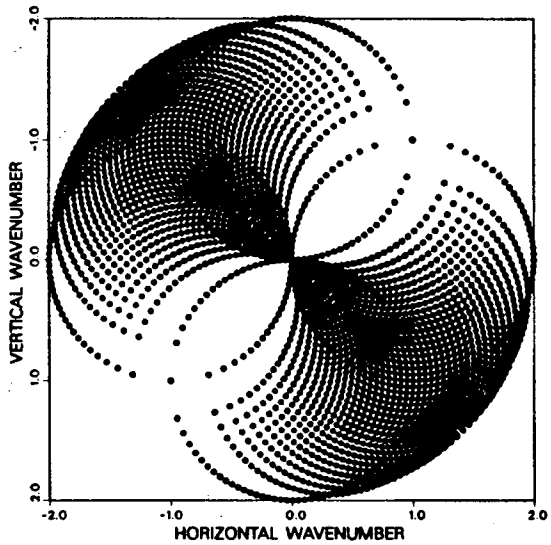

Figure 2.2.2c VSPL geometry.

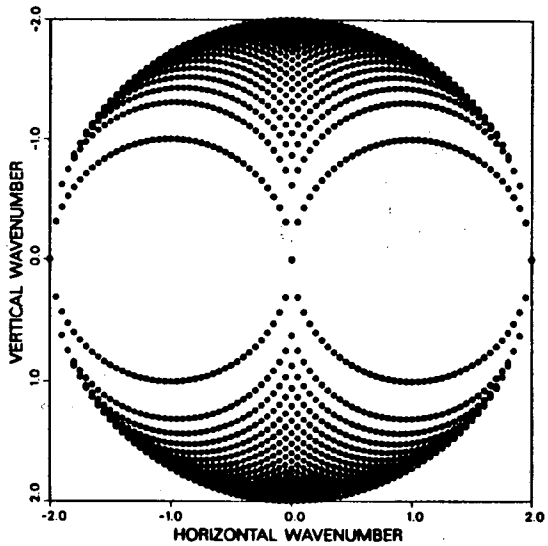

Figure 2.2.2d SRP geometry.

Figure 2.2.2 Coverage of object function in the wavenumber domain

for $\lambda = 2\Delta s = 2\Delta g$.

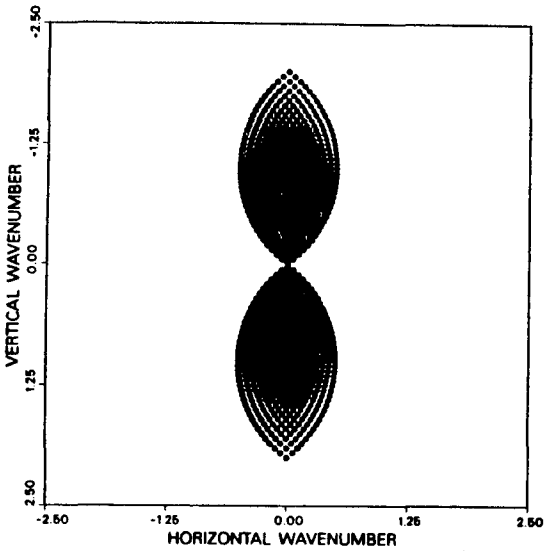

Figure 2.2.3a Crosshole geometry.

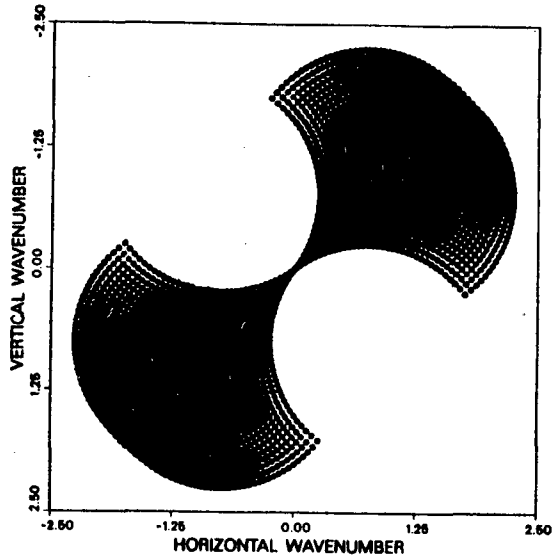

Figure 2.2.3b VSPR geometry.

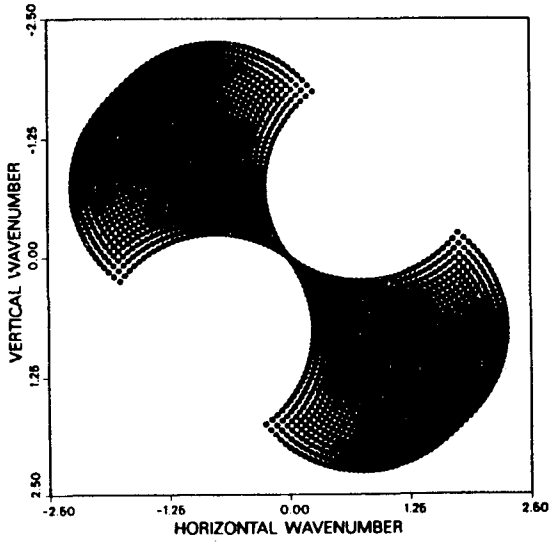

Figure 2.2.3c VSPL geometry.

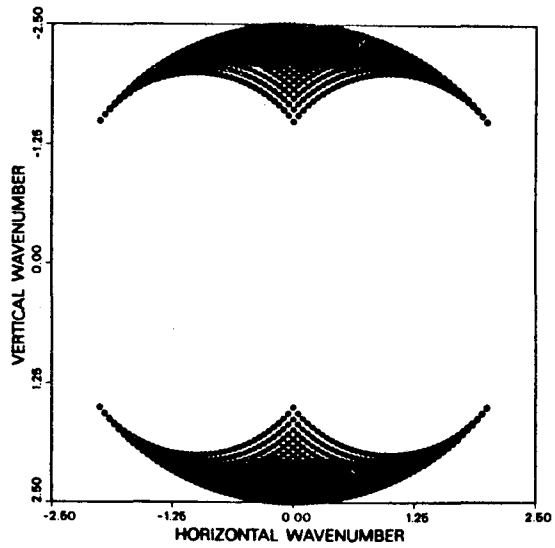

Figure 2.2.3d SRP geometry.

Figure 2.2.3 Coverage of object function in the wavenumber domain

for $\lambda = 1.6\Delta s = 1.6\Delta g$.

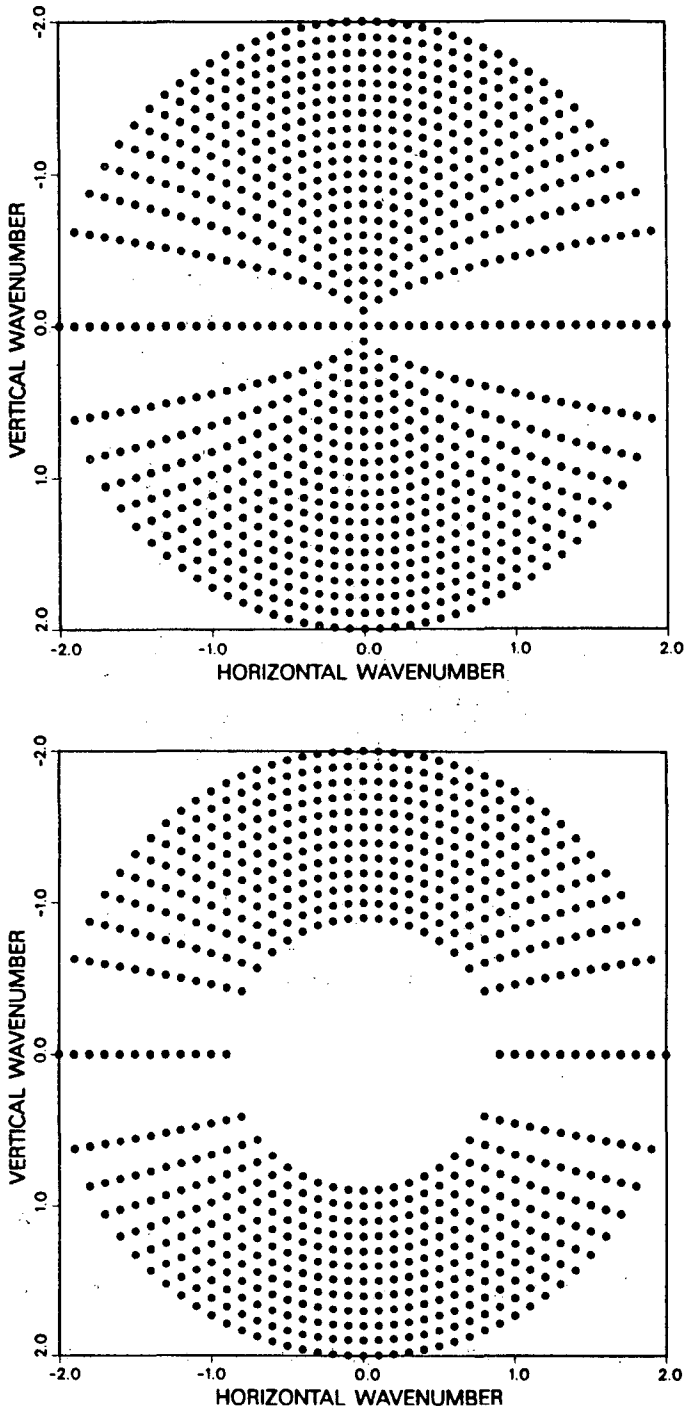

Figure 2.2.4a,b Multi-frequency SRP geometry coverage a) Without (top) and b) With (bottom) the source function.

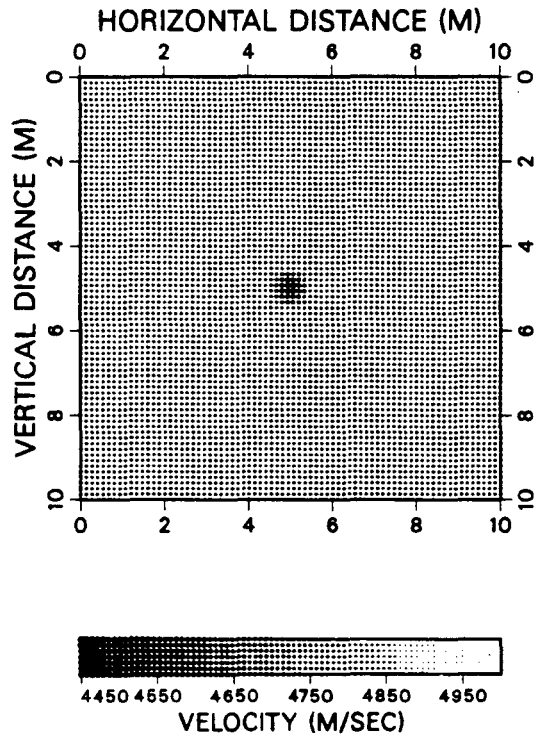

Figure 2.3.1a Input model to the PSFD method. Background velocity is 4800 m/s, diffractor velocity is 4500 m/s. 20 sources are placed on the left boundary, and 20 receivers are placed on each of the top, right and left boundaries of the medium.

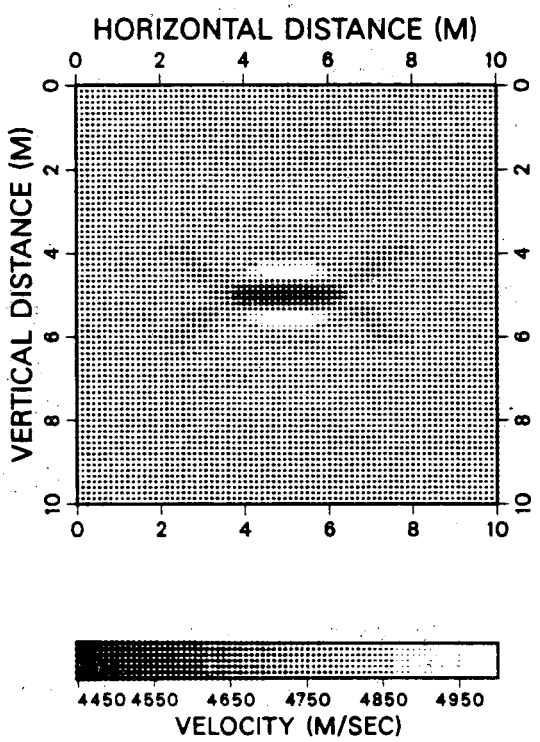

Figure 2.3.1b Crosshole inversion at 4800 Hz.

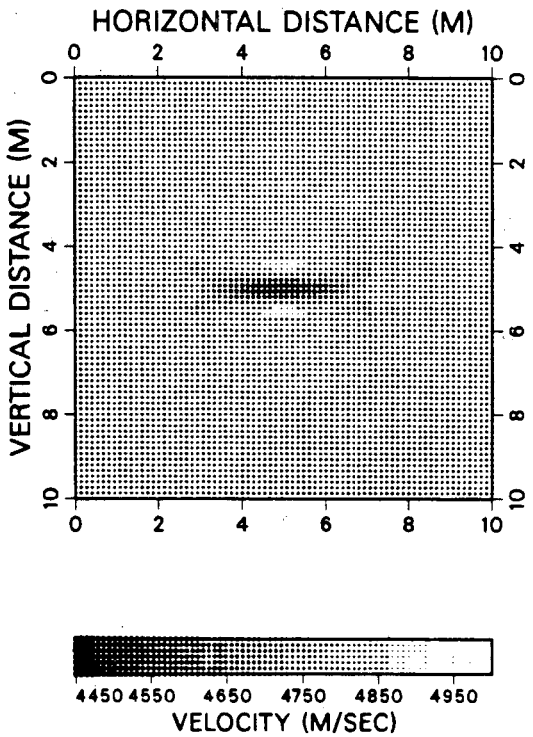

Figure 2.3.1c Average of crosshole inversions from 3900 to 4800 Hz with 122 Hz intervals.

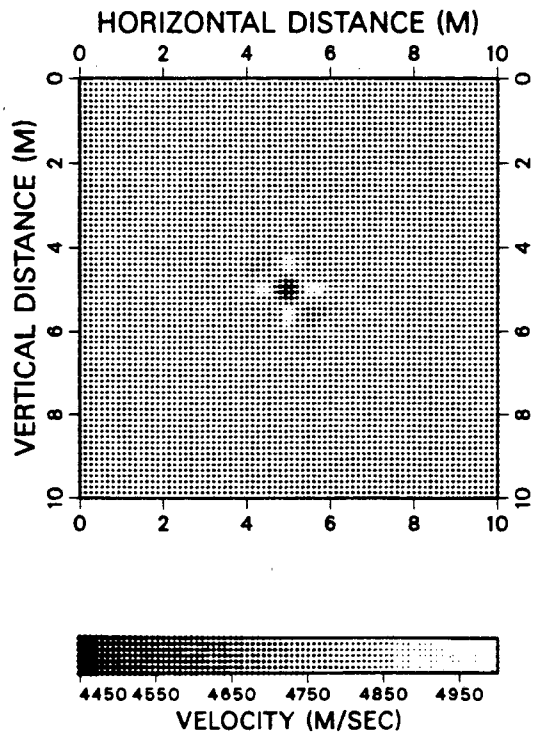

Figure 2.3.1d VSPL inversion at 4800 Hz.

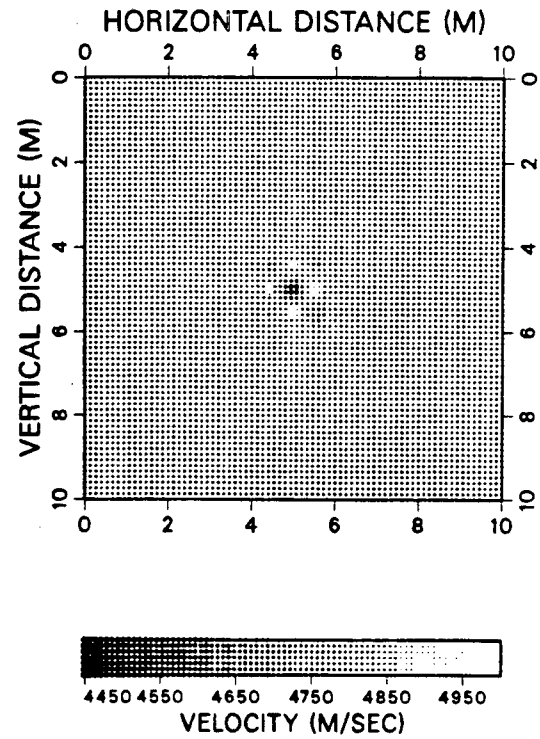

Figure 2.3.1e Average of VSPL inversions from 3900 to 4800 Hz with 122 Hz intervals.

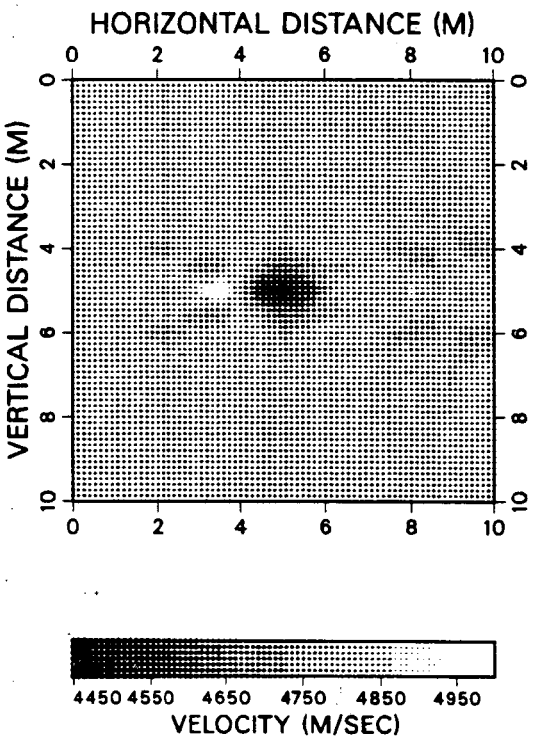

Figure 2.3.1f Backscattering inversion at 4800 Hz.

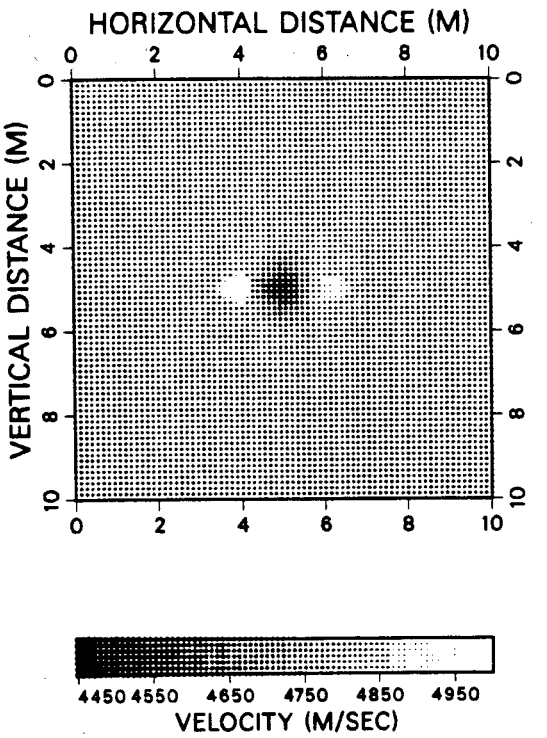

Figure 2.3.1g Average of backscattering inversions from 3900 to 4800 Hz with 122 Hz intervals.

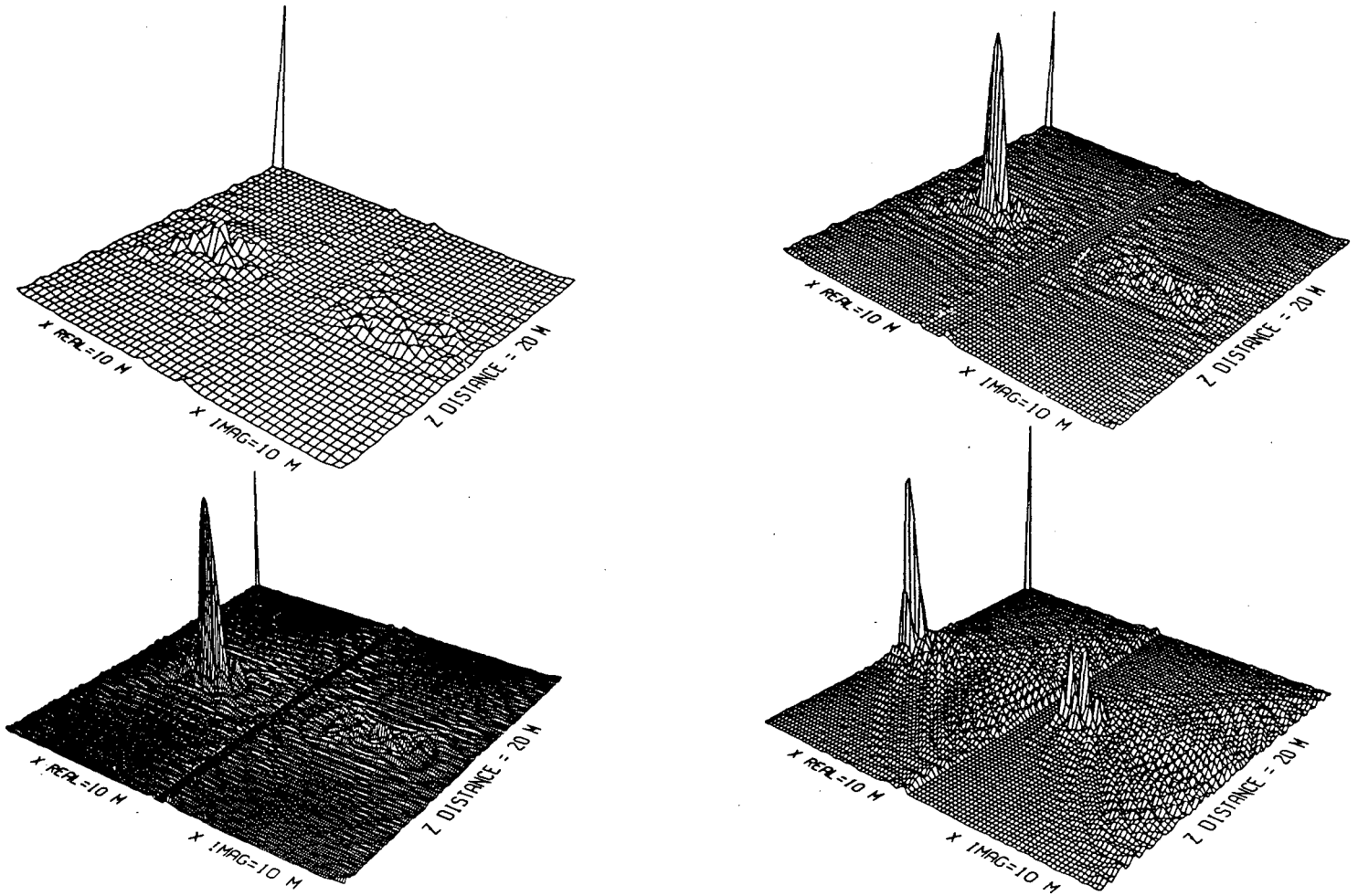

Figure 2.3.2a,b,c,d Inversions with spatial sampling of a) 0.5 m (top-left), b) 0.25 m (top-right) and c) 0.125 m (bottom-left). d) 0.25 m sampling and diffractor at boundary (bottom-right).

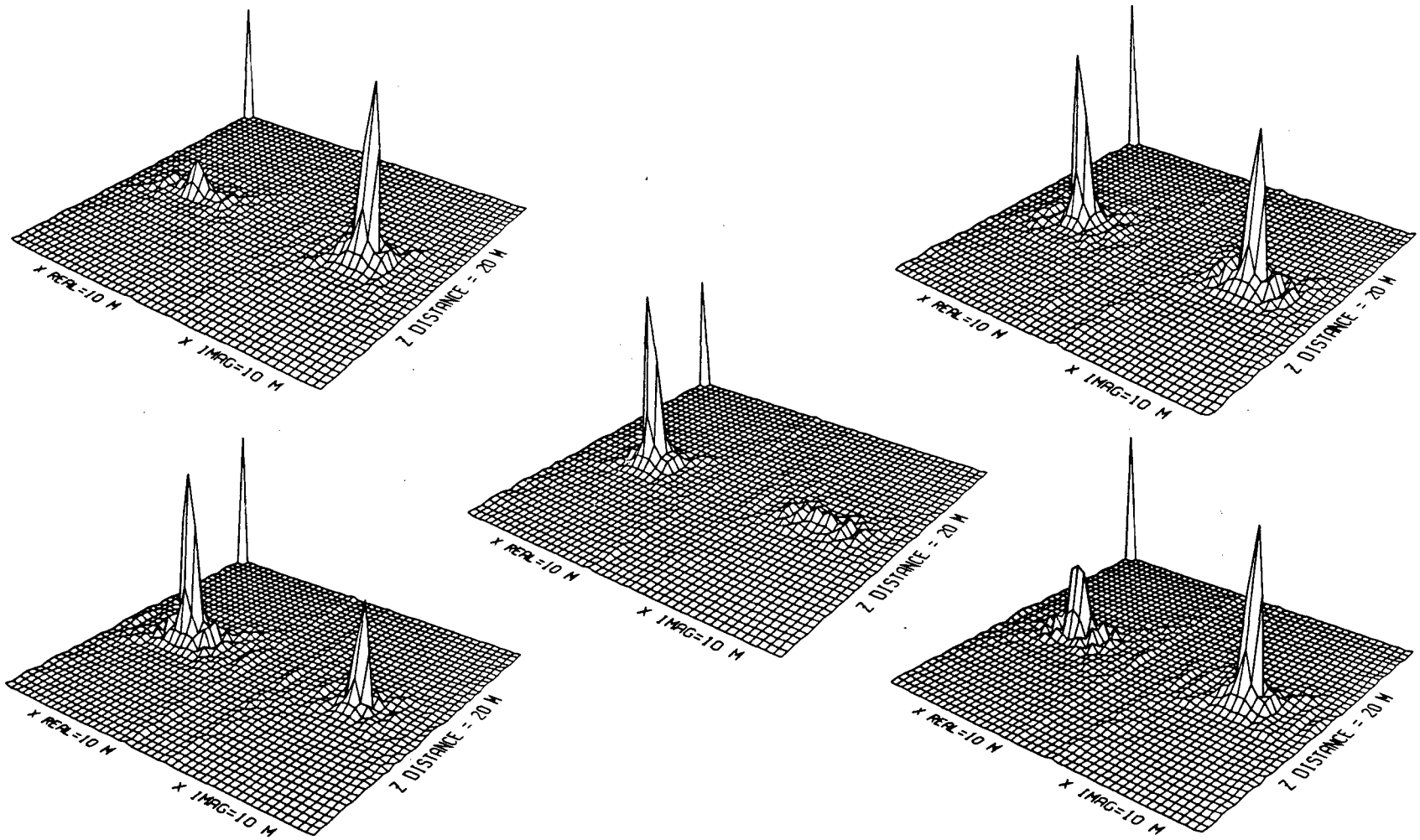

Figure 2.4.1a,b,c,d,e Crosshole inversion at a) 5420 m/s (top-left), b) 5460 m/s (top-right), c) 5500 m/s (center), d) 5540 m/s (bottom-left) and e) 5580 m/s (bottom-right).

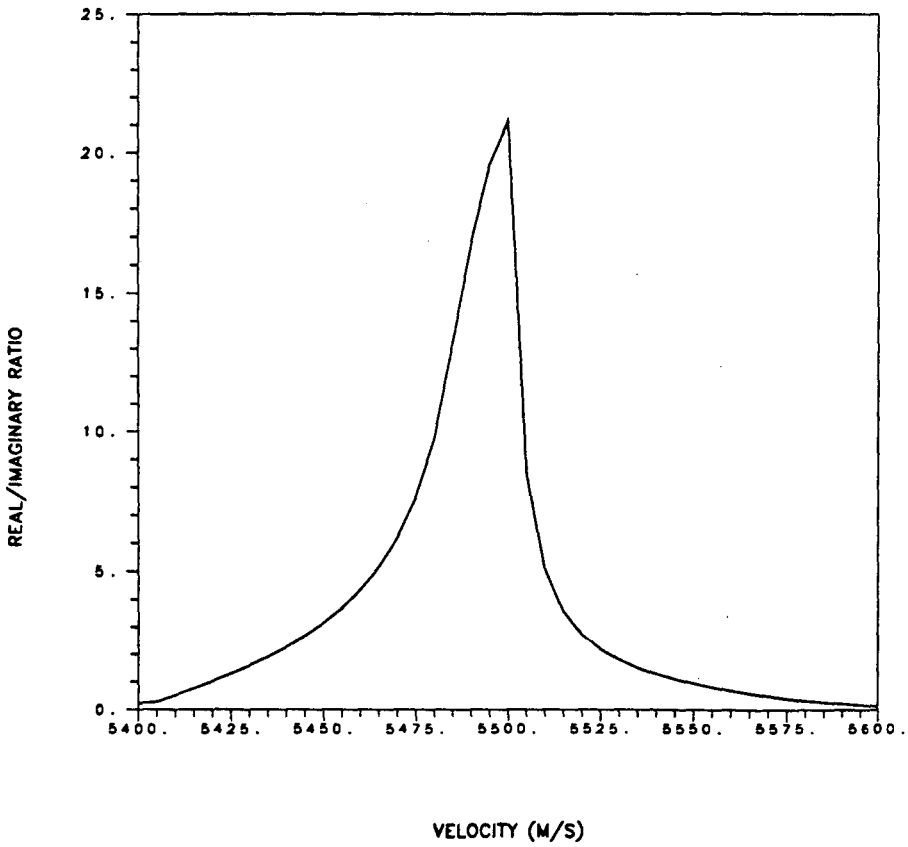

Figure 2.4.2 Real to imaginary ratio of inversion amplitudes with 5 m/s inversion steps.

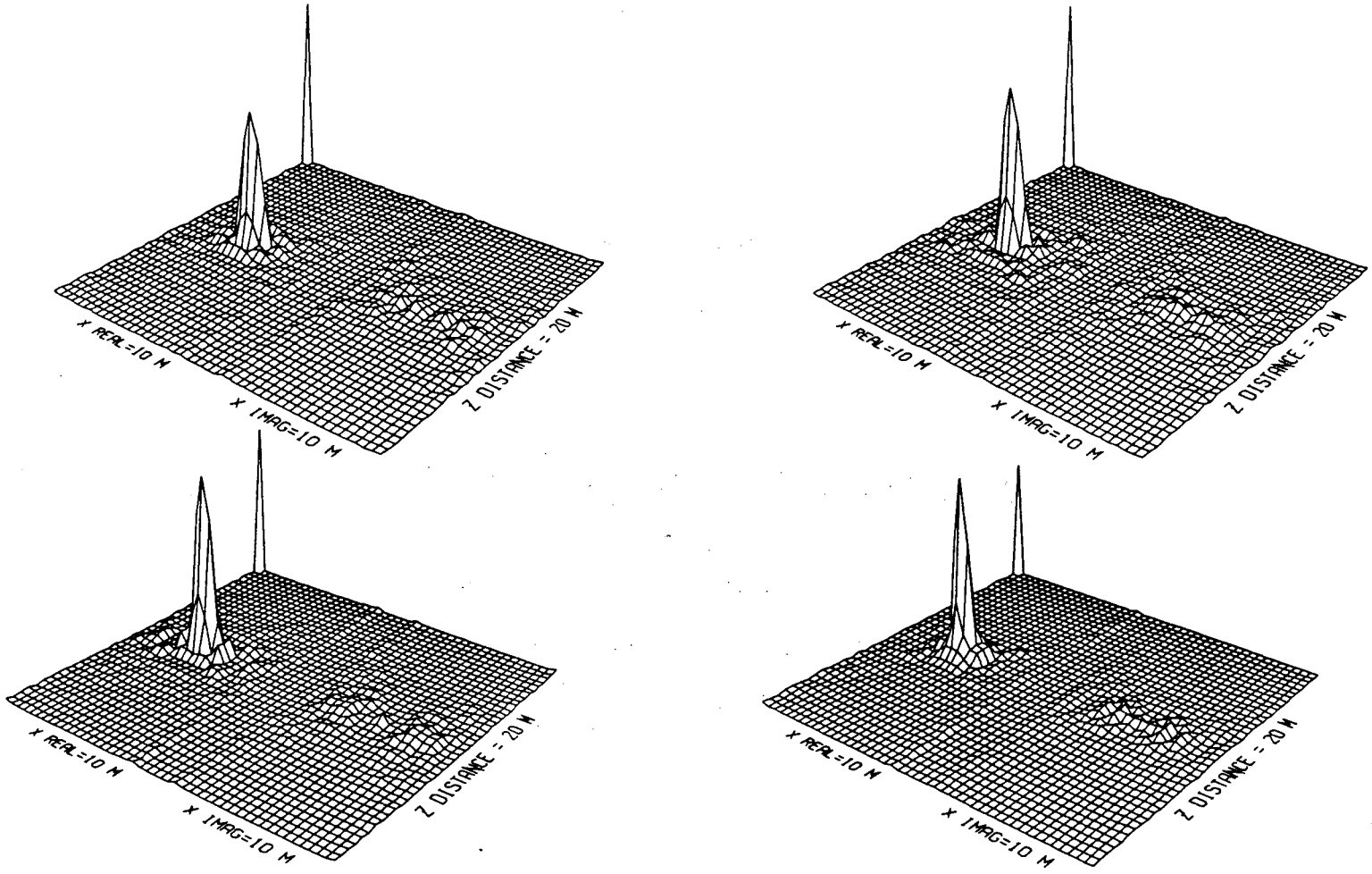

Figure 2.4.3a,b,c,d Crosshole inversion at a) 4028 Hz (top-left), b) 4517 Hz (top-right), c) 5005 Hz (bottom-left) and d) 5493 Hz (bottom-right).

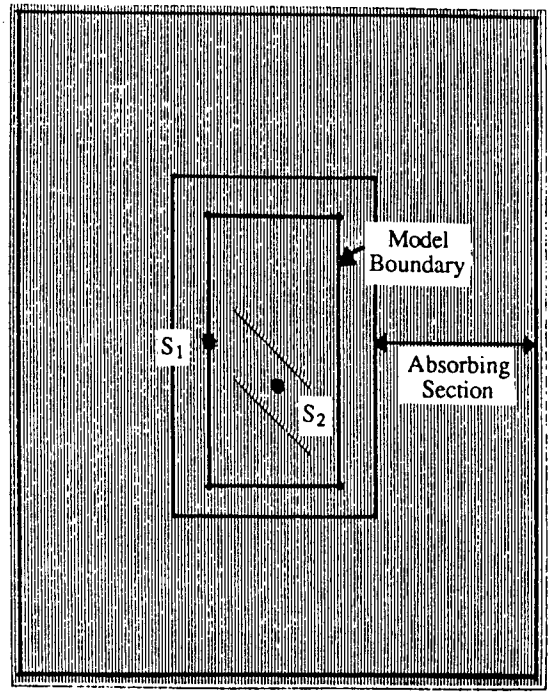

Figure 2.5.1a Input model to the PSFD method and location of sources S_1 and S_2.

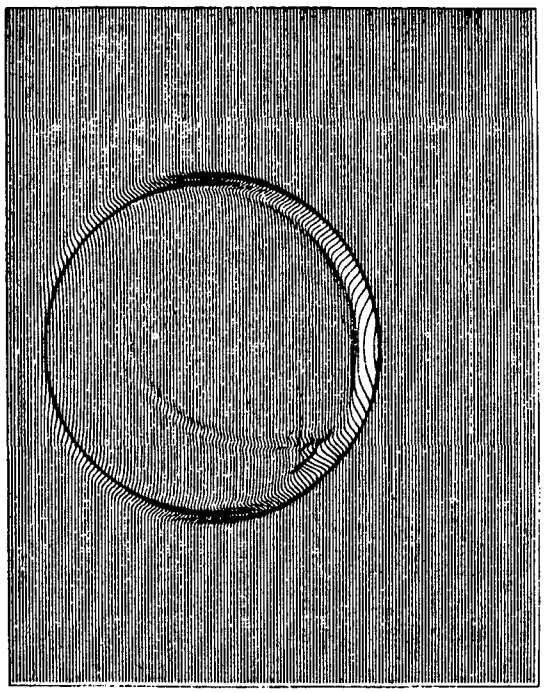

Figure 2.5.1b Wavefield snapshot showing incident and scattered waves (source at S_1).

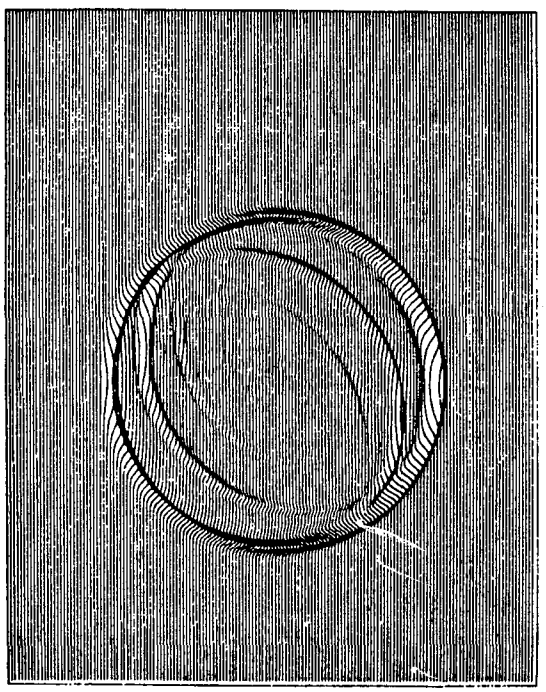

Figure 2.5.1c Wavefield snapshot containing multiply scattered waves (source at S_2).

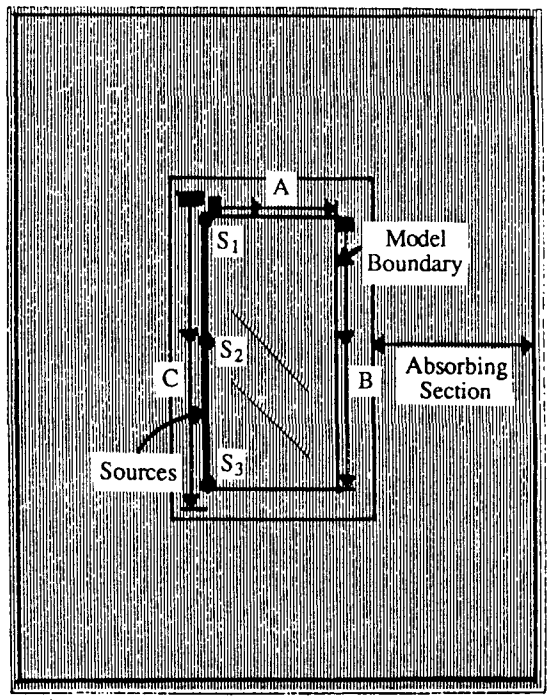

Figure 2.5.2a Input model to the PSFD method. Sources are located on the left boundary and receivers are located along lines A, B and C.

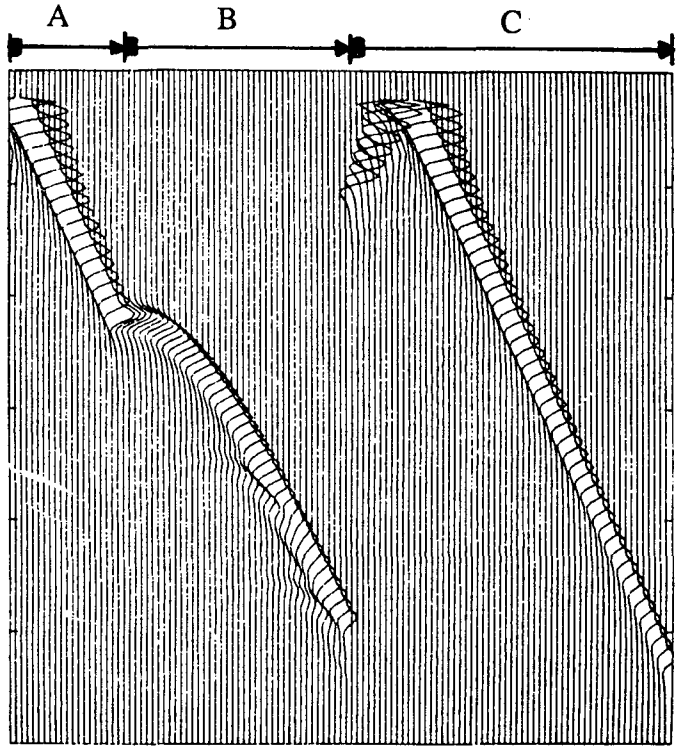

Figure 2.5.2b Seismograms for the source at S_1 and all receivers.

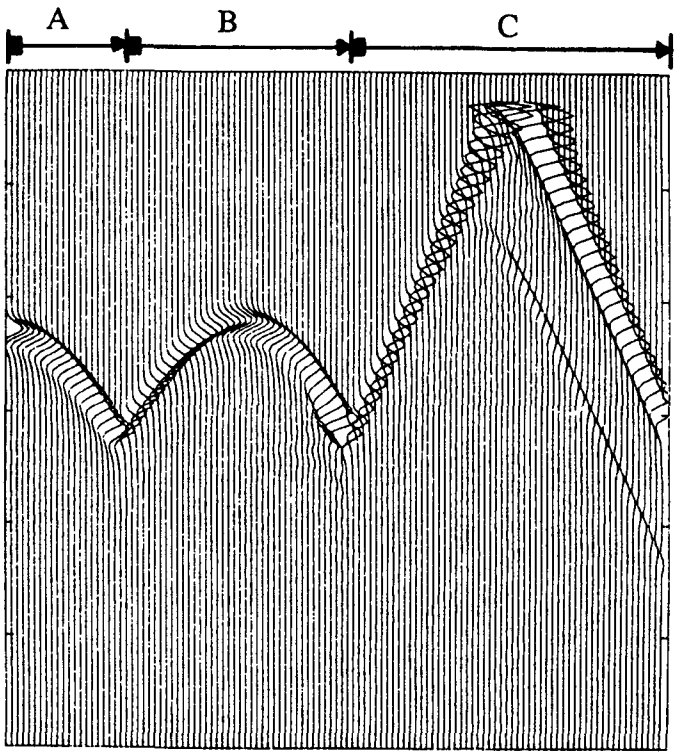

Figure 2.5.2c Seismograms for the source at S_2 and all receivers.

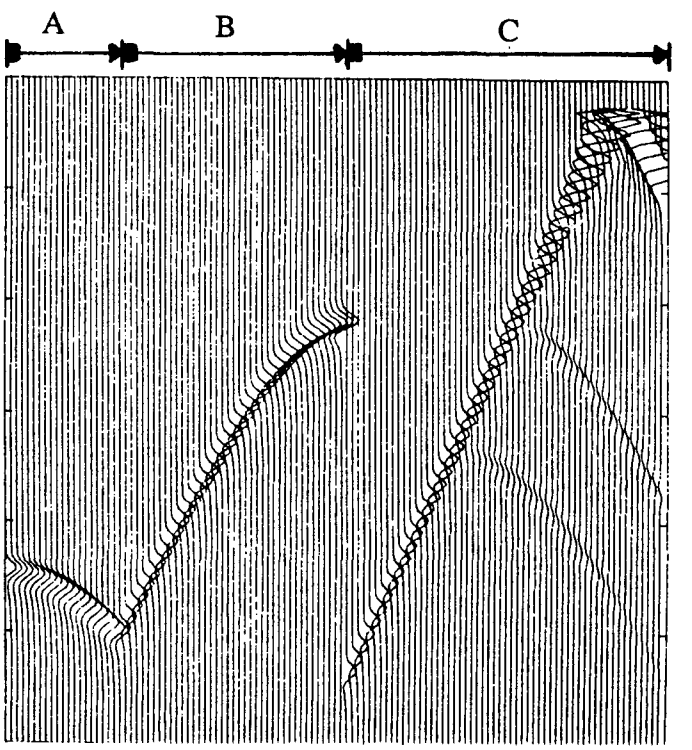

Figure 2.5.2d Seismograms for the source at S_3 and all receivers.

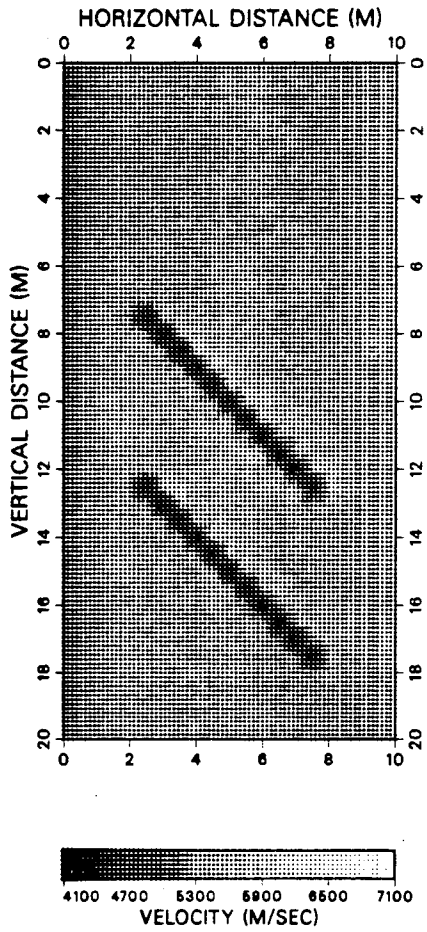

Figure 2.5.3 Input model. Background velocity is 5500 m/s, diffractor velocity is 4500 m/s.

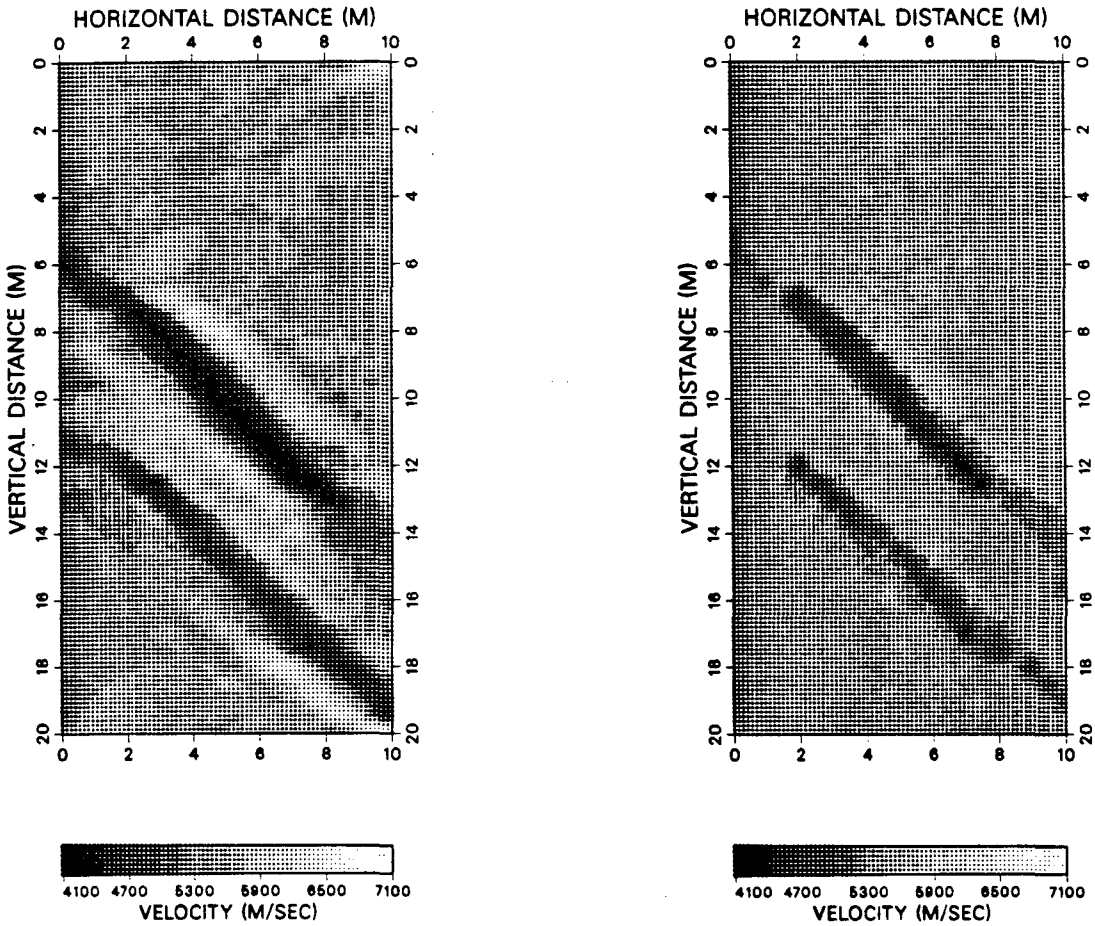

Figure 2.5.4a,b a) Backpropagation (left) and b) Quadratic programming (right) inversion of crosshole geometry data at 5500 Hz.

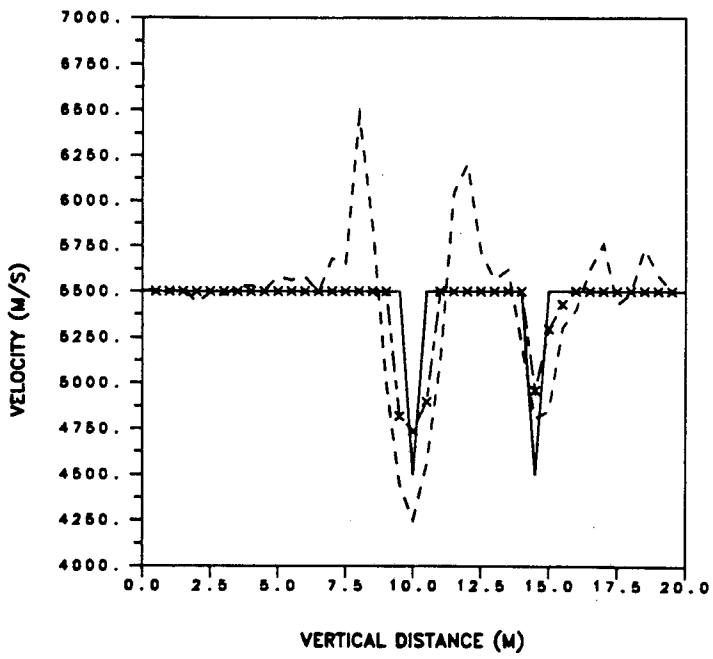

Figure 2.5.4c Cross-section of figures 2.5.3 (solid), 2.5.4a (dashed) and 2.5.4b (dashed with crosses) at 5 m horizontal, in the vertical direction.

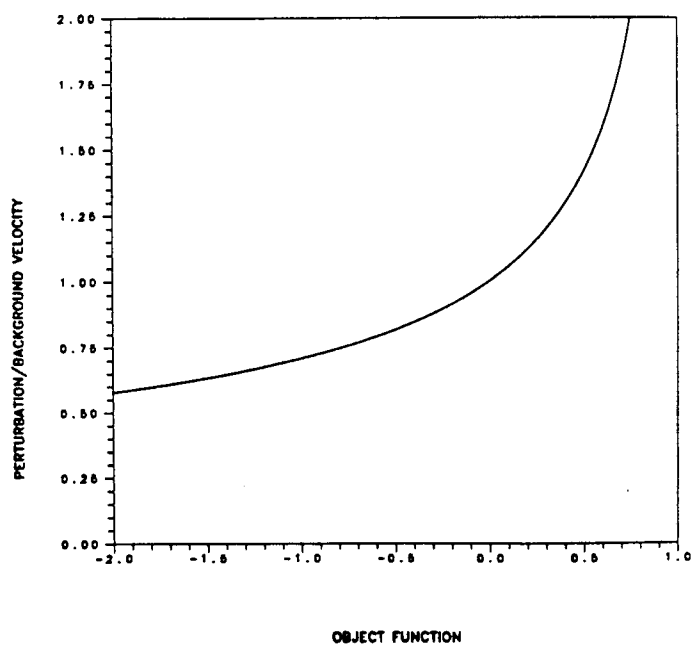

Figure 2.5.4d Mapping of the object function to the velocity domain.

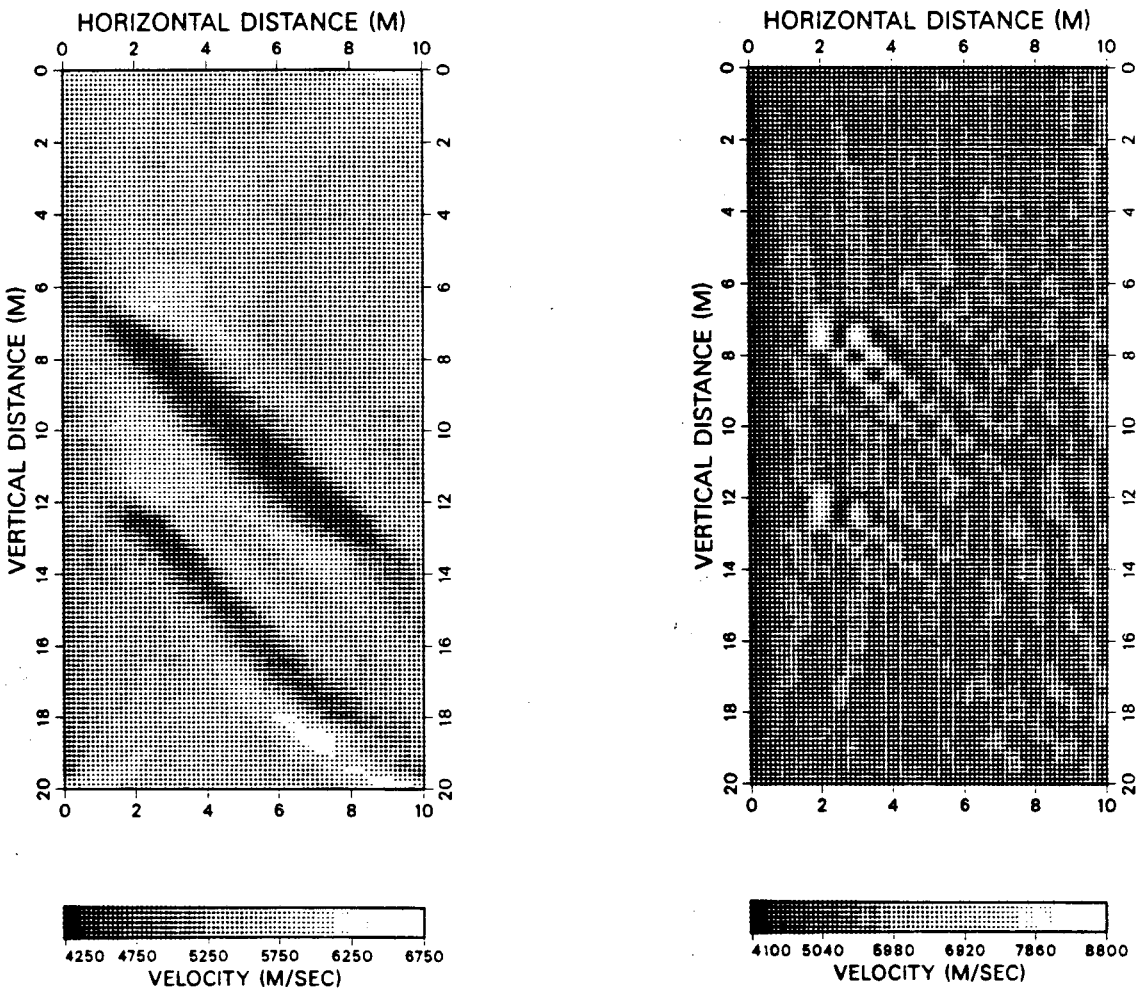

Figure 2.5.4e,f Average of e) Crosshole (left) and f) SRP (right) backpropagation inversions from 2440 to 5500 Hz with 122 Hz intervals.

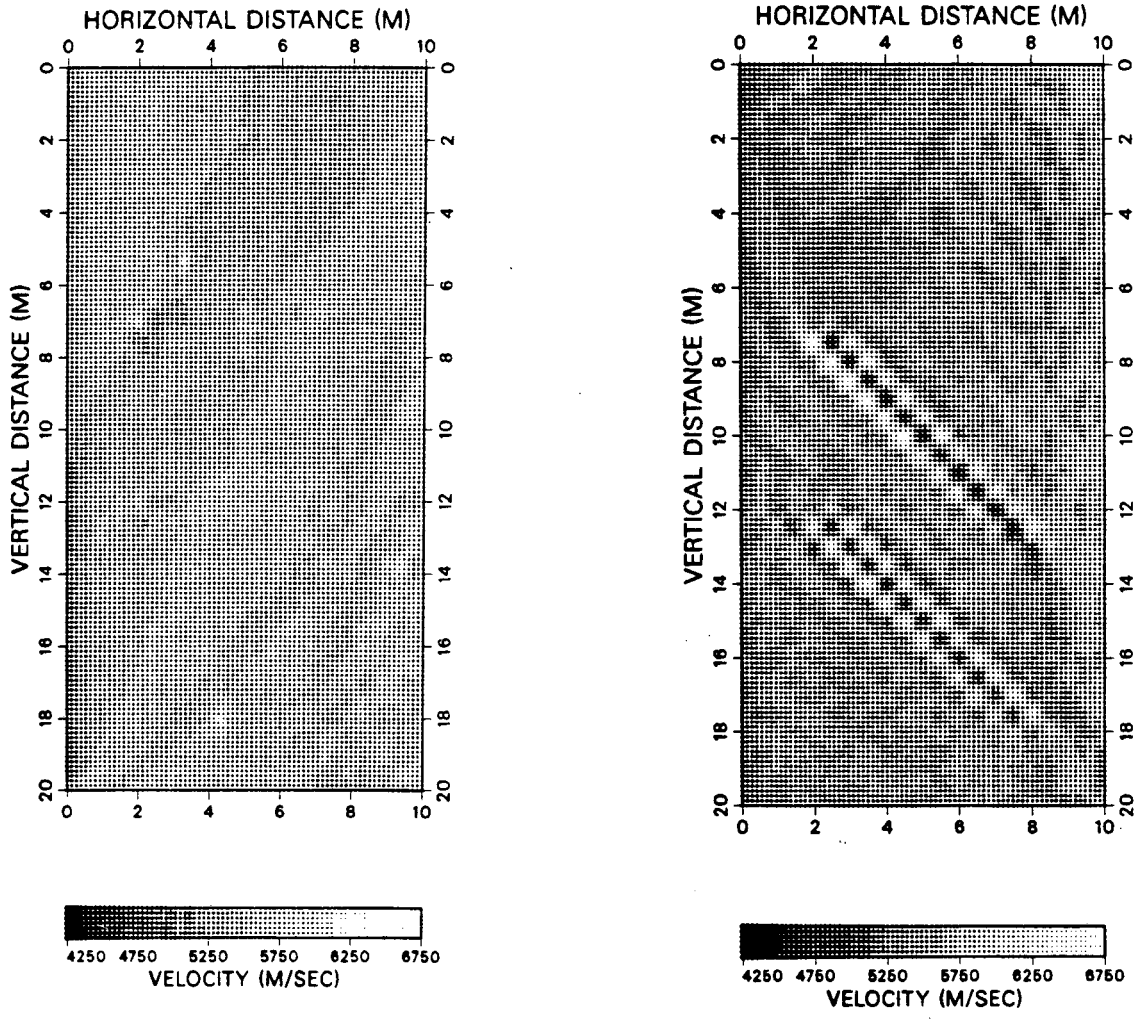

Figure 2.5.4g,h Average of g) VSPL (left) and h) VSPR (right) backpropagation inversions from 2440 to 5500 Hz with 122 Hz intervals.

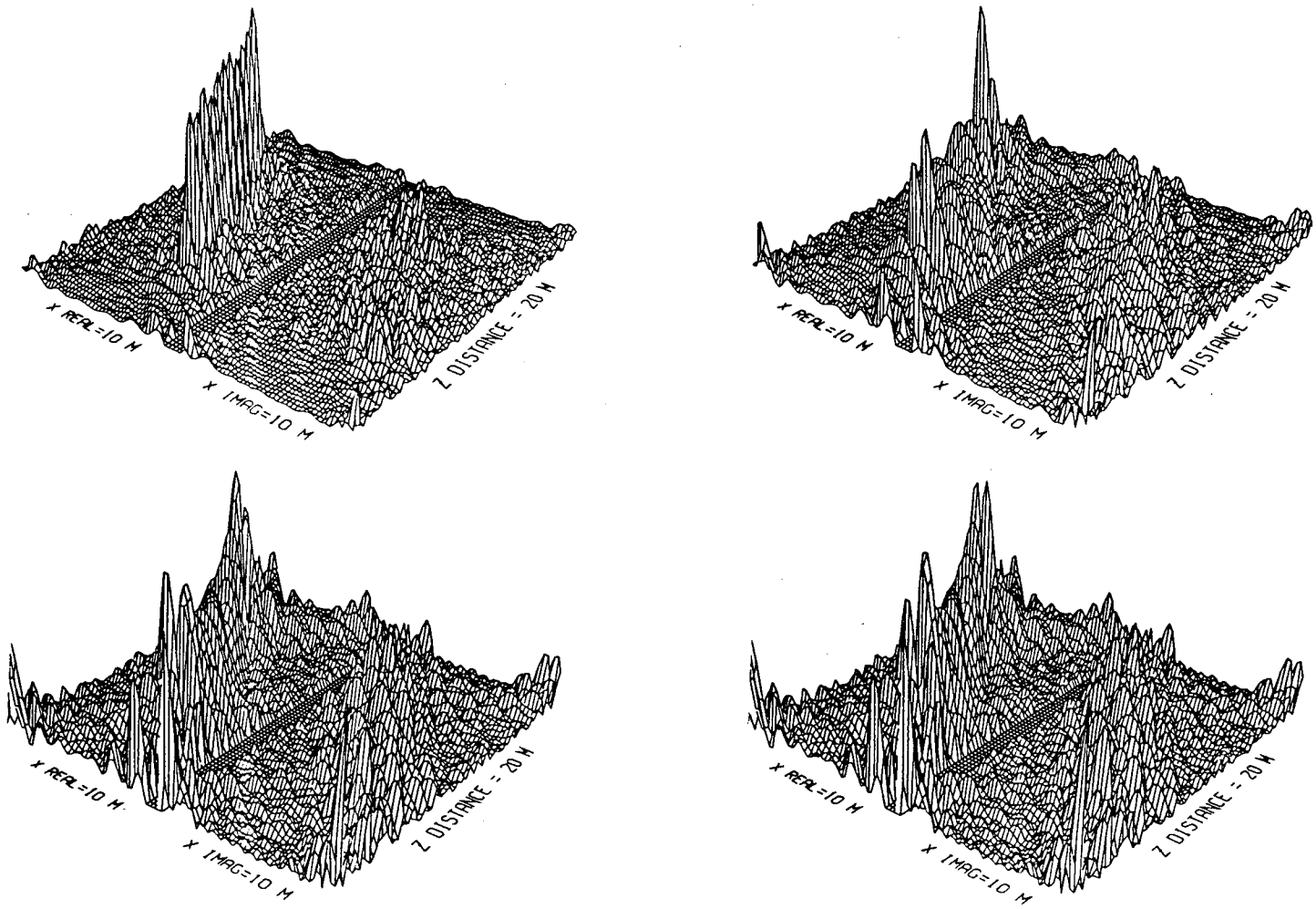

Figure 2.5.5a,b,c,d Inversions with a) 10 (top-left), b) 20 (top-right), c) 200 (bottom-left) and d) 2000 (bottom-right) diffractors on a line.

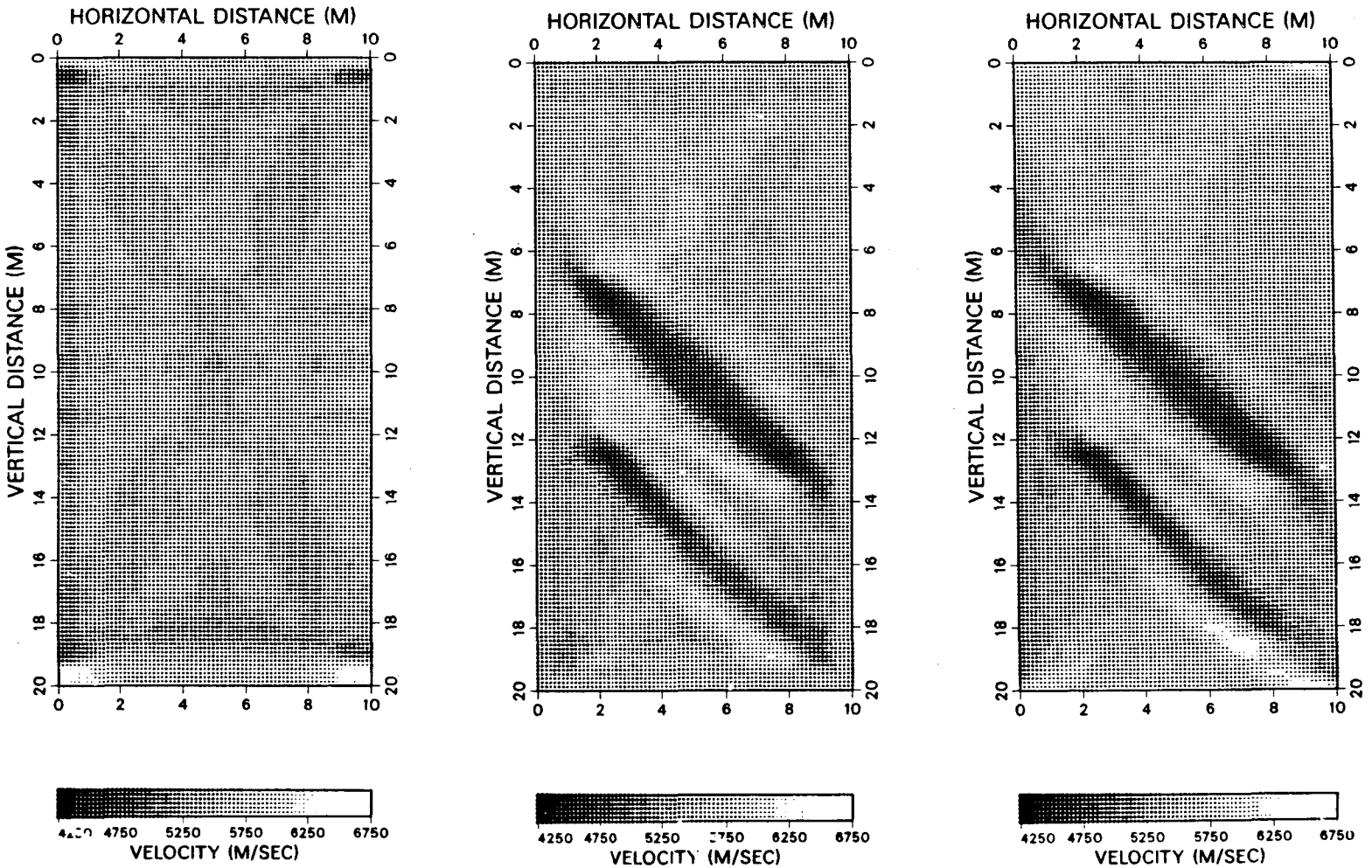

Figure 2.6.1a,b,c a) Incident (left), b) Total (center) and c) (Total-incident) (right) field crosshole backpropagation inversions averaged from 2440 to 5500 Hz with 122 Hz intervals.

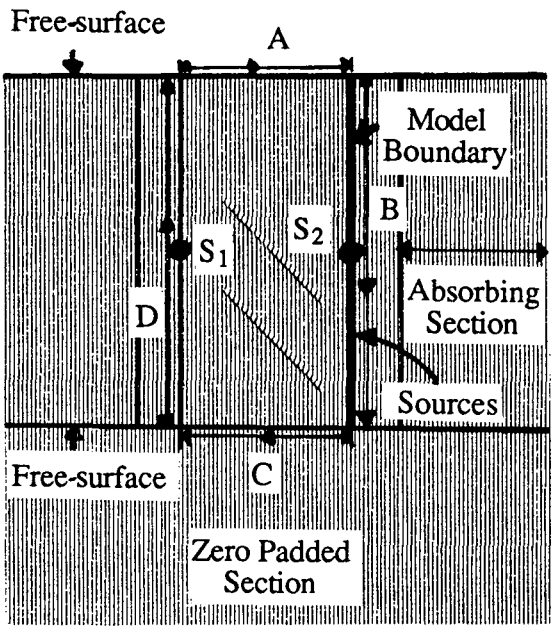

Figure 2.7.1a Input model to the PSFD method. Sources are located on the right boundary and receivers are located along lines A, B, C and D.

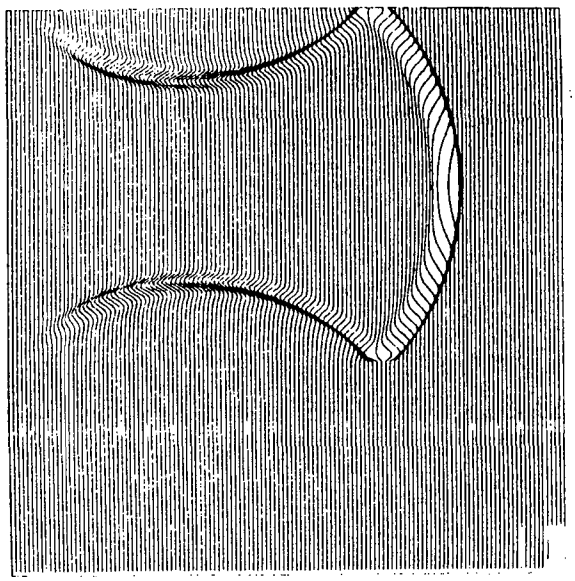

Figure 2.7.1b Snapshot of the wavefield showing the incident field reflecting from the free surfaces (source at S_1).

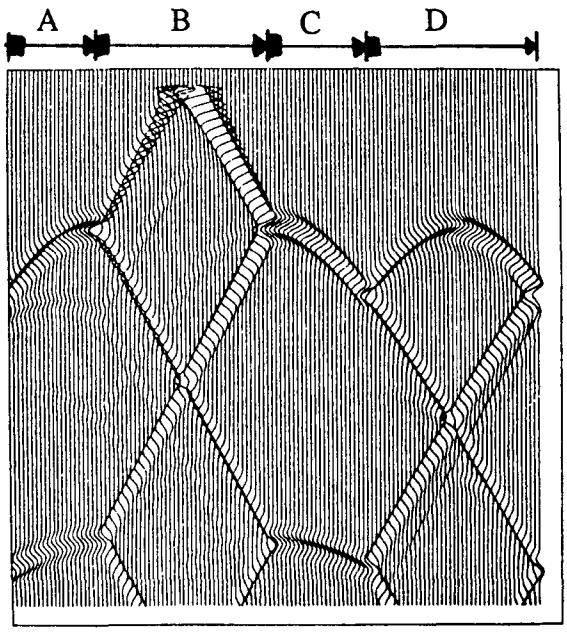

Figure 2.7.1c Seismograms for source at S_2 and all receivers.

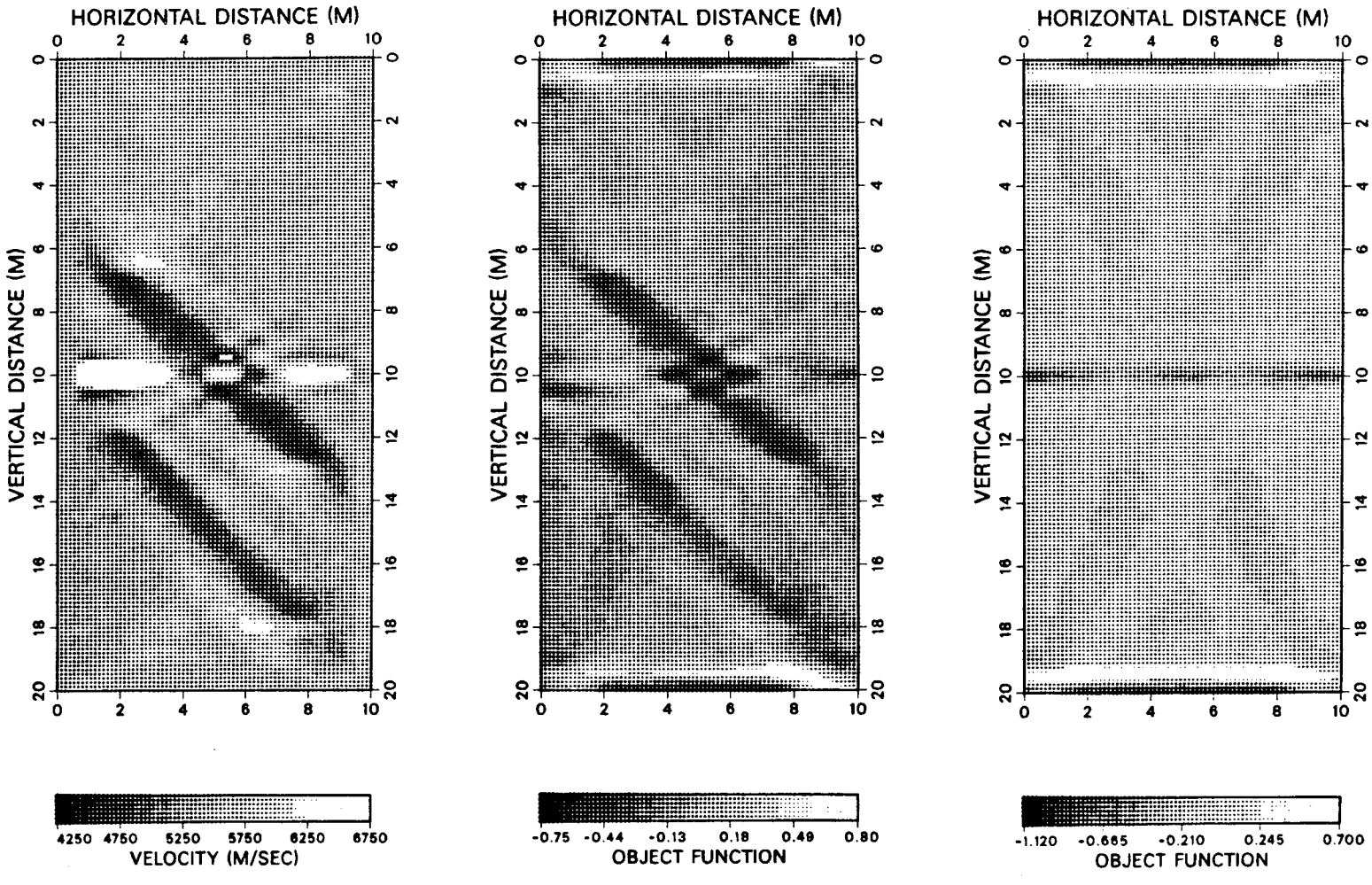

Figure 2.7.2a,b,c a) Scattered (left), b) Total (center) and c) Incident (right) field crosshole backpropagation inversions averaged from 2440 to 5500 Hz with 122 Hz intervals.

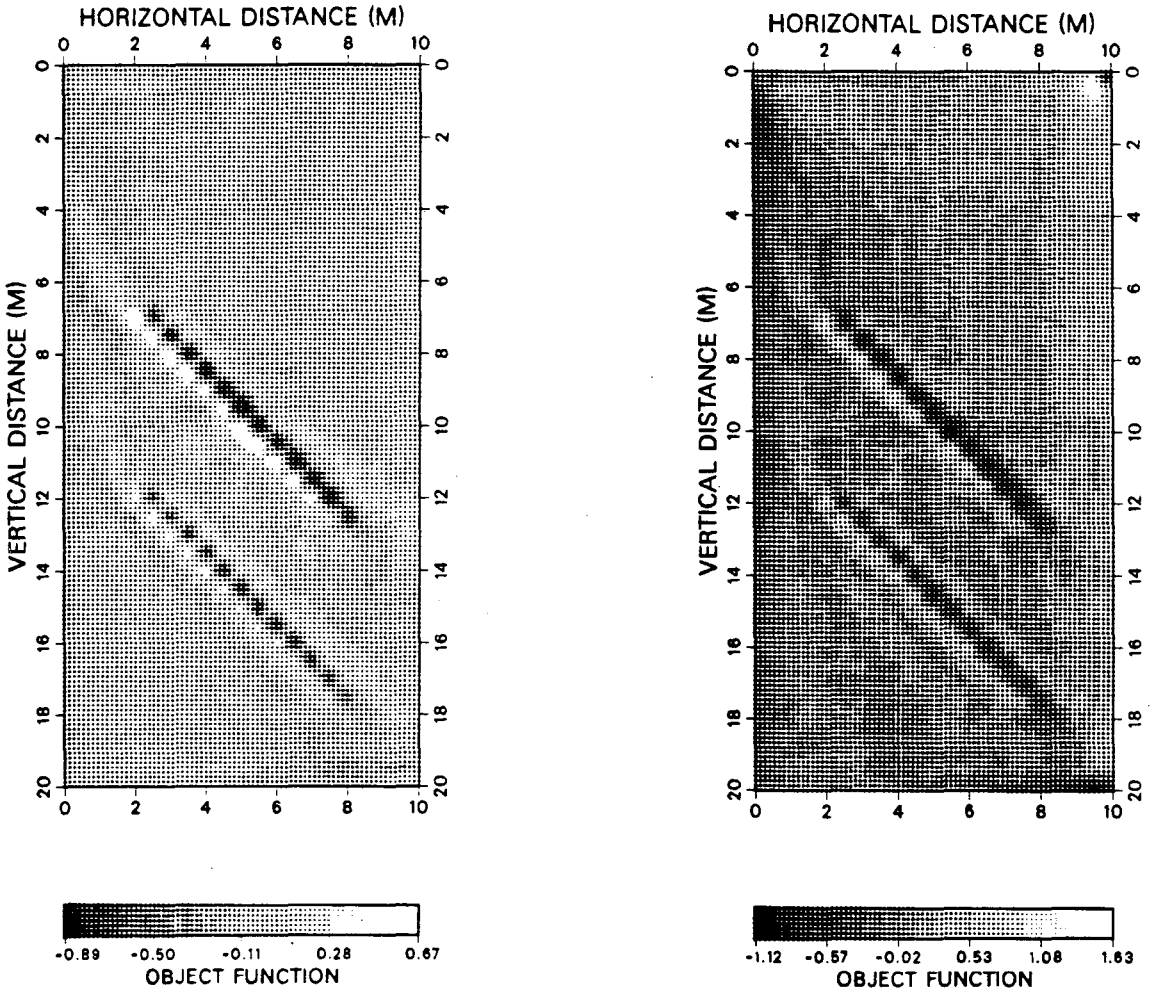

Figure 2.7.2d,e d) Scattered (left) and e) Total (right) VSPR backpropagation inversions averaged from 2440 to 5500 Hz with 122 Hz intervals.

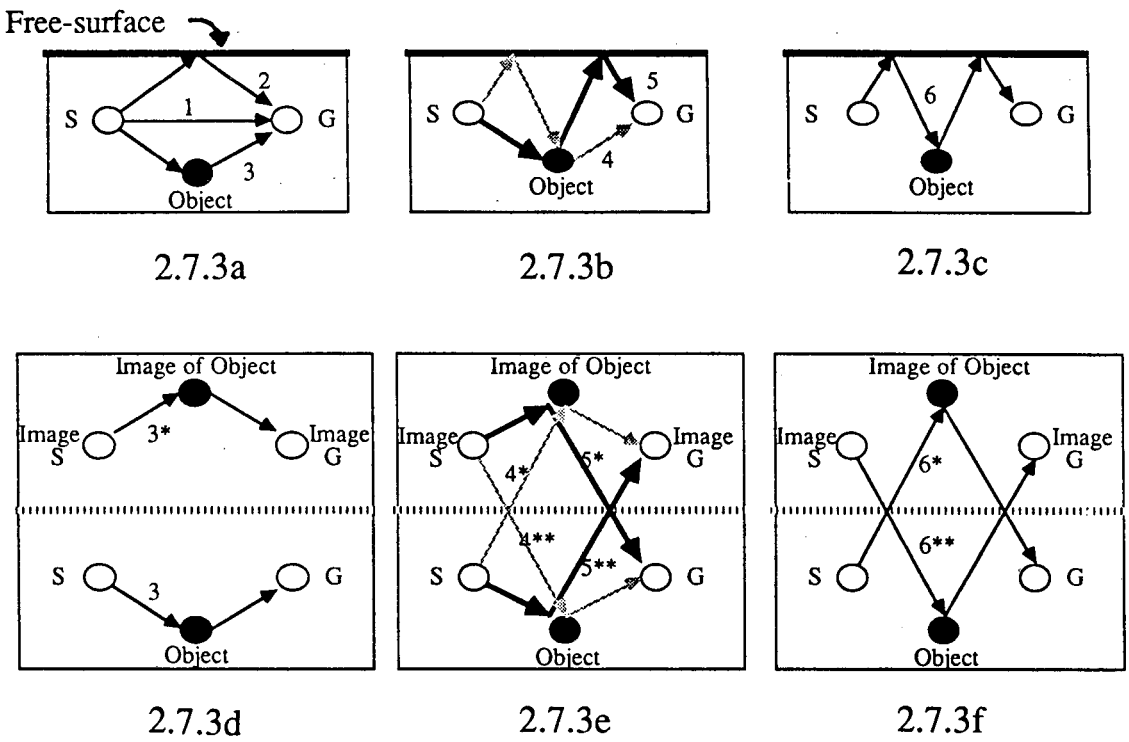

Figure 2.7.3a,b,c,d,e,f The image method and recovered waves (shown in figures 2.7.3e,f).

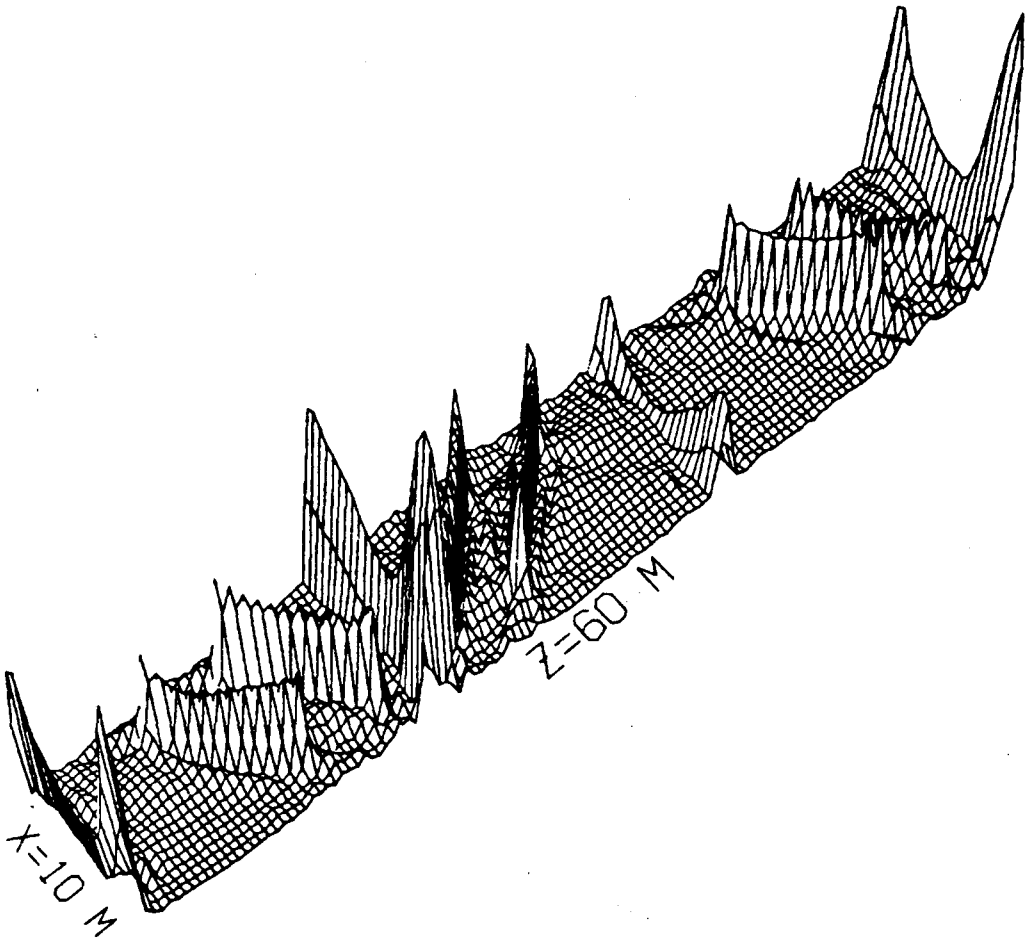

Figure 2.7.4a Scattered field crosshole backpropagation inversion averaged from 2440 to 5500 Hz with 122 Hz intervals.

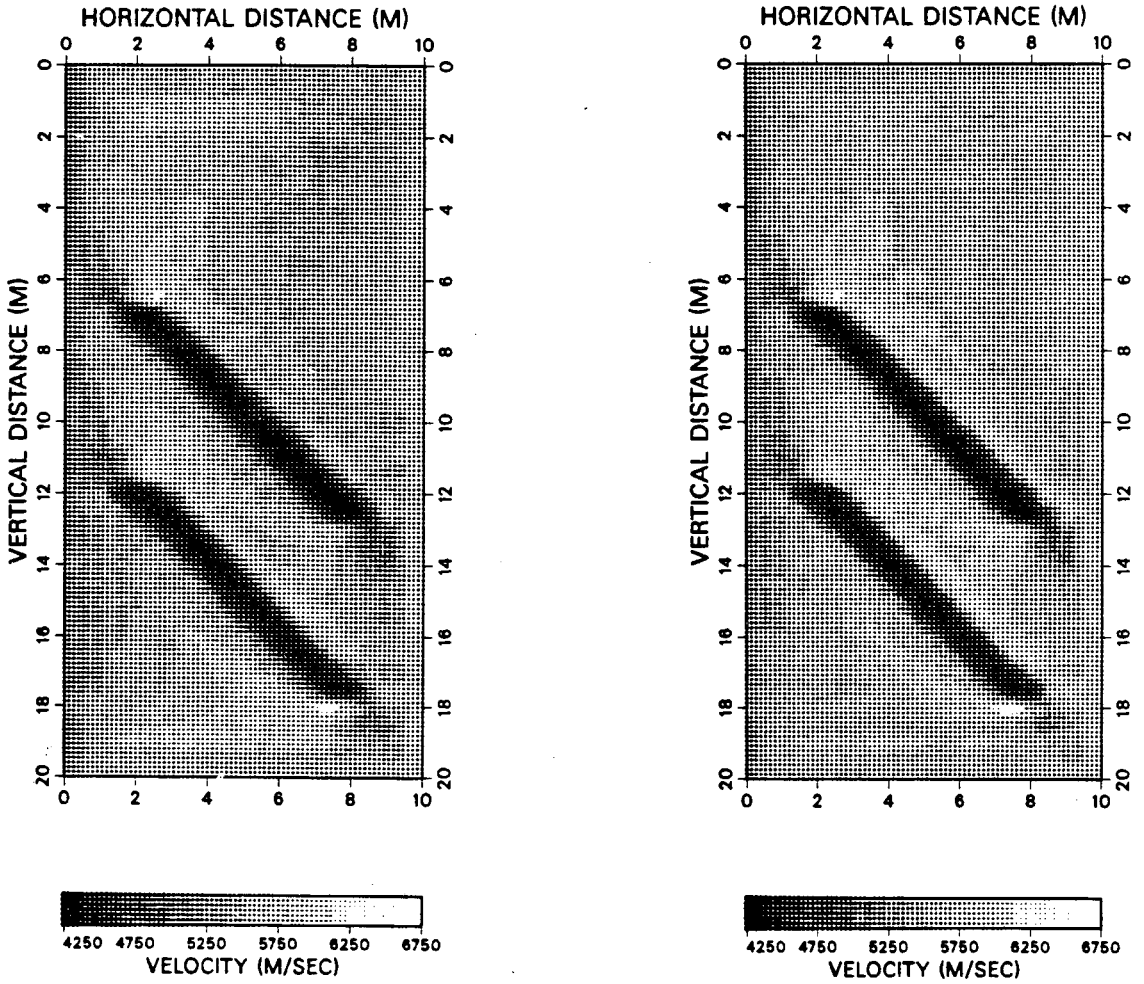

Figure 2.7.4b,c Folded b) Scattered (left) and c) Total (right) field crosshole backpropagation inversions averaged from 2440 to 5500 Hz with 122 Hz intervals.

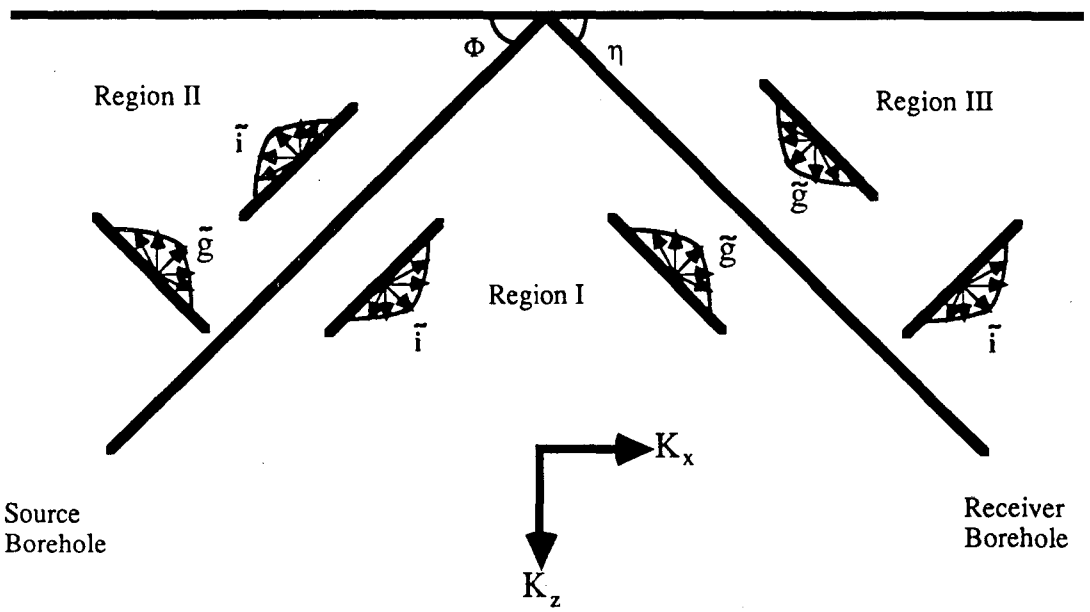

Figure 2.8.1 Geometry of the slanted borehole experiment with the plane-waves that are producible in each region.

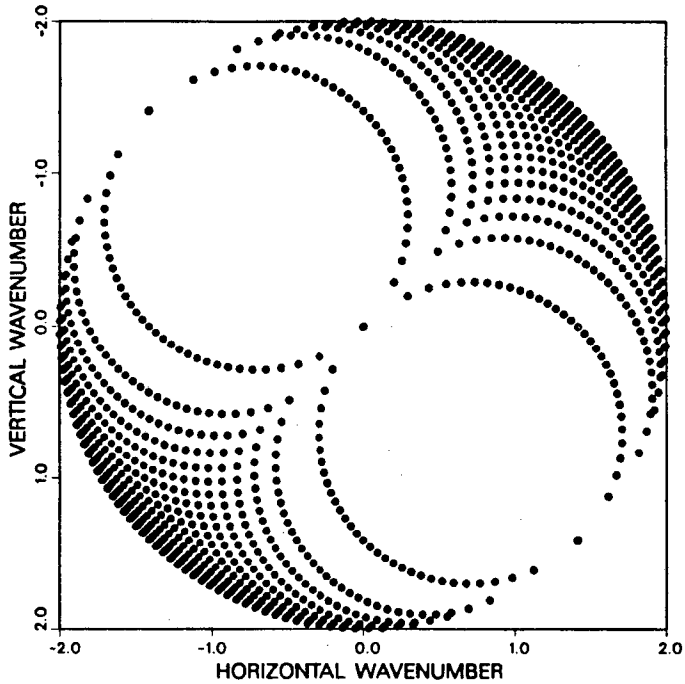

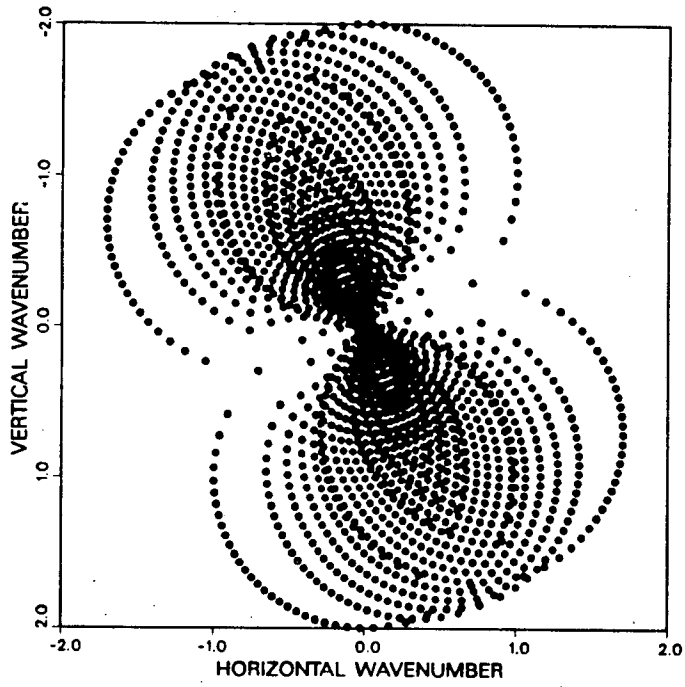

Figure 2.8.2a,b Coverage of object function in the wavenumber domain with a) $\Phi = 135^{o}$ and $\eta = 45^{o}$ (top) and b) $\Phi = 90^{o}$ and $\eta = 45^{o}$ (bottom).

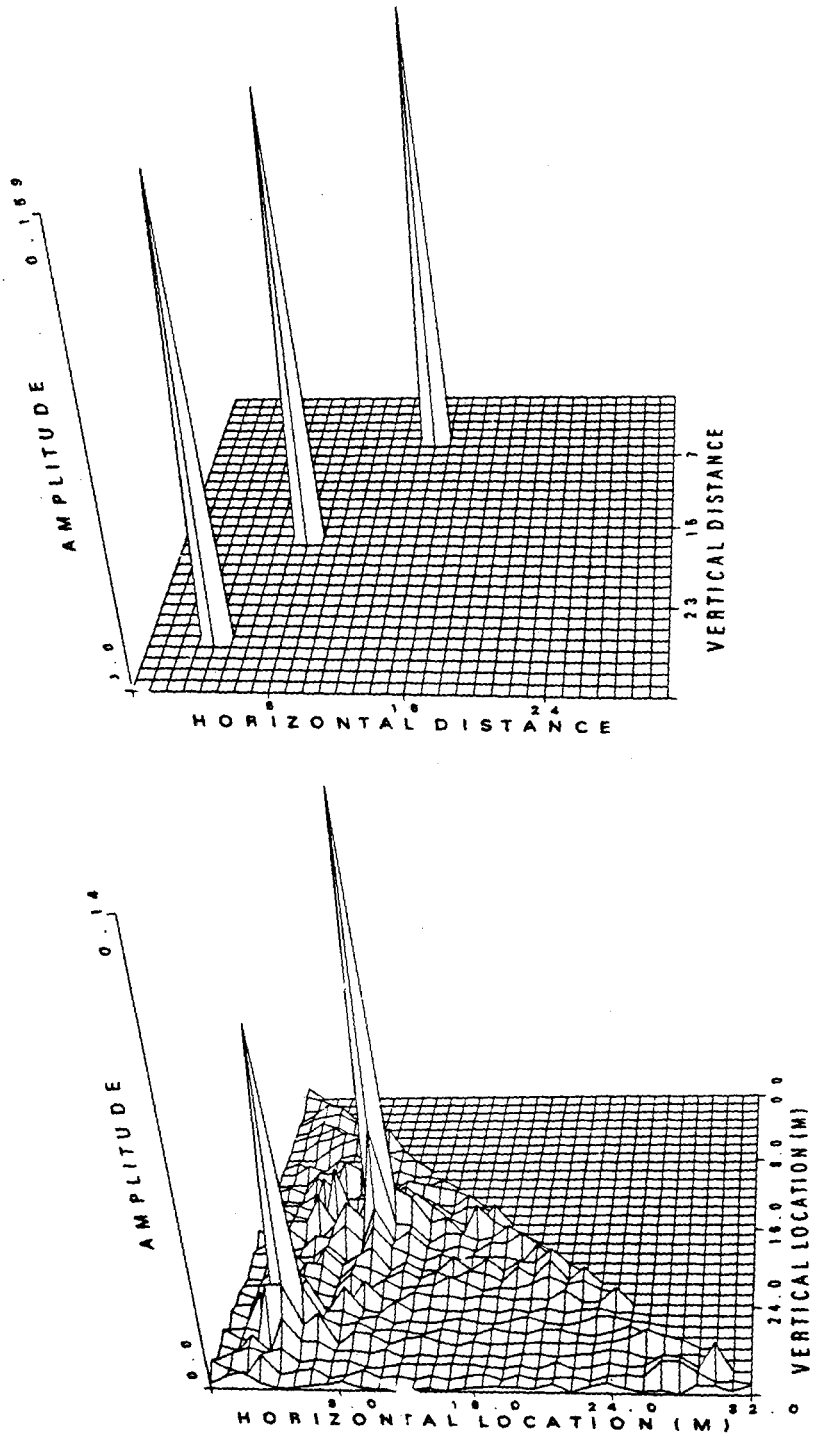

Figure 2.8.3a,b Slanted borehole inversion, a) Input model (top) and b) Backpropagation inversion (bottom) for $\Phi = 90^o$ and $\eta = 45^o$.

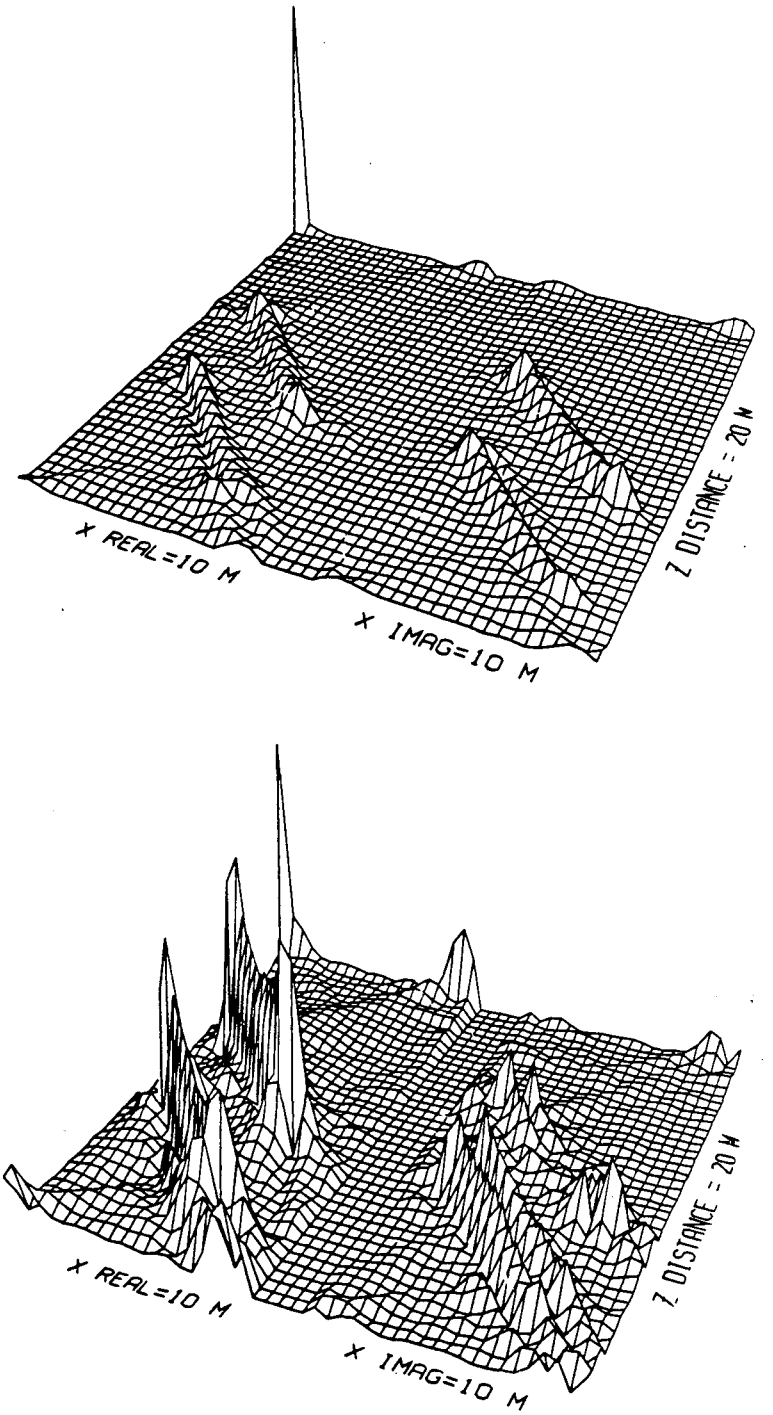

Figure 2.9.1a,b Crosshole 2-D backpropagation inversion of 2.5-D data

a) Uncorrected (top) and b) 2.5-D effects corrected (bottom).

Chapter 3

Application to Field Data

In this chapter, the inversion methods are applied to field data from a region of granitic rock in order to image the fractures it contains. A data processing scheme, necessary to bring the field data into a form that can be used in the inversion algorithms is introduced. The processing scheme is quite different from conventional seismic data processing. This is mainly due to the multi-offset and crosshole nature of the data.

After processing, the data are inverted using the diffraction tomography algorithms and the resulting images are compared to ray tomography inversions. These images are seen not only to be in good agreement with the ray tomography inversions but also with the geological information available on the fracture zones obtained from core samples.

3.1 Geology of the FRI test site

The field data that the methods are applied to is from the FRI site in the southern part of the Grimsel test facility which is located a few hundred meters below the surface inside the Juchlistock mountain in the Swiss alps. This facility is operated by the Swiss National Cooperative for the Storage of Radioactive waste (NAGRA), and joint projects are conducted here with the Lawrence Berkeley Laboratory (LBL) on topics ranging from measurements of rock mechanical properties of the granitic rock to hydrological conductivity studies and detection of fractures in the granitic rock mass. The FRI site consists of two main tunnels which are 21.5 m apart and lying in the north-south direction and are connected by two boreholes oriented in an east-west direction with a 10 m separation. This site is chosen in a region of granitic rock where fractures are known

to exist. The geometry outlined above, together with a geological interpretation of the region is shown in Figure 3.1.1. The fractures intersecting the boreholes, indicated by short lines at the borehole locations, are an interpretation of core samples taken from the boreholes. The geological interpretation of this information together with core samples from the main access tunnel and laboratory tunnel is indicated by a main shear zone. The main shear zone in the experiment area has a nearly vertical dip forming an approximate 2-D medium. Some mafic dykes and associated small fractures are shown as stippled areas and indicated by an L in Figure 3.1.1. In addition, there are a few centimeter thick veins which are generally filled with quartz, feldspar, epidote or aplitic material not shown in Figure 3.1.1. Measured from the laboratory tunnel these veins are seen in borehole BOFR 87.002 at 10-12 m striking north-east, at 12 m and 14 m striking north-west and in borehole BOFR 87.001 at 12.8 m striking north-west.

3.2 Data gathering and analysis

Data were collected for all possible crosshole and VSP geometries around the experiment area with 0.5 m spacing of sources and receivers. An unclamped piezoelectric source was used in the water filled borehole which gave energy up to 10 kHz. The receiver used was a three-component accelerometer clamped to the borehole wall in order to improve coupling and reduce tube-waves. To improve the quality of the data, for each source-receiver pair the experiment was repeated two to nine times and the results averaged. The VSP type data were not used in the diffraction tomography inversions because of tube-wave contamination and limited dynamic range of the recording system. For more detailed information on the equipment used and data gathering procedures, see, Majer et al., 1990.

In the crosshole case, the nearest source location used in the inversions was 1.5 m away from the access tunnels so that prominent tube-waves and surface-generated

waves could be avoided. The data contained some tube-waves from the locations where fractures intersected the boreholes.

In the inversions we use the receiver component perpendicular to the borehole wall. This is done because a wavefield separation method (Devaney and Oristaglio, 1986) when applied to field data did not produce good results, possibly due to tube-waves and spatial sampling of sources and receivers.

An example data set is shown in Figure 3.2.1 for a source located at 7.5 m from the main access tunnel in borehole BOFR 87.002 and receivers between 1.5 m and 19.5 m from the main access tunnel in borehole BOFR 87.001. In this Figure, a fracture-generated tube-wave can be seen starting at the twentieth and continuing through the first receiver at a downward slope of about 45° from the horizontal giving an approximate velocity of 1400 m/s for the tube-wave. We can also see the reverberative nature of the wavelet in this figure which will be discussed in the next section. From field data, transmission ray tomography inversions and laboratory measurements, the background or granitic rock velocity is estimated to be near 5300 m/s. In addition, a 7-8% transverse isotropy with the symmetry axis normal to the plane of fracturing is observed from displaying the first arrival time data as a function of ray angle.

3.3 Data processing

In Figure 3.3.1 we outline the data processing scheme which is used. Initially, a cos (Θ) operator is applied to the data for the radiation correction, where Θ is the angle of the line joining the source and receiver, measured from the horizontal. The cos (Θ) correction operator was found as follows: a source was fixed and receivers were moved in a crosshole fashion in a homogeneous region of granitic rock outside the experiment area. An estimated attenuation correction and a geometrical spreading correction were

applied to this data and amplitudes as a function of angle were matched with possible operators. The cos (Θ) function proved to fit the data best.

In order to estimate the wavelet and a more precise attenuation correction factor (α) of the background medium, we consider the initial portion of the data which contains the waveform of the first arrivals. To this set we initially apply a geometrical spreading correction of R, which is the source-receiver separation. We then estimate α as follows: we correct the data with a certain α value and for each source, we look at the mean deviation of the maximum amplitudes as a function of distance to receiver locations. Next, we sum the mean deviations for all sources to obtain a total mean deviation value for the considered α. We repeat this process for a range of α values and take the α that gives the minimum total mean deviation as the background attenuation factor. In this case, the total mean deviations gave a smooth change with a minimum corresponding to an α value of 0.12 m^{-1}. Using $Q = (\pi f)/(\alpha c_0)$ (Aki and Richards, 1980, p.168) with f = 5500 Hz and c_0 = 5300 m/s gives a Q of 27 for the granitic rock. We apply the attenuation correction with this α to the radiation corrected full-wavefield. This gives us the corrected total field (see Figure 3.3.1).

In order to estimate the wavelet, the attenuation correction is applied to the first arrival waveforms, then the first arrival times are picked and used to align the first arrival waveforms. Further improvements on these picked times are achieved by aligning the first minimums of the traces (Figure 3.3.2 displays the minimums to be near 0.06 ms). We use the first minimums to align the traces in order to avoid possible errors that could result from early arrivals of the scattered field effecting subsequent maxima and minima. Averaging these aligned traces over receivers for a fixed source gives us an estimate of the wavelet for a specific source or a common source gather. Averaging all the common source gather wavelets will give us an average wavelet. In Figure 3.3.2, common source gather wavelets (top) and the average wavelet (bottom) are displayed.

As can be seen the average wavelet has a reverbatory nature. These reverberations are caused by the wavefield being trapped in the water-filled borehole because the arrival times of the multiples correspond to the two-way travel time in the water-filled borehole. We therefore define two sets of wavelets, one a short wavelet (up to 0.2 ms in Figure 3.3.2) which does not include the multiples and another a long wavelet (up to 0.46 ms in Figure 3.3.2) which includes the multiples. For the deconvolution, each common source wavelet can be used to deconvolve its associated source group or the average wavelet can be used to deconvolve all the traces. We discuss which wavelet will be used for deconvolution, including the common receiver gather, in the next section.

The maximum amplitudes of the common receiver gathers for each receiver, which indicates the coupling of the receivers, and common source gathers for each source, which indicates the coupling of the sources, are given in Figures 3.3.3a and b. From these figures, it is seen that although the variations from the average values are not large for both cases, the coupling of the sources and receivers with the medium will affect somewhat the inversion amplitudes.

Continuing with the data processing (Figure 3.3.1), we generate 3-D Green's functions using the corrected first arrival times and then convolve them with the average long wavelet, constructing an estimate of the incident field, which is subtracted from the total field to give the scattered field.

To avoid additional noise entering the inversions, the beginning of the traces are muted using the corrected first arrival times. In addition, the end of the traces are windowed using a one-sided Hamming window in order to exclude arrivals other than the singly scattered field, such as refracted-waves, shear-waves and especially fracture-generated tube-waves in borehole applications. Although these tube-waves carry information on the fractures they need to be removed as completely as possible,

otherwise they can disturb the inversion results at the boundaries. The choice of the window lengths used will be discussed in the next section. The last step before the inversion is the application of the 2.5-D corrections discussed earlier.

3.4 Inversion of the field data

In the application of the inversion some criterion is necessary to assess the quality of the inversion results. In the synthetic data case we used the method of quantitative and visual comparison of the model and inversion results. For the field data this is not possible. Therefore, in the backpropagation method we use the ratio of the maximum of the absolute value of the real part to the maximum of the absolute value of the imaginary part of the obtained images as an indicator of the inversion quality. We will call this test the real to imaginary ratio test. In the acoustic case, when attenuation effects are removed from the wavefield the object function will be real. Therefore, with full coverage in the wavenumber domain this ratio would be infinity. Due to sampling and limited coverage in the crosshole case, a good inversion would mean a high ratio, as discussed in section 2.4. In the field data, with the present formulation of diffraction tomography, not only is the removal of attenuation necessary but the removal of 2.5-D effects and wavefields besides the singly scattered P-waves is necessary as well, but can only be done approximately, therefore this test should be used with caution.

We use the real to imaginary ratio test initially to find an accurate background velocity for the inversion as discussed with the synthetic examples in section 2.4. Application of a range of velocities from 5000 to 5400 m/s gives a smooth variation with a peak in the ratio at 5270 m/s when the short average wavelet is used in the deconvolution. This velocity is consistent with the field data, transmission ray tomography inversions and laboratory measurements, indicating that the data processing

scheme has been useful in removing unwanted effects from the recorded wavefield and the test is reliable in this case.

When the deconvolution is done using common source or receiver gathers with the long wavelet, the variation of the real to imaginary ratio test with respect to velocity is unstable and several peaks appear. This is due to the sharp troughs in the wavelet spectrum which make the deconvolution operator unstable. We therefore prefer to use the average wavelet for doing the deconvolution. The real to imaginary ratio test is also used in order to determine the length of the Hamming window to be applied to the end of the traces. A good ratio is obtained for a window length of up to 7.0 ms.

3.4.1 S-wave and tube-wave reduction

In this section we demonstrate the sensitivity of the inversion algorithm to velocity. Because the inversion is done at the P-wave velocity, we expect the wavefields propagating with different velocities to be weakened in the resulting image. To demonstrate this principle, 2-D Born forward data are generated for two diffractors with the same circular scattering pattern (angle independent) and same amplitude but with different propagation velocities depending on the wavetype. For the following two examples, we consider a 10 by 20 m area with 0.5 m spacing of 40 sources and receivers in a crosshole configuration. For the P-to-S example we consider two diffractors, one diffractor at x = 5 m and z = 5 m with a propagation velocity of 5500 m/s from source to diffractor and diffractor to receiver (P-to-P), and the second diffractor at x = 5 m and z = 15 m with a propagation velocity of 5500 m/s from source to diffractor and 3200 m/s from diffractor to receiver (P-to-S). The 3200 m/s velocity used for the S-waves is in accordance with the field data. Figure 3.4.1a shows the absolute value of the real and imaginary parts of the averaged backpropagation inversion for 24 frequencies. The inversion is performed using a 5500 m/s background velocity.

We see that the P-to-P diffractor is reconstructed well but the P-to-S diffractor is widely distributed and has about one-tenth the amplitude it would have had if it were to be a P-to-P diffractor. Averaging backpropagation inversions is seen to be very effective in further reducing the amplitude of the P-to-S diffractor. In the quadratic programming inversion at 5500 Hz with negativity constraints and no smoothing, we get a similar result but the noise due to the P-to-S diffractor is more pronounced (Figure 3.4.1b).

The same test is carried out for fracture-generated tube-waves with the P-to-P diffractor located at x = 7.5 m and z = 10 m and the P-to-tube diffractor located at x = 0.25 m and z = 10 m, where a tube-wave velocity of 1400 m/s is used for the propagation of the wavefield from the diffractor to the receivers. Because of the slower velocity involved, the P-to-tube diffractor is not imaged as well as the P-to-S diffractor (see Figure 3.4.1a and 3.4.2a). Averaging backpropagation inversions is seen to improve the results similar to the previous case. The two lines at about 45° and - 45° from the horizontal in Figure 3.4.2b result from limited wavenumber domain coverage, as discussed at the end of section 2.3, and are not specific to the tube-wave velocity used. They can also be seen in the backpropagation inversion at a single frequency but are unnoticeable when averaging of images is performed due to the increased coverage (see Figure 3.4.2a).

We infer from these tests that the inversion method will reduce to a certain extent the wavefields propagating with a velocity different from the inversion velocity. The reduction will depend on how far the wave has propagated with this different velocity and how large a contrast this velocity forms with the inversion velocity. We conclude that tube and S-waves should be filtered out of the data set with as little harm to the P wavefield, but if some residues are to remain, the inversion process will also help reduce their effect on the image.

In field data, the amplitude of the S wavefield in crosshole applications will be lower than that generated here if the receiver component perpendicular to the formation is chosen for the inversion (due to the scattering pattern of the P-to-S converted waves) whereas, the amplitude of the fracture-generated tube-waves will in general be larger.

3.4.2 Diffraction tomography inversion results

Figure 3.4.3 is the inversion of crosshole data using 31 source and receiver pairs, starting at 3 m and ending at 18 m, with the top and bottom sections zero padded completing the coverage to 21 m. The zero padding is done to avoid possible tube-waves and boundary-waves generated by the tunnels from entering the inversion. In this case, a short average wavelet is used for deconvolution and images for 22 frequencies from 2685 to 5250 Hz with 122 Hz intervals are averaged. The heavy averaging and short wavelet are used in order to achieve an inversion with smooth variation. In the inversion, the spatial sampling is half the source and receiver sampling or 0.25 m and the inversion result is displayed from 2 to 19 m in this figure. The inversion velocity used is 5270 m/s.

The velocity values in Figure 3.4.3 are obtained directly from the inversion. In a full-waveform inversion, such as diffraction tomography, the amplitudes of the waveforms are utilized as well as the travel times. The source function, coupling of sources and receivers to the formation and the source radiation pattern are some of the factors that will affect the amplitudes of the waveforms measured, therefore the actual velocity values obtained in the inversion will depend on how well these effects are corrected for in the data processing. In the case we consider, the obtained values suggest that the data processing has performed quite well. Figure 3.4.3 is interpreted to indicate two distinct zones. Zone one starts at 8 to 10 m down the left borehole (BOFR 87.001) and ends at 15 to 18 m down the right borehole (BOFR 87.002) with a velocity near

4900 m/s. Zone two starts at 14 to 15 m down the left borehole (BOFR 87.001) and extends to 18 to 20 m down the right borehole (BOFR 87.002) with a somewhat higher velocity near 5000 m/s.

Figure 3.4.4 is the quadratic programming inversion for the crosshole case with 39 sources and receivers and deconvolution of data with the long average wavelet. The inversion frequency is 5250 Hz. We constrain the velocity of the inversion to be less than 5400 m/s and apply horizontal and vertical smoothing. The actual inversion velocity is 5270 m/s. In the inversion, the spatial sampling is equal to the source and receiver sampling or 0.5 m. This sampling is preferred due to computation time considerations.

The inversion agrees well with the fractures indicated by the core samples (see Figure 3.1.1). This is due to imaging of the fracture-generated tube-waves remaining in the data from receiver and source locations close to the fractures, together with scattered P-waves from the fractures. The agreement with the backpropagation method is also quite good. The first zone seen in the backpropagation case can be defined in more detail to be from 9 m down the left borehole (BOFR 87.001) to 17 m down the right borehole (BOFR 87.002). The second zone mentioned in the backpropagation inversion is not very clear here besides the beginning of the zone at 13 m down the left borehole (BOFR 87.001) and the end at 20 m down the right borehole (BOFR 87.002).

3.4.3 Comparison with transmission ray tomography

Figure 3.4.5 is a transmission ray tomography inversion of the crosshole data set with transverse isotropy corrections (for a review of the transmission ray tomography method, see Peterson et. al, 1985; Peterson, 1986). The transverse isotropy corrections to the first arrival times are performed using the method of Backus (1965). The spatial sampling is 0.25 m in the transmission ray tomography inversions of this section.

For the crosshole case, comparing the ray tomography inversion with the wave tomography inversions, we see that in general ray tomography gives the smooth variations in the medium whereas wave tomography gives a higher resolution inversion result. In addition, the inversion area is larger in the wave tomography inversions or regions near the boundaries are better resolved with respect to the transmission ray tomography inversions.

This inversion together with the quadratic programming inversion supports the existence of a possible third zone from 6 m down the left borehole (BOFR 87.001) to about 16 m down the right borehole (BOFR 87.002) in addition to the zone at 12 to 13 m down the left borehole (BOFR 87.001) and 19 m down the right borehole (BOFR 87.002).

In the transmission ray tomography approach, inversions were found to be quite sensitive to the transverse isotropy and corrections to data were necessary to improve the results.

Figure 3.4.6 is the anisotropy corrected transmission ray tomography inversion result using the crosshole data together with the VSP type data. As mentioned before the VSP type data could not be used in the wave tomography inversions due to recording problems affecting the amplitudes at late arrival times. Therefore, a direct comparison between the two methods cannot be carried out in this case.

This image indicates several zones. The main two zones can still be seen but a new strong zone enters the inversion. This zone starts from 12 to 16 m down the left borehole (BOFR 87.001) and intersects the top of the image area at 7 to 9 m horizontal. Traces of this zone can be spotted in the quadratic programming inversion result of Figure 3.4.4 but the angle of the zone is less steep. In Figure 3.4.4, this zone starts from 1 to 5 m down the right borehole (BOFR 87.002) and extends to about 4 to 7 m down the left borehole (BOFR 87.001). The strength of this zone in the ray tomography

inversions may be caused artificially by the deformations in the rock near the boundaries of the tunnels causing ray bending or nonlinear variations and will enter the inversion when the VSP type data are considered.

In addition to the above mentioned zone, there are also some other structures perpendicular to the fracturing direction which start at 19 m (Figure 3.4.4) and 15 to 16 m (Figures 3.4.3, 3.4.4 and 3.4.5) down the left borehole (BOFR 87.001). Several other low-velocity regions exist, one is at 8 m's in the vertical direction (down the borehole) and 6 to 7 m's in the horizontal direction (in the access tunnel) which distinctly appears in all images.

In general, the different inversion results agree well with the core samples and with each other in the crosshole case. The methods can be further improved in order to obtain more accurate results. In the next two sections we consider the extension of the theory to the elastic and transversely isotropic cases, and later apply the transverse isotropy developments to the field data.

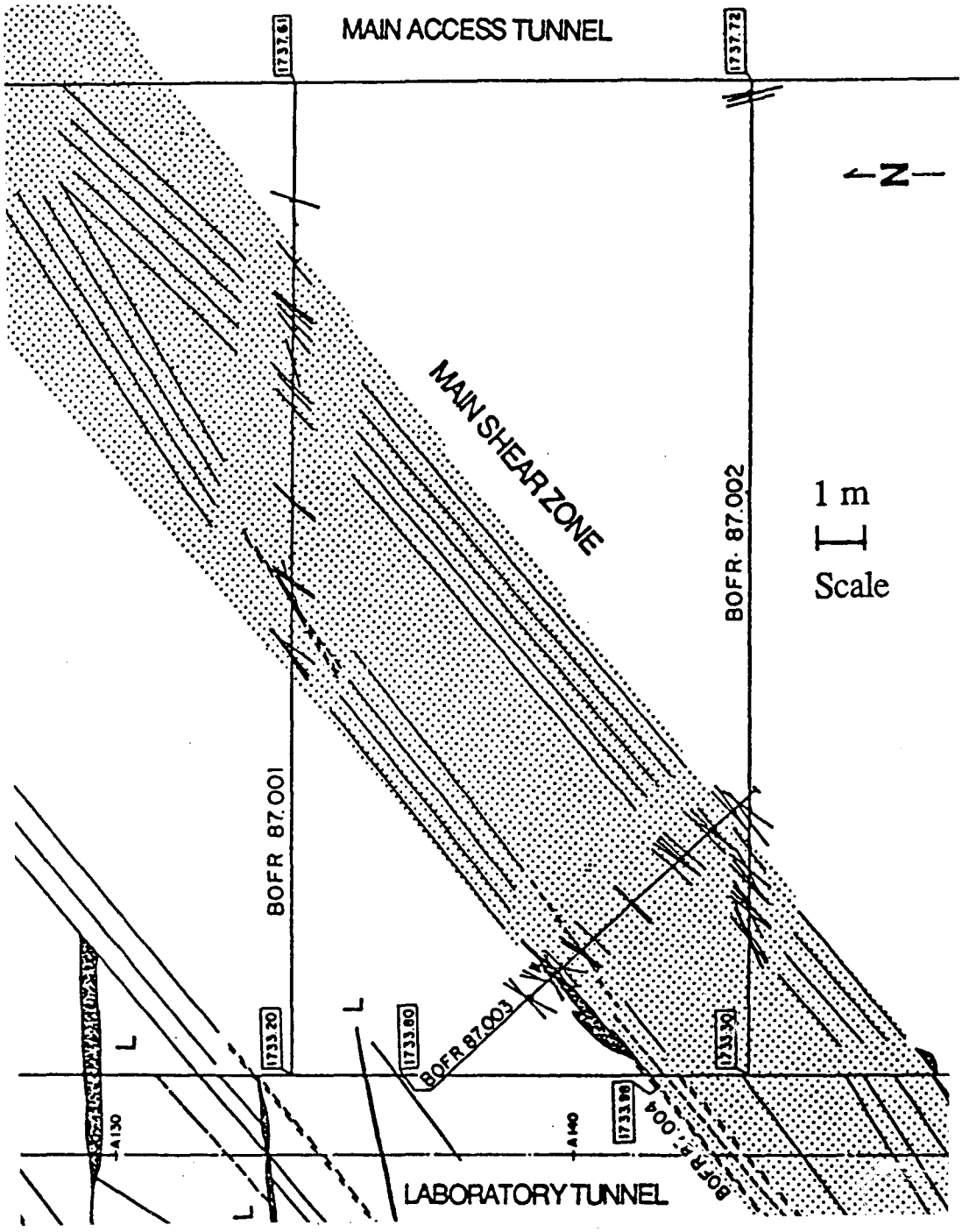

Figure 3.1.1 Geological interpretation of FRI test site and experiment geometry. Fractures seen in core samples are indicated by short lines at the borehole locations.

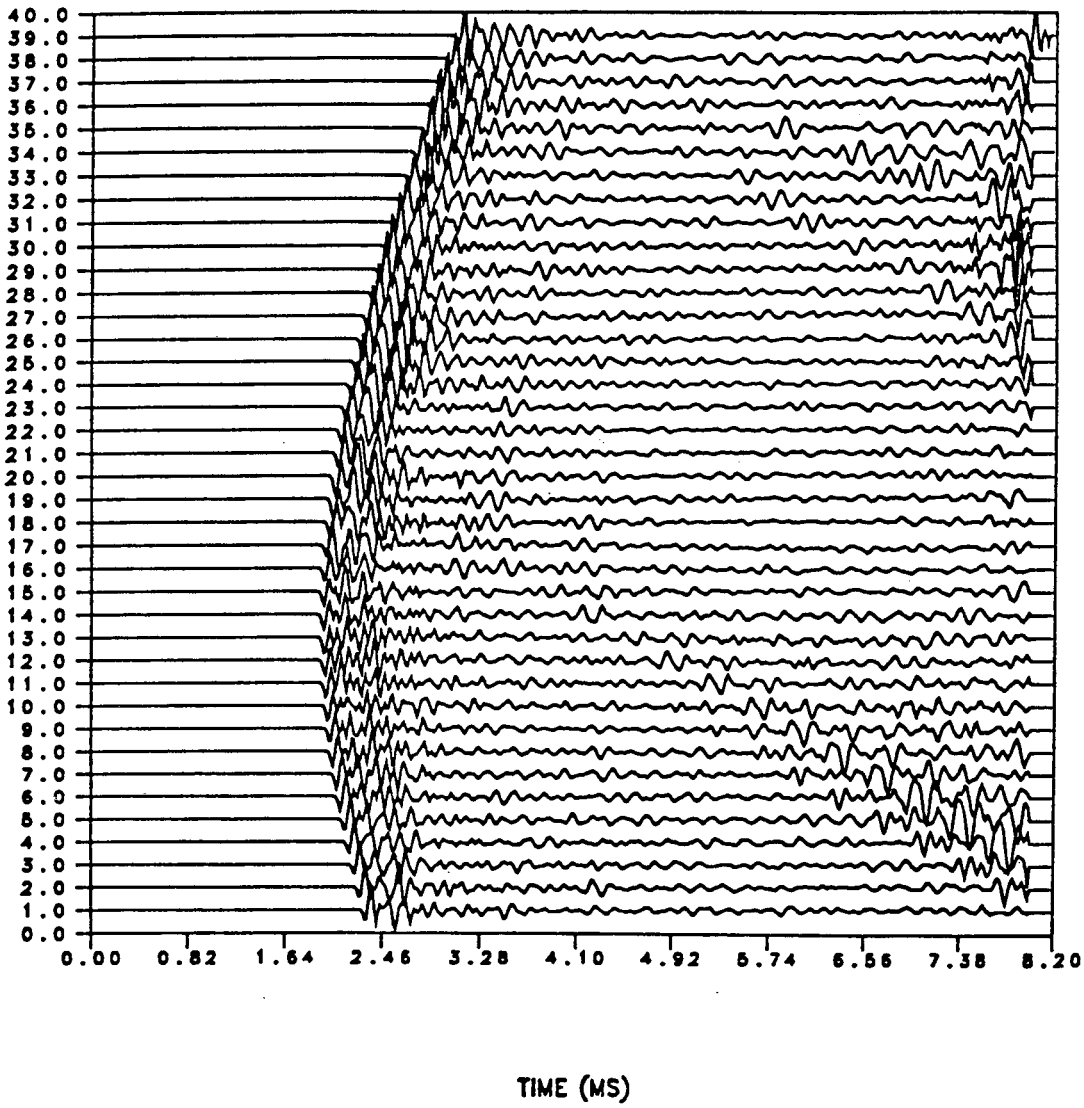

Figure 3.2.1 Crosshole data with source at 7.5 m down borehole BOFR 87.002 and receivers in BOFR 87.001.

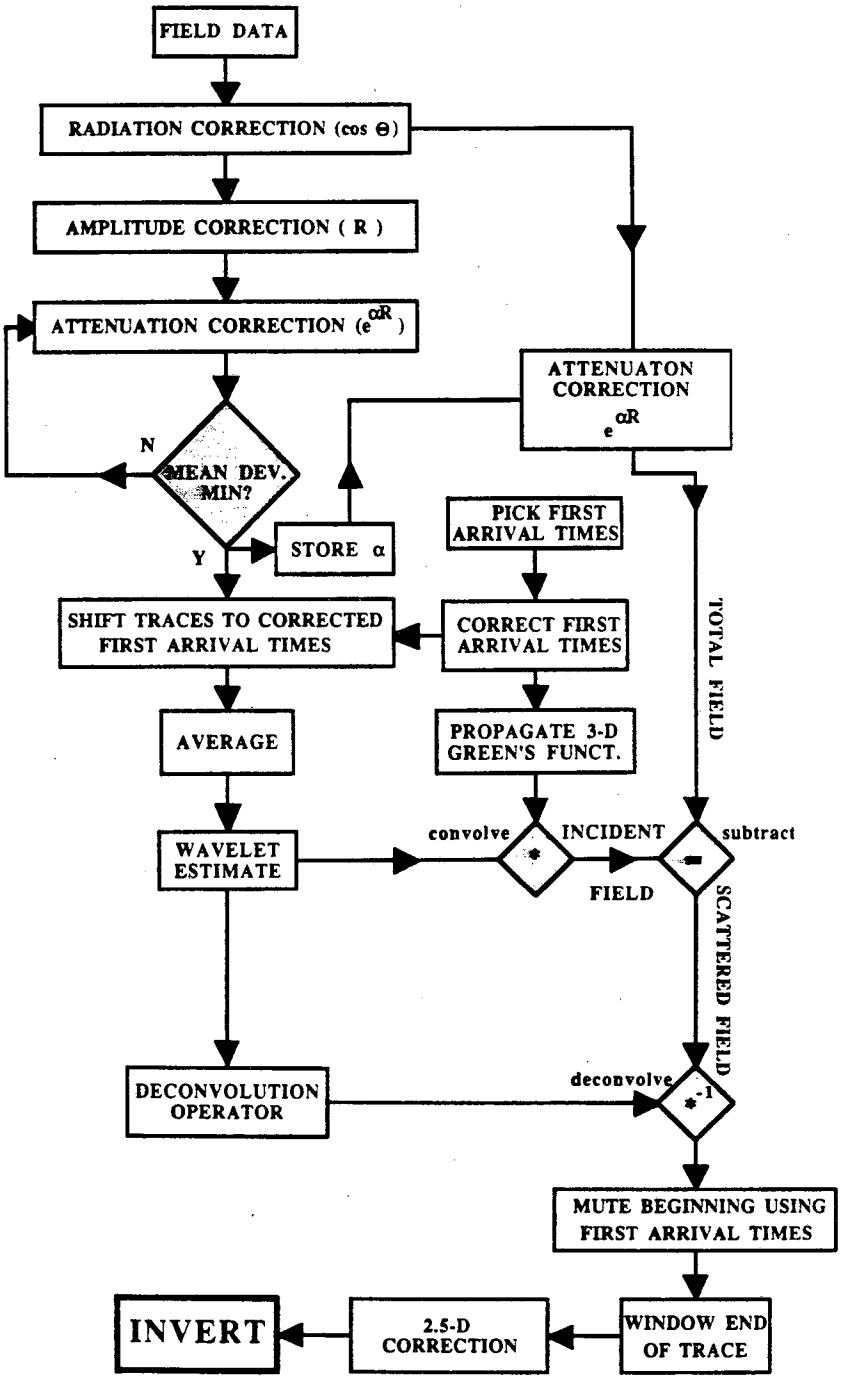

Figure 3.3.1 Data processing scheme.

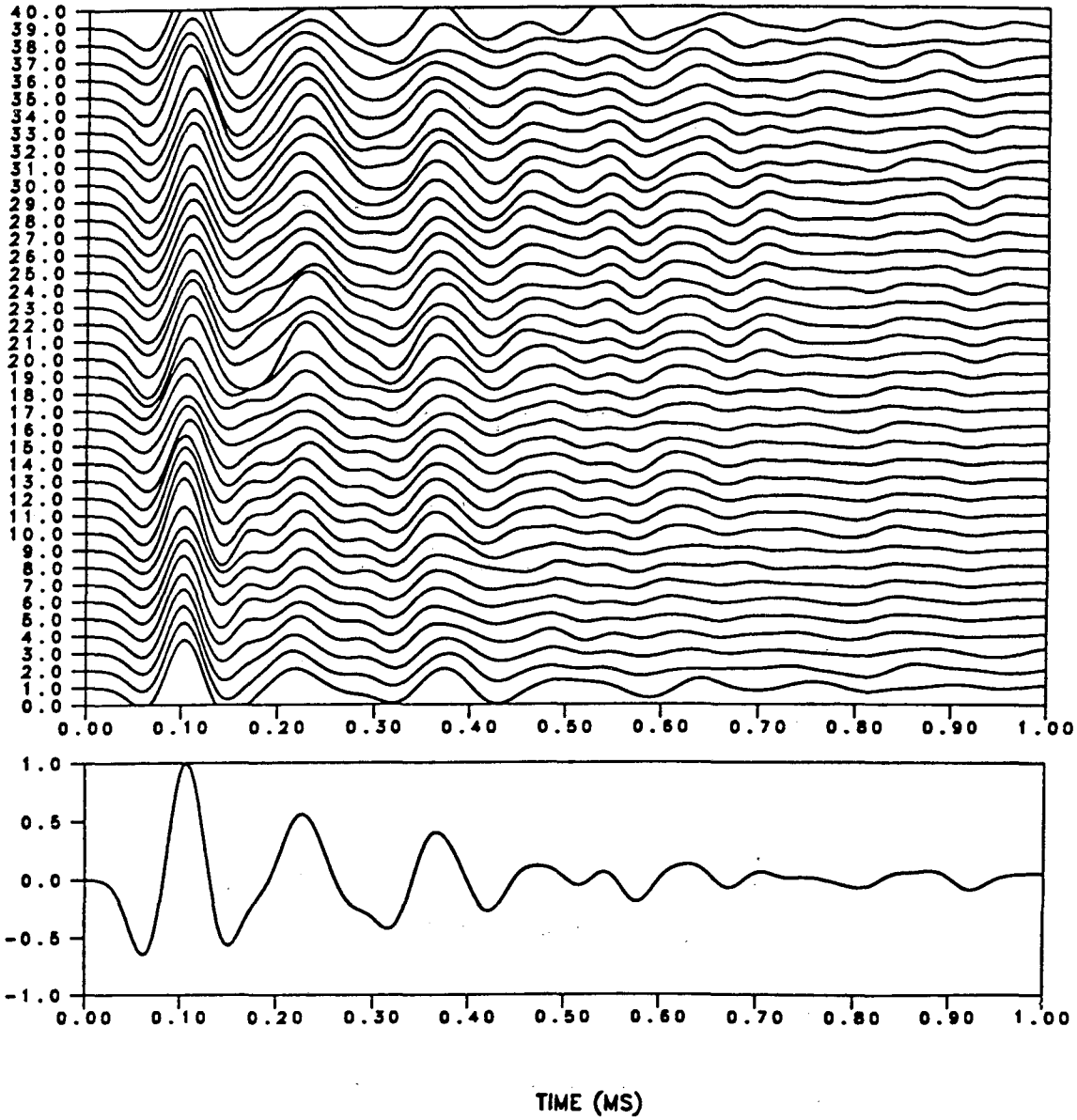

Figure 3.3.2 Common source gather (top) and average of all traces (bottom).

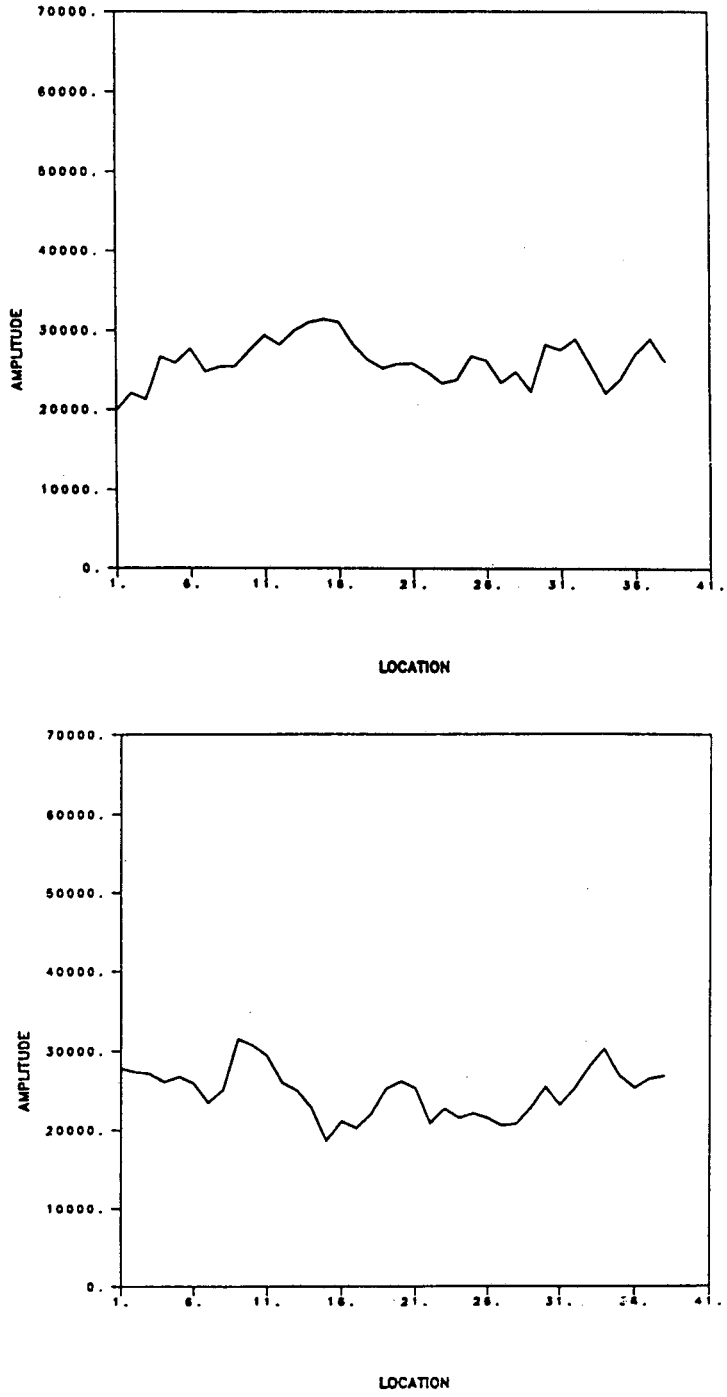

Figure 3.3.3a,b Maximum a) Common receiver gather amplitudes for all receivers (top) and b) Common source gather amplitudes for all sources (bottom).

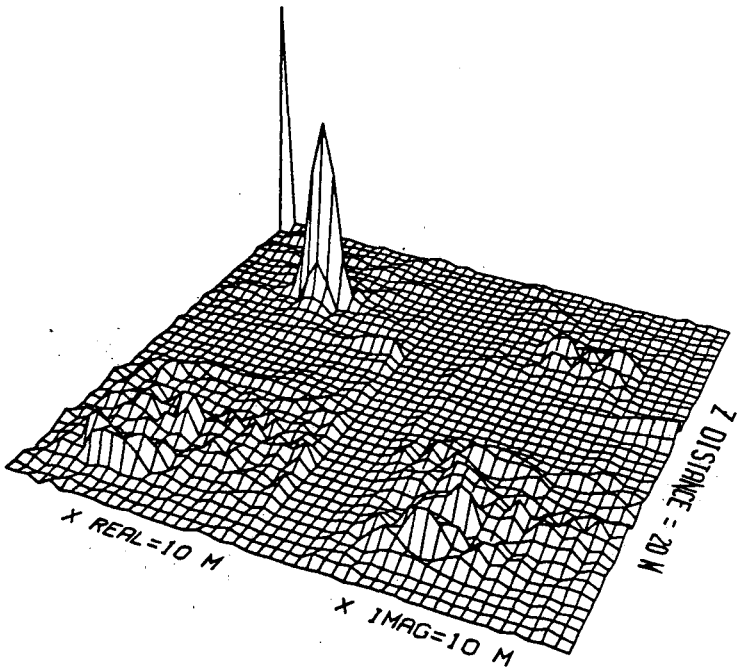

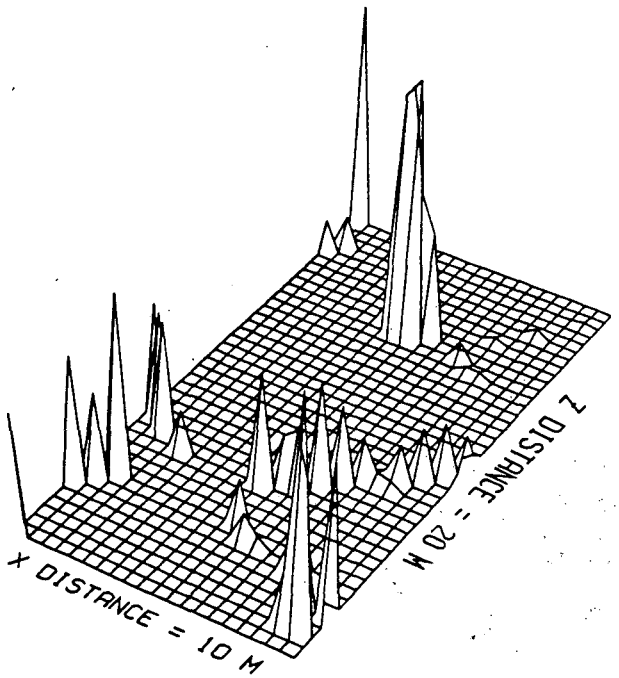

Figure 3.4.1a,b Shear-wave filtering, a) Averaged backpropagation inversion (top) and b) Quadratic programming inversion (bottom).

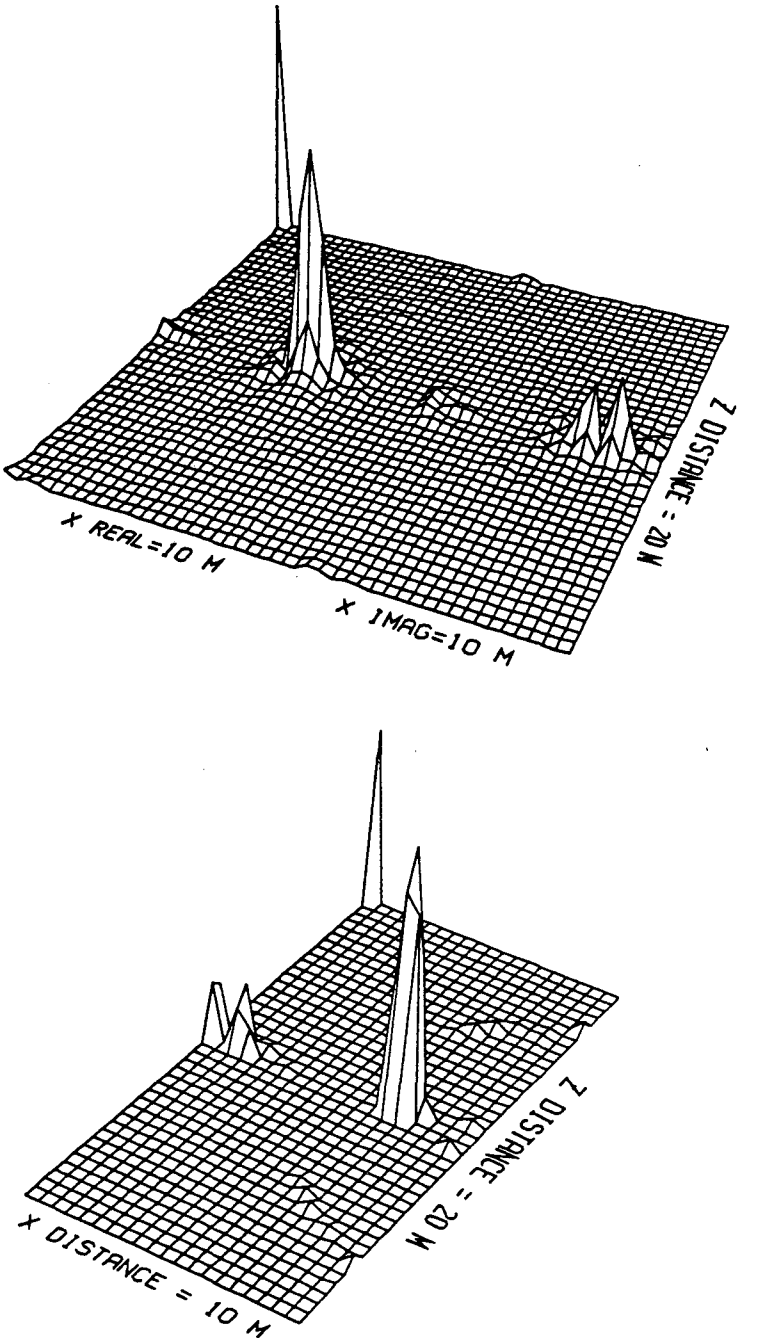

Figure 3.4.2a,b Tube-wave filtering, a) Averaged backpropagation inversion (top) and b) Quadratic programming inversion (bottom).

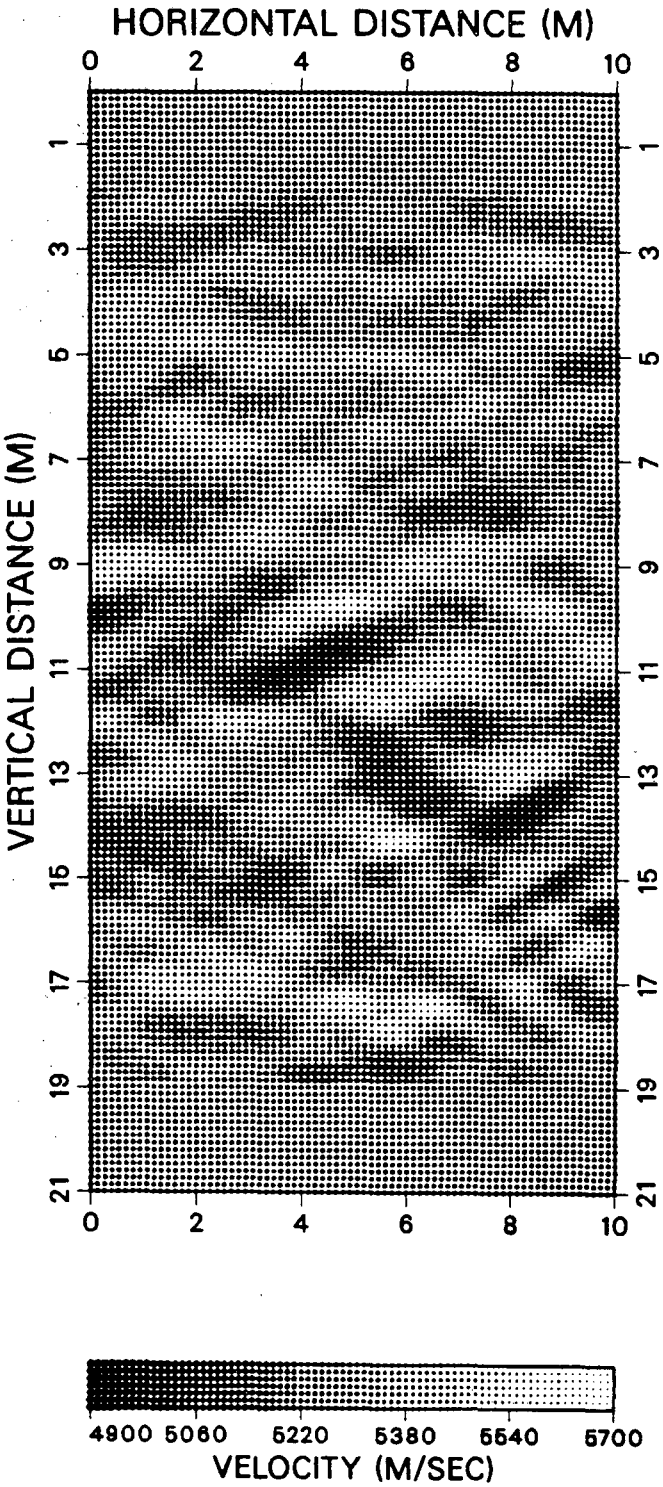

Figure 3.4.3 Averaged backpropagation inversion of crosshole field data from 2685 to 5250 Hz with 122 Hz intervals.

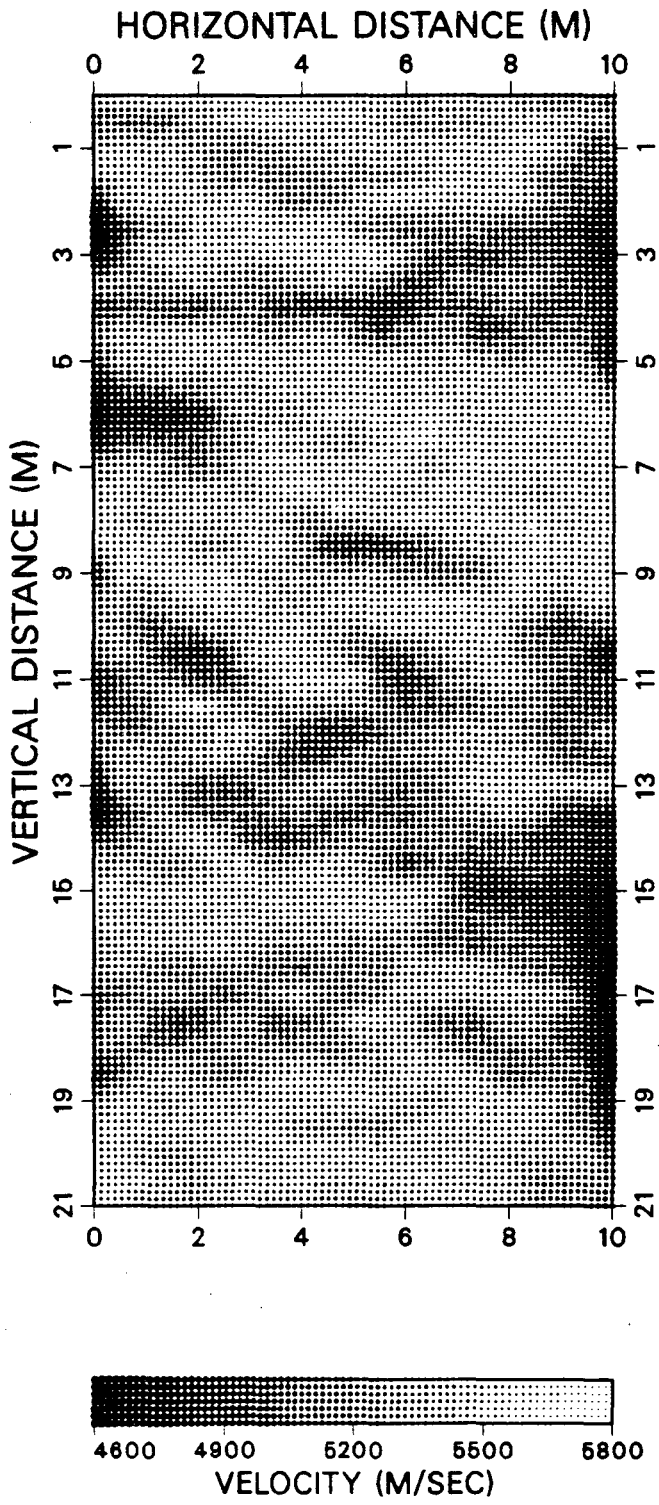

Figure 3.4.4 Quadratic programming inversion of crosshole field data at 5250 Hz.

Velocities are constrained to be lower than 5400 m/s.

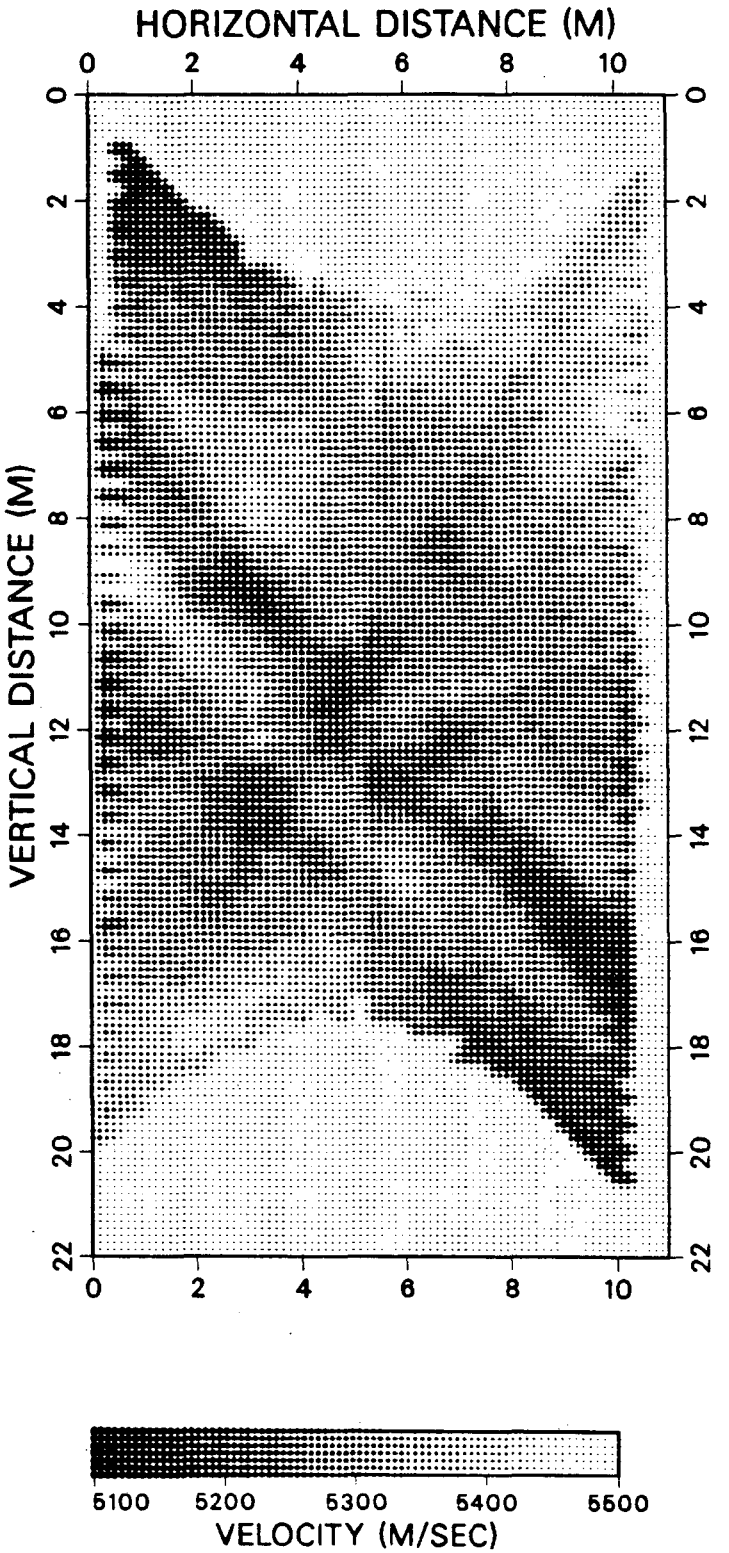

Figure 3.4.5 Transmission ray tomography inversion of crosshole data.

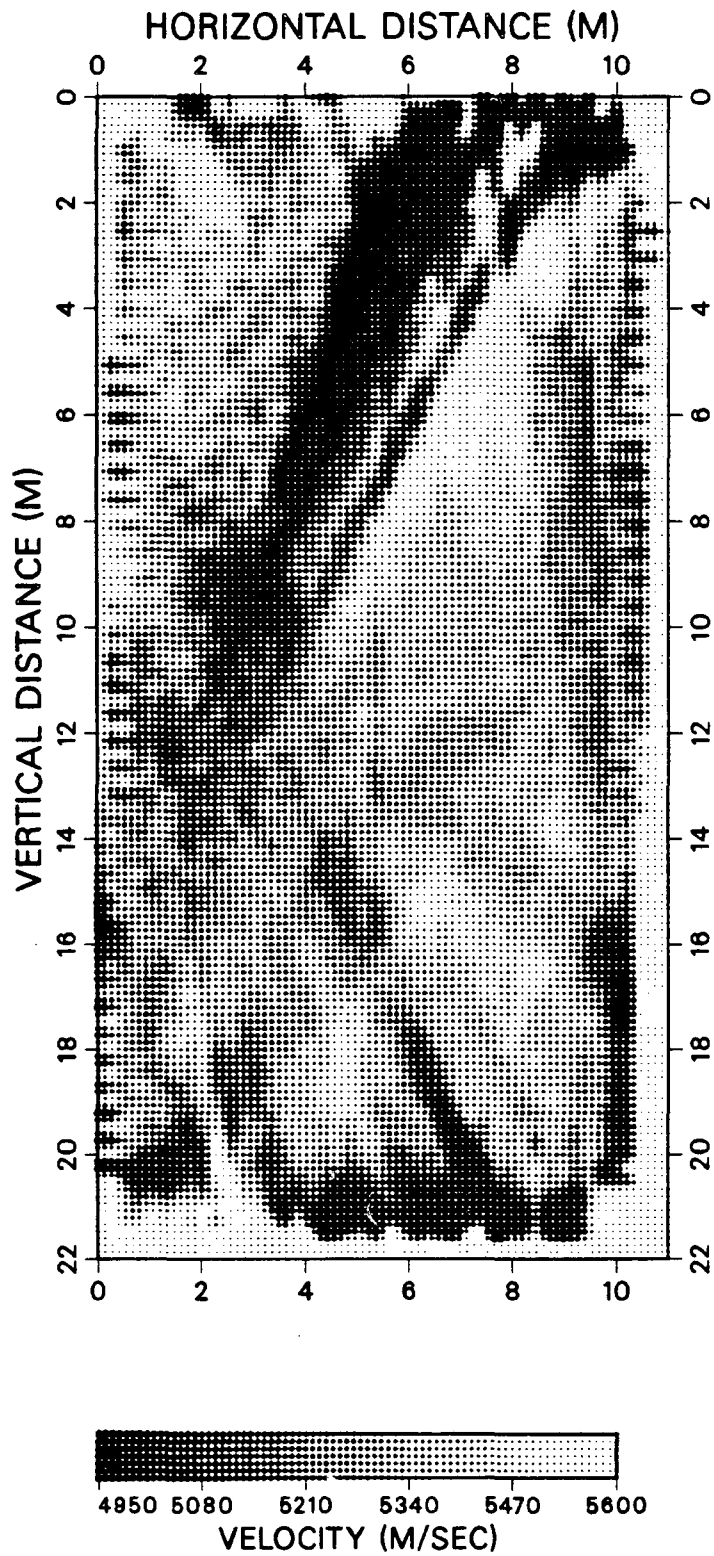

Figure 3.4.6 Transmission ray tomography inversion of the entire data set.

Chapter 4

Elastic Inversion

In this chapter, we extend the inversion theory to an elastic medium. In general, an elastic medium is approximated by an acoustic medium due to the simplicity brought not only to the theoretical formulation but also to the field procedures and the computational requirements making it more economical. The elastic wavefield is a combination of P and S-waves including conversions from P-to-S and S-to-P when a scatterer is encountered. The P wavefield can be approximated by an acoustic wave equation but the success of this approximation will depend on how well this field can be extracted from the total field observed. In addition, in the acoustic inversion the scattering pattern of the observed wavefield is assumed circular or angle independent whereas in actuality it is angle dependent for both P and S-waves. Choosing an appropriate geometry and the right components of the data, by taking into account the scattering patterns of the wavefields (as done in chapter 3), the P wavefield can be represented quite well in the acoustic theory framework. For applications such as fracture detection where the S wavefield carries valuable information and to obtain a high-resolution image for detailed analysis, the elastic wavefield should be used thereby removing some of the approximations made in the formulation.

In this chapter, we assume a 2-D medium and formulate the problem for the SH-waves and the P-SV waves.

4.1 Forward problem

The equation of motion in the source-free region of an elastic, isotropic medium can be given as

$$\rho\ddot{u}_i = (\lambda\nabla\cdot\vec{\mathbf{u}})_{,i} + (\mu(u_{i,j} + u_{j,i}))_{,j} \,, \tag{4.1}$$

where ρ is the density, λ and μ are the Lamé parameters of the medium and $u_i(\vec{\mathbf{r}},t)$ is the displacement in the i *th* direction at location $\vec{\mathbf{r}}$ and at time t. Defining

$$\rho(\vec{\mathbf{r}}) = \rho_0 + \delta\rho(\vec{\mathbf{r}}) \,,$$

$$\mu(\vec{\mathbf{r}}) = \mu_0 + \delta\mu(\vec{\mathbf{r}}) \,,$$

$$\lambda(\vec{\mathbf{r}}) = \lambda_0 + \delta\lambda(\vec{\mathbf{r}}) \,, \tag{4.2}$$

where δ represents the perturbation to a homogeneous background and substituting into equation 4.1, we have

$$\rho_0\ddot{u}_i - (\lambda_0 + \mu_0)(\nabla\cdot\vec{\mathbf{u}})_{,i} - \mu_0\nabla^2 u_i = -\,\delta\rho\ddot{u}_i + (\delta\lambda + \delta\mu)(\nabla\cdot\vec{\mathbf{u}})_{,i} + \delta\mu\nabla^2 u_i$$
$$+ (\delta\lambda)_{,i}\nabla\cdot\vec{\mathbf{u}} + (\delta\lambda)_{,j}(u_{i,j} + u_{j,i}) \,. \tag{4.3}$$

The displacement in equation 4.3 can be represented as a superposition of the incident and scattered displacements or $u_i = u_i^0 + u_i^s$ giving,

$$\rho_0\ddot{u}_i^s - (\lambda_0 + \mu_0)(\nabla\cdot\vec{\mathbf{u}}^s)_{,i} - \mu_0\nabla^2 u_i^s = Q_i \,, \tag{4.4}$$

where

$$Q_i = -\,\delta\rho\ddot{u}_i + (\delta\lambda + \delta\mu)(\nabla\cdot\vec{\mathbf{u}})_{,i} + \delta\mu\nabla^2 u_i + (\delta\lambda)_{,i}\nabla\cdot\vec{\mathbf{u}} + (\delta\mu)_{,j}(u_{i,j} + u_{j,i}) \,. \tag{4.5}$$

To obtain this equation $\rho_0\ddot{u}_i^0 - (\lambda_0 + \mu_0)(\nabla\cdot\vec{\mathbf{u}}^0)_{,i} - \mu_0\nabla^2 u_i^0 = 0$ was used. In equation 4.4, Q_i is an equivalent source. Using Green's theorem and the free-space Green's function we have (see Aki and Richards, 1980; Wu and Aki, 1985),

$$u_i^s = \int_V Q_j(\xi) *_t G_{ij}(\xi)\, dV(\xi) \,, \tag{4.6}$$

Where ' $*_t$ ' denotes convolution in time. Using the Born approximation, $u \rightarrow u^0$ equation 4.5 can be given as

$$Q_i = -\,\delta\rho\ddot{u}_i^0 + (\delta\lambda\nabla\cdot\vec{u}^0)_{,i} + (\delta\mu(u_{i,j}^0 + u_{j,i}^0))_{,j}\,. \tag{4.7}$$

Substituting equation 4.7 into 4.6

$$u_i^s = \int_v \left(-\,\delta\rho\ddot{u}_j^0 *_t G_{ji} + (\delta\lambda\nabla\cdot\vec{u}^0)_{,j} *_t G_{ji} + (\delta\mu(u_{j,k}^0 + u_{k,j}^0))_{,k} *_t G_{ji}\right) dV\,. \tag{4.8}$$

Integrating by parts the terms involving the derivatives of the elastic parameters we have

$$u_i^s = -\int_v \left(\delta\rho\ddot{u}_j^0 *_t G_{ji} + (\delta\lambda\nabla\cdot\vec{u}^0) *_t G_{ji,j} + (\delta\mu(u_{j,k}^0 + u_{k,j}^0)) *_t G_{ji,k}\right) dV\,. \tag{4.9}$$

In the frequency domain and for a source in the l-direction and measurements in the j-direction equation 4.9 becomes

$$u_{lj}^s(\vec{r}_s,\vec{r}_g,\omega) = -\int_v \left(-\,\omega^2\delta\rho G_{li}^s G_{ij}^g + \delta\lambda G_{lk,k}^s G_{ij,i}^g + \delta\mu(G_{li,k}^s + G_{lk,i}^s)G_{ij,k}^g\right) dV\,. \tag{4.10}$$

This equation forms the fundamental equation of the elastic case, obtained by using the Born approximation. Because we have assumed that the background is homogeneous (equation 4.2) the Green's function can be determined analytically. If the background were assumed to be inhomogeneous equation 4.10 would still hold but then the Green's function would have to be determined using high-frequency approximations (for a discussion, see Beydoun and Mendes, 1989; Beylkin and Burridge, 1990). In this equation $G_{ij}^s = G_{ij}(\vec{r},\vec{r}^s)$ for the source and $G_{ij}^g = G_{ij}(\vec{r},\vec{r}^g)$ for the receiver.

The elastic Green's function in 3-D for a homogeneous background can be found in Aki and Richards (1980). In Appendix C and D derivation of the 2-D Green's function for a homogeneous background is discussed (Eastwood, 1988). Here we give the results in the transform domain. For SH-waves

$$G_{yy}(\vec{r},k_s) = \frac{i}{2\mu_0\gamma_s}\exp[i\gamma_s d_s]\exp\left[-\,ik\hat{s}\cdot\vec{r}\right]. \tag{4.11}$$

For P-SV waves

$$G(\vec{r},k_s) = \frac{i}{2\rho_0\omega^2}\begin{bmatrix} (k_x^s)^2 & {}^{\alpha}k_z^s k_x^s \\ {}^{\alpha}k_z^s k_x^s & ({}^{\alpha}k_z^s)^2 \end{bmatrix} \frac{\exp\left[i\left(\gamma_s^{\alpha} d_s - k^{\alpha}\hat{s}\cdot\vec{r}\right)\right]}{\gamma_s^{\alpha}}$$

$$+ \frac{i}{2\rho_0\omega^2}\begin{bmatrix} ({}^{\beta}k_z^s)^2 & -{}^{\beta}k_z^s k_x^s \\ -{}^{\beta}k_z^s k_x^s & (k_x^s)^2 \end{bmatrix} \frac{\exp\left[i\left(\gamma_s^{\beta} d_s - k^{\beta}\hat{s}\cdot\vec{r}\right)\right]}{\gamma_s^{\beta}} . \quad (4.12)$$

Here, ${}^{\alpha}k_z^s$ and ${}^{\beta}k_z^s$ are respectively the vertical wavenumbers over the source line for the P and S-waves. These equations are for the sources and the equations for the receivers (in the Born approximation framework) can be obtained by replacing the s's with g's in the above equations.

4.2 Inversion of SH-waves

For SH-waves in 2-D, equation 4.10 can be written as

$$u_{yy}^s(\vec{r}_s,\vec{r}_g,\omega) = -\int_V \left(-\omega^2\delta\rho G_{yy}^s G_{yy}^g + \delta\mu(G_{yy,x}^s G_{yy,x}^g + G_{yy,z}^s G_{yy,z}^g)\right) dV . \quad (4.13)$$

Similar to the acoustic case, we take the Fourier transform of this equation over the source and receiver lines to form the plane-wave decomposition. The application of this process to the Green's function, together with the derivative operations, is given in Appendix B. For an outgoing wave from the source ($\hat{i} = -\hat{s}$) and an incoming wave to the receiver ($\hat{g}$) we have

$$\tilde{u}_{yy}^s(k_s,k_g,\omega) = \frac{-\exp[i(\gamma_g d_g + \gamma_s d_s)]}{4\mu_0^2\gamma_s\gamma_g}\int_V \left(\omega^2\delta\rho(\vec{r}) + \delta\mu(\vec{r})(k_x^s k_x^g + k_z^s k_z^g)\right)$$

$$\times \exp\left[-i\,k(\hat{g} - \hat{i})\cdot\vec{r}\right] dV, \quad (4.14)$$

where now, $\hat{i} = \bar{x}k_x^s + \bar{z}k_z^s$. Using the dot product and the definitions of the unit vectors we can substitute $(k_x^s k_x^g + k_z^s k_z^g) = k^2(\hat{i}\cdot\hat{g})$ in the above equation yielding

$$\widetilde{u}^s_{yy}(k_s,k_g,\omega) = \frac{-\exp[i(\gamma_g d_g + \gamma_s d_s)]}{4\mu_0^2\gamma_s\gamma_g} \int_V \left(\omega^2\delta\rho(\vec{r}) + k^2\delta\mu(\vec{r})(\hat{i}\cdot\hat{g})\right)$$

$$\times \exp\left[-i\,k(\hat{g} - \hat{i})\cdot\vec{r}\right] dV. \quad (4.15)$$

The right side of this equation is in the form of a Fourier transform, therefore, we can write this equation as

$$\left[\omega^2\widetilde{\delta\rho}(\vec{K}) + k^2\widetilde{\delta\mu}(\vec{K})(\hat{i}\cdot\hat{g})\right] = -\,4\mu_0^2\gamma_s\gamma_g\widetilde{u}^s_{yy}(k_s,k_g,\omega)\exp[-i(\gamma_g d_g + \gamma_s d_s)]\,. \quad (4.16)$$

Equation 4.16 forms the linear relationship between the perturbation in the medium parameters and the observed scattered field. This equation is quite similar to the variable density acoustic case (Devaney, 1985) as can be expected since both wavefields are scalar. The main difference is that in this case we use a different data set and invert for different physical parameters of the medium.

At this point the problem can be solved for the term in the brackets in the above equation simply by following the inversion procedure for the backpropagation or the quadratic programming cases of the acoustic data, chapter 2. In order to obtain the individual physical parameters inside the brackets on the left side of equation 4.16, we must require the same number of independent measurements as the physical parameters and solve the resulting matrix. To obtain independent measurements we see from the terms in the brackets that we can use either the frequency dependence of the parameters, or the dependence of the parameters on the directionality of the plane-waves from the source to the geophone, or both. In general, the resulting matrix to be solved is ill-conditioned (Le Bras, 1985; Beydoun and Mendes, 1989; Beylkin and Burridge, 1990). An inversion method using the directionality of the plane-waves has been considered by Özbek (1988) where the ill-conditioning is taken care of by using multi-angles and performing a least-squares inversion for the parameters. Norton (1983) has proposed a method which uses both the directionality and the frequency dependence of the

parameters in an optimal fashion to stabilize the ill-conditioned problem. We will investigate this approach and extend it to seismic applications in section 4.5. In the diffraction tomography formulation the frequency is fixed and all possible directions of plane-waves are used to reconstruct the object, therefore in this method inversions at different frequencies can be obtained and used to extract the individual parameters sought. In this case the ill-conditioning is taken care of by either choosing two frequencies with a large difference between them or by using multi-frequencies and posing a least-squares problem. The formulation presented here is parallel to that carried out by Devaney (1985) for the variable density acoustic case. The main differences are that we are now investigating the elastic rather than the acoustic problem and considering line sources rather than plane-wave sources. We will also need different filtering operators since we do not have the comfort of the coverage obtainable in medical imaging applications. As a result of the limited view problem, as discussed earlier, seismic inversions cannot be expected to achieve the quality of the inversion results obtainable in medical imaging applications.

To solve for the SH-wave case, as done in the variable density acoustic case, we substitute the following identity

$$\hat{\mathbf{i}}\cdot\hat{\mathbf{g}} = 1 - \frac{1}{2}(\hat{\mathbf{g}} - \hat{\mathbf{i}})^2 = 1 - \frac{1}{2k^2}|\vec{\mathbf{K}}|^2 , \tag{4.17}$$

into equation 4.16 which yields

$$k^2\left(\frac{\widetilde{\delta\rho}(\vec{\mathbf{K}})}{\beta_0^2} + \frac{\widetilde{\delta\mu}(\vec{\mathbf{K}})}{\beta_0^4}\right) + \left(\frac{-\widetilde{\delta\mu}(\vec{\mathbf{K}})}{2\beta_0^4}|\vec{\mathbf{K}}|^2\right) = -4\rho_0^2\gamma_s\gamma_g\tilde{u}^s_{yy}(k_s,k_g,\omega)$$

$$\times \exp[-i(\gamma_g d_g + \gamma_s d_s)] . \tag{4.18}$$

Representing the first two terms on the left-hand side respectively by $A(\vec{K})$ and $B(\vec{K})$ and taking the inverse Fourier transform of equation 4.18 with a change of variables of integration we have

$$\left[k^2A(\vec{r}) + B(\vec{r})\right] = \frac{-4\rho_0^2}{(2\pi)^2}\iint dk_s\, dk_g\, J(K_x,K_z|k_s,k_g)\gamma_s\gamma_g\tilde{u}^s_{yy}\exp[-i(\gamma_g d_g + \gamma_s d_s)]$$

$$\times \exp[i(K_x x + K_z z)]\,, \qquad (4.19)$$

with $\vec{K} = k(\hat{g} - \hat{i}) = K_x\bar{x} + K_z\bar{z}$ where $K_x = k_x^g - k_x^s$ and $K_z = k_z^g - k_z^s$.

From this equation we can see the frequency dependence of the two terms since $k = \omega/\beta_0$. From equation 4.19 we also see that a backpropagation inversion at a fixed frequency will give us the so called raw inversion or the term on the left-hand side of this equation. In order to obtain the individual parameters we can perform an inversion at two distinct frequencies and extract the individual parameters as follows: If we call the raw inversions obtained at two frequencies $f_2 > f_1$ as $F_i(\vec{r})$ we will have

$$\begin{bmatrix} F_1(\vec{r}) \\ H_1(\vec{r}) * F_2(\vec{r}) \end{bmatrix} = \begin{bmatrix} k_1^2 & 1 \\ k_2^2 & 1 \end{bmatrix}\begin{bmatrix} A(\vec{r}) \\ B(\vec{r}) \end{bmatrix}, \qquad (4.20)$$

where $H_1(\vec{r})$ is a filter used to bring the second inversion (high-frequency) to the same frequency content as the first one for reasons of stability. This filter is quite complicated in seismic applications where the coverage is limited and will be discussed in section 4.4 for the crosshole case. In the above equation $A(\vec{r}) = A_1(\vec{r}) = H_1(\vec{r}) * A_2(\vec{r})$ and a similar equation holds for $B(\vec{r})$, with ' * ' denoting spatial convolution. Inverting this matrix we have

$$\begin{bmatrix} A(\vec{r}) \\ B(\vec{r}) \end{bmatrix} = \frac{1}{(k_2^2 - k_1^2)}\begin{bmatrix} -1 & 1 \\ k_2^2 & -k_1^2 \end{bmatrix}\begin{bmatrix} F_1(\vec{r}) \\ H_1(\vec{r}) * F_2(\vec{r}) \end{bmatrix}. \qquad (4.21)$$

Upon obtaining $A(\vec{r})$ and $B(\vec{r})$ from this equation, we take their Fourier transform and solve for the unknown parameters using

$$\widetilde{\delta\mu}(\vec{\mathbf{K}}) = \frac{-2\beta_0^4}{|\vec{\mathbf{K}}|^2} B(\vec{\mathbf{K}}),$$

$$\widetilde{\delta\rho}(\vec{\mathbf{K}}) = \beta_0^2 A(\vec{\mathbf{K}}) + \frac{2\beta_0^2}{|\vec{\mathbf{K}}|^2} B(\vec{\mathbf{K}}) . \tag{4.22}$$

Taking the inverse Fourier transform of these equations will yield the physical parameters in space.

Although this formulation is elegant, in practice a somewhat different approach is used to stabilize the inversion procedure. The problem comes from the divisions in equations 4.22 and is avoided by performing two separate sets of inversions. One is the set just described in equation 4.18 and the other is the inversion of

$$k^2\left(\frac{\widetilde{\delta\rho}(\vec{\mathbf{K}})}{|\vec{\mathbf{K}}|^2\beta_0^2} + \frac{\widetilde{\delta\mu}(\vec{\mathbf{K}})}{|\vec{\mathbf{K}}|^2\beta_0^4}\right) + \left(\frac{-\widetilde{\delta\mu}(\vec{\mathbf{K}})}{2\beta_0^4}\right) = -4\rho_0^2 \frac{\gamma_s\gamma_g}{|\vec{\mathbf{K}}|^2} \widetilde{u}^s_{yy}(k_s,k_g,\omega)$$

$$\times \exp[-i(\gamma_g d_g + \gamma_s d_s)] . \tag{4.23}$$

Representing the first two terms on the left-hand side respectively by $A'(\vec{\mathbf{K}})$ and $B'(\vec{\mathbf{K}})$ and following the above procedure we can now solve the equations for $A'(\vec{\mathbf{K}})$ and $B'(\vec{\mathbf{K}})$. Using $B'(\vec{\mathbf{K}})$ from the second set of solutions and $A(\vec{\mathbf{K}})$ from the first set we can write a stable set of solutions as

$$\widetilde{\delta\mu}(\vec{\mathbf{K}}) = -2\beta_0^4 B'(\vec{\mathbf{K}}),$$

$$\widetilde{\delta\rho}(\vec{\mathbf{K}}) = \beta_0^2 A(\vec{\mathbf{K}}) - \frac{\widetilde{\delta\mu}(\vec{\mathbf{K}})}{\beta_0^2} = \beta_0^2 A(\vec{\mathbf{K}}) + 2\beta_0^2 B'(\vec{\mathbf{K}}) . \tag{4.24}$$

The extension of this method to more than two frequencies can be carried out, using a least-squares method to invert the resulting matrices, and should be used in field data applications.

We proceed to the next section where this technique will be applied to the inversion of P-SV waves with some modifications in order to recover three parameters simultaneously. We will discuss why the method presented here works and when it will not and present synthetic examples after investigating the P-SV wave case.

To formulate the quadratic programming inversion equation 4.14 can be used. In this case, similar to the above procedure, the raw inversion can be obtained at two separate frequencies using equation 4.14 and the resulting 2 by 2 matrix solved to obtain the individual parameters. We do not investigate this case any further since it is a straightforward extension of the above method.

4.3 Inversion of P-SV waves

The displacement for a source in the l-direction and measurements in the j-direction can be represented as a superposition of four wavetypes, namely P-to-P, P-to-S, S-to-P and S-to-S, or equivalently we can write $u^s_{lj} = u^{P\text{-}P}_{lj} + u^{P\text{-}S}_{lj} + u^{S\text{-}P}_{lj} + u^{S\text{-}S}_{lj}$. This representation is a direct consequence of the Green's function representation, equation 4.12. Substituting the appropriate parts of the Green's function into equation 4.10 for each of the four different wavetypes results in:

$$\tilde{u}^{PP}_{lj}(k_s,k_g,\omega) = \frac{-1}{4\rho_0^2\omega^4}\int_v \left\{\delta\lambda k^4 + \delta\rho\omega^2 k^s_i k^g_i + 2\delta\mu k^s_i k^g_i k^s_k k^g_k\right\} k^s_l k^g_j S^P R^P \, dV \, ,$$

$$\tilde{u}^{PS}_{lj}(k_s,k_g,\omega) = \frac{-1}{4\rho_0^2\omega^4}\int_v \left\{\delta\rho\omega^2 k^s_i k^g_I + 2\delta\mu k^s_i k^g_i k^s_k k^g_K\right\} k^s_l k^g_J S^P R^S \, dV \, ,$$

$$\tilde{u}^{SP}_{lj}(k_s,k_g,\omega) = \frac{-1}{4\rho_0^2\omega^4}\int_v \left\{\delta\rho\omega^2 k^s_I k^g_i + 2\delta\mu k^s_i k^g_i k^s_K k^g_k\right\} k^s_L k^g_j S^S R^P \, dV \, ,$$

$$\tilde{u}^{SS}_{lj}(k_s,k_g,\omega) = \frac{-1}{4\rho_0^2\omega^4}\int_v \left\{\delta\rho\omega^2 k^s_I k^g_I + \delta\mu(k^s_i k^g_i k^s_K k^g_K + k^s_i k^g_I k^s_K k^g_k)\right\} k^s_L k^g_J S^S R^S \, dV \, , \quad (4.25)$$

where the summation convention holds for all indices and the indices are for x and z in the 2-D case. A capital index is to be interpreted as follows: i) Switch the index value, ii) If the resulting index values from the interaction of two capital indices are not the same, reverse the sign. For example, for j = x we have $k_J^s k_I^s k_i^g = k_Z^s(k_Z^s k_X^g - k_X^s k_Z^g)$ and for j = z we have $k_J^s k_I^s k_i^g = - k_X^s(k_Z^s k_X^g - k_X^s k_Z^g)$. In addition

$$S^P = \frac{\exp\left[i\left(\gamma_s^\alpha d_s + k^\alpha \hat{\mathbf{i}}\cdot\vec{\mathbf{r}}\right)\right]}{\gamma_s^\alpha} ,$$

$$S^S = \frac{\exp\left[i\left(\gamma_s^\beta d_s + k^\beta \hat{\mathbf{i}}\cdot\vec{\mathbf{r}}\right)\right]}{\gamma_s^\beta} ,$$

$$R^P = \frac{\exp\left[i\left(\gamma_g^\alpha d_g - k^\alpha \hat{\mathbf{g}}\cdot\vec{\mathbf{r}}\right)\right]}{\gamma_g^\alpha} ,$$

$$R^S = \frac{\exp\left[i\left(\gamma_g^\beta d_g - k^\beta \hat{\mathbf{g}}\cdot\vec{\mathbf{r}}\right)\right]}{\gamma_g^\beta} . \tag{4.26}$$

The above equations are now in the form required by the quadratic programming method.

Using the dot and cross product representations in equation 4.25, we have

$$\tilde{u}_{Ij}^{PP}(k_s,k_g,\omega) = \frac{-1}{4\rho_0^2}\int_v \left\{\frac{\delta\lambda}{\alpha_0^4} + \frac{\delta\rho}{\alpha_0^2}(\hat{\mathbf{i}}\cdot\hat{\mathbf{g}}) + \frac{2\delta\mu}{\alpha_0^4}(\hat{\mathbf{i}}\cdot\hat{\mathbf{g}})^2\right\} k_I^s k_j^g S^P R^P \, dV ,$$

$$\tilde{u}_{Ij}^{PS}(k_s,k_g,\omega) = \frac{-1}{4\rho_0^2}\int_v \left\{\frac{\delta\rho}{\alpha_0\beta_0}\left|\hat{\mathbf{i}}\times\hat{\mathbf{g}}\right| + \frac{2\delta\mu}{\alpha_0^2\beta_0^2}\left|\hat{\mathbf{i}}\times\hat{\mathbf{g}}\right|(\hat{\mathbf{i}}\cdot\hat{\mathbf{g}})\right\} k_I^s k_j^g S^P R^S \, dV ,$$

$$\tilde{u}_{Ij}^{SP}(k_s,k_g,\omega) = \frac{1}{4\rho_0^2}\int_v \left\{\frac{\delta\rho}{\alpha_0\beta_0}\left|\hat{\mathbf{i}}\times\hat{\mathbf{g}}\right| + \frac{2\delta\mu}{\alpha_0^2\beta_0^2}\left|\hat{\mathbf{i}}\times\hat{\mathbf{g}}\right|(\hat{\mathbf{i}}\cdot\hat{\mathbf{g}})\right\} k_L^s k_j^g S^S R^P \, dV ,$$

$$\tilde{u}_{lj}^{SS}(k_s,k_g,\omega) = \frac{-1}{4\rho_0^2}\int_V \left\{\frac{\delta\rho}{\beta_0^2}(\hat{\mathbf{i}}\cdot\hat{\mathbf{g}}) + \frac{\delta\mu}{\beta_0^4}\left((\hat{\mathbf{i}}\cdot\hat{\mathbf{g}})^2 - |\hat{\mathbf{i}}\times\hat{\mathbf{g}}|^2\right)\right\} k_L^s k_J^g S^S R^S \, dV \,. \tag{4.27}$$

In this equation, for the P-to-S and S-to-P modes, we have $k_J = k_L = k_z$ for $j = l = x$ and $k_J = k_L = -k_x$ for $j = l = z$. Also, the convention for capital indexes given above holds for the S-to-S mode.

To obtain the backpropagation formulation we use the Fourier transform relations to get

$$\left\{\frac{\delta\lambda(\vec{\mathbf{K}}^{PP})}{\alpha_0^4} + \frac{\delta\rho(\vec{\mathbf{K}}^{PP})}{\alpha_0^2}(\hat{\mathbf{i}}\cdot\hat{\mathbf{g}}) + \frac{2\delta\mu(\vec{\mathbf{K}}^{PP})}{\alpha_0^4}(\hat{\mathbf{i}}\cdot\hat{\mathbf{g}})^2\right\} k_l^s k_j^g = -4\rho_0^2\gamma_g^\alpha\gamma_s^\alpha\tilde{u}_{lj}^{PP}\exp\left[-i\left(\gamma_s^\alpha d_s + \gamma_g^\alpha d_g\right)\right],$$

$$\left\{\frac{\delta\rho(\vec{\mathbf{K}}^{PS})}{\alpha_0\beta_0}|\hat{\mathbf{i}}\times\hat{\mathbf{g}}| + \frac{2\delta\mu(\vec{\mathbf{K}}^{PS})}{\alpha_0^2\beta_0^2}|\hat{\mathbf{i}}\times\hat{\mathbf{g}}|(\hat{\mathbf{i}}\cdot\hat{\mathbf{g}})\right\} k_l^s k_J^g = -4\rho_0^2\gamma_s^\alpha\gamma_g^\beta\tilde{u}_{lj}^{PS}\exp\left[-i\left(\gamma_s^\alpha d_s + \gamma_g^\beta d_g\right)\right],$$

$$\left\{\frac{\delta\rho(\vec{\mathbf{K}}^{SP})}{\alpha_0\beta_0}|\hat{\mathbf{i}}\times\hat{\mathbf{g}}| + \frac{2\delta\mu(\vec{\mathbf{K}}^{SP})}{\alpha_0^2\beta_0^2}|\hat{\mathbf{i}}\times\hat{\mathbf{g}}|(\hat{\mathbf{i}}\cdot\hat{\mathbf{g}})\right\} k_L^s k_j^g = 4\rho_0^2\gamma_s^\beta\gamma_g^\alpha\tilde{u}_{lj}^{SP}\exp\left[-i\left(\gamma_s^\beta d_s + \gamma_g^\alpha d_g\right)\right],$$

$$\left\{\frac{\delta\rho(\vec{\mathbf{K}}^{SS})}{\beta_0^2}(\hat{\mathbf{i}}\cdot\hat{\mathbf{g}}) + \frac{\delta\mu(\vec{\mathbf{K}}^{SS})}{\beta_0^4}\left((\hat{\mathbf{i}}\cdot\hat{\mathbf{g}})^2 - |\hat{\mathbf{i}}\times\hat{\mathbf{g}}|^2\right)\right\} k_L^s k_J^g = -4\rho_0^2\gamma_s^\beta\gamma_g^\beta\tilde{u}_{lj}^{SS}\exp\left[-i\left(\gamma_s^\beta d_s + \gamma_g^\beta d_g\right)\right], \tag{4.28}$$

with $\vec{\mathbf{K}}^{PP} = k^\alpha\hat{\mathbf{g}} - k^\alpha\hat{\mathbf{i}}$, $\vec{\mathbf{K}}^{PS} = k^\beta\hat{\mathbf{g}} - k^\alpha\hat{\mathbf{i}}$, $\vec{\mathbf{K}}^{SP} = k^\alpha\hat{\mathbf{g}} - k^\beta\hat{\mathbf{i}}$ and $\vec{\mathbf{K}}^{SS} = k^\beta\hat{\mathbf{g}} - k^\beta\hat{\mathbf{i}}$.

This equation shows the relation between the physical parameters and the observed scattered field for each of the four modes, in the transform domain. For simplicity, in the extension of the SH-wave inversion formulation to this case we will only consider the P-to-P mode and give guidelines for the remaining modes since these modes can be inverted using the same procedure as done for the P-to-P mode with minor adjustments. In addition we note that since only the P-to-P mode contains all three parameters, it is necessary and sufficient to solve the multi-parameter inverse problem.

This wavefield and can be obtained by using sources and receivers immersed in a fluid or extracted from the data by post-processing the data set (see Dankbaar, 1985; Devaney, 1986). In addition, as we concluded in section 3.4.1, inverting the data for a specific mode will implicitly reduce the contributions from the other modes since the propagation velocities are different for the different modes.

From equation 4.28 we see that the problem we are faced with is indeed quite similar to the variable density acoustic or the SH-wave case. Once again the problem can be solved for the terms in the brackets in these equations simply by following the inversion procedures for the backpropagation or the quadratic programming cases. It is clear that in this case for the measurements used in the inversion to be independent, or the determinant of the resulting matrix (used to obtain the individual parameters) to be nonzero, neither the directional dependence of the measurements nor combinations of the different modes can be used. This can be seen by noting that the terms in the brackets do not depend on these variables. In other words, the directional dependence and the different modes cannot be used to extract the individual parameters but can be used to stabilize the inversion of the resulting matrices. We see once again from the terms in the brackets that we can use either the frequency dependence of the parameters, or the directionality of the plane-waves from the source to the geophone, or both. In Beylkin and Burridge (1990) a generalized Radon transform is used to perform the multi-parameter inversion for a variable background medium whereas Beydoun and Mendes (1989) use a least-squares approach to solve the full nonlinear problem for multi-parameters both making use of the variations in the parameters with the directionality of the plane-waves. In conventional seismic methods this is referred to as Amplitude Versus Offset (AVO).

We will now investigate the diffraction tomography formulation for the P-to-P mode using three frequencies and give guidelines for the other modes which require a minimum of two frequencies.

4.3.1 P-to-P scattering inversion

To display the frequency dependence of the P-to-P scattering term in equation 4.28 and to remove the dot product the following identity

$$\hat{\mathbf{i}}\cdot\hat{\mathbf{g}} = 1 - \frac{1}{2}(\hat{\mathbf{g}} - \hat{\mathbf{i}})^2 = 1 - \frac{1}{2k^2}|\vec{\mathbf{K}}|^2 \quad ,$$

$$(\hat{\mathbf{i}}\cdot\hat{\mathbf{g}})^2 = 1 + \frac{1}{4k^4}|\vec{\mathbf{K}}|^4 - \frac{1}{k^2}|\vec{\mathbf{K}}|^2 \quad , \tag{4.29}$$

is substituted into the PP term in equation 4.28 yielding

$$\left(\frac{\delta\lambda(\vec{\mathbf{K}})}{\alpha_0^4} + \frac{\delta\rho(\vec{\mathbf{K}})}{\alpha_0^2} + \frac{2\delta\mu(\vec{\mathbf{K}})}{\alpha_0^4}\right) + \frac{1}{\omega^2}\left(-\frac{|\vec{\mathbf{K}}|^2\delta\rho(\vec{\mathbf{K}})}{2} - \frac{2|\vec{\mathbf{K}}|^2\delta\mu(\vec{\mathbf{K}})}{\alpha_0^2}\right) + \frac{1}{\omega^4}\left(\frac{|\vec{\mathbf{K}}|^4\delta\mu(\vec{\mathbf{K}})}{2}\right)$$

$$= -4\rho_0^2\gamma_g^\alpha\gamma_s^\alpha \frac{\tilde{u}_{ij}^{PP}}{k_i^s k_j^g} \exp\left[-i\left(\gamma_s^\alpha d_s + \gamma_g^\alpha d_g\right)\right] . \tag{4.30}$$

Representing the first three terms in parentheses on the left-hand side respectively by $A(\vec{\mathbf{K}})$, $B(\vec{\mathbf{K}})$, and $C(\vec{\mathbf{K}})$ and taking the inverse Fourier transform with a change of variables on the right-hand side we have

$$\left\{A(\vec{\mathbf{r}}) + \frac{B(\vec{\mathbf{r}})}{\omega^2} + \frac{C(\vec{\mathbf{r}})}{\omega^4}\right\} = \frac{1}{(2\pi)^2}\iint dk_s\, dk_g \frac{-4\rho_0^2\gamma_g^\alpha\gamma_s^\alpha\tilde{u}_{ij}^{PP}}{k_i^s k_j^g} \exp\left[-i\left(\gamma_s^\alpha d_s + \gamma_g^\alpha d_g\right)\right]$$

$$\times\ J(K_x, K_z | k_s, k_g) \exp[i(K_x x + K_z z)] . \tag{4.31}$$

From equation 4.31 we see that a backpropagation inversion at a fixed frequency will give us the raw parameters or the term on the left-hand side of this equation. To obtain the individual parameters, we can perform inversions at three distinct frequencies

and extract the individual physical parameters as follows: If we call the raw parameters $F_i(\vec{r})$, obtained from inversions at three distinct frequencies $\omega_3 > \omega_2 > \omega_1$ we will have

$$\begin{bmatrix} F_1(\vec{r}) \\ H_1(\vec{r}) * F_2(\vec{r}) \\ H_1(\vec{r}) * F_3(\vec{r}) \end{bmatrix} = \begin{bmatrix} 1 & \omega_1^{-2} & \omega_1^{-4} \\ 1 & \omega_2^{-2} & \omega_2^{-4} \\ 1 & \omega_3^{-2} & \omega_2^{-4} \end{bmatrix} \begin{bmatrix} A(\vec{r}) \\ B(\vec{r}) \\ C(\vec{r}) \end{bmatrix}, \tag{4.32}$$

where $H_1(\vec{r})$ is a filter used to bring the second and third inversions (high-frequencies) to the same frequency content as the first. As mentioned in the SH-wave case, this filter is quite complicated in seismic applications where the coverage is limited and will be discussed in section 4.4 for the crosshole case. In the above equation $A(\vec{r}) = A_1(\vec{r}) = H_1(\vec{r}) * A_2(\vec{r}) = H_1(\vec{r}) * A_3(\vec{r})$ and a similar equation holds for $B(\vec{r})$ and $C(\vec{r})$. Substituting $\sigma_i = \omega_i^{-2}$, we see that the coefficients of equation 4.32 are in the form of a Vandermode matrix (Boyse and Keller, 1986), therefore we can write the inverse as

$$\begin{bmatrix} A(\vec{r}) \\ B(\vec{r}) \\ C(\vec{r}) \end{bmatrix} = \det(W) \begin{bmatrix} \sigma_2^2\sigma_3 - \sigma_3^2\sigma_2 & \sigma_3^2\sigma_1 - \sigma_1^2\sigma_3 & \sigma_1^2\sigma_2 - \sigma_2^2\sigma_1 \\ \sigma_3^2 - \sigma_2^2 & \sigma_1^2 - \sigma_3^2 & \sigma_2^2 - \sigma_1^2 \\ \sigma_2 - \sigma_3 & \sigma_3 - \sigma_1 & \sigma_1 - \sigma_2 \end{bmatrix} \begin{bmatrix} F_1(\vec{r}) \\ H_1(\vec{r}) * F_2(\vec{r}) \\ H_1(\vec{r}) * F_3(\vec{r}) \end{bmatrix}, \tag{4.33}$$

with $\det(W) = \{(\sigma_1 - \sigma_2)(\sigma_1 - \sigma_3)(\sigma_2 - \sigma_3)\}^{-1}$. Upon obtaining $A(\vec{r})$, $B(\vec{r})$ and $C(\vec{r})$ their Fourier transforms are taken and from equation 4.30 and 4.31 the parameters can be given as

$$\delta\mu(\vec{K}) = \frac{2}{|\vec{K}|^4} C(\vec{K}),$$

$$\delta\rho(\vec{K}) = -\frac{8}{|\vec{K}|^4 \alpha_0^2} C(\vec{K}) - \frac{2}{|\vec{K}|^2} B(\vec{K}),$$

$$\delta\lambda(\vec{K}) = \frac{4}{|\vec{K}|^4} C(\vec{K}) + \frac{2\alpha_0^2}{|\vec{K}|^2} B(\vec{K}) + \alpha_0^4 A(\vec{K}). \tag{4.34}$$

Taking an inverse Fourier transform of equations 4.34 would yield the solution of the inverse problem.

As observed by various researchers (for a review, see Beylkin and Burridge, 1990) this matrix is ill-conditioned and rather than reconstructing the individual physical parameters it is more stable to reconstruct certain combinations of these parameters such as impedance. The instability results not only from the matrix being solved but also from the subtraction operations that need to be performed. If the above method is to be used for extracting the parameters of the medium a least-squares inversion with multi-frequencies must be used to stabilize the inverse problem. After considering synthetic examples we will present a method where the most difficult parameter in the SH-wave case and the P-to-P scattering case can be obtained with good accuracy. This work is an extension of the work carried out by Norton (1983) for the medical imaging problem. We also note here that by using the SH-wave case and P-to-P scattering case all the physical parameters existing in an isotropic medium can be obtained. From the more unstable P-to-P scattering we only require that $\delta\lambda(\vec{\mathbf{r}})$ be extracted accurately which can be accomplished with the method we will present later on.

To formulate the quadratic programming inversion equation 4.25 can be used. In this case, similar to the above procedure, the raw inversion can be obtained at three distinct frequencies using equation 4.25 and the resulting 3 by 3 matrix solved to obtain the individual parameters.

4.3.2 Inversion of other modes

The remaining three modes in equation 4.28 require a minimum of two frequencies to perform the inversion. As a result, the method for SH-waves can be used to invert for these modes as well with some additional identities to equation 4.29 in

order to account for the cross products. These identities can be obtained from the orthogonality of the dot and cross products and can be given as

$$|\hat{\mathbf{i}}\times\hat{\mathbf{g}}| = |\vec{\mathbf{K}}|\sqrt{1 - \frac{1}{4}|\vec{\mathbf{K}}|^2}\ ,$$

$$|\hat{\mathbf{i}}\times\hat{\mathbf{g}}|^2 = |\vec{\mathbf{K}}|^2 - \frac{1}{4}|\vec{\mathbf{K}}|^4\ . \tag{4.35}$$

These operators are quite different from the previous dot product operators and their properties will be discussed in the next section.

4.4 Parameter operators and synthetic examples

Before proceeding to the multi-parameter case we will demonstrate the SH-wave inversion without density variations (equation 4.16 with $\delta\rho = 0$) for a point diffractor example. Here we will only investigate the crosshole case, but due to the similarity in the equations between the non-variable density acoustic and the SH-wave cases, all conclusions of chapters 2 and 3 will hold for this and other geometries.

For the crosshole geometry of Figure 2.1.1a, $k_x^s = -\gamma_s$, $k_x^g = -\gamma_g$, $k_z^s = -k_s$, and $k_z^g = k_g$ (these equations are obtained directly from their counterparts in chapter 1 but now they are given for $\hat{\mathbf{i}} = -\hat{\mathbf{s}}$, therefore the signs involving the source terms are switched). With this, equation 4.16 can be given as

$$\delta\mu(\vec{\mathbf{r}}) = \frac{-\mu_0^2}{\pi^2}\iint dk_s\, dk_g\, \tilde{u}_{yy}^s \frac{|k_s\gamma_g + k_g\gamma_s|}{(\gamma_s\gamma_g - k_s k_g)} \exp[-i(\gamma_g d_g + \gamma_s d_s)]$$

$$\times \exp[i((\gamma_s - \gamma_g)x + (k_s + k_g)z)]\ . \tag{4.36}$$

To demonstrate the inversion of SH-waves, we generate Born forward data for a point diffractor using equation 4.14. The geometry considered is a 10 m horizontal by 20 m vertical area with 40 source and receiver pairs placed at 0.5 m intervals in a crosshole fashion. Equation 4.36 is used to invert the Born forward data for the SH-

wave case. In order to display the similarity we perform the same inversion for the P-wave case using equation 2.7 to generate Born forward data and equations 2.9 together with 2.10 to invert the data. The inversion results for 24 frequencies are averaged and displayed in Figure 4.4.1a and b. The expected or reference value is displayed in the upper-left corner of the plots. The similarity of the two methods is apparent although in the final result Figure 4.4.1a displays the P-wave velocity of the medium whereas Figure 4.4.1b displays the S-wave velocity.

We begin the multi-parameter case by displaying the dot and cross product operators involved in equations 4.16 and 4.28 in Figures 4.4.2 for a fixed frequency. Here, the figures are in cylindrical coordinates and are normalized by the background wavenumber. As a result, these figures can be extended to any background wavenumber by simply multiplying the axis and the scale with the appropriate $k = \omega/c_0$. Figure 4.4.2a is the unitary operator acting on $\delta\rho$ in the SH-wave case and $\delta\lambda$ in the P-to-P mode, Figure 4.4.2b is the $(\hat{\mathbf{i}}\cdot\hat{\mathbf{g}})$ operator acting on $\delta\mu$ in the SH-wave case and on $\delta\rho$ in the P-to-P and SV-to-SV modes, Figure 4.4.2c is the $(\hat{\mathbf{i}}\cdot\hat{\mathbf{g}})^2$ operator acting on $\delta\mu$ in the P-to-P mode, Figure 4.4.2d is the $|\hat{\mathbf{i}}\times\hat{\mathbf{g}}|$ operator acting on $\delta\rho$ in the P-to-SV and SV-to-P modes, Figure 4.4.2e is the $|\hat{\mathbf{i}}\times\hat{\mathbf{g}}|^2$ operator that will be used further on, Figure 4.4.2f is the $(\hat{\mathbf{i}}\cdot\hat{\mathbf{g}})|\hat{\mathbf{i}}\times\hat{\mathbf{g}}|$ operator acting on $\delta\mu$ in the P-to-SV and SV-to-P modes and Figure 4.4.2g is the $\left((\hat{\mathbf{i}}\cdot\hat{\mathbf{g}})^2 - |\hat{\mathbf{i}}\times\hat{\mathbf{g}}|^2\right)$ operator acting on $\delta\mu$ in the SV-to-SV mode.

Noting that the different properties of these operators are what we have to use to extract the individual parameters we can arrive at the following conclusions. The coverage in Figures 4.4.2a and b indicate that the separation of the parameters in the SH-wave case and the variable density acoustic case is quite feasible since the operators have different properties. In the P-to-P mode recovery of $\delta\rho$ and $\delta\mu$ will be difficult since the operators in Figures 4.4.2b and c are similar. Here, only the sign difference in the backscattering experiment can really be used. This can be seen by noting that the

radial distance in these figures represents the angle between the incident and the scattered waves. At the origin, this angle is 0° (forward scattering) and at the rim this angle is 180° (backscattering). In the P-to-P mode the recovery of $\delta\lambda$ is quite feasible due to the difference in Figures 4.4.2a, and b and c. In the P-to-SV or SV-to-P modes we have Figures 4.4.2d and f. This case presents itself as a manageable case as well but the differences in the operators are not as large as they are in SH-wave case. This difference in the operators between the two wavetypes can be expected to affect a backpropagation type inversion but not the type of inversion we will present in the next section, where the inversion is performed at the locations where one of the operators is identically zero or very small. We note that if one parameter were to have an operator with zero values at every point in the wavenumber domain, this parameter would drop out of the equations. This has been demonstrated in the inversion in Figure 4.4.1b, since in this case setting $\delta\rho$ to zero is equivalent to keeping $\delta\rho$ and setting its associated operator to zero. Finally, from Figures 4.4.2b and 4.4.2g we see that in the SV-to-SV mode the parameters will be separable since the peak amplitudes of one figure coincides with the zeros of the other.

The operators we have discussed above will not change the shape of the coverage diagrams for the different geometries, they will only change the amplitudes since they are multiplied with the parameters. In Figure 4.4.2h we show the effect of the $(\hat{\mathbf{i}}\cdot\hat{\mathbf{g}})$ operator on the normalized amplitudes of the crosshole case. In fact, this is the coverage and amplitude information we have used to accomplish the reconstruction in Figure 4.4.1b.

In Figure 4.4.3a, we display the model that will be used to demonstrate the inversion technique for the multi-parameter SH-wave case. This model consists of four diffractors and is a basic model to test such algorithms (Le Bras, 1985; Beydoun and Mendes, 1989). The first two diffractors are of type $\delta\rho$ and $\delta\mu$ and are superimposed at

8 m horizontal and 8 m vertical with amplitudes of 0.5. The third diffractor is at 12 m horizontal and 10 m vertical and is of type $\delta\mu$ with unit amplitude, and the last one is at 8 m horizontal and 12 m vertical and is of type $\delta\rho$ with unit amplitude. In this example we use 40 source and receiver pairs in a crosshole fashion with 0.5 m spacing. The data are generated at two frequencies with a background shear-wave velocity of 5500 m/s using equation 4.14 with the Born approximation. As a result, the data will not take into account the multiple scattering in the medium. The method outlined in section 4.2 is applied to the data set at 5500 Hz and at 3500 Hz. Figure 4.4.3b shows the raw inversion at 5500 Hz with the application of a low-pass filter which has a cut-off at 3500 Hz. This filter denoted by $H_1(\vec{r})$ in sections 4.2 and 4.3 is a special filter designed for the crosshole case and must be similarly designed for different geometries depending on the coverage of the considered geometry in the wavenumber domain. The aim of this filter is to reduce the frequency content of the high-frequency inversions to the frequency content of the lowest frequency inversion in order to stabilize the following operations that are performed on the inversions. The filter we use in this case can be outlined as follows: For each (K_x,K_z) pair being inverted at the high-frequency (in this case 5500 Hz) we measure the radial wavenumber of the considered pair and compare it to the boundaries formed by the coverage diagram of the lower frequency (in this case 3500 Hz). If the radial value obtained from the considered pair is larger than the boundary value we set its amplitude to zero. If it is smaller than the boundary value, the amplitudes are gradually increased to their original values depending on how far the radial distance considered is from the lower frequency boundaries. This is done to avoid Gibbs phenomena that can result from a sharp cut-off. This filter is also applied to the lowest frequency coverage. We also note that because the filter is coordinate dependent it will cause an increase in the required computation time.

Returning to Figure 4.4.3b we see that the filtered raw inversion at 5500 Hz is quite good since in this case we are performing no averaging of the resulting images as done in previous examples.

Figures 4.4.3c and d show the separate reconstructions of $\delta\mu$ and $\delta\rho$. Here we see that the reconstruction of $\delta\mu$ is quite good whereas the reconstruction of $\delta\rho$ is not so good. As discussed earlier this result can be improved by using multi-frequencies in exchange for computation time.

Examining the operator diagrams, Figures 4.2.2, or equivalently equation 4.28 we see that the recovery of the parameters in the P-to-P mode will be very difficult due to the increased ill-conditioning since in this case we are faced with three unknowns.

4.5 A stable inversion method

The method we will discuss in this section is the extension of an approach proposed by Norton (1983) for variable density acoustic imaging. The specific application considered by Norton is in medical imaging which has several advantages regarding the flexibility in the experiment setup over the seismic problem. Here we bring this idea into a form applicable to acoustic and elastic seismic imaging and demonstrate it on synthetic examples.

The idea comes from the physics of the problem by noticing that for some specific angles between the incident plane-wave and the measured plane-wave some parameters produce no scattering. The task here is to combine the frequency and angle dependence of the operators acting on the parameters in such a way as to cancel out one or more of the parameters from the equations.

Let us consider the SH-wave case where the operators are as shown in Figures 4.4.2a and b. If we consider a 90° angle between the incident and scattered wavefields we will have the operator values on a circle of radius $\sqrt{2}k = \sqrt{2}$ in these figures. It will be

on a circle because we send the incident wavefield at various angles toward the object but always receive it perpendicular to the direction it was sent. In this case we see that the operator in Figure 4.4.2a has unit amplitude whereas the operator in Figure 4.4.2b is identically zero. This means that for this specific recording angle the $\delta\mu$ term will drop out of the equations. In addition to this we can change the radius of this circle to sample the wavenumber domain completely simply by varying the frequency since the circle radius is defined by $\sqrt{2}k = \sqrt{2}\omega/c_0$. This idea forms the basis of the method and can be applied in medical imaging straightforwardly since the angle between the source and receiver can be preset arbitrarily. In practice, a minimum of two separate angles are used in order to extract two parameters. For the variable density acoustic case or the SH-wave case a straightforward choice for this second angle is 180° or the backscattering angle since at this angle we will be on the outer rim of the operator diagrams in Figures 4.4.2a and b, and at this radius the absolute value of the amplitude of the second operator is maximum. The inversion results of the first parameter obtained in the 90° case can be used to extract the second parameter using the measurements at 180°.

From equation 4.16 this method can be given mathematically as

$$\left[\widetilde{\delta\rho}(\vec{K}) + \beta_0^{-2}\widetilde{\delta\mu}(\vec{K})\cos(\theta)\right] = \widetilde{F}_\theta \,, \tag{4.37}$$

with θ being the angle between the incident and the scattered plane-wave and

$$\widetilde{F}_\theta = -\,4\mu_0^2 \frac{\gamma_s\gamma_g}{\omega^2}\,\widetilde{u}^s_{yy}(k_s,k_g,\omega)\exp[-\,i\,(\gamma_g d_g + \gamma_s d_s)] \,. \tag{4.38}$$

For a pair of fixed angles, θ_1 and θ_2 we can write

$$\begin{bmatrix} F^1_\theta(\vec{K}) \\ F^2_\theta(\vec{K}) \end{bmatrix} = \begin{bmatrix} \beta_0^{-2}\cos(\theta_1) & 1 \\ \beta_0^{-2}\cos(\theta_2) & 1 \end{bmatrix} \begin{bmatrix} \widetilde{\delta\mu}(\vec{K}) \\ \widetilde{\delta\rho}(\vec{K}) \end{bmatrix} , \tag{4.39}$$

and inverting we have

$$\begin{bmatrix} \widetilde{\delta\mu}(\vec{\mathbf{K}}) \\ \widetilde{\delta\rho}(\vec{\mathbf{K}}) \end{bmatrix} = \frac{1}{\left(\cos(\theta_2) - \cos(\theta_1)\right)} \begin{bmatrix} -\beta_0^2 & \beta_0^2 \\ \cos(\theta_2) & -\cos(\theta_1) \end{bmatrix} \begin{bmatrix} F_\theta^1(\vec{\mathbf{K}}) \\ F_\theta^2(\vec{\mathbf{K}}) \end{bmatrix} . \quad (4.40)$$

Although any angle can be used in these equations we use the angles $\theta_1 = 90^o$ and $\theta_2 = 180^o$ which will yield the most stable results as

$$\widetilde{\delta\rho}(\vec{\mathbf{K}}) = F_\theta^1(\vec{\mathbf{K}}) ,$$

$$\widetilde{\delta\mu}(\vec{\mathbf{K}}) = \beta_0^2\left(F_\theta^1(\vec{\mathbf{K}}) - F_\theta^2(\vec{\mathbf{K}})\right) . \quad (4.41)$$

This inversion process can also be performed for multi-angles to stabilize the inversion if necessary.

Considering Figures 4.4.2, in the P-to-P mode $\delta\lambda$ can be obtained similarly by choosing the angle θ to be 90°. As discussed previously the recovery of the other parameters in this case can be quite difficult. In the P-to-SV or SV-to-P modes again the 90° angle can be used to recover $\delta\rho$ but the recovery of $\delta\mu$ will be difficult. As for the SV-to-SV mode the 90° and the 180° angles can be used to reconstruct $\delta\rho$ and $\delta\mu$. In the cases where the parameters are difficult to reconstruct and do not decouple easily it is suggested that multi-angles be used to reduce the ill-conditioning of the resulting matrices.

In the seismic cases, the problem is not as straightforward since the angles that the plane-waves are generated and recorded is determined by the discrete values of the Fourier transform taken over the source and receiver lines. We must look at where the samples will lie in the wavenumber domain if we are to apply a constraint on the acceptable range of angles. The coverage in the wavenumber domain for 100 frequency samples and 40 source and receiver pairs is displayed in Figure 4.4.4a when a bound is enforced on the chosen angles to be in the neighborhood of 90°. In Figures 4.4.4 the amplitudes displayed are the values of the cos (θ) function and reflect the leakage of the

unwanted parameter into the inversion, therefore our aim is to minimize the values in these plots. When the bound is tightened, Figure 4.4.4b, we see that the amplitudes decrease which is advantageous but the number of nodes satisfying the bounds decrease as well. For 200 frequency samples and 40 source and receiver pairs the resulting coverage, Figure 4.4.4c, is quite good and the amplitudes obtained are quite low, as required. We note here that the maximum amplitudes displayed in Figures 4.4.4 is 5% of 1.0 or the maximum amplitude obtainable (see the scales in Figures 4.4.4). This means that if all the samples in these figures had the maximum value of their associated scales, only 5% of the unwanted parameters amplitude would leak into the inversion, which is quite low. Therefore, in practice, a fewer amount of frequencies can be used and the constraint on the acceptable range of angles can be loosened.

In these figures we see that the discrete values obtained lie on lines at 45° angles from the horizontal and at nodes with steps of $\sqrt{2}\Delta k$. This is a consequence of the discrete Fourier transform taken over the source and receiver lines and forms the basis of the method we develop here.

Since the parameters we are considering are real (no attenuation), the positive wavenumbers in the vertical direction can be reconstructed by taking the complex conjugates of their associated negative ones. Therefore, we will only consider the top two quadrants in Figures 4.4.4 for the following developments. Since we now know that the obtained discrete values can be minimized on lines at 45° angles from the horizontal and at nodes with steps of $\sqrt{2}\Delta k$, we initially chose these specific locations and try to find the wavenumber values that minimize the cos (θ) operator. This is done in order to obtain a regular grid. The result of this search is displayed in Figure 4.4.4d for a quick search with large margins on the variation from 90° and for a more comprehensive search, Figure 4.4.4e, where the margins are reduced. It can be seen that the comprehensive search produces lower amplitudes which is advantageous.

The next step is to obtain the values on a rectangular grid, so that the inversion results can be obtained by a 2-D inverse Fourier transform. For this we zero pad the regions outside the sampled area and choose the appropriate values inside the sampled area. In Figure 4.4.4f we show the zero padded sections by small dots and the sections where we actually have coverage by large dots. In this case we have increased the sampling steps to $2\Delta k$ by discarding the values that do not lie on the rectangular mesh. We note that an interpolation procedure could have been employed as well where in this case the sampling would have been chosen to be in steps of Δk. Once the samples on this mesh are obtained the inversion process involves a simple 2-D inverse Fourier transform of the obtained mesh.

We demonstrate this method on the model given in Figure 4.4.3a. The inversion result of this model for the reconstruction of $\delta\rho$ is shown in Figure 4.4.5a. This result is better than the one obtained in Figure 4.4.3d which shows the effectiveness of this technique.

For the P-to-P mode inversion we consider a model with six diffractors, Figure 4.4.5b. The first three are of type $\delta\lambda$, $\delta\rho$ and $\delta\mu$ at 8 m horizontal and 8 m vertical and with amplitudes of 0.33. At 12 m horizontal and 8 m vertical we have a diffractor of type $\delta\mu$ of unit amplitude, at 8 m horizontal and 12 m vertical we have a diffractor of type $\delta\rho$ of unit amplitude and at 12 m horizontal and 12 m vertical we have a diffractor of type $\delta\lambda$ of unit amplitude. Here we use the above outlined multi-frequency method to recover the parameter $\delta\lambda$ using a 90° angle for θ.

The result of the application of the method is shown in Figure 4.4.5c and the reconstruction is quite good. In this figure, the diffractor at 8 m horizontal and 8 m vertical is reconstructed well also but cannot be seen very clearly in this figure due to its low-amplitude value of 0.33.

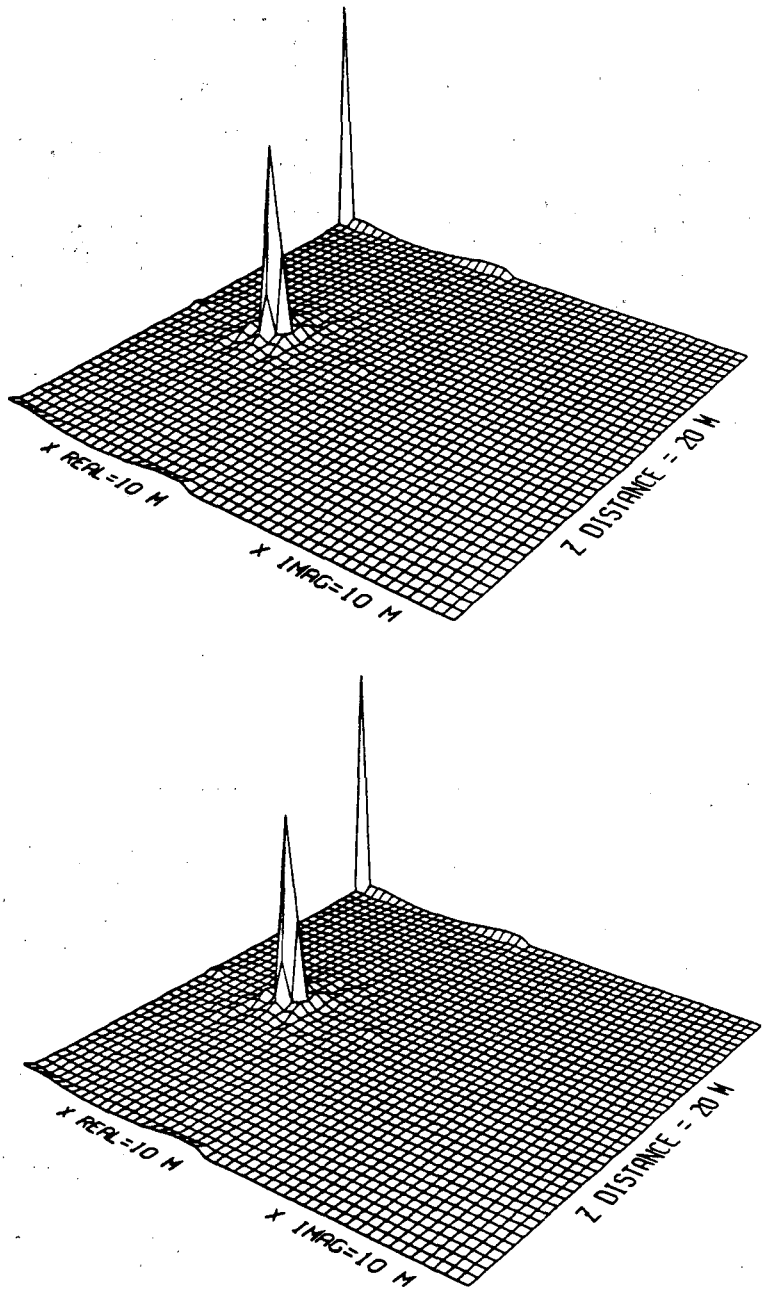

Figure 4.4.1a,b Average of crosshole backpropagation inversions of a) P-waves (top) and b) SH-waves (bottom) from 2440 to 5500 Hz with 122 Hz intervals.

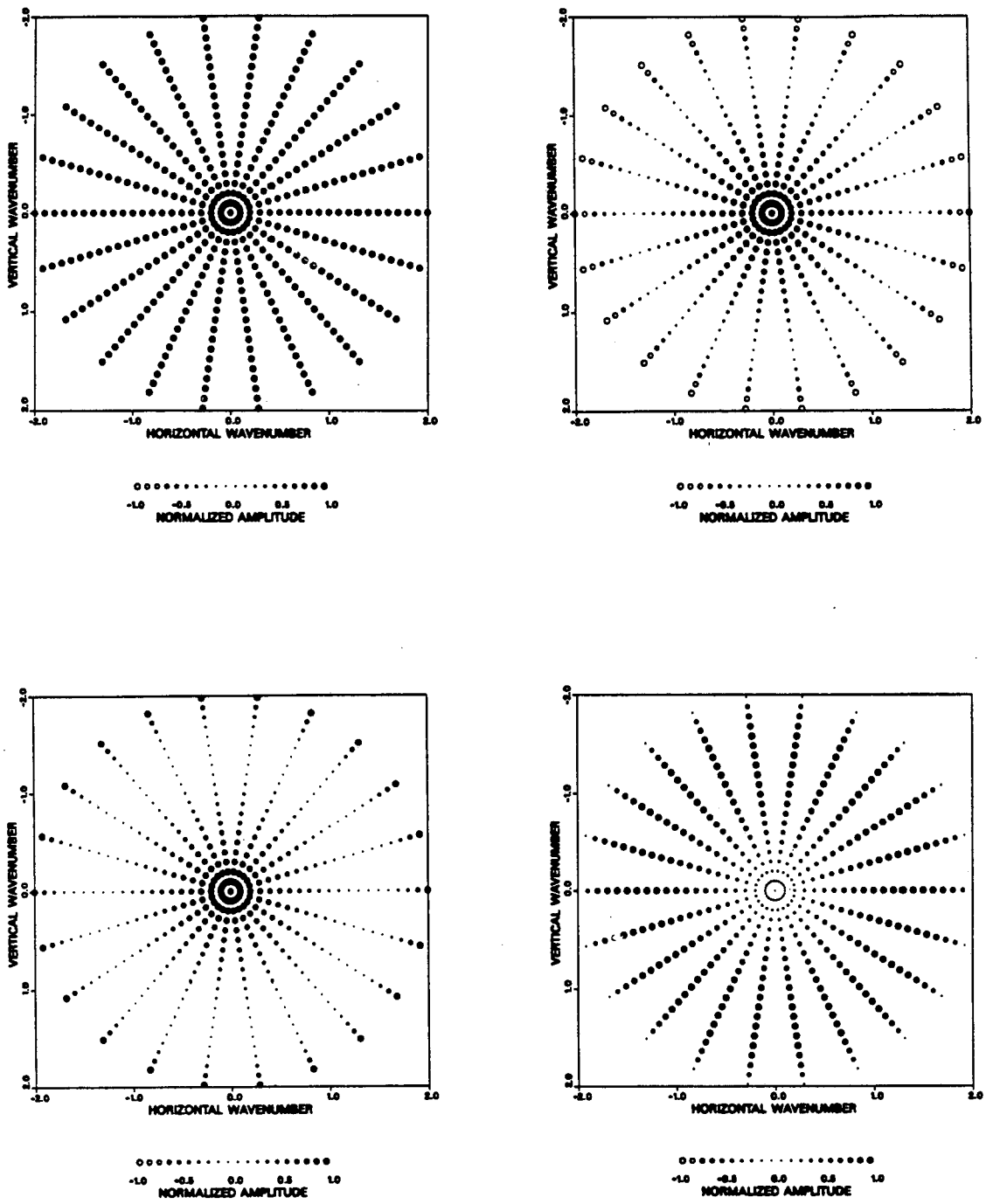

Figure 4.4.2a,b,c,d Normalized plots of the operators a) Unitary (top-left), b) $\hat{\mathbf{i}} \cdot \hat{\mathbf{g}}$ (top-right), c) $(\hat{\mathbf{i}} \cdot \hat{\mathbf{g}})^2$ (bottom-left) and d) $|\hat{\mathbf{i}} \times \hat{\mathbf{g}}|$ (bottom-right) in the wavenumber domain.

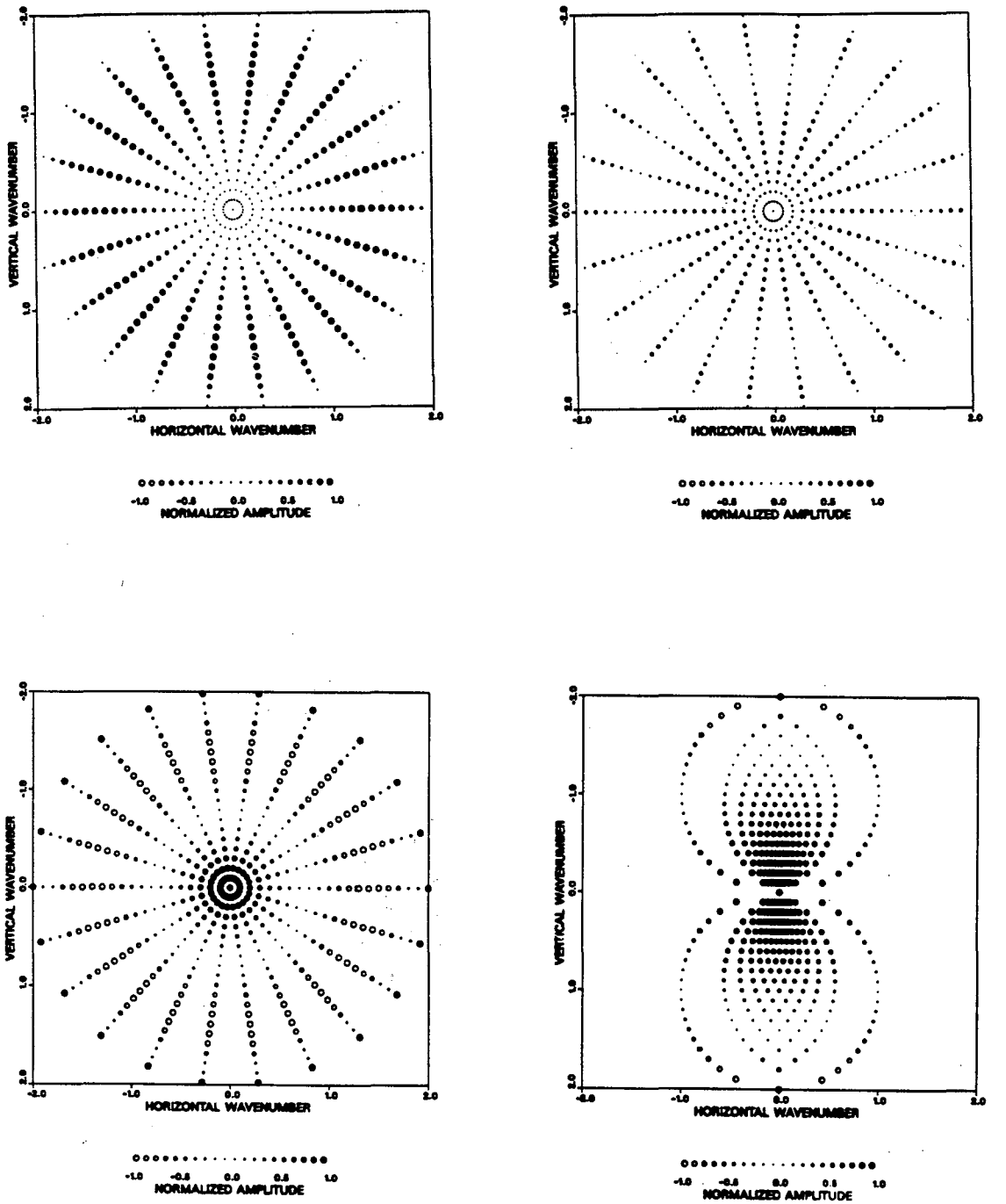

Figure 4.4.2e,f,g,h Normalized plots of the operators e) $|\hat{\mathbf{i}}\times\hat{\mathbf{g}}|^2$ (top-left), f) $(\hat{\mathbf{i}}\cdot\hat{\mathbf{g}})|\hat{\mathbf{i}}\times\hat{\mathbf{g}}|$ (top-right) and g) $\left\{(\hat{\mathbf{i}}\cdot\hat{\mathbf{g}})^2 - |\hat{\mathbf{i}}\times\hat{\mathbf{g}}|^2\right\}$ (bottom-left) in the wavenumber domain. h) Operator $\hat{\mathbf{i}}\cdot\hat{\mathbf{g}}$ superimposed on the crosshole coverage diagram (bottom-right).

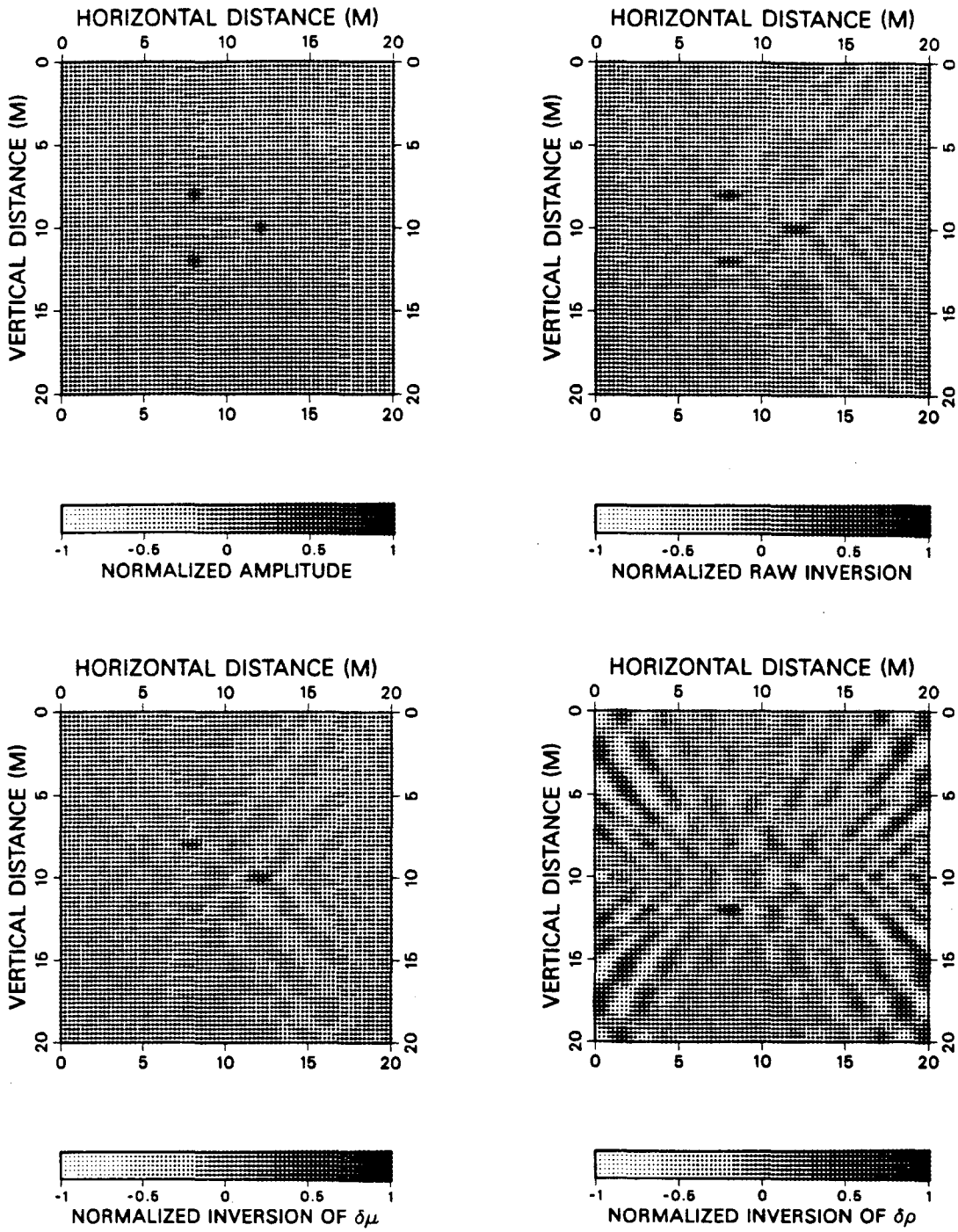

Figure 4.4.3a,b,c,d a) Model (top-left), b) Raw inversion (top-right), c) Inversion for $\delta\mu$ (bottom-left) and d) Inversion for $\delta\rho$ (bottom-right) using two frequencies and the backpropagation algorithm.

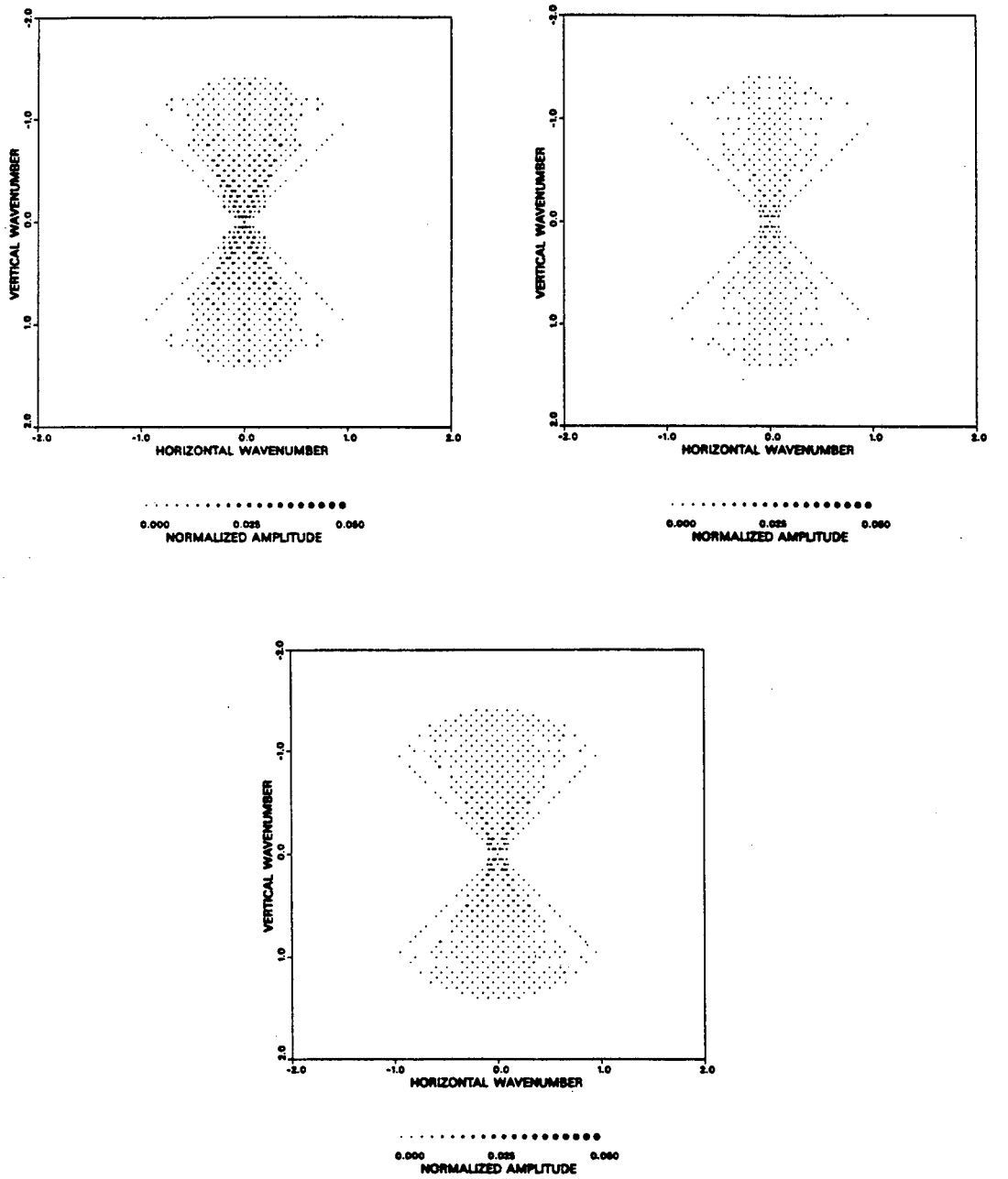

Figure 4.4.4a,b,c Coverage in the wavenumber domain for constrained angles, a) 100 frequency samples and large bounds (top-left), b) 100 frequency samples and small bounds (top-right) and c) 200 frequency samples and small bounds (bottom).

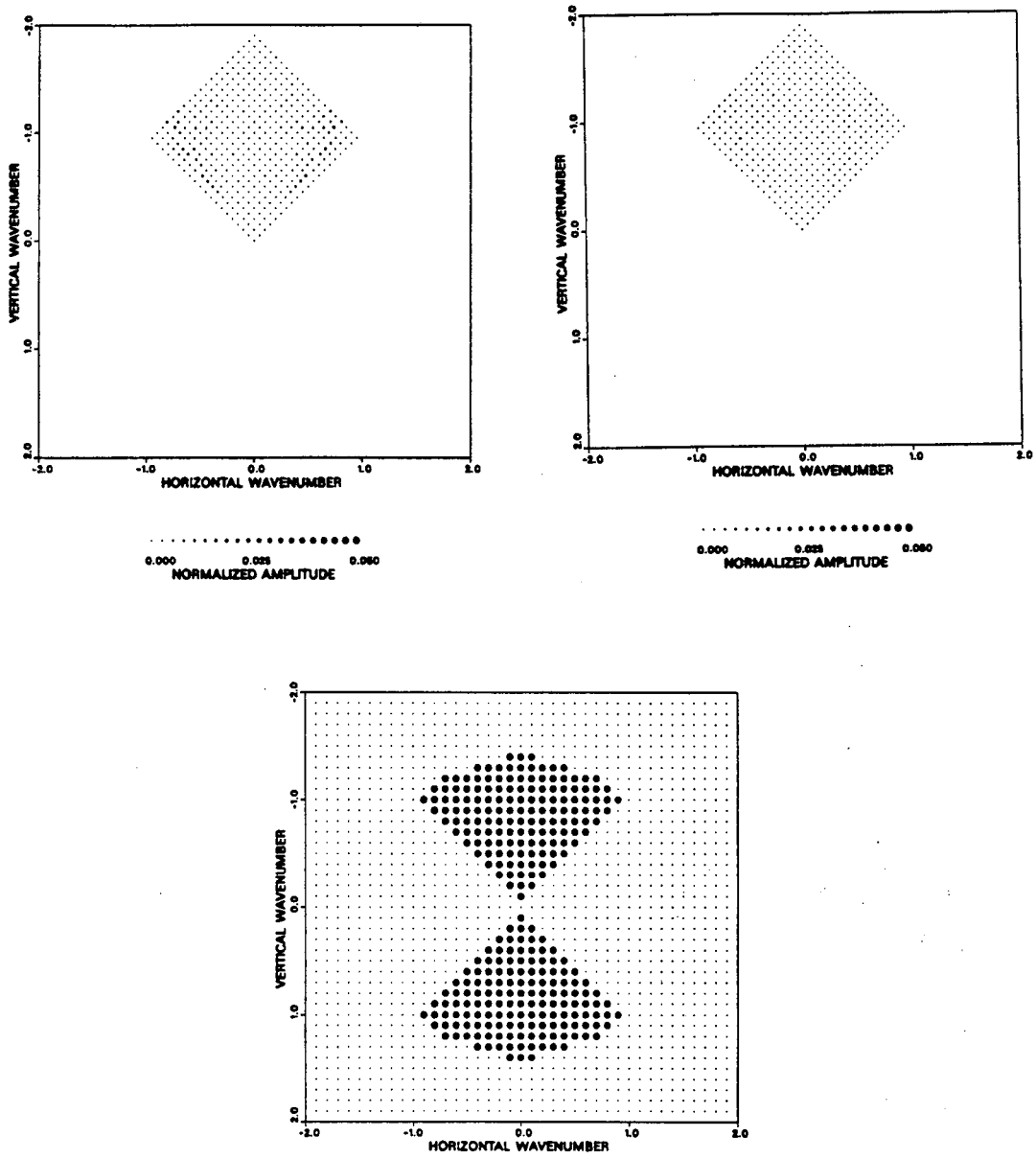

Figure 4.4.4d,e,f Reconstruction of the upper quadrants d) 200 frequencies and large bounds (top-left), e) 200 frequencies and small bounds (top-right).

f) extrapolation of e) to from a rectangular grid (bottom).

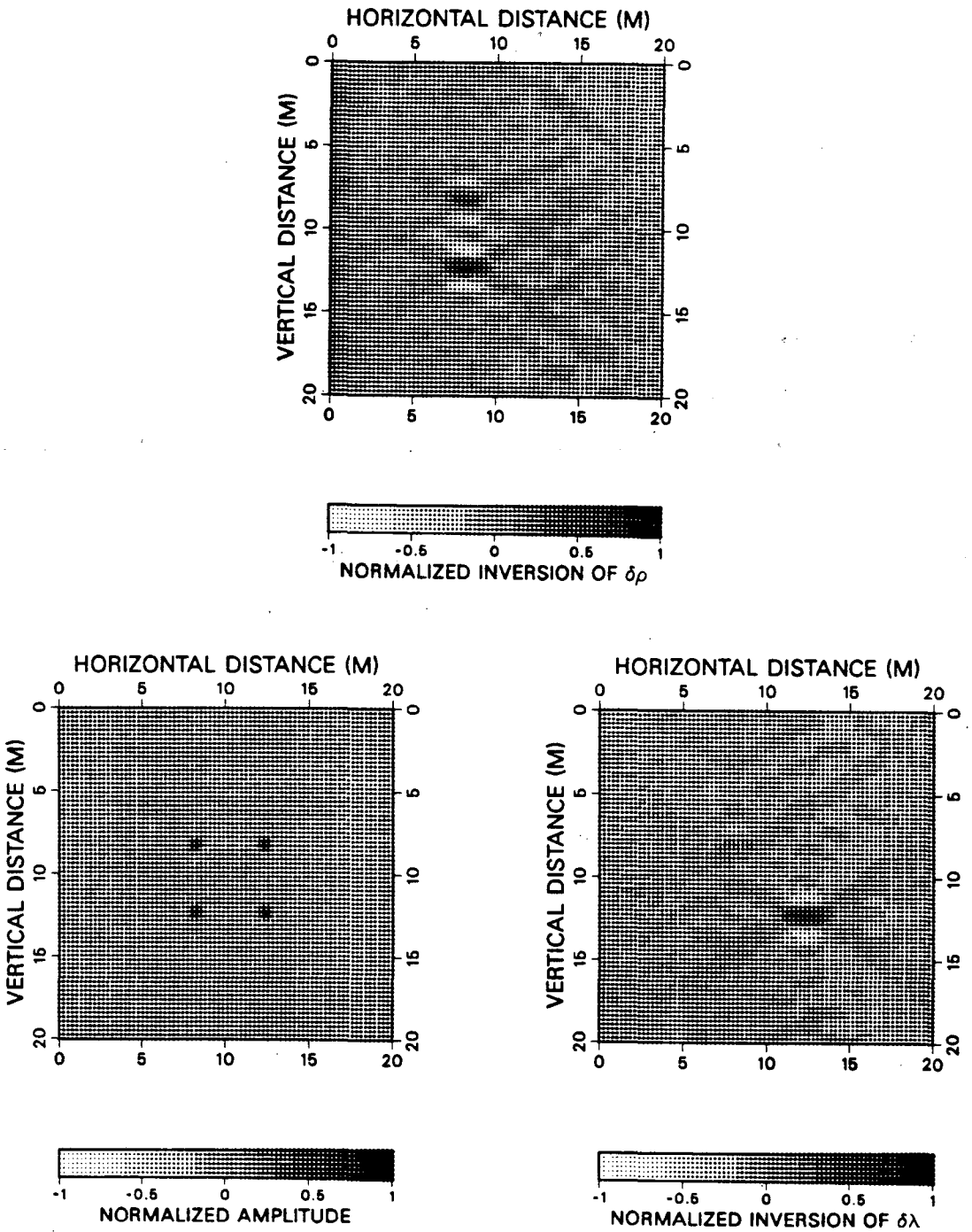

Figure 4.4.5a,b,c Constrained angle inversions, a) SH-wave case for $\delta\rho$ (top), b) Model for the P-to-P case (bottom-left) and c) P-to-P inversion for $\delta\lambda$ (bottom-right).

Chapter 5

Inversion in a Transversely Isotropic Medium

In this chapter we investigate the extension of the inversion methods to a transversely isotropic (TI) medium. Transverse isotropy is seen to be the most common form of anisotropy encountered in geophysical applications occurring due to thin sedimentary layers and alignment of pores and fractures due to the stress conditions affecting the medium.

In the Grimsel test site case investigated in chapter 3, there is reason to believe that the medium is transversely isotropic. This is seen from plotting all the observed first arrival times of P-waves as a function of ray-angle. From this arrival time information there is seen to be a 7-8% P-wave velocity variation in two perpendicular directions. Although this does suggest the presence of anisotropy and improves the ray tomography inversion results, the ray-angle results are not on a microscopic scale and may also be interpreted as being due to inhomogeneities introduced by the alignment of fractures.

In this section we develop the diffraction tomography formulation for the wave equation in elliptical form, discuss the wavenumber domain coverage and present the application of the formulation to the field data from the Grimsel test site.

5.1 SH-wave forward problem

The SH-wave equation in the source-free region of a transversely isotropic medium (see Appendix E) can be given as

$$(Au_{y,x} + Bu_{y,z})_{,x} + (Cu_{y,z} + Bu_{y,x})_{,z} - \rho\ddot{u}_y = 0 , \tag{5.1}$$

with

$$A = C_{66} \cos^2\theta + C_{55} \sin^2\theta ,$$

$$B = \sin\theta \cos\theta \, (C_{55} - C_{66}) ,$$

$$C = C_{55} \cos^2\theta + C_{66} \sin^2\theta . \tag{5.2}$$

Defining

$$C_{66}(\vec{r}) = C_{66}^0 + \delta C_{66}(\vec{r}) ,$$

$$C_{55}(\vec{r}) = C_{55}^0 + \delta C_{55}(\vec{r}) ,$$

$$\rho(\vec{r}) = \rho_0 + \delta\rho(\vec{r}) , \tag{5.3}$$

where δ represents the perturbation to a homogeneous background we have

$$A = A^0 + \delta A(\vec{r}) ,$$

$$B = B^0 + \delta B(\vec{r}) ,$$

$$C = C^0 + \delta C(\vec{r}) . \tag{5.4}$$

Substituting in equation 5.1 we get

$$\rho_0 \ddot{u}_y - (A^0 u_{y,xx} + 2B^0 u_{y,xz} + C^0 u_{y,zz}) = Q_y , \tag{5.5}$$

where

$$Q_y = - \delta\rho \ddot{u}_y + (\delta A u_{y,x} + \delta B u_{y,z})_{,x} + (\delta C u_{y,z} + \delta B u_{y,x})_{,z} . \tag{5.6}$$

The displacement in equation 5.5 can be represented as a superposition of the incident and scattered displacements or $u_y = u_y^0 + u_y^s$ yielding

$$\rho_0 \ddot{u}_y^s - (A^0 u_{y,xx}^s + 2B^0 u_{y,xz}^s + C^0 u_{y,zz}^s) = Q_y . \tag{5.7}$$

To obtain this equation, $\rho_0 \ddot{u}_y^0 - (A^0 u_{y,xx}^0 + 2B^0 u_{y,xz}^0 + C^0 u_{y,zz}^0) = 0$, was used. In equation 5.7, Q_y is an equivalent source. Using Green's theorem and the free-space Green's function we have (see Aki and Richards, 1980),

$$u_y^s = \int_v Q_y(\xi) *_t G_y(\xi)\, dV(\xi) \ . \tag{5.8}$$

Using the Born approximation, $u \rightarrow u^0$ equation 5.6 becomes

$$Q_y = - \delta\rho \ddot{u}_y^0 + (\delta A u_{y,x}^0 + \delta B u_{y,z}^0)_{,x} + (\delta C u_{y,z}^0 + \delta B u_{y,x}^0)_{,z} \ . \tag{5.9}$$

Substituting into equation 5.8

$$u_y^s = \int_v \left(- \delta\rho \ddot{u}_y^0 *_t G_y + (\delta A u_{y,x}^0 + \delta B u_{y,z}^0)_{,x} *_t G_y + (\delta C u_{y,z}^0 + \delta B u_{y,x}^0)_{,z} *_t G_y\right) dV. \tag{5.10}$$

Integrating out terms involving the derivatives of the elastic parameters using integration by parts we have

$$u_y^s = \int_v \left(- \delta\rho \ddot{u}_y^0 *_t G_y - (\delta A u_{y,x}^0 + \delta B u_{y,z}^0) *_t G_{y,x} - (\delta C u_{y,z}^0 + \delta B u_{y,x}^0) *_t G_{y,z}\right) dV. \tag{5.11}$$

In the frequency domain and for a line source in the y-direction and measurements in the y-direction equation 5.11 becomes

$$u_{yy}^s = \int_v \left(\omega^2 \delta\rho G_y^s G_y^g - \delta A G_{y,x}^s G_{y,x}^g - \delta B G_{y,z}^s G_{y,x}^g - \delta B G_{y,x}^s G_{y,z}^g - \delta C G_{y,z}^s G_{y,z}^g\right) dV \ . \tag{5.12}$$

This equation is the fundamental equation for the SH-waves in a transversely isotropic medium, obtained by using the Born approximation. In this equation $G_y^s = G_y(\vec{r},\vec{r}^s)$ for the source and $G_y^g = G_y(\vec{r},\vec{r}^g)$ for the receiver.

In Appendix F we derive the 2-D Green's function for SH-waves in a homogeneous background transversely isotropic medium. The result in the Fourier transform domain for the source line can be given as

$$G_y(\vec{r},k_s) = \frac{i}{2C^0\gamma_s^{II}} \exp\left[- i\left|\gamma_s^{I}\right|d_s + i\,\gamma_s^{II}d_s\right] \exp\left[- ik\hat{s}\cdot\vec{r}\right], \tag{5.13}$$

with

$$\gamma_s^{I} = -\frac{B^0k_s}{C^0} \text{ and } \gamma_s^{II} = \frac{\sqrt{(B^0k_s)^2 + C^0\rho\omega^2 - C^0A^0k_s^2}}{C^0}. \tag{5.14}$$

The result for the receiver line can be obtained (in the Born approximation framework) by replacing the s's with g's.

We see that the main difference between the isotropic (equation 4.11) and the transversely isotropic Green's function for SH-waves is that the perpendicular wavenumber to the source and receiver line is modified in order to account for an elliptical wavefront.

5.2 SH-wave inverse problem

We follow the same procedure as in the previous sections to invert the equations. We take the Fourier transform of equation 5.12 over the source and receiver lines to form the plane-wave decomposition. The application of this process to the Green's function of the acoustic case is given in Appendix B and can be similarly applied to the Green's function given in equation 5.13. With this, equation 5.12 becomes

$$\tilde{u}_{yy}^{s} = \frac{-\exp[i(\gamma_g d_g + \gamma_s d_s)]}{4C_s^0C_g^0\gamma_s^{II}\gamma_g^{II}} \int_V \left(\omega^2\delta\rho + \delta Ak_x^sk_x^g + \delta Bk_z^sk_x^g + \delta Bk_x^sk_z^g + \delta Ck_z^sk_z^g\right)$$

$$\times \exp\left[- i\,(k_\phi^s\hat{g} - k_\phi^g\hat{i})\cdot\vec{r}\right] dV, \tag{5.15}$$

with

$$\gamma_s = \gamma_s^I + \gamma_s^{II} = \frac{-B_s^0 k_s}{C_s^0} + \frac{\sqrt{(B_s^0 k_s)^2 + C_s^0 \rho\omega^2 - C_s^0 A_s^0 k_s^2}}{C_s^0},$$

$$\gamma_g = \gamma_g^I + \gamma_g^{II} = \frac{-B_g^0 k_g}{C_g^0} + \frac{\sqrt{(B_g^0 k_g)^2 + C_g^0 \rho\omega^2 - C_g^0 A_g^0 k_g^2}}{C_g^0}, \tag{5.16}$$

where $A_{s,g}^0$, $B_{s,g}^0$, $C_{s,g}^0$ are determined via equation 5.2 using θ_s and θ_g which are respectively the angles between the source and receiver lines and the symmetry axis, $k_\phi^{s,g} = \omega/c_\phi^{s,g}$ with $c_\phi^{s,g}$ being the velocity in the direction of propagation of plane-waves $\hat{\mathbf{i}}$ and $\hat{\mathbf{g}}$ and ω is the angular frequency. In this equation the sign of $\gamma_{s,g}^{II}$ will be determined by the geometry as in the previous sections whereas the sign of $\gamma_{s,g}^{I}$ is always positive.

5.2.1 Single parameter inversion

For the application to field data we will simplify the problem by setting $\delta\rho = 0$ and also $\delta C_{55} = \delta C_{66}$ or $\delta B = 0$ and $\delta C = \delta B$. This second condition implies that the perturbation is isotropic whereas the background is transversely isotropic. With these assumptions equation 5.15 becomes

$$\tilde{u}_{yy}^s = \frac{-\exp[i(\gamma_g d_g + \gamma_s d_s)]}{4C_s^0 C_g^0 \gamma_s^{II} \gamma_g^{II}} (k_x^s k_x^g + k_z^s k_z^g) \int_V \delta A(\vec{r}) \exp\left[-i(k_\phi^s \hat{\mathbf{g}} - k_\phi^g \hat{\mathbf{i}}) \cdot \vec{\mathbf{r}}\right] dV. \tag{5.17}$$

The right side of this equation is in the form of a Fourier transform, therefore we can write this equation as

$$\delta A(k_\phi^s \hat{\mathbf{g}} - k_\phi^g \hat{\mathbf{i}}) = -\tilde{u}_{yy}^s \frac{4C_s^0 C_g^0 \gamma_s^{II} \gamma_g^{II}}{(k_x^s k_x^g + k_z^s k_z^g)} \exp[-i(\gamma_g d_g + \gamma_s d_s)]. \tag{5.18}$$

This equation forms the linear relationship between the perturbation and the observed scattered field. Taking the inverse Fourier transform and changing the integration variables from K_x, K_z to k_s, k_g we have

$$\delta A(\vec{r}) = \frac{-1}{\pi^2}\iint dk_s\, dk_g\, J(K_x,K_z|k_s,k_g)\tilde{u}^s_{yy}\frac{C^0_s C^0_g \gamma^{II}_s \gamma^{II}_g}{(k^s_x k^g_x + k^s_z k^g_z)}\exp[-i(\gamma_g d_g + \gamma_s d_s)]$$

$$\times \exp[i(K_x x + K_z z)]\,. \quad (5.19)$$

This equation is the solution of the inverse problem for SH-waves in a 2-D transversely isotropic medium which will yield the parameter $\delta A(\vec{r}) = \delta C_{55}(\vec{r}) = \delta\mu(\vec{r})$. The mapping from K_x, K_z to k_s, k_g is the same as in chapter 2 but now the sign of $\gamma^I_{s,g}$ must remain positive as discussed.

5.2.2 Multi-parameter inversion

Substituting the transverse isotropy parameters from equation 5.2 into equation 5.15 we have

$$\tilde{u}^s_{yy} = \frac{-\exp[i(\gamma_g d_g + \gamma_s d_s)]}{4C^0_s C^0_g \gamma^{II}_s \gamma^{II}_g}\int_V \left(\omega^2\delta\rho + \delta C_{66}O_{66}(\theta,k^s,k^g) + \delta C_{55}O_{55}(\theta,k^s,k^g)\right)$$

$$\times \exp\left[-i\,(k^s_\phi \hat{\mathbf{g}} - k^g_\phi \hat{\mathbf{i}})\cdot\vec{\mathbf{r}}\right] dV, \quad (5.20)$$

where

$$O_{66}(\theta,k^s,k^g) = k^s_x k^g_x \cos^2(\theta) + k^s_z k^g_z \sin^2(\theta) - (k^s_z k^g_x + k^s_x k^g_z)\cos(\theta)\sin(\theta)\,,$$

$$O_{55}(\theta,k^s,k^g) = k^s_x k^g_x \sin^2(\theta) + k^s_z k^g_z \cos^2(\theta) + (k^s_z k^g_x + k^s_x k^g_z)\cos(\theta)\sin(\theta)\,. \quad (5.21)$$

In equation 5.20 there are three unknowns. In order to reconstruct these individual parameters we again have to use the properties of the operators acting on these parameters. The operator acting on $\delta\rho$ is unitary (see Figure 4.4.2a). The operators O_{66} and O_{55} acting on δC_{66} and δC_{55} are dependent on the angle that the axis of symmetry makes with the vertical, or θ, and on the direction of the plane-waves considered. For an isotropic background and for an axis of symmetry in the vertical direction ($\theta = 0^o$), the operators acting on the parameters δC_{66} and δC_{55} are plotted in

Figures 5.2.1a and b, for the crosshole geometry. In this case the operators are not radially symmetric (compare with Figures 4.4.2) and have their own distinctive characteristics. It can be seen by tracing the outer boundary of Figure 5.2.1a or from Figure 5.2.1c that for an axis of symmetry in the vertical direction or for $\theta = 0^o$, the operator acting on δC_{66} has zero values, or δC_{66} produces no scattering, when the direction of propagation of incoming or outgoing plane-waves make an angle of 0° or 180° with the vertical (see Figure 2.2.1). As can be seen from Figure 5.2.1b or from Figure 5.2.1d, for the same axis of symmetry, the operator acting on δC_{55} has zero values when the direction of propagation of incoming or outgoing plane-waves make an angle of 90° or 270° with the vertical. Figures 5.2.1c and d are geometry independent and are shown to better illustrate the above points.

The method discussed in section 4.5, which uses only the part of the observed wavefield where all parameters other than the one being inverted for produce no scattering, can be applied to this case as well. The multi-frequency extension of Figures 5.2.1c and d will give the zero values of the operators as concentric circles in the dark areas of Figures 5.2.2a and b. As a result, by choosing only the incident or scattered plane-waves whose direction of propagation makes a 0° or 180° angle with the vertical over a range of frequencies, δC_{66} can be dropped out of equation 5.20 in the limited region indicated by the dark areas in Figure 5.2.2a. Similarly, δC_{55} can be dropped out of equation 5.20, in the limited region indicated by the dark areas in Figure 5.2.2b, by choosing the previous angles to be 90° or 270°. We see from Figures 5.2.2a and b that the region which the operators can be minimized is less than a circle of radius 2k which was the coverage in the elastic case where radial symmetry existed. An important result of this is that outside the dark areas of Figures 5.2.2a and b the operators cannot be decoupled or resolved well. For the crosshole geometry and with $\theta = 0^o$, the sections where δC_{66} and δC_{55} can be minimized is shown in Figures 5.2.2c and d. It can be

seen from this figure that δC_{66} can be canceled out of equation 5.20 quite well but this does not hold for δC_{55}. If the boreholes were to be placed horizontally rather than vertically, the opposite would happen and δC_{55} could be canceled out from equation 5.20 quite well. These two data gathering geometries would suggest themselves as ideal data gathering geometries for this angle of the symmetry axis, since the zeros of the operators have the same coverage as the two crosshole coverages.

The extension of the above multi-parameter inversion method to cases where the symmetry axis makes an arbitrary angle with the vertical is straightforward. The plane-wave angles that zero an operator and therefore the axis of the mappings given above vary together with the axis of symmetry angle. For example, for an axis of symmetry at 45° clockwise from the vertical, Figures 5.2.1c and d and Figures 5.2.2a and b would be rotated clockwise by 45° as shown in Figures 5.2.3a-d. Therefore, the operator δC_{66} would have zero values when the direction of propagation of incident or scattered plane-waves make a clockwise angle of 45° or 225° from the vertical and δC_{55} would have zero values for a clockwise angle of 135° or 315°. As a result, depending on the axis of symmetry, an optimal data gathering geometry can be chosen (in this case, two crosshole geometries where the boreholes make a clockwise angle of 45° and 135° from the vertical would be preferable).

5.3 Quasi-P wave inverse problem

The differential equations that govern the propagation of P and SV-waves in a transversely isotropic medium can be obtained in the same way as done for the SH-waves in Appendix E. In this case, the separation of P and SV-waves is not a trivial matter. The approaches used up to now involve substitution of plane-waves into the coupled differential equations and retrieval of quasi-P and quasi-S waves (see Auld, 1973; White, 1982; Meadows, 1985). In general, the SV-wave group velocities can

form cusps and a numerical migrator's equation cannot be derived for such waves (Meadows, 1985). A paper by Dellinger and Etgen (1990) deals with the separation of quasi-P and quasi-S waves in a general anisotropic medium with the use of a plane-wave decomposition method.

Although the problem is quite complicated, it has been shown by Levin (1979) that as long as the anisotropy is less than about 15% the propagation of quasi-P waves can be approximated by an elliptical form. This property was used by Verwest (1989) to derive a migration operator in an elliptically anisotropic (EA) medium with a symmetry axis in the vertical or z-axis direction.

As mentioned in the introduction of this chapter, in the field case we are considering the anisotropy is estimated to be near 7-8% from the travel time data, therefore, the elliptical form approximation to the quasi-P wave propagation is used in our applications and is expected to be a reasonable approximation.

In the previous section we derived the inversion algorithm for SH-waves in the elliptical form. Comparing equation 4.36 and 5.19 we see that the main difference from the isotropic case is that in the phase the vertical wavenumber is modified to account for the ellipticity of the wavefield and $\gamma_s \rightarrow \gamma_s^{II}$ and $\gamma_g \rightarrow \gamma_g^{II}$ in the amplitudes. Using the similarity between the acoustic (equation 2.9 and 2.10) and the SH-wave (equation 4.36) cases, the backpropagation algorithm for the acoustic case in the elliptical form can be given with the above modifications to equation 2.9 and 2.10.

5.3.1 Wavenumber domain coverage

Before proceeding to field data applications we look at how TI or EA effects the wavenumber domain coverage.

To demonstrate this we initially consider a constrained measurement of plane-waves which are observed only in the directions they are generated at a fixed frequency.

In Figures 5.3 the line with empty dots represents the isotropic case with a normalized background velocity if 1 m/s whereas the line with filled dots represents the elliptically anisotropic case with a velocity of 1.1 m/s along the axis of symmetry and 0.9 m/s in the perpendicular direction. These figures are for 40 source and receiver pairs and are normalized as was done in Chapter 1. Figure 5.3.1a is the coverage of the SRP geometry with a θ (the clockwise angle of the axis of symmetry from the vertical) of 90°. We see the elliptical form and the dense coverage for the large vertical wavenumbers. Figure 5.3.1b shows the same case when $\theta = 0^o$. Here the ellipse is cut in the vertical direction at the tips due to the requirement that the wavenumbers be real.

The crosshole case with $\theta = 0^o$ is shown in Figure 5.3.1c. In this case the coverage is dense for the large horizontal wavenumbers and is not cut at the top and bottom since now we do not exceed the maximum value at the top and bottom. Changing the symmetry axis to $\theta = 90^o$ in the crosshole case, Figure 5.3.1.d, we see that the ellipse is now cut at the top and bottom again to keep the wavenumber values real. The last example, Figure 5.3.1e, is the case when $\theta = 150^o$ which represents the transverse isotropy axis observed from the travel time plots of the field data.

We now extend the previous coverage diagrams to the multi-frequency case again when the plane-wave is observed only in the direction it is generated. Figure 5.3.2a is the multi-frequency SRP coverage with $\theta = 90^o$ for 40 source and receiver pairs. To observe their differences we can compare these figures to the isotropic case Figures of 2.2.4. We see that the area covered is quite similar in both cases but in the elliptical anisotropy case samples are obtained on ellipses rather than circles as can be expected. Figure 5.3.2b is the same example for $\theta = 0^o$ and Figure 5.3.2c is for $\theta = 150^o$ which represents the observed transverse isotropy direction from the travel times of the field data.

We now look at the unconstrained single frequency coverage diagrams. For the following examples 32 source and receiver pairs were used in order to better resolve the interior of the coverage diagrams. Figure 5.3.3a shows the crosshole coverage when $\theta = 90^o$. We see that in this case the coverage is further reduced in the horizontal wavenumber direction (see Figure 2.2.2a). When $\theta = 0^o$, Figure 5.3.3b, the contrary happens and for this case the coverage is quite good. Figure 5.3.3a and b suggest that better results from crosshole inversions can be expected from a medium with an axis of symmetry in the vertical direction rather than a medium with an axis of symmetry in the horizontal direction. For $\theta = 150^o$, Figure 5.3.3c, the coverage is again quite good but it can be seen that some sections are now multiply covered or over sampled.

The unconstrained single frequency coverage diagram for the SRP case is given in Figure 5.3.4a for $\theta = 90^o$, Figure 5.3.4b for $\theta = 0^o$ and Figure 5.3.4c for $\theta = 150^o$. We see that in the single frequency cases the coverage diagrams are affected more severely by the elliptical anisotropy than they are in the multi-frequency cases (Figures 5.3.2). This is due to the well distributed coverage in the multi-frequency case. In the single frequency SRP case, contrary to the crosshole case, the coverage is better when $\theta = 90^o$ rather than when $\theta = 0^o$.

The single frequency coverage diagrams for the VSPL geometry is given in Figure 5.3.5a is for $\theta = 90^o$ and Figure 5.3.5b is for $\theta = 0^o$. In this case the isotropic figure is stretched straightforwardly in the appropriate directions (see Figure 2.2.2c). The VSPR case is not demonstrated here due to its resemblance to the VSPL case (see Figures 2.2.2b and c).

5.4 Application to field data

As discussed earlier, the first arrival times of the P-waves suggest the presence of transverse isotropy with an angle of symmetry of 150° clockwise from the vertical.

Although this angle is expected to be robust, the velocities obtained from the arrival time observations as a function of angle may not be. Therefore, we will perform the inversions at a fixed angle and for a range of velocity values in the neighborhood of 5270 m/s, the background velocity used in the isotropic inversions, and compare the resulting images.

The following backpropagation velocities were used in the elliptical inversions in Figures 5.4.1a, b, c, d, e, f, g and h: 5570 m/s, 5420 m/s, 5370 m/s, 5320 m/s, 5220 m/s, 5170 m/s, 5120 m/s, and 4970 m/s in the direction making a clockwise angle of 150° from the vertical and 4970 m/s, 5120 m/s, 5170 m/s, 5220 m/s, 5320 m/s, 5370 m/s, 5420 m/s and 5570 m/s in the direction making a clockwise angle of 60° from the vertical. In simpler terms, we start form a 300 m/s velocity variation from the isotropic background value in the 150° direction and reduce it to 150 m/s, 100 m/s, 50 m/s, - 50 m/s, - 100 m/s, - 150 m/s and - 300 m/s while the opposite is done in the vertical direction or in the 60° direction. At the end of this process, the fast velocity axis (150°) has the slowest velocity whereas the slow velocity axis (60°) has the fastest velocity.

From these figures it can be seen by comparison that the $\pm$ 300 m/s case, Figures 5.4.1a and h, displays an overly corrected image. This can be observed from noticing the abnormal stretch of the inhomogeneities caused by defocusing. Even the $\pm$ 150 m/s case, Figures 5.4.1b and g, suggest themselves as being over corrected which represents a nearly 6% variation. From these initial results several conclusions can be drawn. It is possible that the large anisotropy values observed in the travel time plots are not microscopic and are due to the inhomogeneities caused by the presence of fractures. It is also possible that the diffraction tomography method or a full-waveform inversion method is not as sensitive to anisotropy as is a ray theory based method. It is virtually impossible to separate anisotropic effects and effects caused by fracture induced inhomogeneities in the inversion results when a smaller velocity range is used for the

anisotropy corrections. The only way to make a distinction is to rely on the robust estimate of the transverse isotropy angle observed from the P-wave arrival time plots, which is near 150°, and therefore to considered the results in Figures 5.4.1c and d to be more representative of the medium.

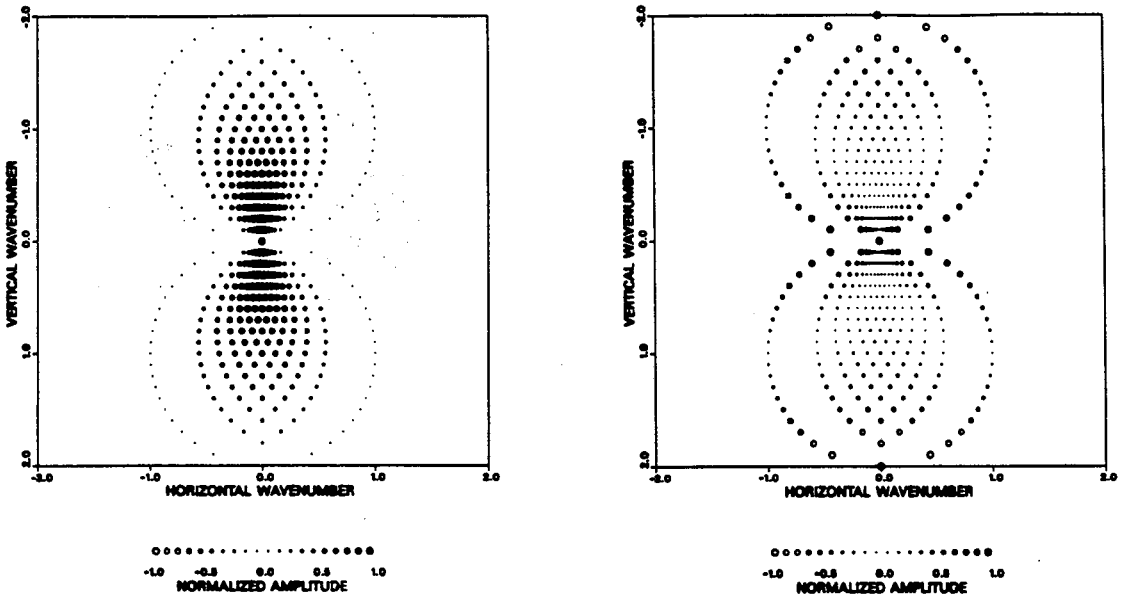

Figure 5.2.1a,b Normalized plots of the operators acting on a) δC_{66} (left) and b) δC_{55} (right) for $\theta = 0^o$ superimposed on the crosshole geometry.

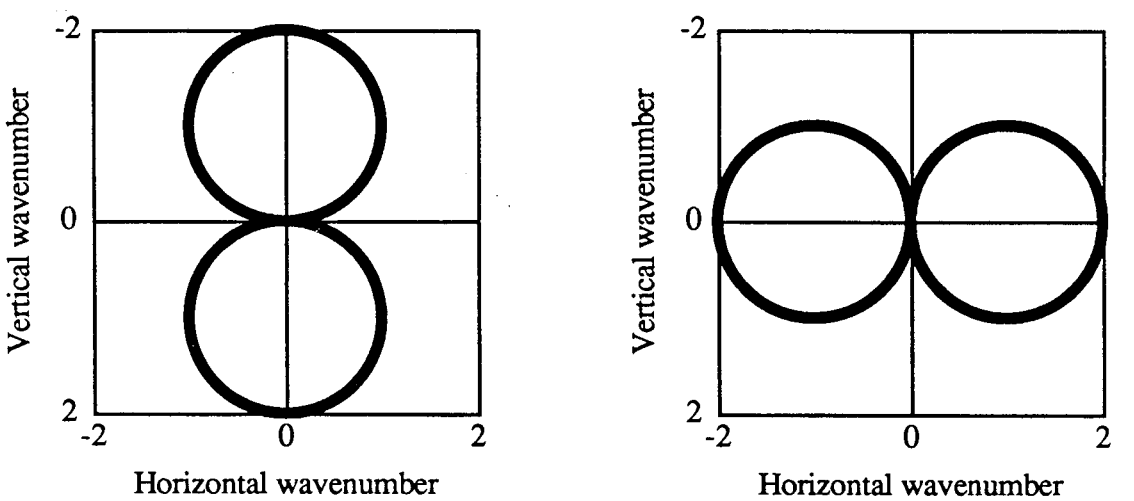

Figure 5.2.1c,d Zeros of the operators acting on c) δC_{66} (left) and d) δC_{55} (right) for $\theta = 0^o$.

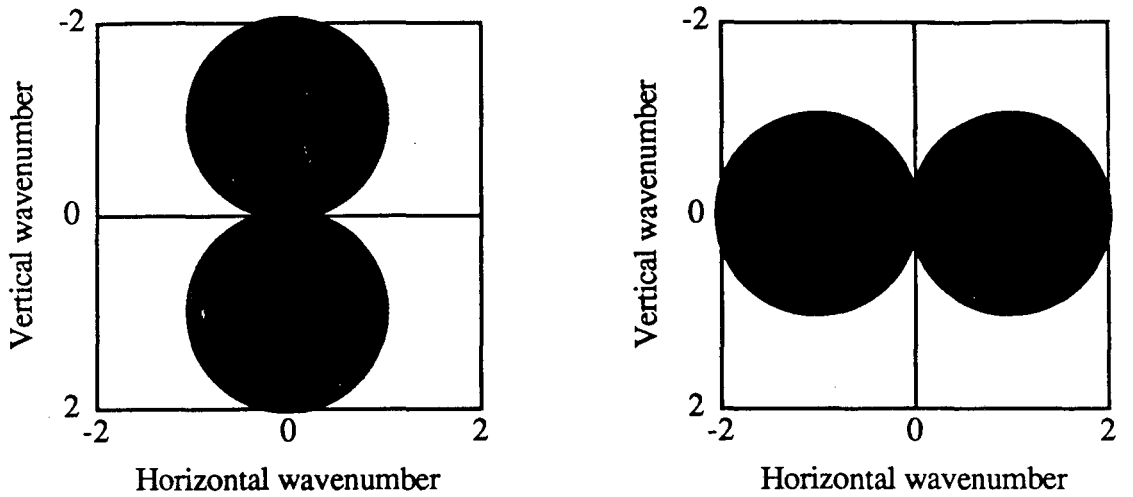

Figure 5.2.2a,b Multi-frequency coverage of the zeros of the operators acting on a) δC_{66} (left) and b) δC_{55} (right) for $\theta = 0^{o}$.

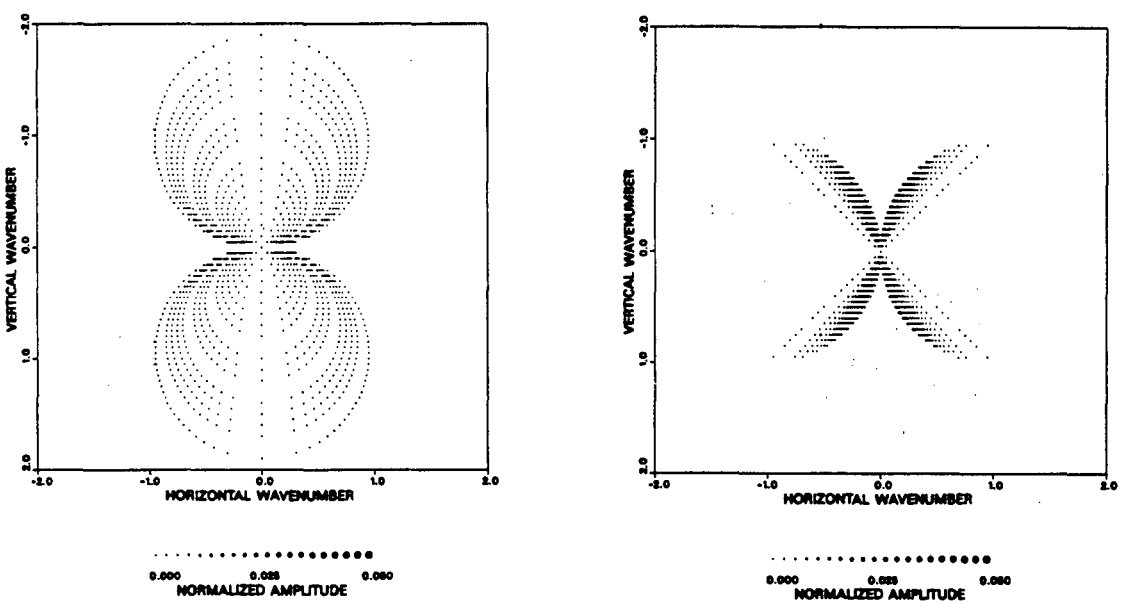

Figure 5.2.2c,d Multi-frequency coverage of the zeros of the operators acting on c) δC_{66} (left) and d) δC_{55} (right) in the crosshole geometry and for $\theta = 0^{o}$.

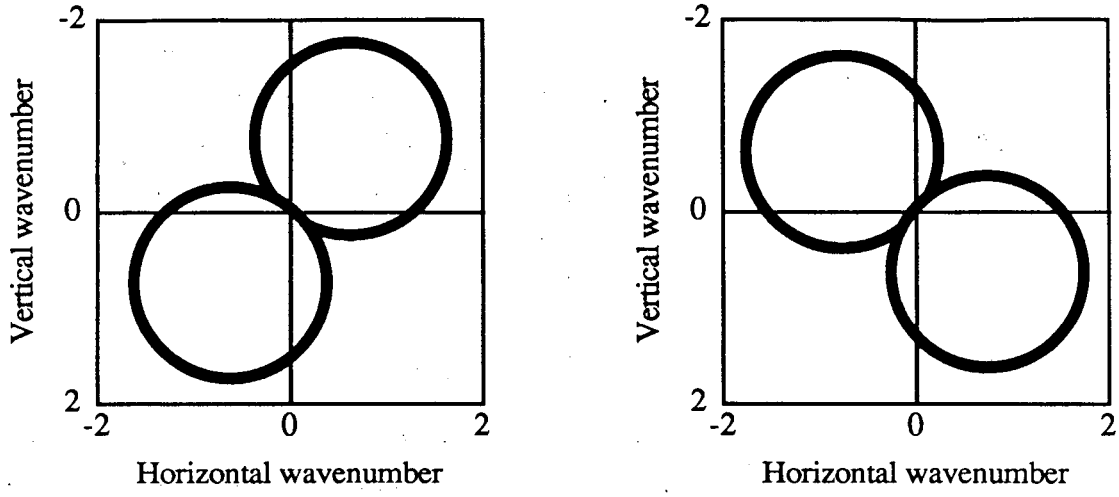

Figure 5.2.3a,b Zeros of the operators acting on a) δC_{66} (left) and b) δC_{55} (right) for $\theta = 45^{o}$.

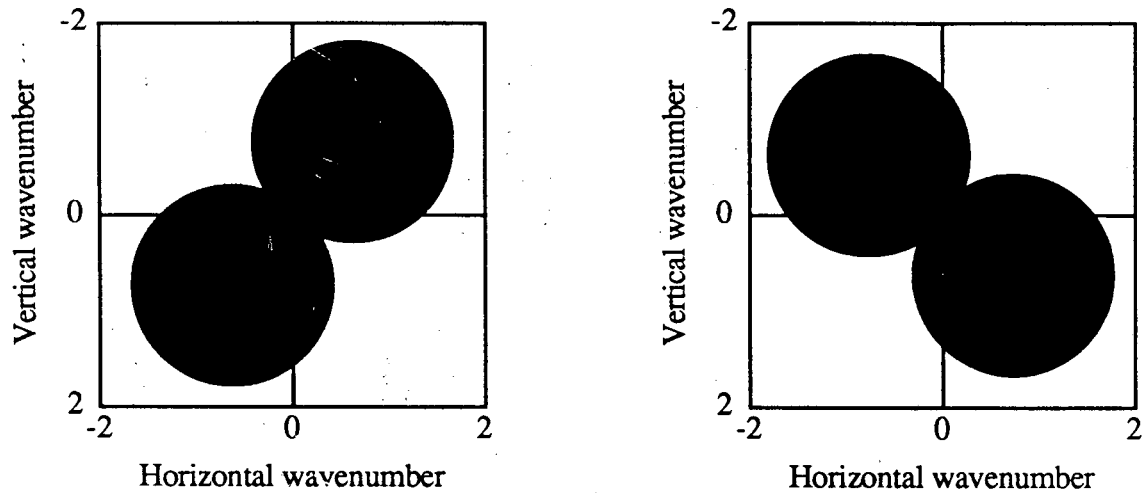

Figure 5.2.3c,d Multi-frequency coverage of the zeros of the operators acting on c) δC_{66} (left) and d) δC_{55} (right) for $\theta = 45^{o}$.

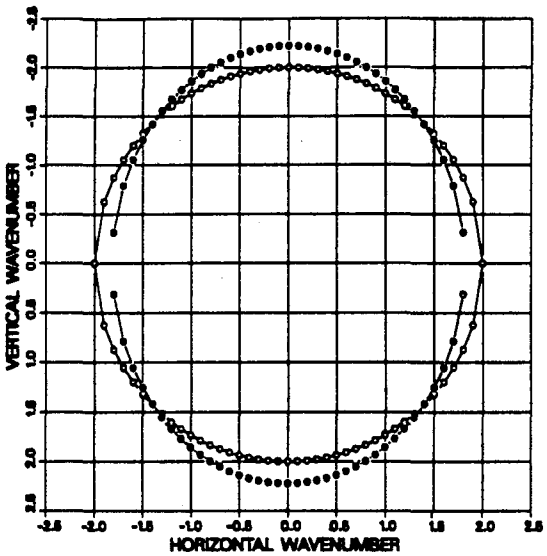

Figure 5.3.1a Constrained single frequency SRP coverage in TI or EA medium with $\theta = 90^{o}$.

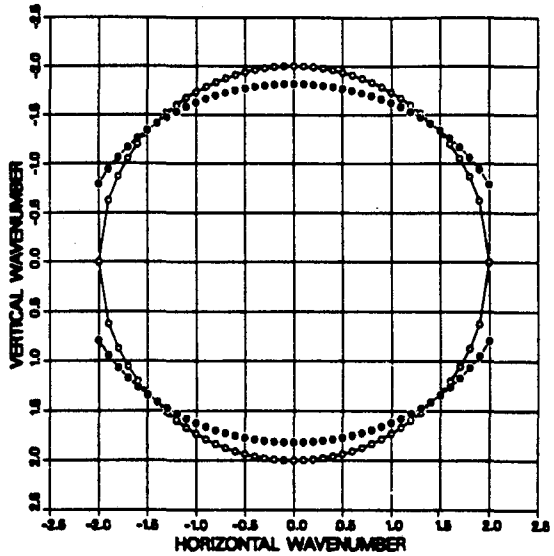

Figure 5.3.1b Constrained single frequency SRP coverage in TI or EA medium with $\theta = 0^{o}$.

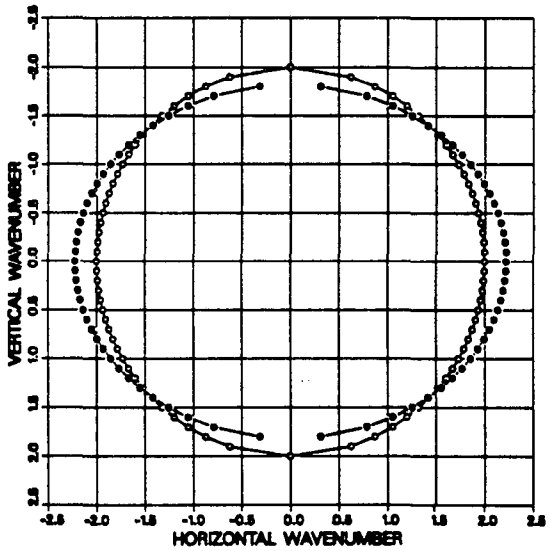

Figure 5.3.1c Constrained single frequency crosshole coverage in TI or EA medium with $\theta = 0^{o}$.

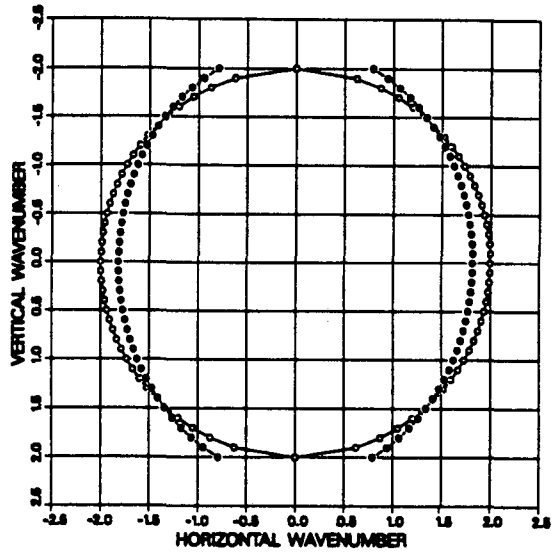

Figure 5.3.1d Constrained single frequency crosshole coverage in TI or EA medium with $\theta = 90^{o}$.

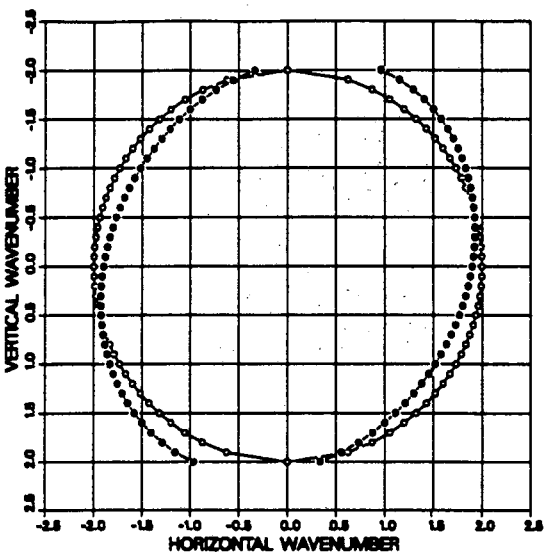

Figure 5.3.1e Constrained single frequency crosshole coverage in TI or EA medium with $\theta = 150^{o}$.

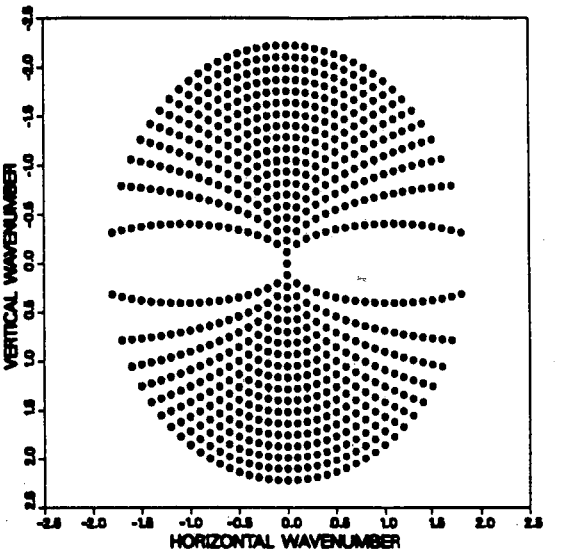

Figure 5.3.2a Constrained multi-frequency SRP coverage in TI or EA medium with $\theta = 90^{o}$.

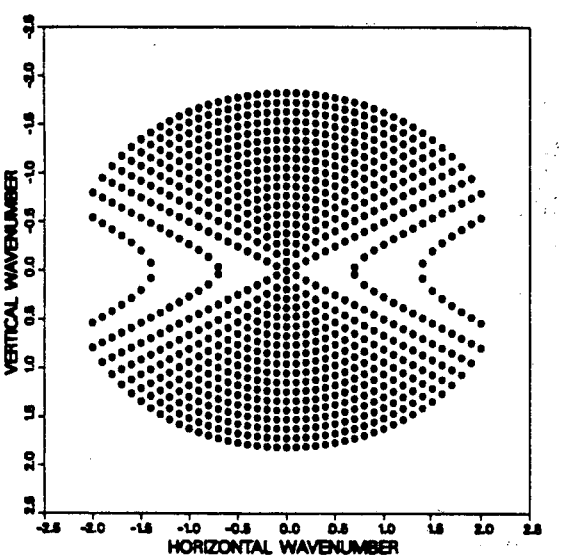

Figure 5.3.2b Constrained multi-frequency SRP coverage in TI or EA medium with $\theta = 0^{o}$.

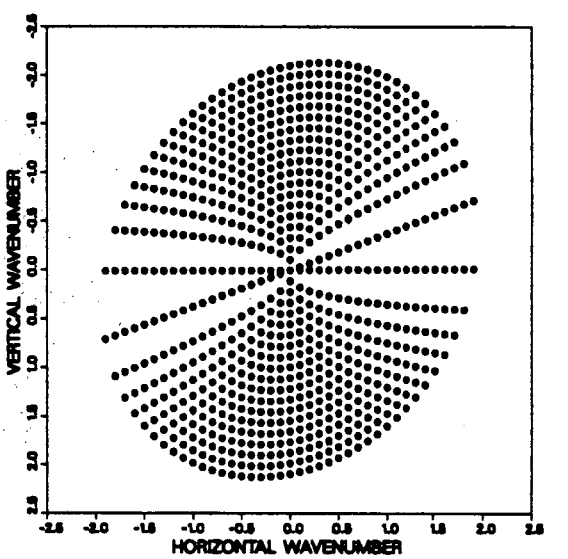

Figure 5.3.2c Constrained multi-frequency SRP coverage in TI or EA medium with $\theta = 150^{o}$.

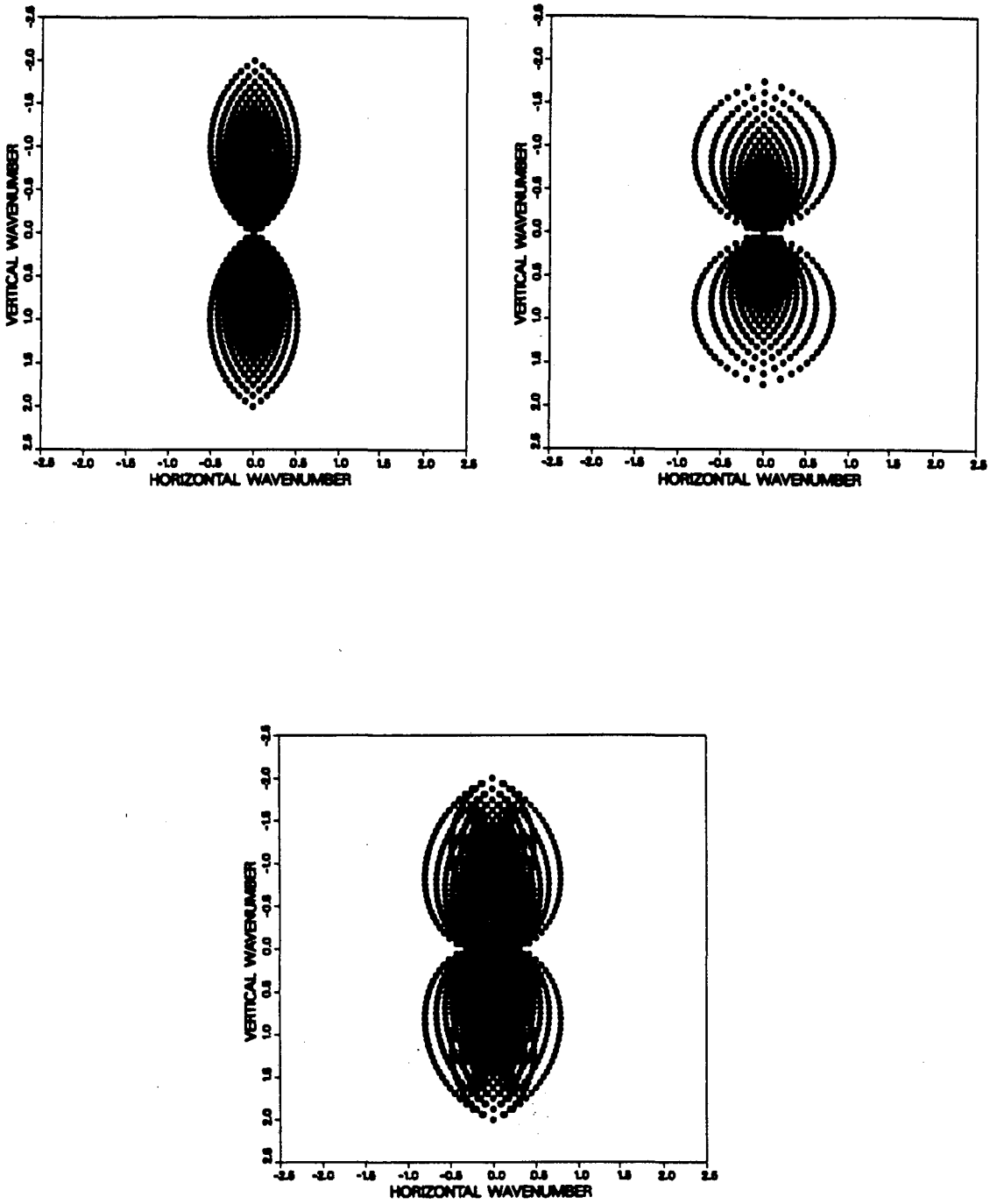

Figure 5.3.3a,b,c Single frequency crosshole coverage in TI or EA medium with a) $\theta = 90^{o}$ (top-left), b) $\theta = 0^{o}$ (top-right) and c) $\theta = 150^{o}$ (bottom).

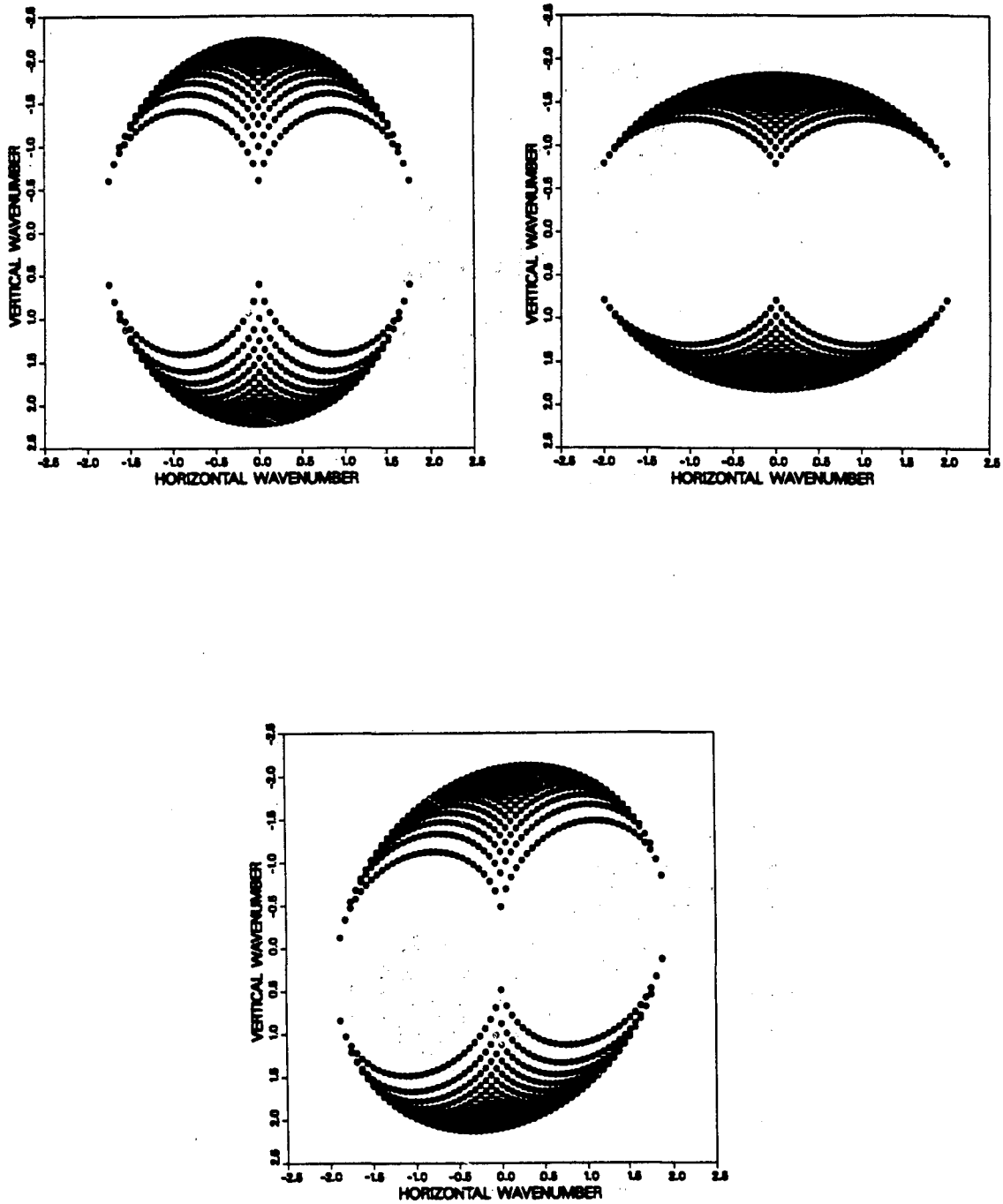

Figure 5.3.4a,b,c Single frequency SRP coverage in TI or EA medium with a) $\theta = 90^{o}$ (top-left), b) $\theta = 0^{o}$ (top-right) and c) $\theta = 150^{o}$ (bottom).

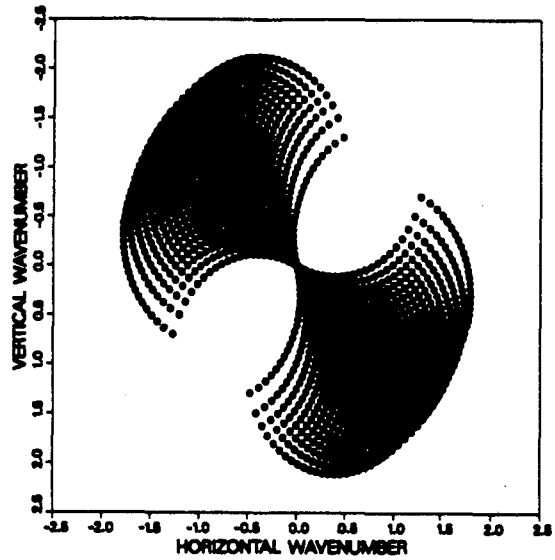

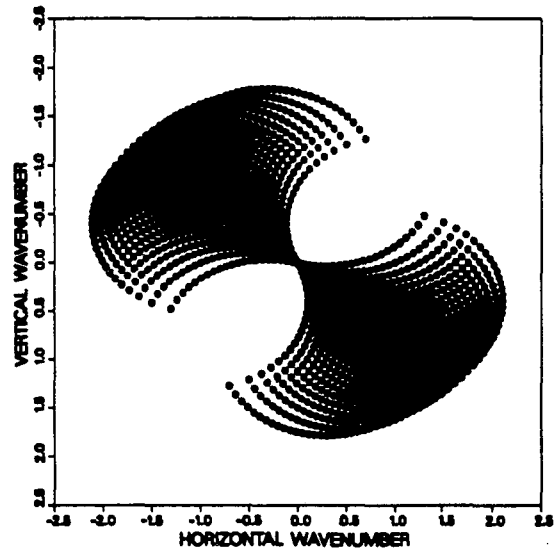

Figure 5.3.5a,b Single frequency VSPL coverage in TI or EA medium with a) $\theta = 90^{o}$ (top) and b) $\theta = 0^{o}$ (bottom).

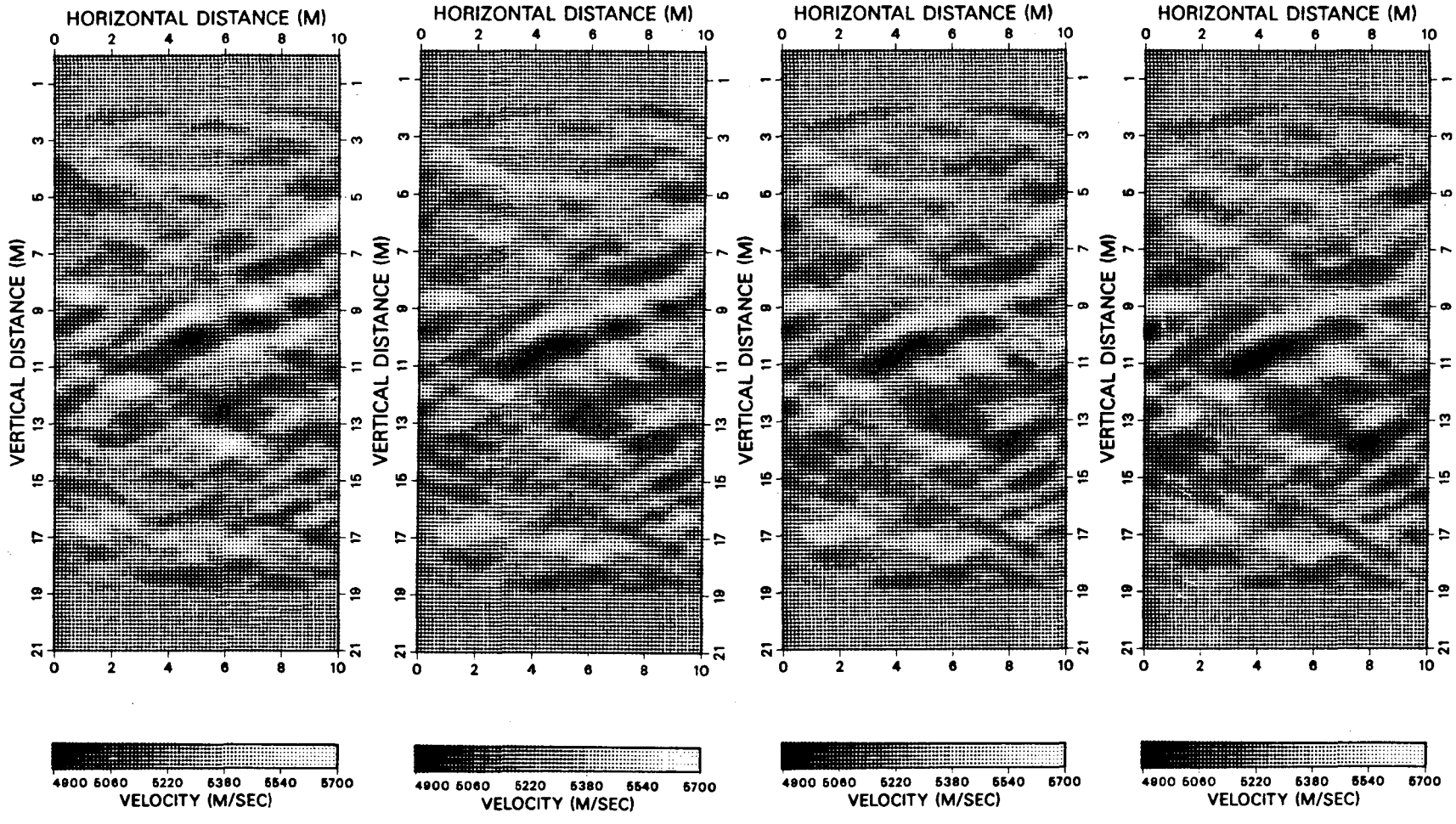

Figure 5.4.1a,b,c,d Crosshole EA backpropagation inversion of field data for $\theta = 150^{o}$ and for (left-to-right) a) $\pm$ 300 m/s, b) $\pm$ 150 m/s, c) $\pm$ 100 m/s and d) $\pm$ 50 m/s variation from the isotropy velocity of 5270 m/s along (+) and perpendicular to (-) the symmetry axis.

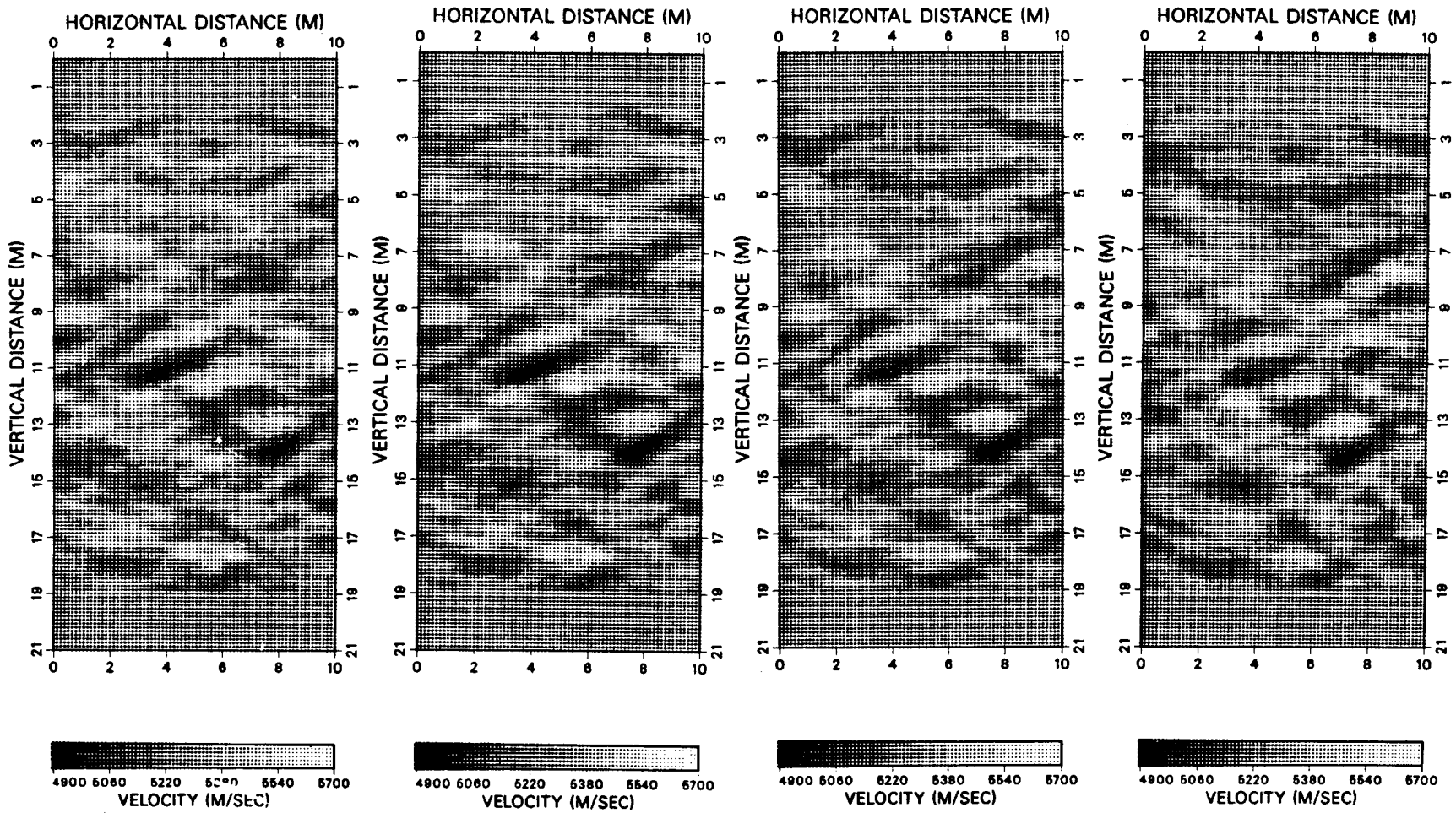

Figure 5.4.1e,f,g,h Crosshole EA backpropagation inversion of field data for $\theta = 60^{o}$ and for (left-to-right) e) $\pm$ 50 m/s, f) $\pm$ 100 m/s, g) $\pm$ 150 m/s and h) $\pm$ 300 m/s variation from the isotropy velocity of 5270 m/s along (+) and perpendicular to (-) the symmetry axis.

Chapter 6

Discussion and Conclusions

In this thesis, we have considered the development and application of waveform imaging methods to the problem of fracture detection and characterization. As observed by many researchers, the general inverse problem is a difficult one, therefore, we have made use of various common approximations suitable for the fracture detection problem. Before considering the conclusions we will briefly state which approximations were made, for what reasons, and why they are expected to work.

As can be seen in the theory presented, the general inverse problem is nonlinear. There have been many approaches to the nonlinear inverse problem (see Chapter 1) but in general these approaches have not proven successful in practice, at least in cases where the nonlinearity is strong. This is because most methods proposed are iterative in nature and as a result, if the discrepancy is large the iterations can diverge. In cases where the scattering is weak, linearized inversion of the data can produce good results. In the fracture case considered here, we expect the scattering to be weak and therefore use the Born approximation for linearization. The reason for the scattering being weak and the choice of the Born approximation arises from the fractures being thin structures forming sharp contrasts. For this reason another popular approximation, the Rytov approximation, is not used.

In the theory discussed, the background medium is assumed homogeneous. If the rock considered is homogeneous prior to fracturing, this approximation is expected to be quite valid. In the field case considered, the background granite can be assumed homogeneous, but in large scale applications where the considered rock can be inhomogeneous prior to fracturing, caution must be taken. With this approximation, the

analytical form of the exact Green's function can be used in the theory. If the background were assumed inhomogeneous, the Green's function would have to be obtained in an approximate form.

Finally, we have assumed the medium to be two-dimensional (2-D). In the specific field case we consider, the fractures intersect the inversion area near vertically, therefore, if the 3-D effects of the point sources and receivers are corrected for, as carried out in section 2.9, this approximation will be quite valid as well. We note that extension of the methods to 3-D will require data on planes rather than lines. In this case the free-space Green's function will have to be approximated, even for a homogeneous background, in order to obtain the plane-wave decomposition which is necessary for the inversion methods discussed here.

The analytical formulation obtained in the framework of these approximations gives considerable insight into the nature of the problem with its wavenumber domain coverage diagrams. Here, we extend these diagrams to the elastic and the transversely isotropic cases. Such diagrams, together with the a priori knowledge available, can and should be used in designing the experiments.

In the acoustic case the following conclusions can be drawn:

i) Averaging of inversions at various frequencies is useful in improving the inversion results and will also improve the signal-to-noise ratio and should therefore be carried out in field applications.

ii) When the parameter being imaged is assumed to be real (or the attenuation corrected for), a useful criterion for estimating the background velocity can be developed using the real to imaginary ratio of the resulting images.

iii) If a priori knowledge relevant to the parameters being imaged is available, it can be used in the quadratic programming method to constrain the inversion.

iv) As observed in the synthetic examples given here, including the total field in the inversions may not necessarily deteriorate the image quality. In addition, the total field effects can be removed after the inversion rather than before.

v) Free-surfaces cannot only be accounted for, but can also be used in the inversions to improve the results.

vi) The theory can and is extended to cases where the boreholes are slanted.

In the application of the methods to field data the following conclusions can be drawn:

i) For the methods to perform well on field data a comprehensive data processing scheme, such as the one developed here, must be used.

ii) The recovery of the scattering amplitudes and therefore the actual values of the physical parameters is a difficult task in field data applications.

iii) Separation or filtering of unwanted wavefields from the data forms another difficult task in the field data applications.

iv) Wave modes propagating with different velocities than the inversion velocity will not be able to interact constructively in the resulting images.

v) The inversion results indicate that the method is useful for fracture detection applications.

vi) The waveform inversion results give high-resolution images with respect to transmission ray tomography results.

In the elastic case the following conclusions can be drawn:

i) Properties of the operators acting on the parameters in the elastic case are used to obtain the individual parameters.

ii) This problem is in general ill-conditioned.

iii) The ill-conditioning can be reduced by a new method proposed which makes optimal use of the characteristics of the operators acting on the parameters.

iv) Due to the similarity in the inversion methods, all conclusions drawn for the acoustic case will hold for the elastic case.

v) The data processing techniques developed can be used in the elastic case with some modifications.

In the transverse isotropy case the following conclusions can be drawn:

i) Weak amounts of transverse isotropy can be accounted for by using an elliptical formulation for the quasi-P waves.

ii) The characteristics of the operators acting on the individual anisotropy parameters can be used once again to recover these parameters.

iii) For multi-parameter inversion in the transverse isotropy case, the axis of symmetry should be taken into consideration in the experiment setup.

iv) Due to the similarity in the inversion methods, all conclusions drawn in the acoustic wave case will hold for the SH-wave case in a transversely isotropic medium and the quasi-P wave case in an elliptically anisotropic medium.

v) The data processing techniques developed can and are used for the inversion of quasi-P waves in an elliptically anisotropic medium and can also be used for the inversion of SH-waves in a transversely isotropic medium.

vi) Application of the inversion methods accounting for an elliptically anisotropic medium to field data is seen to improve results in fractured medium applications. Inversion results indicate that the anisotropy may not be as strong as the levels observed from the first arrival time data.

Several improvements and developments can be brought to the investigated methods, besides improvements on the previously mentioned assumptions. These can be given as follows:

i) Extension of inversion methods to account for attenuation. This case can be formulated by considering Laplace transforms rather than Fourier transforms.

ii) Development of techniques and apparatus to accurately obtain the actual scattering amplitudes and to separate or eliminate the unwanted wavefields from the data.

iii) Development of quantitative methods for evaluating the quality of the obtained images and to form a basis for comparison of inversion results obtained with different methods. One such method could involve the generation of forward data using the inversion results and developing a method, possibly using the residual error, to compare this data set with the field data.

iv) Inversion for anisotropic parameters in an anisotropic medium. The methods given in Chapter 5 can be further developed to account for such cases.

v) The application of the elastic and anisotropic developments to scale model and field data.

Appendix A

Acoustic Green's Function

In this thesis, the Fourier transform over time and space are defined as

$$F(\omega) = \int_{-\infty}^{\infty} f(t)\exp[i\omega t]\,dt\,, \quad \text{and} \quad F(\vec{K}) = \int_{V\to\infty} f(\vec{R})\exp\left[-i\vec{K}\cdot\vec{R}\right]d\vec{R}\,. \qquad (A.1)$$

The solution of the homogeneous wave equation $\nabla^2\Phi + k^2\Phi = 0$, in the frequency domain can be obtained by taking a Fourier transform over x yielding $(\partial^2\Phi/\partial z^2) - k_x^2\Phi + k^2\Phi = 0$. As a result, the upgoing and downgoing wavefield satisfying the radiation condition is obtained as $\Phi^U = \exp[-ik_z z]$ for $z < z_s$, and $\Phi^U = \exp[+ik_z z]$ for $z > z_s$, where $k_z = \sqrt{k^2 - k_x^2}$.

The general 2-D inhomogeneous scalar wave equation in the frequency domain can be given as

$$K\frac{\partial^2 G_\Phi}{\partial x^2} + K\frac{\partial^2 G_\Phi}{\partial z^2} + \rho\omega^2 G_\Phi = -\,\delta(x - x_s)\delta(z - z_s), \qquad (A.2)$$

taking the Fourier transform over x

$$\frac{\partial^2 G_\Phi}{\partial z^2} - k_x^2 G_\Phi + k^2 G_\Phi = -\,\delta(z - z_s)\frac{\exp[-ik_x x_s]}{K}\,, \qquad (A.3)$$

where $k = \omega/c$ and $c^2 = K/\rho$. The solution of this equation can be given as $G_\Phi^D = a_1\Phi^D$ for $z > z_s$, and $G_\Phi^U = a_2\Phi^U$ for $z < z_s$, with $G_\Phi^D = G_\Phi^U$, and $(\partial G_\Phi^D/\partial z) - (\partial G_\Phi^U/\partial z) = -\exp[-ik_x x_s]/K$ at $z = z_s$. The second equation at $z = z_s$ is derived by integrating equation A.3 from $z_s + \Delta$ to $z_s - \Delta$ over z and letting $\Delta \to 0$. The coefficients a_1 and a_2 can be obtained using the above conditions or by solving

$$\begin{bmatrix} \exp[ik_z z_s] & -\exp[-ik_z z_s] \\ ik_z \exp[ik_z z_s] & ik_z \exp[-ik_z z_s] \end{bmatrix} \begin{bmatrix} a_1 \\ a_2 \end{bmatrix} = \begin{bmatrix} 0 \\ -K^{-1} \exp[-ik_x x_s] \end{bmatrix}. \tag{A.4}$$

Substituting the obtained coefficients and the solutions of the homogeneous equation, Φ^D and Φ^U, into the solution of the inhomogeneous equation, the Green's function is found to be

$$G_\Phi = \frac{i \exp[\, i(k_z |z - z_s| - k_x x_s)]}{2k_z K}, \tag{A.5}$$

taking the inverse Fourier transform over x

$$G_\Phi = \frac{i}{4K} \left[\frac{1}{\pi} \int_{-\infty}^{\infty} \frac{\exp[\, ik_z |z - z_s| + ik_x(x - x_s)]}{k_z} \, dk_x \right], \tag{A.6}$$

or

$$G_\Phi = \frac{i}{4K} H_0^{(1)}(\omega |\vec{r} - \vec{r}_s|/c), \tag{A.7}$$

where $H_0^{(1)}$ is the zero order Hankel function of the first-kind.

Equation A.2 will represent the inhomogeneous acoustic wave equation if the delta functions on the right-hand side are multiplied by K (compare equation A.2 with equation 2.1). This substitution will yield the Green's function for the acoustic case as

$$G_\Phi = \frac{i}{4} H_0^{(1)}(\omega |\vec{r} - \vec{r}_s|/c), \tag{A.8}$$

where c is now the acoustic wave velocity of the medium.

Appendix B

I. Decomposition of the Green's Function

The plane-wave decomposition of the 2-D Green's function along the source line can be given by writing the Green's function obtained in Appendix A as (see Morse and Feshbach, 1953, p.823)

$$G(\vec{r},\vec{r}_s) = \frac{i}{4K} H_0^{(1)}(k|\vec{r} - \vec{r}_s|) = \frac{i}{4K}\left[\frac{1}{i\pi^2}\iint_{-\infty}^{\infty} \frac{\exp[ik_z|z - z_s| + ik_x(x - x_s)]}{k_z^2 + k_x^2 - k^2}\, dk_x\, dk_z\right]. \tag{B.1}$$

This equation is in the form of a Fourier transform and from the rotation property of the Fourier transform can be given as

$$G(\vec{r},\vec{r}_s) = \frac{i}{4K}\left[\frac{1}{i\pi^2}\iint_{-\infty}^{\infty} \frac{\exp[ik_z'|z' - z_s'| + ik_x'(x' - x_s')]}{k_z'^2 + k_x'^2 - k^2}\, dk_x'\, dk_z'\right]. \tag{B.2}$$

The integration over k_z' can be evaluated yielding

$$G(\vec{r},\vec{r}_s) = \frac{i}{2K}\left[\frac{1}{2\pi}\int_{-\infty}^{\infty} \frac{\exp[ik_z'|z' - z_s'| + ik_x'(x' - x_s')]}{k_z'}\, dk_x'\right], \tag{B.3}$$

with $k_z' = \sqrt{k^2 - k_x'^2}$. For the decomposition over the source line we choose $k_x' = k_s$ where k_s is the wavenumber over the source line and $k_z' = \gamma_s$ where γ_s is the wavenumber perpendicular to the source line. With these substitutions, equation B.3 becomes

$$G(\vec{r},\vec{r}_s) = \frac{i}{2K}\left[\frac{1}{2\pi}\int_{-\infty}^{\infty} \frac{\exp\left[-ik\hat{s}\cdot\vec{r}_s\right]\exp\left[ik\hat{s}\cdot\vec{r}\right]}{\gamma_s}\, dk_s\right]. \tag{B.4}$$

To obtain this equation we assume $z' > z'_s = d_s$ with d_s being the perpendicular distance from the source line to the origin (see Figure 2.1.1a) and the appropriate sign associated with γ_s will be substituted depending on the inversion area being in between the source line and the origin or not. In addition, in this equation $\hat{s} = \bar{x}\frac{k_x^s}{k} + \bar{z}\frac{k_z^s}{k} = \tilde{x}\frac{k_s}{k} + \tilde{z}\frac{\gamma_s}{k}$, $\vec{r}_s = \bar{x}x_s + \bar{z}z_s = \tilde{x}x'_s + \tilde{z}d_s$ and $\vec{r} = \bar{x}x + \bar{z}z = \tilde{x}x' + \tilde{z}z'$. Equation B.4 is for an outgoing wave, if we consider an incoming wave or $\hat{s} \rightarrow -\hat{s}$ we have

$$G(\vec{r},\vec{r}_s) = \frac{i}{2K}\left[\frac{1}{2\pi}\int_{-\infty}^{\infty} \frac{\exp\left[ik\hat{s}\cdot\vec{r}_s\right]\exp\left[-ik\hat{s}\cdot\vec{r}\right]}{\gamma_s}\, dk_s\right]. \tag{B.5}$$

This equation can be given as

$$G(\vec{r},\vec{r}_s) = \frac{i}{2K}\left[\frac{1}{2\pi}\int_{-\infty}^{\infty} \left(\frac{\exp\left[i\gamma_s d_s\right]\exp\left[-ik\hat{s}\cdot\vec{r}\right]}{\gamma_s}\right)\exp\left[ik_s x'_s\right] dk_s\right]. \tag{B.6}$$

The last step is noting that the equation in brackets is in the form of an inverse Fourier transform, therefore we can write

$$G(\vec{r},k_s) = \frac{i}{2K\gamma_s}\exp\left[i\gamma_s d_s\right]\exp\left[-ik\hat{s}\cdot\vec{r}\right]. \tag{B.7}$$

This equation gives the individual components of the plane-wave decomposition of the 2-D Green's function along the source line. The plane-wave decomposition along the receiver line can be obtained by replacing the s's with g's in equation B.7.

II. Derivatives of the Green's Function

In applications concerning elastic wave propagation, the derivatives of the Green's function in the horizontal and vertical directions will be required. By partial differentiation or

$$\frac{\partial G}{\partial x} = \frac{\partial G}{\partial x'}\frac{\partial x'}{\partial x} + \frac{\partial G}{\partial z'}\frac{\partial z'}{\partial x},$$

$$\frac{\partial G}{\partial z} = \frac{\partial G}{\partial x'}\frac{\partial x'}{\partial z} + \frac{\partial G}{\partial z'}\frac{\partial z'}{\partial z}, \tag{B.8}$$

the derivatives of the Green's function can be obtained over the source or receiver lines. For the source line, from equation B.2 we have

$$\frac{\partial G}{\partial x} = ik_x' G\frac{\partial x'}{\partial x} + ik_z' \mathrm{sgn}(z' - z_s')G\frac{\partial z'}{\partial x},$$

$$\frac{\partial G}{\partial z} = ik_x' G\frac{\partial x'}{\partial z} + ik_z' \mathrm{sgn}(z' - z_s')G\frac{\partial z'}{\partial z}, \tag{B.9}$$

and a similar equation can be obtained for the receiver line by replacing the s's with g's.

The rotation from the unprimed to the primed axis is for a fixed angle for the source Green's function and again a fixed but different angle for the receiver Green's function. Since this angle is determined by the geometry of the source and receiver lines, we would like to obtain a general formula and substitute the associated values depending on the geometry considered. Therefore, we write the above equation as

$$\frac{\partial G^{s,g}}{\partial x} = ik_x^{s,g} G^{s,g},$$

$$\frac{\partial G^{s,g}}{\partial z} = ik_z^{s,g} G^{s,g}, \tag{B.10}$$

where $k_x^{s,g}$, $k_z^{s,g}$ are determined from k_s, γ_s, k_g, and γ_g for the geometry considered and $G^{s,g}$ can be given from equation B.7.

Appendix C

SH-wave Green's Function

In this appendix, we derive the SH-wave Green's function for a 2-D homogeneous background medium with the use of Appendix A.

The equation of motion in an elastic, isotropic medium can be given as

$$\rho \ddot{u}_i - (\lambda u_{k,k})_{,i} - (\mu(u_{i,j} + u_{j,i}))_{,j} = F_i \ . \tag{C.1}$$

In the y-direction or for i = y we have

$$\rho \ddot{u}_y - (\lambda u_{k,k})_{,y} - (\mu(u_{y,j} + u_{j,y}))_{,j} = F_y \ . \tag{C.2}$$

In the 2-D case, $(u_{k,k})_{,y} = \lambda_{,y} = u_{j,yj} = 0$ and for a homogeneous background medium $\mu_{,j} = 0$, therefore we have

$$\rho \ddot{u}_y - \mu u_{y,xx} - \mu u_{y,zz} = F_y \ . \tag{C.3}$$

To obtain the homogeneous background Green's function we write the explicit form of equation C.3 in the frequency domain for a line source and measurements in the y-direction as

$$\rho \omega^2 G_{yy} + \mu G_{yy,xx} + \mu G_{yy,zz} = - \delta(x - x_s)\delta(z - z_s) \ . \tag{C.4}$$

We see that this equation is identical to equation A.2 (Appendix A) with $K = \mu$. Therefore, using equation A.5, we can write

$$G_{yy} = \frac{i \exp[i(k_z|z - z_s| - k_x x_s)]}{2k_z\mu} \ , \tag{C.5}$$

or taking the inverse Fourier transform over x

$$G_{yy} = \frac{i}{4\mu} H_0^{(1)}(\omega|\vec{r} - \vec{r}_s|/\beta) \ , \tag{C.6}$$

where β is the shear wave velocity of the medium.

Following Appendix B, the individual components of the plane-wave decomposition of the Green's function along the source line can be given as

$$G_{yy}(\vec{r},k_s) = \frac{i}{2\mu\gamma_s} \exp[i\gamma_s d_s] \exp\left[- ik\hat{s}\cdot\vec{r}\right] , \tag{C.7}$$

where now $k = \omega/\beta$ and the decomposition along the receiver line can be obtained by replacing the s's with g's in equation C.7.

Appendix D

P-SV wave Green's Function

In this appendix, the P-SV wave Green's function for a 2-D medium with a homogeneous background is derived following Eastwood (1988).

The equation of motion in an elastic, isotropic medium was given in Appendix C as

$$\rho \ddot{u}_i - (\lambda u_{k,k})_{,i} - (\mu(u_{i,j} + u_{j,i}))_{,j} = F_i \,. \tag{D.1}$$

For a homogeneous background 2-D medium, in the x-direction or for i = x we have

$$\rho \ddot{u}_x - \lambda(u_{x,xx} + u_{z,xz}) - 2\mu u_{x,xx} - \mu(u_{x,zz} + u_{z,xz}) = F_x \,, \tag{D.2}$$

and in the z-direction or for i = z we have

$$\rho \ddot{u}_z - \lambda(u_{x,xz} + u_{z,zz}) - 2\mu u_{z,zz} - \mu(u_{x,xz} + u_{z,zz}) = F_z \,. \tag{D.3}$$

The displacements can be represented in terms of potentials (Aki and Richards, 1980, p.68) as

$$\begin{bmatrix} u_x \\ u_z \end{bmatrix} = \begin{bmatrix} \phi_{,x} \\ \phi_{,z} \end{bmatrix} + \begin{bmatrix} -\psi_{,z} \\ \psi_{,x} \end{bmatrix} \quad \text{and} \quad \begin{bmatrix} F_x \\ F_z \end{bmatrix} = \begin{bmatrix} \Phi_{,x} \\ \Phi_{,z} \end{bmatrix} + \begin{bmatrix} -\Psi_{,z} \\ \Psi_{,x} \end{bmatrix}, \tag{D.4}$$

where the potentials satisfy

$$\ddot{\phi} - \alpha^2 \nabla^2 \phi = \Phi/\rho \,;$$

$$\ddot{\psi} - \beta^2 \nabla^2 \psi = \Psi/\rho \,, \tag{D.5}$$

with $\alpha = \sqrt{(\lambda + 2\mu)/\rho}$ being the P-wave velocity and $\beta = \sqrt{\mu/\rho}$ the S-wave velocity in the considered medium. Referring to Appendix A, the upgoing and downgoing wavefields for the potentials can be given in the Fourier transform domain as

$$\phi^D = \exp[ik_z^\alpha z] \quad \text{and} \quad \psi^D = \exp[ik_z^\beta z] \quad \text{for } z > z_s ,$$

$$\phi^U = \exp[-ik_z^\alpha z] \quad \text{and} \quad \psi^U = \exp[-ik_z^\beta z] \quad \text{for } z < z_s . \tag{D.6}$$

Rewriting the explicit form of equations D.2 and D.3 in the frequency domain we obtain

$$\begin{bmatrix} (\lambda + 2\mu)\partial_x^2 + \mu\partial_z^2 + \rho\omega^2 & (\lambda + \mu)\partial_x\partial_z \\ (\lambda + \mu)\partial_x\partial_z & (\lambda + 2\mu)\partial_z^2 + \mu\partial_x^2 + \rho\omega^2 \end{bmatrix} \begin{bmatrix} G_{xx} & G_{xz} \\ G_{zx} & G_{zz} \end{bmatrix} =$$

$$-\begin{bmatrix} \delta(x - x_s)\delta(z - z_s) & 0 \\ 0 & \delta(x - x_s)\delta(z - z_s) \end{bmatrix} . \tag{D.7}$$

Taking the Fourier transform over x

$$\begin{bmatrix} -(\lambda + 2\mu)k_x^2 + \mu\partial_z^2 + \rho\omega^2 & i(\lambda + \mu)k_x\partial_z \\ i(\lambda + \mu)k_x\partial_z & (\lambda + 2\mu)\partial_z^2 - \mu k_x^2 + \rho\omega^2 \end{bmatrix} \begin{bmatrix} \tilde{G}_{xx} & \tilde{G}_{xz} \\ \tilde{G}_{zx} & \tilde{G}_{zz} \end{bmatrix} =$$

$$-\begin{bmatrix} \delta(z - z_s) & 0 \\ 0 & \delta(z - z_s) \end{bmatrix} \exp[-ik_x x_s] . \tag{D.8}$$

Using the potentials and equation D.4, the solution of equation D.8 can be given as

$$\tilde{G}^D = \begin{bmatrix} ic_1k_x\phi^D - c_3\partial_z\psi^D & ic_5k_x\phi^D - c_7\partial_z\psi^D \\ c_1\partial_z\phi^D + ic_3k_x\psi^D & c_5\partial_z\phi^D + ic_7k_x\psi^D \end{bmatrix} \quad \text{for } z > z_s ,$$

$$\tilde{G}^U = \begin{bmatrix} ic_2k_x\phi^U - c_4\partial_z\psi^U & ic_6k_x\phi^U - c_8\partial_z\psi^U \\ c_2\partial_z\phi^U + ic_4k_x\psi^U & c_6\partial_z\phi^U + ic_8k_x\psi^U \end{bmatrix} \quad \text{for } z < z_s , \tag{D.9}$$

with the conditions,

$$\tilde{G}^D = \tilde{G}^U \quad \text{and} \quad \partial_z\tilde{G}^D - \partial_z\tilde{G}^U = -\begin{bmatrix} 1/\mu & 0 \\ 0 & 1/(\lambda + 2\mu) \end{bmatrix} \exp[-ik_x x_s] . \tag{D.10}$$

Solving for the coefficients c_1 to c_8 we get

$$c_1 = c_2 = \frac{k_x}{2\rho\omega^2 k_z^\alpha} , \quad c_4 = -c_3 = c_5 = -c_6 = \frac{1}{2\rho\omega^2} , \quad c_7 = c_8 = \frac{k_x}{2\rho\omega^2 k_z^\beta} . \tag{D.11}$$

Substituting back

$$\widetilde{G} = \begin{bmatrix} k_x^2 & \mathrm{sgn}(z - z_s)k_x k_z^\alpha \\ \mathrm{sgn}(z - z_s)k_x k_z^\alpha & (k_z^\alpha)^2 \end{bmatrix} \frac{i \exp[ik_z^\alpha|z - z_s|] \exp[-ik_x x_s]}{2\rho\omega^2 k_z^\alpha}$$

$$+ \begin{bmatrix} (k_z^\beta)^2 & \mathrm{sgn}(z_s - z)k_x k_z^\beta \\ \mathrm{sgn}(z_s - z)k_x k_z^\beta & k_x^2 \end{bmatrix} \frac{i \exp[ik_z^\beta|z - z_s|] \exp[-ik_x x_s]}{2\rho\omega^2 k_z^\beta}, \qquad \text{(D.12)}$$

or equivalently

$$\widetilde{G} = \begin{bmatrix} \dfrac{\partial^2}{\partial x^2} & \dfrac{\partial^2}{\partial x^2 \partial z^2} \\ \dfrac{\partial^2}{\partial x^2 \partial z^2} & \dfrac{\partial^2}{\partial z^2} \end{bmatrix} \frac{\exp[ik_z^\alpha|z - z_s| - ik_x x_s]}{-i2\rho\omega^2 k_z^\alpha} + \begin{bmatrix} \dfrac{\partial^2}{\partial z^2} & \dfrac{-\partial^2}{\partial x^2 \partial z^2} \\ \dfrac{-\partial^2}{\partial x^2 \partial z^2} & \dfrac{\partial^2}{\partial x^2} \end{bmatrix} \frac{\exp[ik_z^\beta|z - z_s| - ik_x x_s]}{-i2\rho\omega^2 k_z^\beta}.$$

(D.13)

Taking the inverse Fourier transform we have

$$G = \begin{bmatrix} \dfrac{\partial^2}{\partial x^2} & \dfrac{\partial^2}{\partial x^2 \partial z^2} \\ \dfrac{\partial^2}{\partial x^2 \partial z^2} & \dfrac{\partial^2}{\partial z^2} \end{bmatrix} \int_{-\infty}^{\infty} \frac{\exp[ik_z^\alpha|z - z_s| + ik_x(x - x_s)]}{-i2\rho\omega^2 k_z^\alpha} dk_x$$

$$+ \begin{bmatrix} \dfrac{\partial^2}{\partial z^2} & \dfrac{-\partial^2}{\partial x^2 \partial z^2} \\ \dfrac{-\partial^2}{\partial x^2 \partial z^2} & \dfrac{\partial^2}{\partial x^2} \end{bmatrix} \int_{-\infty}^{\infty} \frac{\exp[ik_z^\beta|z - z_s| + ik_x(x - x_s)]}{-i2\rho\omega^2 k_z^\beta} dk_x. \qquad \text{(D.14)}$$

Once again following Appendix B, the individual components of the plane-wave decomposition of the Green's function along the source line can be given as

$$\widetilde{G}(\vec{r}, k_s) = \frac{i}{2\rho\omega^2} \begin{bmatrix} (k_x^s)^2 & {}^\alpha k_z^s k_x^s \\ {}^\alpha k_z^s k_x^s & ({}^\alpha k_z^s)^2 \end{bmatrix} \frac{\exp[i\gamma_s^\alpha d_s - ik^\alpha \hat{s}\cdot\vec{r}]}{\gamma_s^\alpha}$$

$$+ \frac{i}{2\rho\omega^2} \begin{bmatrix} ({}^\beta k_z^s)^2 & -{}^\beta k_z^s k_x^s \\ -{}^\beta k_z^s k_x^s & (k_x^s)^2 \end{bmatrix} \frac{\exp[i\gamma_s^\beta d_s - ik^\beta \hat{s}\cdot\vec{r}]}{\gamma_s^\beta}, \qquad \text{(D.15)}$$

with

$$\tilde{\mathbf{G}} = \begin{bmatrix} \tilde{G}_{xx} & \tilde{G}_{xz} \\ \tilde{G}_{zx} & \tilde{G}_{zz} \end{bmatrix}, \tag{D.16}$$

where $k^{\alpha} = \omega/\alpha$, $k^{\beta} = \omega/\beta$ and ${}^{\alpha}k_z^s$ and ${}^{\beta}k_z^s$ are respectively the vertical wavenumbers over the source line for the P and S-waves. The decomposition along the receiver line can be obtained by replacing the s's with g's in equation D.15.

Appendix E

SH-waves in a Transversely Isotropic Medium

The 2-D inhomogeneous SH-wave equation in a transversely isotropic medium is derived here following Auld (1973) and Meadows (1985).

The equilibrium of momentum in an elastic anisotropic medium can be given as

$$\sigma_{ij,j} = \rho \ddot{u}_i - f_i \,, \tag{E.1}$$

where $\ddot{u}_i$ is the second derivative of the component of displacement in the i *th* direction over time, f_i is the component of force acting in the i *th* direction and $\sigma_{ij,j}$ is the derivative of the stress tensor in the j *th* direction.

Hooke's law in an anisotropic medium can be given as $\sigma_{ij} = c_{ijkl}e_{kl}$ with $e_{ij} = \frac{1}{2}(u_{i,j} + u_{j,i})$. In a transversely isotropic medium with the axis of symmetry along the z-axis or vertical direction this equation becomes

$$\vec{\sigma} = \begin{bmatrix} \sigma_{xx} \\ \sigma_{yy} \\ \sigma_{zz} \\ \sigma_{yz} \\ \sigma_{xz} \\ \sigma_{xy} \end{bmatrix} = \begin{bmatrix} C_{11} & C_{12} & C_{13} & & & \\ C_{12} & C_{11} & C_{13} & & 0 & \\ C_{13} & C_{13} & C_{33} & & & \\ & & & C_{55} & & \\ & 0 & & & C_{55} & \\ & & & & & C_{66} \end{bmatrix} \begin{bmatrix} \varepsilon_{xx} \\ \varepsilon_{yy} \\ \varepsilon_{zz} \\ 2\varepsilon_{yz} \\ 2\varepsilon_{xz} \\ 2\varepsilon_{xy} \end{bmatrix} = C \cdot \vec{\varepsilon} \,, \tag{E.2}$$

where $\vec{\sigma}$ is now the abbreviated stress vector, $\vec{\varepsilon}$ is the abbreviated strain vector and **C** is the elastic parameter matrix in the transversely isotropic medium with an axis of symmetry in the vertical direction and with $C_{12} = C_{11} - 2C_{66}$.

The SH-wave equation in a homogeneous transversely isotropic elastic medium whose axis of symmetry lies in the (x',z') plane along the z'-axis, which is a clockwise rotation from the vertical or z-axis by an angle of θ, can be found by a transformation of the wave equation from the primed to the unprimed coordinate system. This requires the

rotation of the actual (unabbreviated) stress and strain tensors through an angle θ using a counterclockwise rotation operator or

$$\sigma_{ij} = a_{ik}a_{jl}\sigma'_{kl} ,$$

$$e_{ij} = a_{ik}a_{jl}e'_{kl} , \tag{E.3}$$

with

$$\mathbf{a} = \begin{bmatrix} \cos\theta & 0 & \sin\theta \\ 0 & 1 & 0 \\ -\sin\theta & 0 & \cos\theta \end{bmatrix} . \tag{E.4}$$

The Bond stress transformation (Auld, 1973, p. 75) is obtained by substituting the abbreviated forms of equation E.3 into equation E.2 yielding

$$\vec{\sigma} = \mathbf{M}\mathbf{C}'\mathbf{M}^{\mathbf{T}}\vec{\varepsilon} , \tag{E.5}$$

where

$$\mathbf{M} = \begin{bmatrix} \cos^2\theta & 0 & \sin^2\theta & 0 & \sin 2\theta & 0 \\ 0 & 1 & 0 & 0 & 0 & 0 \\ \sin^2\theta & 0 & \cos^2\theta & 0 & -\sin 2\theta & 0 \\ 0 & 0 & 0 & \cos\theta & 0 & -\sin\theta \\ \frac{-\sin 2\theta}{2} & 0 & \frac{\sin 2\theta}{2} & 0 & \cos 2\theta & 0 \\ 0 & 0 & 0 & \sin\theta & 0 & \cos\theta \end{bmatrix} , \tag{E.6}$$

and

$$\vec{\sigma} = \mathbf{M}\vec{\sigma}' ,$$

$$\vec{\varepsilon} = \mathbf{M}^{\mathbf{T}^{-1}}\vec{\varepsilon}' ,$$

$$\mathbf{C} = \mathbf{M}\mathbf{C}'\mathbf{M}^{\mathbf{T}} . \tag{E.7}$$

The 2-D inhomogeneous SH-wave equation can obtained from equation E.1 as

$$\rho \ddot{u}_y = \sigma_{yx,x} + \sigma_{yz,z} + f_y \,, \tag{E.8}$$

where

$$\sigma_{yx} = 2\varepsilon_{yz}C_{64} + 2\varepsilon_{xy}C_{66} \,,$$

$$\sigma_{yz} = 2\varepsilon_{yz}C_{44} + 2\varepsilon_{xy}C_{46} \,. \tag{E.9}$$

Using $\mathbf{C} = \mathbf{M}\,\mathbf{C}'\,\mathbf{M}^T$ we find

$$C_{44} = M_{44}C'_{44}M_{44} + M_{46}C'_{66}M_{46} \,,$$

$$C_{66} = M_{64}C'_{44}M_{64} + M_{66}C'_{66}M_{66} \,,$$

$$C_{64} = M_{64}C'_{44}M_{44} + M_{66}C'_{66}M_{46} \,,$$

$$C_{46} = M_{44}C'_{44}M_{64} + M_{46}C'_{66}M_{66} \,. \tag{E.10}$$

Substituting the values of M_{ij} from equation E.6 and using $C'_{44} = C'_{55}$ we get

$$\rho \ddot{u}_y = ([C_{66}\cos^2\theta + C_{55}\sin^2\theta]u_{y,x} + [\sin\theta\cos\theta\,(C_{55} - C_{66})]u_{y,z})_{,x}$$

$$+ ([C_{55}\cos^2\theta + C_{66}\sin^2\theta]u_{y,z} + [\sin\theta\cos\theta\,(C_{55} - C_{66})]u_{y,x})_{,z} + f_y \,, \tag{E.11}$$

where the primes are removed from the C_{ij} for convenience. For a homogeneous transversely isotropic medium this equation becomes

$$\rho \ddot{u}_y = [C_{66}\cos^2\theta + C_{55}\sin^2\theta]u_{y,xx} + [2\sin\theta\cos\theta\,(C_{55} - C_{66})]u_{y,xz}$$

$$+ [C_{55}\cos^2\theta + C_{66}\sin^2\theta]u_{y,zz} + f_y \,, \tag{E.12}$$

as the 2-D SH-wave equation in a homogeneous medium.

Appendix F

SH-wave Green's Function for Transverse Isotropy

In this appendix, we derive the SH-wave Green's function in a homogeneous 2-D transversely isotropic medium.

The equation we are considering was derived in Appendix E and for the source-free homogeneous case can be given as

$$A^0\Phi_{,xx} + 2B^0\Phi_{,xz} + C^0\Phi_{,zz} - \rho\ddot{\Phi} = 0 , \tag{F.1}$$

with

$$A^0 = C^0_{66}\cos^2\theta + C^0_{55}\sin^2\theta ,$$

$$B^0 = \sin\theta\cos\theta\,(C^0_{55} - C^0_{66}) ,$$

$$C^0 = C^0_{55}\cos^2\theta + C^0_{66}\sin^2\theta . \tag{F.2}$$

Taking a Fourier transform, as defined in Appendix A, over x, z and t we get

$$k_x^2A^0\Phi + 2k_xk_zB^0\Phi + k_z^2C^0\Phi - \rho\omega^2\Phi = 0 , \tag{F.3}$$

which yields the dispersion relation for SH-waves in a transversely isotropic medium to be

$$k_z = k_z^I \pm k_z^{II} = -\frac{B^0k_x}{C^0} \pm \frac{\sqrt{(B^0k_x)^2 + C^0\rho\omega^2 - C^0A^0k_x^2}}{C^0} . \tag{F.4}$$

Returning to equation F.1 and taking the Fourier transform over x and t we get

$$-k_x^2A^0\Phi + 2ik_xB^0\Phi_{,z} + C^0\Phi_{,zz} + \rho\omega^2\Phi = 0 . \tag{F.5}$$

Therefore, using the dispersion relation, the upgoing and downgoing wavefield can be given as $\Phi^D = \exp[i(k_z^I + k_z^{II})z]$ for $z > z_s$, and $\Phi^U = \exp[i(k_z^I - k_z^{II})z]$ for $z < z_s$.

The general 2-D inhomogeneous SH-wave equation in the frequency domain can be given from Appendix E as

$$A^0 G_{\Phi,xx} + 2B^0 G_{\Phi,xz} + C^0 G_{\Phi,zz} + \rho\omega^2 G_\Phi = -\,\delta(x - x_s)\delta(z - z_s)\,. \tag{F.6}$$

Taking the Fourier transform over x we have

$$G_{\Phi,zz} + ik_x \frac{2B^0}{C^0} G_{\Phi,z} - k_x^2 \frac{A^0}{C^0} G_\Phi + \frac{\rho\omega^2}{C^0} G_\Phi = -\,\delta(z - z_s)\frac{\exp[-ik_x x_s]}{C^0}\,. \tag{F.7}$$

The solution of this equation can be given as $G_\Phi^D = a_1\Phi^D$ for $z > z_s$, and $G_\Phi^U = a_2\Phi^U$ for $z < z_s$, with $G_\Phi^D = G_\Phi^U$ and $(\partial G_\Phi^D/\partial z) - (\partial G_\Phi^U/\partial z) = -\exp[-ik_x x_s]/C^0$ at $z = z_s$. The coefficients a_1 and a_2 can be obtained from the above conditions or by solving

$$\begin{bmatrix} \exp[i(k_z^I + k_z^{II})z_s] & -\exp[i(k_z^I - k_z^{II})z_s] \\ i(k_z^I + k_z^{II})\exp[i(k_z^I + k_z^{II})z_s] & -i(k_z^I - k_z^{II})\exp[i(k_z^I - k_z^{II})z_s] \end{bmatrix} \begin{bmatrix} a_1 \\ a_2 \end{bmatrix} = \begin{bmatrix} 0 \\ -\dfrac{\exp[-ik_x x_s]}{C^0} \end{bmatrix}. \tag{F.8}$$

Substituting the obtained coefficients and the solutions Φ^D and Φ^U of the homogeneous equation, the Green's function is found to be

$$G_\Phi = \frac{i\,\exp\left[i\left(k_z^I \mathrm{sgn}(z - z_s) + k_z^{II}\right)|z - z_s| - i\,k_x x_s\right]}{2k_z^{II} C^0}\,. \tag{F.9}$$

Once again following Appendix B, the individual components of the plane-wave decomposition of the Green's function along the source line can be given as

$$G_\phi(\vec{r}, k_s) = \frac{i}{2C^0\gamma_s^{II}} \exp\left[i\left(-|\gamma_s^I| d_s + \gamma_s^{II} d_s\right)\right] \exp\left[-ik\hat{s}\cdot\vec{r}\right], \tag{F.10}$$

where $k = \omega/\beta$ and the decomposition along the receiver line can be obtained by replacing the s's with g's.

References

Aki, K., and Richards, P. G., 1980, Quantitative seismology, Theory and methods: vol. **1** & **2**, Freeman and Co., San Fransisco.

Auld, B. A., 1973, Acoustic fields and waves in solids, vol. 1: John Wiley and Sons, Inc.

Backus, G., 1965, Possible forms of seismic anisotropy in the uppermost mantle under oceans: Journal of Geophysical Research, **70**, 3429-3439.

Berggren, M. J., Johnson, S. A., Carruth, B. L., Kim, W. W., Stenger, F., and Kuhn, P. L., 1986, Performance of fast inverse scattering solutions for the exact Helmholtz equation using multiple frequencies and limited views: *in* Jones, H. W., Ed., Acoustical imaging, **15**, 193-201.

Beydoun, W. B., Cheng, C. H., and Toksöz, M. N., 1985, Detection of open fractures with vertical seismic profiling: J. Geophys. Res., **90**, 4557-4566.

Beydoun, W. B., and Mendes, M., 1989, Elastic ray-Born l_2-migration/inversion. J. Geophys. Res., **97**, 151-160.

Beylkin, G., and Burridge, R., 1990, Linearized inverse scattering problems in acoustics and elasticity: Wave motion, **12**, 15-52.

Brekhovskikh, L. M., 1980, Waves in layered media: Academic Press, p.239.

Boyse, W. E., and Keller, J. B., 1986, Inverse scattering in three dimensions: J. Acoust. Soc. Am., **79**, p. 215-218.

Carswell, A., and Moon, W. M., 1989, Application of multioffset vertical seismic profiling in fracture mapping: Geophysics, **54**, 737-746.

Chang, W. F., and McMechan, G. A., 1986, Reverse time migration of offset VSP data using the excitation-time imaging condition: Geophysics, **51**, 67-84.

Clayton, R. W., and Stolt, R. H., 1981, A Born-WKBJ inversion method for acoustic reflection data: Geophysics, **46**, 1559-1567.

Cohen, J. K., and Bleistein, N., 1979, Velocity inversion procedure for acoustic waves: Geophysics, **44**, 1077-1087.

Constable, S. C., Parker, R. L., and Constable, C. G., 1987, Occam's inversion: A practical algorithm for generating smooth models from electromagnetic sounding data: Geophysics, **52**, 289-300.

Crary, S., Boyeldieu, C., Brown, S., et al., 1987, Fracture detection with logs: The Technical Review, **37**, 22-34.

Dankbaar, J. W. M., 1985, Separation of P- and S- waves: Geophysical Prospecting, **33**, 970-986.

Dellinger, J., and Etgen, J., 1990, Wavefield separation in 2-D anisotropic media: Submitted to Geophysics.

Devaney, A. J., 1984, Geophysical diffraction tomography: IEEE Trans. Geosci. Remote Sensing, **GE-22**, 3-13.

---------- , 1985, Variable density acoustic tomography: J. Acoust. Soc. Am., **78**, 120-130.

Devaney, A. J., and Oristaglio, A. M., 1986, A plane-wave decomposition for elastic wave fields applied to the seperation of P-waves and S-waves in vector seismic data: Geophysics, **51**, 419-423.

Duchêne, B., Lesselier, D., and Tabbara, W., 1985, Diffraction tomography approach to acoustical imaging and media characterization: Optical Society of America, **2**, 1943-1953.

---------- , 1987, Acoustical imaging of 2D fluid buried in a half-space: A diffraction tomography approach: IEEE Trans. Ultrasonics, Ferroelectrics, and Frequency Control, **5**, 540-549.

----------, 1988, Experimental investigations of a diffraction tomography technique in fluid ultrasonics: IEEE Trans. Ultrasonics, Ferroelectrics, and Frequency Control, **4**, 437-444.

Eastwood, F. S., 1988, Preprint of Ph.D. thesis, Uni. of California at Berkeley, and personal communications.

Esmersoy, C., 1986, The backpropagated field approach to multidimensional velocity inversion: Ph.D. thesis, Massachusetts Institute of Technology.

Fehler, M., and Pearson, C., 1984, Cross-hole seismic surveys: Applications for studying subsurface fracture systems at a hot dry rock geothermal site: Geophysics, **49**, 37-45.

Gardner, G. H. F., 1985, Migration of seismic data: Geophisical reprint series, **4**, SEG, Tulsa, Oklahoma.

Gazdag, J., 1981, Modeling of the acoustic wave equation with transform methods: Geophysics, **46**, 854-859.

Geoltrain, S., and Cohen, J. K., 1989, Asymptotic solutions to direct and inverse scattering in anisotropic elastic media: Presented at the 59th Ann. Internat. Mtg. Soc. Expl. Geophys., Dallas, Texas.: Expanded abstracts, 938-942.

Green, A. G., and Mair, J. A., 1983, Subhorizontal fractures in a granitic pluton: Their detection and implications for radioactive waste disposal: Geophysics, **48**, 1428-1449.

Hardin, E. L., and Cheng, C. H., 1987, Fracture characterization by means of attenuation and generation of tube waves in fractured crystalline rock at Mirror lake, New Hampshire: J. Geophys. Res., **92**, 7989-8006.

Hornby, B. E., 1989, Imaging of near-borehole structure using full-waveform sonic data: Geophysics, **54**, 747-757.

Johnson, S. A., and Tracy, M. L., 1983, Inverse scattering solutions by a sinc basis, multiple source, moment method - Part I: Theory: Ultrasonic Imaging, **5**, 361-375.

Johnson, S. A., Zhou, Y., Tracy, M. L., Berggren, M. J., and Stenger, F., 1983, Inverse scattering solutions by a sinc basis, multiple source, moment method - Part III: Fast algorithms: Ultrasonic Imaging, **6**, 103-116.

Kak, A. C., and Slaney, M., 1987, Principles of computerized tomographic imaging: IEEE Press.

Kosloff, D. D., and Baysal, E., 1982, Forward modelling by a Fourier method: Geophysics, **47**, 1402-1412.

Le Bras, R., 1985, Methods of multiparameter inversion of seismic data using the acoustic and elastic Born approximations: Ph.D. thesis, Caltech.

Lesselier, D., and Vuillet-Laurent, D., 1985, Itterative solutions of some direct and inverse problems in electromagnetics and acoustics: Electromagnetics, **5**, 147-189.

Levin, F. K., 1979, Seismic velocities in transversely isotropic media: Geophysics, **44**, 918-936.

Lines, L. R., and Levin, F. K., 1988, Inversion of geophysical data: Geophysical reprint series, **9**, SEG, Tulsa, Oklahoma.

Lo, T., Toksöz, M. N., Xu, S., and Wu, R., 1988, Ultrasonic laboratory tests of geophysical tomographic reconstruction: Geophysics, **53**, 947-956.

Majer, E. L., McEvilly, T. V., Eastwood, F. S., and Myer, L. R., 1988, Fracture detection using P-wave and S-wave vertical seismic profiling at the Geysers: Geophysics, **53**, 76-84.

Majer, E. L., Peterson, J. E., Karasaki, K., Myer, L. R., Long, J. C. S., Martel, S. J., Blumling, P., and Vomvoris, S., 1990, Results of fracture research investigation: Lawrence Berkeley Laboratory report, LBL-27913, and NAGRA report, NDC-14.

Meadows, M. A., 1985, The inverse problem of a transversely isotropic elastic medium: Ph.D. Thesis, University of California, Berkeley.

Mora, P., 1987, Nonlinear two-dimensional elastic inversion of multioffset seismic data: Geophysics, **52**, 1211-1228.

Morse, M. P., and Feshbach, H., 1953, Methods of theoretical physics: vol. 1 & 2, Mc Graw-Hill book Co.

Norton, S. J., 1983, Generation of seperate density and compressibility images in tissue: Ultrasonic imaging, **5**, 240-252.

Olsson, O., Duran, O., Jamtlid, A., and Stenberg, L., 1984, Geophysical investigations in Sweden for the characterization of a site for radioactive waste disposal - An overview: Geoexploration, **22**, 187-201.

Özbek, A., 1988, Simultaneous linearized inversion of velocity and density profiles for multidimensional acoustic media: Submitted to J. Acoust. Soc. Am.

Peterson, J. E., Paulsson, B. N. P., and McEvilly, T. V., 1985, Applications of algebraic reconstruction techniques to crosshole seismic data: Geophysics, **50**, 1566-1580.

Peterson, J. E., 1986, The application of algebraic reconstruction techniques to geophysical problems: Ph.D. thesis, Uni. of California at Berkeley.

Pratt, R. G., and Worthington, M. H., 1988, The application of diffraction tomography to cross-hole seismic data: Geophyscis, **53**, 1284-1294.

Pratt, R.G., and Goultry, N. R., 1989, High resolution tomography using the wave equation; Results with physical data: Presented at the 59th Ann. Internat. Mtg. Soc. Expl. Geophys., Dallas, Texas.: Expanded abstracts, 70-74.

Stewart, R. R., Turpening, R. M., and Toksöz, M. N., 1981, Study of a subsurface fracture zone by vertical seismic profiling: Geophys. Res. Lett., **8**, 1132-1135.

Suau, J., and Gartner, J., 1980, Fracture detection from well logs: The Log Analyst, **21**, 3-13.

Tarantola, A., 1984, Inversion of seismic reflection data in the acoustic approximation: Geophysics, **49**, 1259-1266.

Tracy, M. L., and Johnson, S. A., 1983, Inverse scattering solutions by a sinc basis, multiple source, moment method - Part II: Numerical evaluation: Ultrasonic Imaging, **5**, 376-392.

Tura, M. A. C., and Zhou, Q., 1989, Diffraction and diffusion tomography: A comparitive study: Lawrence Berkeley Laboratory annual report (1988), LBL-26362.

Verwest, B. J., 1989, Seismic migration in eliptically anisotropic media, Geophysical Prospecting, **37**, 149-166.

White, J. E., 1982, Computed waveforms in transversely isotropic media: Geophysics, **47**, 771-783.

Wolf, E., 1969, Three-dimensional structure determination of semitransparent objects from holographic data: Optics Communications, **1**, 153-156.

Wong, J., Hurley, P., and West, G. F., 1984, Crosshole audiofrequency seismology in granitic rocks using piezoelectric transducers as sources and detectors: Geoexploration, **22**, 261-279.

Wu, R. and Aki, K., 1985, Scattering characteristics of elastic waves by an elastic heterogeneity: Geophysics, V.50, **4**, 582-595.

Wu, R. and Toksöz, M. N., 1987, Diffraction tomography and multisource holography applied to seismic imaging: Geophysics, **52**, 11-25.

Zhou, Q., 1989, Audio frequency electromagnetic numerical modeling and tomographic inversion for reservoir evaluation: Ph.D. thesis, Uni. of California at Berkeley.

LAWRENCE BERKELEY LABORATORY
TECHNICAL INFORMATION DEPARTMENT
1 CYCLOTRON ROAD
BERKELEY, CALIFORNIA 94720